

A Thesis Submitted for the Degree of PhD at the University of Warwick

Permanent WRAP URL:

<http://wrap.warwick.ac.uk/163171>

Copyright and reuse:

This thesis is made available online and is protected by original copyright.

Please scroll down to view the document itself.

Please refer to the repository record for this item for information to help you to cite it.

Our policy information is available from the repository home page.

For more information, please contact the WRAP Team at: wrap@warwick.ac.uk

Developing an aptamer-based biosensor against the phytohormone auxin

By

Sireethorn Tungsirisurp

A thesis submitted in partial fulfilment of the requirements for the degree of
Doctor of Philosophy in Biological Sciences

School of Life Sciences, University of Warwick

August, 2021

Table of contents

Table of Contents	i
List of Figures	vi
List of Tables	x
Acknowledgements	xii
Declarations	xiv
Abstract	xv
List of Abbreviations	xvi
Chapter 1 Introduction	1
1.1 Auxin and its physiology	2
1.2 Current techniques for phytohormones analysis	4
1.2.1 Mass Spectrometry	5
1.2.2 Biosensors	5
1.3 An aptamer-based biosensor	7
1.4 DNA aptamers as biosensor biological recognition	7
1.4.1 Aptamer selection methods	8
1.4.2 Developed aptamers against plant targets	12
1.4.2.1 ATP aptamer	12
1.4.2.2 ABA aptamer	13
1.4.2.3 Trans-zeatin aptamer	13
1.4.3 DNA aptamer affinity maturation techniques	14
1.5 Carbon-based polymer nanoparticles (CPNs) as biosensor delivery and signalling system	17
1.6 Aims and objectives	21
Chapter 2 Materials and Methodology	22
2.1 Materials and reagents	23
2.2 PCR optimisation	23
2.3 Direct-SELEX	24
2.3.1 Direct-SELEX library, primers, and control molecules	24
2.3.2 IAA-PEG and its immobilisation onto streptavidin-coated magnetic beads	24
2.3.3 Direct-SELEX process	25
2.4 Solution-SELEX	26
2.4.1 Solution-SELEX library, capture oligos, and primers	26
2.4.2 Immobilisation of capture oligos onto streptavidin-coated magnetic beads	27
2.4.3 Solution-SELEX process	27
2.5 Cloning and sequencing	29
2.6 Enzyme linked oligonucleotide assay (ELONA)	29

2.6.1	Preparation of SELEX sub-libraries for ELONA	29
2.6.2	Reagents, instrument, and streptavidin-coated 96-well plates	30
2.6.3	ELONA positive IAA immobilisation check with anti-IAA antibodies	30
2.6.4	ELONA biotinylated IAA concentration check with anti-IAA antibodies	31
2.6.5	ELONA	31
2.7	Microscale thermophoresis (MST)	32
2.7.1	MST instrumentation and software	32
2.7.2	Preparation of aptamer candidates for MST	32
2.7.3	MST binding check experiment	32
2.7.4	MST binding affinity experiment	32
2.7.5	Assay buffer screening	33
2.7.6	Aptamers specificity tests	33
2.7.7	Alternative MST using fluorescent auxins as target	34
2.7.7.1	Preparation of aptamer candidates for alternative MST experiments	34
2.7.7.2	Assay optimisation	35
2.7.7.3	MST binding check experiment	35
2.7.7.4	Aptamer-IAA binding affinity experiments	35
2.8	Thioflavin T (ThT) assay	35
2.8.1	Thioflavin T, assay buffer, and fluorescence measurements	35
2.8.2	Preparation of aptamer candidates for ThT assay	36
2.8.3	Assay optimisation	36
2.8.4	ATP aptamer for assay validation	36
2.8.5	ThT assay	36
2.9	Surface plasmon resonance (SPR)	37
2.9.1	Biacore platform and consumables	37
2.9.2	Biotinylated probe and poly-A tail aptamer candidates	37
2.9.3	Immobilisation of aptamer candidates	38
2.9.4	SPR assay	38
2.10	Isothermal titration calorimetry (ITC)	39
2.10.1	ITC instrumentations and assay buffer	39
2.10.2	Single injection method (SIM) mode	39
2.10.3	Serial injection experiments	40
2.11	Circular dichroism (CD)	40
2.11.1	Aptamer, IAA, and buffers	40
2.11.2	CD instrumentations and experimental parameters	40
2.12	Carbon-based polymer nanoparticles synthesis and characterisation	41
2.13	Plant samples preparations	41
2.13.1	<i>Arabidopsis Thaliana</i> and growth condition	41

2.13.2	<i>A. Thaliana</i> root protoplast isolation	42
2.13.2.1	Protoplast solutions and consumables	42
2.13.2.2	Protoplast isolation	42
2.13.3	Apoplastic fluid extraction	43
2.14	CPNs evaluation in plant samples	43
2.14.1	Stability evaluation under gel electrophoresis	43
2.14.2	Confocal microscopy	40
Chapter 3	Auxin aptamer selection through SELEX processes and secondary screenings	44
3.1	Selection of aptamers against IAA using direct-SELEX	45
3.2	Selection of aptamers against IAA using solution-SELEX	48
3.3	Comparative sequencing analysis of direct- and solution-SELEX	53
3.4	ELONA for primary screening of aptamer sub-libraries	56
3.4.1	Assay optimisation	56
3.4.2	ELONA assay	58
3.5	MST for secondary screening of aptamer candidates	61
3.5.1	Assay validation using fluorescent aptamers against ATP and ABA	61
3.5.2	Assay optimisations	62
3.5.3	Secondary screening of aptamer candidates against IAA dilution series	63
3.5.4	Fluorescent auxins as alternative MST screening	65
3.6	Discussion	68
Chapter 4	Affinity maturation of aptamer candidates to enhance binding affinity against IAA	70
4.1	Hybridisation inhibition (HI)	71
4.1.1	Hybridisation inhibition of ABapt	72
4.1.2	Hybridisation inhibition of ST-57	73
4.1.3	Hybridisation inhibition of ST-34d	73
4.2	Sequence truncation	74
4.2.1	Sequence truncation of ABapt	76
4.2.2	Sequence truncation of ST-57	77
4.3	Single G-mutations to improve IAA binding affinity	79
4.3.1	Single G-mutations on ST-57-5	80
4.3.2	Single G-mutations on STA-3	83
4.4	Optimisation of experimental conditions	86
4.5	Discussion	88

Chapter 5	Further characterisation of auxin aptamers towards development of a quantification assay	90
5.1	Auxin aptamer binding specificities	91
5.1.1	Binding specificity of STA-3	92
5.1.2	Binding specificity of STA-3-9	94
5.2	Salt composition effects on aptamer-IAA binding quality	95
5.2.1	STA-3 auxin binding quality in different salt compositions	96
5.2.2	STA-3-9 auxin binding quality in different salt compositions	98
5.3	Thioflavin T assay as fluorescence IAA quantification assay	100
5.3.1	Assay validation using an aptamer against ATP	100
5.3.2	Auxin quantification using STA-3 and STA-3-9 on ThT assay	101
5.4	SPR platform for IAA quantification assay	102
5.4.1	Assay validation using an aptamer against trans-zeatin	103
5.4.2	Auxin quantification by STA-3 and STA-3-9 on SPR platform	105
5.5	Further IAA aptamer characterisation	106
5.5.1	Isothermal titration calorimetry (ITC)	106
5.5.1.1	Assay validation using an aptamer against trans-zeatin	107
5.5.1.2	STA-3-9 IAA binding characterisation using ITC	108
5.5.2	CD for G-quadruplex structure characterisation	110
5.6	Discussion	112
Chapter 6	Aptamers and biosensor delivery and signalling system evaluation <i>in planta</i>	114
6.1	Aptamer stability evaluation in apoplastic fluid	115
6.2	Aptamer evaluation in <i>A. Thaliana</i> protoplasts	117
6.3	CPNs design and synthesis	118
6.4	Stability evaluation of CPNs samples in apoplastic fluid	121
6.5	CPN evaluation in intact roots of <i>A. Thaliana</i>	123
6.5.1	CPN surface charge effect on root penetrance and accumulation	123
6.5.2	CPN size effect on root penetrance and accumulation	127
6.5.3	CPN polymer chemistry effect on root penetrance and accumulation	130
6.5.4	Aptamer conjugated CPNs on root penetrance and accumulation	133
6.6	CPN time dependent evaluation in intact roots of <i>A. Thaliana</i>	136
6.7	CPN evaluation in isolated protoplasts from <i>A. Thaliana</i>	139
6.8	Discussion	143

Chapter 7	Conclusion and future work	150
7.1	SELEX processes can select auxin aptamers	152
7.2	Affinity maturation techniques can improve auxin binding affinities and specificities of the chosen aptamer candidates	153
7.3	The developed auxin aptamers can as biosensor recognition components in <i>A. Thaliana</i> seedlings	154
7.4	CPNs can be selected to target apoplast and evaluated as a suitable biosensor delivery and signalling system in <i>A. Thaliana</i> seedlings	156
7.5	A novel nano-sensor can be devised which may map auxin gradient <i>in planta</i> .	157
7.6	Future work	157
7.6.1	Further development of auxin aptamer as biosensor recognition component	157
7.6.2	Further development of CPNs as biosensor delivery and signalling system	159
	References	161
	Appendices	173
Appendix A:	Phylogenetic trees of SELEX sub-libraries	174
Appendix B:	Penetration level of negatively charged CPNs with different sizes followed the same trend as those of neutral CPNs	180
Appendix C:	A sheet-like accumulation of positively charged CPNs was observed regardless of the particle sizes	183
Appendix D:	Sheet-like accumulation of +(20 nm) around <i>A. Thaliana</i> intact roots over time	186

List of Figures

Figure 1.1	Chemical structure of tryptophan precursor and predominant auxin indole-3-acetic acid (IAA)	2
Figure 1.2	Simplified schematic depiction of auxin mediated gene expression (a) and auxin polar transport in plant (b).	3
Figure 1.3	A genetically encoded biosensor, R2D2, designed for intercellular, semi-quantitative auxin response.	4
Figure 1.4	General schematic illustration of the SELEX process for DNA aptamer.	9
Figure 1.5	The frequency or relative abundance of selected aptamer candidate “A” through successive rounds of SELEX.	11
Figure 2.1	Chemical structures of biotinylated IAA-PEG derivative and control molecules used in SELEX process.	24
Figure 2.2	Compounds and their chemical structures used for MST specificity tests.	33
Figure 2.3	Chemical structures of fluorescent auxins and benzoic acid used in MST secondary screening.	34
Figure 3.1	4% agarose gel electrophoresis of PCR optimisation.	46
Figure 3.2	4% agarose gel electrophoresis of PCR products using different volumes of product from first round of SELEX for IAA aptamers.	46
Figure 3.3	Schematic timeline of direct-SELEX process.	47
Figure 3.4	Chemical structures of control molecules used in SELEX process.	48
Figure 3.5	Solution-SELEX for selection of DNA aptamers against auxin.	49
Figure 3.6	Analysis of denaturing urea-PAGE of pool PCR products from first round of solution-SELEX showing SELEX product amplification.	50
Figure 3.7	Schematic workflow of overall solution-SELEX process.	52
Figure 3.8	Multiple sequence alignments of consensus sequences generated from clustering of sub-libraries by phylogenetic trees.	55
Figure 3.9	General scheme of ELONA assay.	56
Figure 3.10	ELONA positive immobilisation check using three different anti-IAA antibodies.	57
Figure 3.11	ELONA immobilisation concentration check.	58
Figure 3.12	ELONA was used to select IAA sensitive aptamers.	59
Figure 3.13	MST technique was validated using aptamers against ATP (a) and ABA (b).	61

Figure 3.14	Binding screening for MST experiments.	62
Figure 3.15	Analysis of fitted dose response curves of ST-57 and ST-49 preliminarily showed IAA binding.	64
Figure 3.16	Chemical structures of fluorescent auxins and benzoic acid used in MST secondary screening.	65
Figure 3.17	Analysis of fitted dose response curves of aptamer candidates against C2-NBA-IAA (a) and C2-NBD-benzoic acid (b) demonstrated some IAA binding.	67
Figure 4.1	Analysis of fitted dose response curves of ABapt HI experiment indicating potential use of HI for sequence optimisation.	72
Figure 4.2	Analysis of fitted dose response curves of ST-57 HI experiment indicated improvements in IAA binding.	73
Figure 4.3	No optimisation was observed from ST-34d HI experiments.	74
Figure 4.4	Sequence truncation of ABapt enhanced ABA binding.	76
Figure 4.5	Sequence truncation of ABapt revealed IAA binding affinity.	77
Figure 4.6	Detailed sequence truncation of ST-57 slightly improved IAA binding affinity.	78
Figure 4.7	G-mutation experiments on ST-57-5 improved IAA binding affinity by 50-fold.	82
Figure 4.8	Single G-mutation variants of STA-3 improved IAA binding.	85
Figure 4.9	Analysis of fitted dose response curves of Cy-5 aptamers in different buffers showed optimal IAA binding.	88
Figure 5.1	Chemical structures of compounds used for auxin aptamers specificity evaluations.	92
Figure 5.2	Analysis of fitted dose response curves revealed moderate auxin binding specificity of STA-3.	92
Figure 5.3	Enhanced binding specificity was observed with STA-3-9.	94
Figure 5.4	Analysis of fitted dose response curves of STA-3 showed different IAA binding ability in different salt compositions.	97
Figure 5.5	Analysis of fitted dose response curves of STA-3-9 indicated salt composition effect on IAA binding.	99
Figure 5.6	ThT assay was validated with aptamer against ATP.	101
Figure 5.7	Analysis of ThT assay of STA-3 and STA-3-9 showed no dose dependent fluorescence change.	102
Figure 5.8	SPR platform was validated using tZ aptamer against tZ dilution series.	103

Figure 5.9	Binding specificity of tZ aptamer could be evaluated through SPR platform.	104
Figure 5.10	SPR buffer screening analysis of STA-3-9 did not show positive IAA binding.	105
Figure 5.11	tZ binding of tZ aptamer could be evaluated using ITC.	108
Figure 5.12	The analysis of ITC thermogram of IAA to STA-3-9 single injection showed no significant enthalpy change due to IAA binding interaction.	109
Figure 5.13	No buffer effect was observed in the analysis of CD spectra of STA-3-9.	110
Figure 5.14	CD spectra analysis of STA-3-9 in absence (red) and presence (blue) of 250 μ M IAA revealed no conformational change of aptamer upon IAA interaction.	111
Figure 5.15	The analysis of CD thermal melt experiments of STA-3-9 in absence (red) and presence (blue) of 250 μ M IAA did not show significant shift in melting temperature of the aptamer upon IAA binding.	112
Figure 6.1	Stability of unmodified (a, left panel) and fluorescent (b, right panel) aptamers was reduced upon incubation in extracted apoplastic fluid from <i>Nicotiana benthamiana</i> leaves (Ap) in comparison to those incubated in distilled water (w).	116
Figure 6.2	Integrated density of unmodified (a) and fluorescent (b) aptamers suggested degradation in apoplastic fluid (pattern cyan) in comparison to those in water (solid blue).	116
Figure 6.3	High accumulation of Cy5-STA-3-9 in cell debris while no penetration was observed in protoplasts.	117
Figure 6.4	Chemical structures of monomers used for the synthesis of various CPNs (Table 6.1).	120
Figure 6.5	Preliminary fluorescence evaluation of BODIPY-CPNs under UV light showed no visual difference in the fluorescence intensities between samples.	121
Figure 6.6	Comparable stability of CPNs upon incubation in extracted apoplastic fluid from <i>Nicotiana benthamiana</i> leaves (Ap) in comparison to those incubated in distilled water (w).	122
Figure 6.7	Neutral and negatively charged CPNs were stable in apoplastic fluid (pattern cyan) and in water (solid blue).	122
Figure 6.8	No autofluorescence of plant compounds detected in untreated <i>A. thaliana</i> roots using BODIPY settings.	123
Figure 6.9	Surface charges of small CPNs significantly affected penetrance and accumulation in <i>A. thaliana</i> root tips.	124

Figure 6.10	Surface charges of small CPNs significantly affected penetrance and accumulation in <i>A. thaliana</i> root hair zones.	125
Figure 6.11	Cross-section images of root hair zones revealed different level of the cell penetrance and uptake level of small CPNs with different surface charges.	126
Figure 6.12	Significant influence of CPN size on penetrance in <i>A. Thaliana</i> root tips.	128
Figure 6.13	CPN size significantly affected penetration in <i>A. Thaliana</i> root hair zones.	129
Figure 6.14	Polymer compositions of neutral CPNs demonstrated an effect on penetration in different root tip cell types.	130
Figure 6.15	Polymer compositions of neutral CPNs revealed a cell-specific accumulation and penetrance in root hair zones.	131
Figure 6.16	Cross-section images of root hair zones revealed a cell-specific penetrance and uptake of N ₁ (20 nm) and N _z (19 nm).	132
Figure 6.17	Aptamer conjugated CPNs demonstrated similar uptake and penetrance behaviours as their core CPNs in root tips.	133
Figure 6.18	Aptamer conjugated CPNs demonstrated similar uptake and penetrance behaviours as their core CPNs in root hair zones.	134
Figure 6.19	N ₁ (ATPapt) did not demonstrate FRET.	136
Figure 6.20	Cell penetrance and root uptake of Θ (25 nm) was time dependent in contrast to the accumulation of N ₁ (20 nm) and N _z (19 nm).	137
Figure 6.21	N ₁ (ATPapt) revealed time-independent accumulation in root hair zones.	138
Figure 6.22	Surface charges of small CPN samples (20 nm \varnothing) influenced accumulation and toxicity in protoplasts.	139
Figure 6.23	Sizes of neutral CPNs influenced penetrance in protoplasts and accumulation in cell debris.	141
Figure 6.24	Sizes of positively charged CPNs did not adversely affect the cytotoxicity level in protoplasts.	142
Figure 7.1	Schematic illustration of the optimal aptasensor deployed in apoplastic matrix as suitable tool to map intercellular auxin gradient <i>in planta</i> .	160

List of Tables

Table 1.1	Features of nucleic acid aptamers and monoclonal antibodies.	8
Table 1.2	Comparison of different types of selection processes.	10
Table 1.3	Comparison of different types of nanoparticles developed for bioimaging application.	19
Table 2.1	Sequences of SELEX libraries, primers, and capture oligos.	23
Table 2.2	Different conditions of PCR reaction optimised.	24
Table 2.3	PCR setup for products from each round of direct-SELEX.	26
Table 2.4	PCR setup for products from each round of solution-SELEX.	28
Table 2.5	Summary of plasmid DNA sent for GATC sequencing.	29
Table 2.6	Compositions of all buffers used in experimental analysis	33
Table 2.7	Lists of aptamer sequences performed on Biacore platform.	38
Table 2.8	Samples loaded on the sample cell and auto-pipette for SIM mode.	39
Table 2.9	Injection (a) parameters for SIM mode experiments and experimental (b) parameters set on VPViewer for all ITC measurements except stated otherwise.	40
Table 2.10	Buffer composition of protoplast (a) and enzyme (b) solutions used for protoplast isolation.	42
Table 3.1	Summary of SELEX products sent for sequencing.	53
Table 3.2	Names and sequences of aptamer candidates selected for MST secondary screening.	60
Table 3.3	Buffer screening for MST experiments.	63
Table 3.4	MST binding affinity data of ST-57 and ST-49.	64
Table 3.5	Optimised concentrations of fluorescent auxins and benzoic acid.	66
Table 3.6	Qualitative analysis of binding interactions between aptamer candidates and fluorescent auxins and benzoic acid.	67
Table 4.1	Oligonucleotide probes used for hybridisation inhibition (HI) experiments.	71
Table 4.2	All truncated variants of ABAPt and ST-57 used in aptamer sequence optimisation.	75
Table 4.3	Estimated K_D values of ST-57 and its truncated variants from MST binding experiments.	79
Table 4.4	ST-57-5 and its mutated variants for sequence optimisation experiments.	80

Table 4.5	MST qualitative binding to determine positive IAA binding of ST-57-5 and its mutated variants.	81
Table 4.6	Estimated K_D of ST-57-5 and its mutated variants from MST binding experiments.	82
Table 4.7	Mutated variants of STA-3 synthesized for sequence optimisation experiments.	83
Table 4.8	MST qualitative binding to determine positive IAA binding of STA-3 and its mutated variants.	84
Table 4.9	Estimated K_D of STA-3 and its mutated variants from MST binding experiments.	85
Table 4.10	Buffer screening of 5'-FAM-STA-3-9.	86
Table 4.11	Additional buffer screening of 5'-Cy5 aptamers.	87
Table 5.1	Estimated K_D values of STA-3 from auxin binding specificity evaluations.	93
Table 5.2	Estimated K_D values of STA-3-9 from auxin binding specificity evaluation.	95
Table 5.3	MES buffer salt concentration screenings with STA-3.	96
Table 5.4	Estimated K_D values of STA-3 auxin binding affinities in different salt conditions.	97
Table 5.5	HEPES buffer salt concentration screenings with STA-3-9.	98
Table 5.6	Estimated K_D values of STA-3-9 auxin binding affinities in various salt conditions.	99
Table 5.7	List of compounds evaluated for binding specificity of tZ aptamer using SPR platform and their estimated K_D values.	105
Table 5.8	Optimisation of ITC experimental parameters.	107
Table 6.1	CPN samples synthesized and evaluated for accumulation and permeation into plants.	119
Table 6.2	A summary table of CPNs evaluation for cell penetration and accumulation and uptake of <i>A. thaliana</i> intact roots.	143
Table 6.3	A summary table of CPNs evaluation for cell penetration and cytotoxicity level in <i>A. thaliana</i> isolated protoplasts.	148
Table 7.1	A summary table of the achievements towards the project objectives and further studies.	151

Acknowledgements

I would like to express my deepest gratitude towards my supervisor, Prof Richard Napier, for all his guidance and support both academically and personally throughout my PhD journey. I am grateful for his trust and belief in me to work on this challenging project. His encouragement and optimism have kept me motivated through times when I was doubting myself. I also would like to thank my co-supervisor, Prof Rachel O'Reilly for all her advice and support. I also would like to take this opportunity to thank my funding body: Leverhulme Trust for financial supporting this ambitious research.

It has been a wonderful experience working alongside all past and present members of the Napier group, C10, and C46 lab. Especially, Dr Veselina Uzunova who, on numerous occasions, willingly put up with all my questions and tedious troubleshooting. A special thanks to Dr Charo Del Genio for his support and explanation of simple command lines and secondary structure predictions. I also would like to thank Richard Stark for all his assistance on NGS data analysis and bioinformatics. I am grateful for all the help and support fellow researchers in SLS have given to me over the past three and a half years. It was a pleasure to work with our collaborators in the University of Birmingham. Special thanks to Turgay, Amrita, and Sam for welcoming me to the world of polymer chemistry. I also would like to thank my advisory panels, Prof Alexander Cameron and Prof Matthew Gibson for their kind and useful advice throughout the years.

A special thanks to all the lovely people I've met along this journey and been lucky to call them my friends:

To the Victoria Court gang: Linda Westermann and Eleonora Silvano (including Laurie, brother Ralph P, and beloved Hercules). You have made the pandemic so much more bearable! Thank you for all your love and support and believing in me. I will miss our times doing all the cooking and baking, the 4000-pieces jigsaw puzzles, the climbing sessions, the dance workouts and yoga, the late-

night chatting, the back-and-forth reminders that we can do this PhD, and so much more.

Thank you so much for the friendship. To the tea/coffee break group that I successfully invaded: Séverine, Audam, Holly, Branko (and more). Thank you for all the interesting conversations and keeping me sane between long experiments.

To Martina, thank you being the only other PhD student understanding the struggle of DNA aptamers against small molecule ligands. I appreciate all the lovely cups of coffees and your friendship.

I am grateful for the support I have received from my parents: ขอบคุณป๊าหม่ามามากสำหรับทุกอย่างนะคะแพรวคงไม่สามารถมาขึ้นอยู่ดูๆนี้ได้ถ้าไม่ได้ป๊าม่าคอยเป็นกำลังใจและสนับสนุนแพรวอยู่ตลอด ขอบคุณที่เชื่อมั่นในตัวแพรวนะคะ. To my sisters: Yu, Bell, Bloom and Ben who have been tirelessly listening to my science non-sense and always happy for my ups and lift me up through my downs. Thank you for all the video calls to keep me company and make homesick not too hard to deal with. To my love: Laurence Woodford for believing that I can do great things. Thank you for always being by my side, your support and encouragement really kept me going, especially these last few months. To the Woodford family: thank you for being so kind and making me feel like home when I'm so far away from mine.

Declarations

This thesis is submitted to the University of Warwick in support of my application for the degree of Doctor in Philosophy. It has been composed by myself in supervision of Prof. Richard Napier and has not been submitted in any previous application for any degree.

We declare the contribution from colleagues at the Polymer group at the University of Birmingham: Prof. Rachel O'Reilly and Dr Sam Parkinson for synthesizing and characterising the series of carbon-based polymer nanoparticles presented in Chapter 6 as part of the project collaboration.

We also declare the contributed work by a colleague at the Department of Chemistry: Dr Ann Dixon for assisting with circular dichroism experiments in section 5.5.2 in Chapter 5.

Abstract

Auxin (Indole-3-acetic acid; IAA) has been one of the most widely studied phytohormones due to its vital roles in plant growth and development. Techniques including mass spectrometry and genetically-encoded biosensors have provided us with valuable information on its intracellular activities. However, there is still a lack of quantitative data on its intercellular distribution with high spatial and temporal resolution.

This study aimed to develop a novel auxin-specific, aptamer-based biosensor as an alternative tool to provide a more sensitive and detailed intercellular IAA gradient. As the biosensor recognition component, we evaluated two methods of systematic evolution of ligands by exponential enrichment (SELEX) for the selection of aptamer sequences with potential auxin binding affinity and specificity. Secondary screenings, including enzyme linked oligonucleotides assay (ELONA) and microscale thermophoresis (MST), were used to identify and characterise aptamer candidates with reasonable IAA affinity. Furthermore, several affinity maturation techniques, including hybridisation inhibition, sequence truncation, and single G-mutations, successfully improved IAA binding affinities and specificities of chosen aptamer candidates. The optimised IAA aptamer, STA-3-9, were further evaluated for suitable auxin quantification assays using fluorescence thioflavin T (ThT) assay and surface plasmon resonance (SPR). Meanwhile, an in-depth characterisation of STA-3-9 using isothermal titration calorimetry (ITC) and circular dichroism (CD) suggested its ligand binding mechanism as auxin intercalation within the pre-existed parallel G-quadruplex tertiary structure.

As the biosensor delivery and signalling system, we evaluated a set of carbon-based polymer nanoparticles (CPNs) with various physicochemical properties under the fluorescence confocal microscopy. Several CPNs including the aptamer conjugated CPNs demonstrated a great potential as suitable delivery and signalling vehicles for *in planta* application. While intercellular auxin measurement has not yet achieved, this nano-sensor system is a new state-of-the-art and the first step towards a mapping tool for a sensitive and detailed intercellular IAA gradient.

List of Abbreviations

$^1\text{H-NMR}$	Proton nuclear magnetic resonance
<i>A. thaliana</i>	<i>Arabidopsis thaliana</i>
AA	Acrylic acid
ABA	Abscisic acid
ADP	Adenosine diphosphate
AMP	Adenosine monophosphate
ARF	Auxin response factor
ATP	Adenosine triphosphate
AuNPs	Gold nanoparticles
AUX/IAA	Auxin-IAA proteins
BB	Binding buffer
BSA	Bovine serum albumin
CD	Circular dichroism
CPBS	Conserved primer binding sites
CPNs	Carbon-based polymer nanoparticles
DAA	Diacetone acrylamide
DLS	Dynamic light scattering
DMA	Dimethyl acrylamide
DMAEMA	Dimethyl aminoethyl acrylamide
DMAPS	3-dimethyl (methacryloyloxyethyl) ammonium propane sulfonate
DMSO	Dimethyl Sulfoxide
DNA	Deoxyribonucleic acid
dNTPs	deoxyribonucleotide triphosphate
DP	Differential power
EDC	1-ethyl-3-(3-dimethyl aminopropyl)carbodiimide
EDTA	Ethylenediaminetetraacetic acid
ELISA	Enzyme-linked immunosorbent assay
ELONA	Enzyme linked oligonucleotide assays
FAM	fluorescein
FLIM	Fluorescence-lifetime imaging microscopy
FRET	Fluorescence resonance energy transfer/ Förster resonance energy transfer

G	guanine
GO	Graphene oxide
HEPES	4-(2-hydroxyethyl)-1-piperazineethanesulfonic acid
HI	Hybridisation inhibition
HPLC	High-performance liquid chromatography
IAA	Indole-3-acetic acid
IBA	Indole-3-butyric acid
ICA	Indole-3-carboxylic acid
IPA	Indole-3-propionic acid
ISM	<i>in silico</i> maturation
ITC	Isothermal titration calorimetry
KCl	Potassium chloride
K _D	dissociation constants
LSM	Laser scanning microscopy
MD	Molecular dynamics
MES	2-(N-morpholino)ethanesulfonic acid
mM	Millimolar
MS	Mass spectrometry
MS media	Murashige and Skoog media
MST	Microscale thermophoresis
Mw	molecular weight
NAA	Naphthyl acetic acid
NaCl	Sodium chloride
NADH	Nicotinamide adenine dinucleotide
NaOH	Sodium hydroxide
NGS	Next generation sequencing
nM	Nanomolar
NPs	Nanoparticles
OD	Optical density
OTA	Ochratoxin A
PAA	Phenylacetic acid
PAGE	Polyacrylamide gel electrophoresis
PBS	Phosphate buffered saline

PCR	Polymerase chain reaction
PEG	Polyethylene glycol
PI	Propidium iodide
PID	Percentage identity distance
PISA	Polymerisation-induced self-assembly
pM	Picomolar
POD	Peroxidase
PP	Polypropylene
QDMAEMA	Quaternised dimethyl aminoethyl methacrylate
QDs	Quantum dots
QGRS	Quadruplex forming G-Rich Sequences
RAFT	Reverse addition-fragmentation chain-transfer
RNA	Ribonucleic acid
RT	Room temperature
RU	Response unit
SA	Streptavidin
SB	Selection buffer
SELEX	Systematic evolution of ligands by exponential enrichment
SIM	Single injection method
SPR	Surface plasmon resonance
ssDNA	single stranded deoxyribonucleic acid
TBE	Tris/Borate/EDTA
TE	Tris/EDTA
TIR1	Transport inhibitor resistant 1
tZ	Trans-zeatin
UV	Ultraviolet
μL	microlitre
μM	Micromolar

Chapter 1 Introduction

1.1 Auxin and its physiology

The study of phytohormones has always been of particular interest in plant biology to accomplish better understanding of the mechanisms of growth and development. Auxin is one of the classical plant hormones responsible for regulating cell division, elongation, and differentiation amongst many other physiological responses (Růžicka and Hejátko, 2017). Since Charles Darwin and his son first hypothesized its activity in 1880, followed by its isolation half decade later (Enders and Strader, 2015), tremendous amounts of research have been conducted to study its chemical structure and its effect on plant systems.

Indole-3-acetic acid (IAA) is the most abundant natural auxin in plants. It is generally agreed that the compound derives from a tryptophan precursor, an essential amino acid abundantly found in living organisms (Figure 1.1; (Tivendale et al., 2014)). IAA interacts with several proteins that, in turn, promote gene expression or regulation, such as in the simplified mechanism of AUX/IAA gene expression process (Figure 1.2a; (Chapman and Estelle, 2009)). The cell-to-cell communications are essential for plant development and are regulated through fluxes of plant hormones such as auxin for intercellular signalling (Lofke et al., 2013). It is believed that auxin is distributed throughout the plant system through a polar auxin transport involving AUX1/LAX proteins as influx permeases and PIN-type proteins as efflux carriers (Armengot et al., 2016).

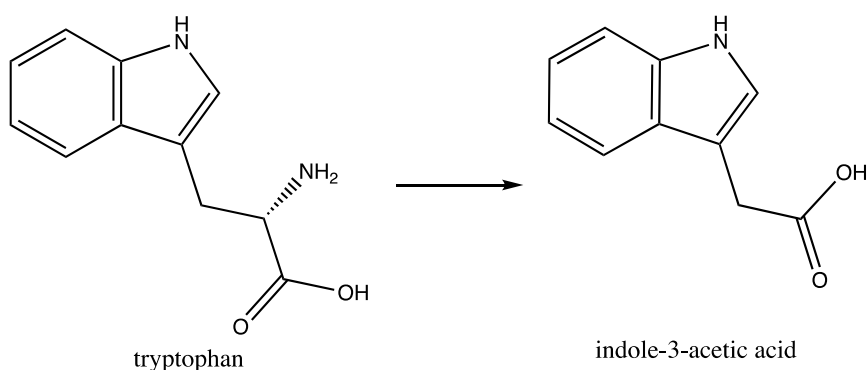


Figure 1.1. Chemical structure of tryptophan precursor and predominant auxin indole-3-acetic acid (IAA).

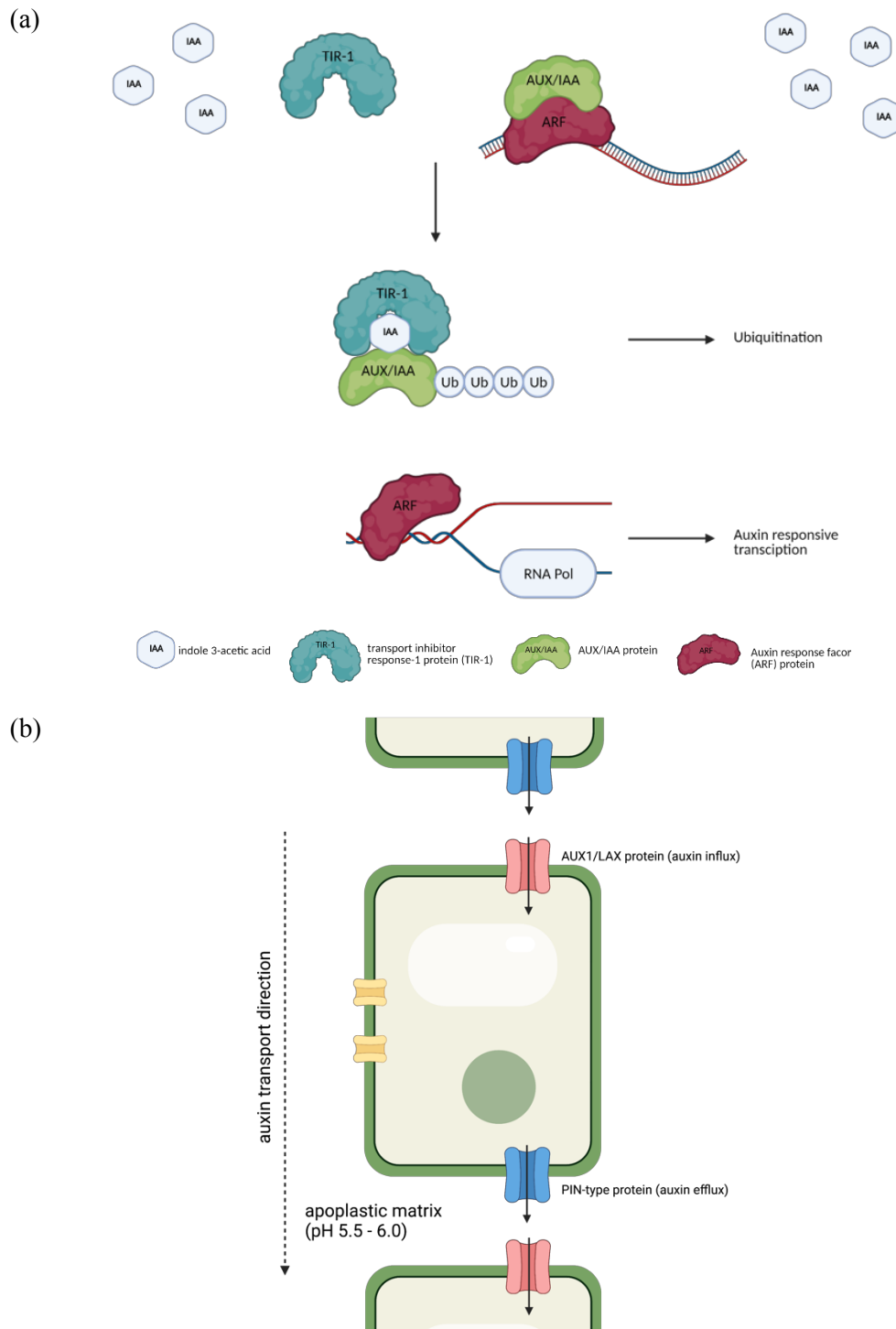


Figure 1.2. **Simplified schematic depiction of auxin mediated gene expression (a) and auxin polar transport in plant (b).** (a) TIR-1 protein interacted with Auxin and the induced interaction of TIR-1 and AUX/IAA occurred, releasing AUX/IAA from its original complex formation with ARF. This release allows gene expression with RNA polymerase while the ubiquitination results in degradation of proteasome. Illustrative mechanism adapted from (Woodward and Bartel, 2005) and created with BioRender.com. (b) Auxin is transported in and out of plant cells through AUX1/LAX and PIN-type proteins, respectively. Illustrative scheme adapted from (Lofke et al., 2013) and created with BioRender.com.

Studies suggested that the differential distribution of auxin is one of the main triggers for plant's growth and development (Enders and Strader, 2015). Many studies have utilised the auxin mediated gene expression (Figure 1.2a) to developed genetically encoded biosensors. Although there are several reports on its gradients using genetically encoded biosensors, all are limited to a qualitative intracellular IAA detection (Sadanandom and Napier, 2010, Ottenschlager et al., 2003, Liao et al., 2015). R2D2 report demonstrated an exception with the ability to semi-quantify auxin activities in most dividing cells (Liao et al., 2015). However, this still is limited to intracellular auxin response (Figure 1.3, (Liao et al., 2015)). The auxin flux between cells are distributed through a polar transport involving AUX1/LAX and PIN-type proteins passing through the apoplastic environment (Figure 1.2b). Therefore, it is vital to achieve a clearer depiction of IAA's true quantitative distribution between cells with high spatial and temporal resolution.

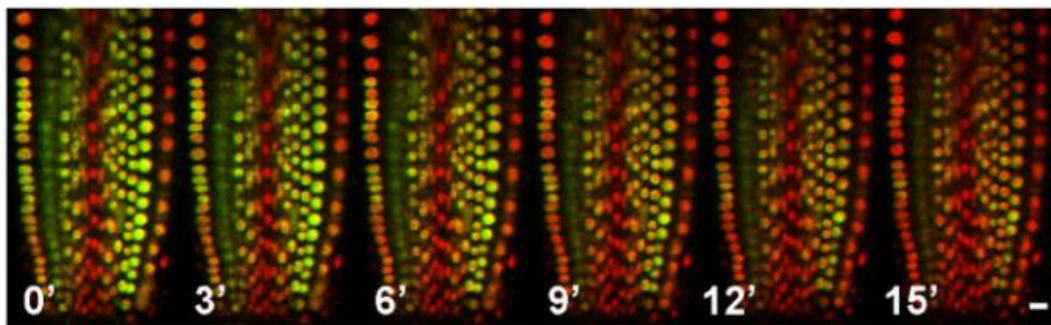


Figure 1.3. A **genetically encoded biosensor, R2D2, designed for intercellular, semi-quantitative auxin response**. R2D2 reporter utilised engineered DR5 and DomainII reporters for a complete intracellular auxin quantification in *A. thaliana* roots with temporal distribution. Image reproduced with permission of the copyright holder from (Liao et al., 2015).

1.2 Current techniques for phytohormones analysis

Various techniques have been established throughout the past decades on the detection and quantification of phytohormones including auxin ranging from chromatography to biosensors. While each and every technique have been improved to obtain high resolution and valuable data, none are without flaws and shall be discussed here.

1.2.1 *Mass Spectrometry*

For tissue-level and cell-based quantitative measurements of small molecules in plants including auxin, the method of choice remains mass spectrometry (MS), often using antibodies for sample clean-up prior to measurement (Novak et al., 2017). Chromatography technique is coupled with MS to successfully perform both qualitative and quantitative analysis of this phytohormone (Porfirio et al., 2016). Extracted plant samples are purified using gas or liquid chromatography then subjected to analysis using MS. With more advanced technology, auxin and its various metabolites can be quantified from minimal amounts of plant materials (Muller et al., 2002, Lu et al., 2008). Nonetheless, this time-consuming and finely tuned purification technique, even though it gives valuable *ex vivo* quantitative analysis of auxin, fails to provide representation of auxin distribution or gradient in real time.

1.2.2 *Biosensors*

In the past few years, focus has been mainly on biosensors. In brief, a biosensor is a synthetic device that specifically interacts with a target molecule and produces a measurable signal (Sadanandom and Napier, 2010). It is designed with two main components, the biological recognition moiety and a signalling module designed according to the sensor's application. Various types of biosensors have been developed to evaluate phytohormones and other plant analytes, including electrochemical and genetically encoded biosensors.

Electrochemical sensors have been developed to measure the concentration of phytohormones and compounds in plants (Sadanandom and Napier, 2010, Novak et al., 2017), although most have been for the food processing industries rather than studies of plant biology. An exception is the use of cytokinin oxidase (cytokinin dehydrogenase) coupled with platinum microelectrode to successfully measure cytokinin concentrations in tomato root exudate (Tian et al., 2014). However, in general there are no suitable redox enzymes for similar devices against other phytohormones or metabolites, which limits the deployment of microelectrode sensors. Another drawback being the designed local measurement requires close

proximity of electrode and compound of interest, which can be problematic for the analysis. Moreover, as it is an invasive technique, results may be manipulated by the response to invasion rather than true concentration of the phytohormone.

In plant biology, genetically encoded biosensors have been established for spatial and temporal quantification of many analytes, including auxin and sugars (Herud-Sikimic et al., 2021, Jones et al., 2014, Brunoud et al., 2012, Chaudhuri et al., 2011, Isoda et al., 2021). For example, monosaccharide reporters were developed from bacterial periplasmic-binding proteins fused to a pair of fluorophores with overlapping emission spectra to give FRET nano-sensors (Chaudhuri et al., 2011). A set of FRET-based sensors for abscisic acid (ABA) was engineered from the ABA receptor complex (Jones et al., 2014). For auxin measurements, ratiometric sensors for the phytohormone auxin were constructed by coupling Domain II of an Aux/IAA protein with VENUS to monitor intracellular auxin signalling in *Arabidopsis thaliana* roots at high spatial and temporal resolution (Brunoud et al., 2012). The DR5-GFP reporter system successfully illustrated the auxin level changes in root tips due to gravity *in vivo* (Ottenschlager et al., 2003). A recent development of genetically encoded biosensor coupled an engineered auxin binding pocket with fluorescent proteins which allow real time measurements of auxin intracellularly with high spatial and temporal resolution (Herud-Sikimic et al., 2021). All these sensors work well in intracellular compartments, but the extracellular plant apoplast remains a challenge, not least because of the well-structured cell wall barrier.

With valuable information and understanding on auxin having been achieved using techniques mentioned above, there is still a lack of true representation of the compound in living plants. Precise quantitative analysis of auxin in whole tissue samples is achieved only by MS while *in vivo* applications, like genetically encoded biosensors, only provide semi-quantitative and poorly time-resolved intracellular results. It is in great desire to develop a novel biosensor that can evaluate and quantify concentration of auxin extracellularly *in vivo* with both spatial and temporal resolution with a non-invasive delivery and detection system.

1.3 An aptamer-based biosensor for auxin measurement

Here, we propose an aptamer-based biosensor as an alternative technique for real-time *in planta* distribution of auxin. As mentioned, a biosensor is a powerful device designed with specific interactions to a target molecule to produce a measurable signal (Sadanandom and Napier, 2010). Biosensors are not confined to *ex vivo* diagnoses and they can be used to monitor physiological phenomena in virtually any biological system (Gooch et al., 2017), including *in vivo* with little to no trauma to the organism. One must consider the application of biosensor upon designing the suitable biological recognition moiety and the signalling system. The biological recognition component is designed with respect to the target molecules and its application. Examples are, a peptide sequence was used to recognize protease enzyme in human blood for medical application (Morita et al., 1977) while antibodies possess specific interactions with their antigens (Grennan et al., 2003). In recent decades, focus has been shifted towards aptamer development due to its superiority to other recognition components such as antibodies which will be discussed in greater detail in section 1.4. DNA aptamer provides ease of modification including conjugation to output signalling system for appropriate application. Meanwhile, the signalling system of biosensor is greatly dependent to the downstream application. Optical remains amongst the most popular signalling component due to ease of use and detection sensitivity. Fluorescent proteins were designed as part of genetically encoded biosensors allowed visualisation corresponding to intracellular auxin in intact roots (Herud-Sikimic et al., 2021, Jones et al., 2014). In recent years, fluorescent nanoparticles are gaining interests as a potential delivery and signalling carrier for biosensor due to their size and photostability (Bhunia et al., 2013, Choi and Frangioni, 2010). Here, the development of DNA aptamer as the auxin biological recognition will be thoroughly discussed along with the application of fluorescent carbon-based polymer nanoparticles (CPNs) as the biosensor signalling system.

1.4 DNA aptamers as biosensor biological recognition

Aptamers offer an alternative biological recognition element for sensor development. An aptamer is a short, synthetic oligonucleotide selected to have a

specific binding interaction with target molecules (Mayer, 2016). Aptamers have a comparable sensitivity and specificity to antibodies while having significant advantages, including ease of synthesis, well-known chemistry and cost-effectiveness (Table 1.1). While a more accessible engineered antibodies have been developed, DNA aptamers are still generally preferred due to its longer shelf life. Since their development in the 1990s, numerous DNA and RNA aptamers have been identified for a wide spectrum of target ligands ranging from small molecules to whole cells. The versatility of aptamers allows them to be coupled with diverse sensing platforms for different applications, such as enzyme linked oligonucleotide assays (ELONA), electrochemical devices, nanoparticles for microscopy and diagnostics, and surface plasmon resonance (SPR) (Kim et al., 2018, Le et al., 2014, Nguyen et al., 2007). With the additional reverse transcription steps within the RNA aptamer selection process, DNA aptamers were chosen for our study.

Table 1.1. **Features of nucleic acid aptamers and monoclonal antibodies.**

	Aptamers	Antibodies
Synthesis	Chemically synthesized in short period of time	Complex extensive processing, often requiring immunisation
Cost	inexpensive	High production cost
Stability	Nuclease degradation Degradation via UV exposure	Short biological half-life Specific storage conditions
Target	Wide range from whole cell to small molecules	Wide range from whole cell to small molecules
Specificity	High	High
Affinity	High	High

1.4.1 Aptamer selection methods

Aptamers are developed through systematic evolution of ligands by exponential enrichment (SELEX; Figure 1.4) where target-specific aptamer sequences emerge through sequential affinity-based enrichment from a highly diverse oligonucleotide library (Ellington and Szostak, 1990). Each round of SELEX consists of three phases: selection, partition, and amplification. Introduction of target ligand to

the oligonucleotide library pool allows binding and selection of ligand-binding sequences. These ligand-binding sequences are partitioned from the rest of the pool and subjected to amplification via polymerase chain reaction.

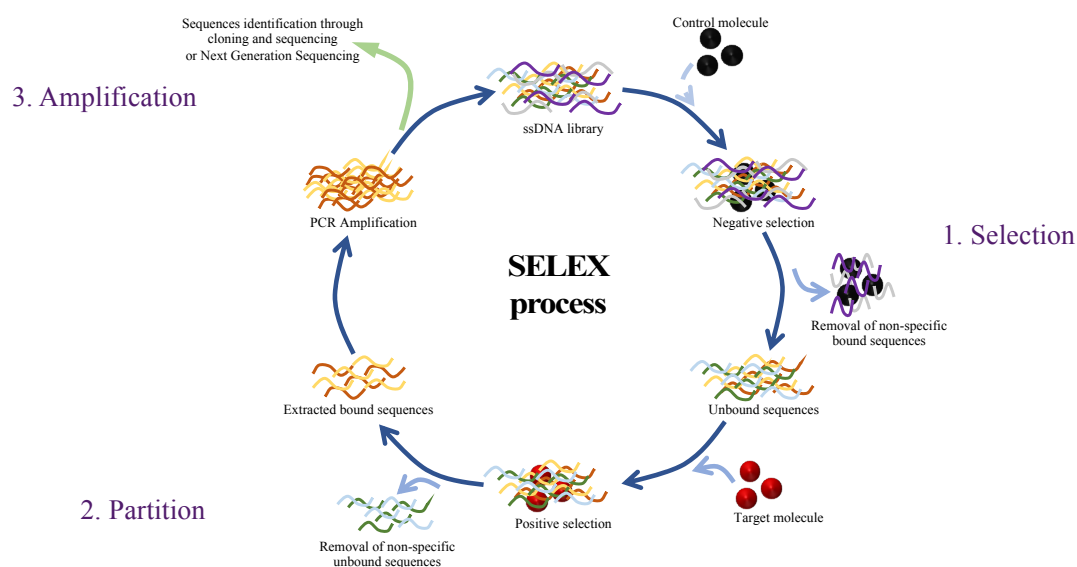


Figure 1.4. **General schematic illustration of the SELEX process for DNA aptamer.** The process starts with a ssDNA library with high diversity ($\sim 10^{15}$). Selection phase allows ligand-specific aptamers to bind. In some cases, counter-selection steps can be introduced by incubating the library with control molecules to eliminate non-specific binders from successive sub-libraries. A range of partitioning techniques can be used to separate ligand-specific aptamers from the pool. The separated aptamers are then amplified and subjected to further rounds of SELEX.

Several selection and partition techniques can be implemented during SELEX depending on various factors, including the nature of target ligands and the intended application of the aptamer (Table 1.2). Frequently, ligands are immobilised onto agarose or magnetic beads to facilitate the separation of ligand-specific sequences from the non-specific ones (McKeague et al., 2014). Implementation of a fluorescent tag using a labelled primer, such as in FluMag-SELEX allows monitoring of the efficiency of sequence partition and recovery (Stoltenburg et al., 2005). However, immobilisation of target ligands can pose a serious drawback for small molecule targets as modifications to these ligands can change their surface chemistry, alters the available functional groups and the biophysical properties of the small molecules, negatively impacting the chance of selecting appropriate aptamer binding interactions (Pfeiffer and Mayer, 2016). An attractive alternative is solution-SELEX, also known

as capture-SELEX, where the DNA library is instead hybridised onto a short complementary oligonucleotide which is displayed on magnetic beads. This allows incubation with free, unaltered target ligand (Stoltenburg et al., 2012) to select for aptamers for which ligand interaction causes aptamer conformational changes and interrupts the hybridisation with the capture oligo. Graphene oxide (GO)-SELEX method allows selection of aptamers without any immobilisation of either library or target ligands (Park et al., 2012). After incubation of DNA library with the target, the solution is introduced to GO where unbound sequences are removed by adsorption onto GO due to π - π stacking interactions.

Table 1.2. Comparison of different types of selection processes.

SELEX types	Examples of target ligands	Methods	References
Direct-SELEX	Proteins Macromolecules	Immobilisation of target ligand onto agarose or magnetic beads to facilitate separation of specific binders from the unbound pool.	(Yoshitomi et al., 2020, Lautner et al., 2010, Mayer and Hover, 2009)
FluMag-SELEX	Proteins Macromolecules	Fluorescent tag introduced in PCR amplification allows monitoring of DNA recovery through SELEX rounds.	(Stoltenburg et al., 2005)
Solution-SELEX	Small molecules toxins	A complementary oligonucleotide is used to hybridise to and immobilise the aptamer library. After washing steps, incubation with the target ligand allows ligand binders to undergo conformational change around target for collection in solution.	(Stoltenburg et al., 2012, Reinemann et al., 2016)
Cell-SELEX	Whole cells	The DNA library is incubated with whole cells for the selection process. Separation of bound sequences can be done by centrifugation.	(Sefah et al., 2010)
CE-SELEX	Proteins Higher molecular weight ligands	Ligand-specific sequences are separated due to the difference in size and charge of the complex.	(Mendonsa and Bowser, 2004)
GO-SELEX	Proteins	Graphene oxide sheet absorbs and remove unbound sequences through π - π stacking.	(Park et al., 2012)

The number of SELEX rounds necessary for selecting specific aptamers varies greatly but is generally above 5 (Figures 1.5, (Blank, 2016), with elution stringency to be raised or for counter-selection steps to be included in the later rounds. These will tend to improve the affinity or the specificity of successive sub-libraries, respectively.

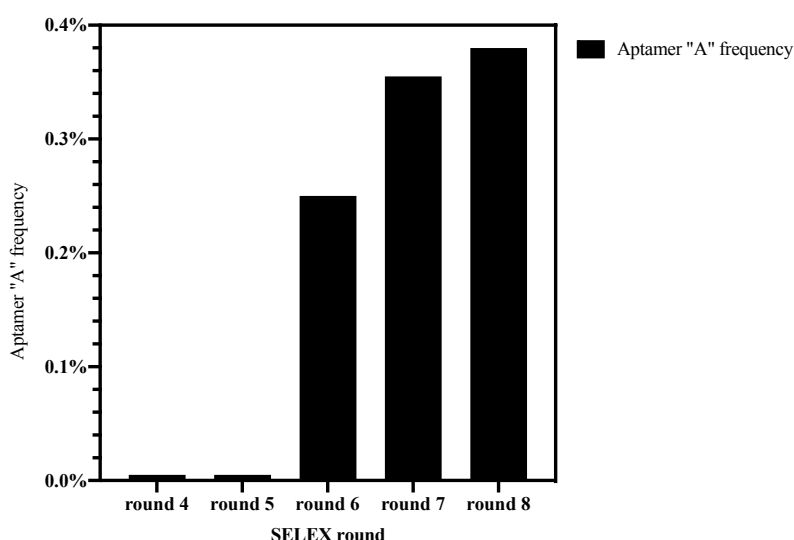


Figure 1.5. **The frequency or relative abundance of selected aptamer candidate “A” through successive rounds of SELEX.** The relative abundance of aptamer ‘A’ rises above background from round 6 with its highest frequency being less than 0.4% in the last round. (Figure adapted from (Blank, 2016).

Aptamer sequences can be highly enriched at the end of the SELEX process, but are frequently present at less than 1% of the remaining diversity (Figure 1.5). Whilst this represents enrichments of over 10^{12} – fold, secondary selection processes are necessary to identify the best reagents. Therefore, sequence analyses also play an important role in aptamer selections. Conventional cloning and sequencing methods have been used extensively to sequence aptamers obtained from the last round of SELEX, but only a finite number of sequences can be handled with these methods. In recent years, the high capacity of next generation sequencing (NGS) has allowed the sub-libraries of many rounds of SELEX to be sequenced in one reaction. Unique oligonucleotide ‘barcodes’ can be added to sub-libraries from each round as part of sample preparation allowing them to be deep sequenced on the same NGS run (Mayer, 2016). This not only identifies the sequences most enriched but can also illustrate the enrichments of certain sequences throughout the SELEX rounds (Mayer, 2016). NGS gives a better insight to the enrichment profiles of the aptamers and can also reveal particular motifs segregating with target interactions (Hoinka et al., 2018).

1.4.2 Developed aptamers against plant targets

1.4.2.1 *ATP aptamer*

Adenosine trisphosphate (ATP) is increasingly being recognised as a signalling molecule in plants (Pietrowska-Borek et al., 2020, Tanaka et al., 2014, Tanaka et al., 2010, Chivasa et al., 2005) as it is in animals (Dale, 2020, Schwiebert and Zsembery, 2003). Importantly, since its identification in 1995, an aptamer to ATP has been the most widely studied small molecule DNA aptamer. Modification of ATP was performed to immobilise the target onto agarose beads for the conventional direct SELEX process (Huizenga and Szostak, 1995). From a starting library with a diversity of 2×10^{14} single-strand DNA (ssDNA) sequences, 21% of the ssDNA input was eluted by ATP in SELEX round 8. Whilst this suggested that diversity could now be as few as 5 sequences, all 17 clones sequenced were different and the accumulating aptamer literature shows that target frequencies at this stage are seldom more than a few percent.

The ssDNA starting library consisted of 72 random bases flanked by 20-mer extensions on each end for primer binding sites (Huizenga and Szostak, 1995). Two of the aptamer clones were synthesised and shown to bind to immobilised ATP. One was selected for affinity maturation studies, which included sequence truncations and mutagenesis to determine binding motifs and to enhance the binding affinity, experiments later extended by others (Zhang and Liu, 2018, Zhang et al., 2017b). The ATP-binding site was first determined to be within the 72 random bases, but mutagenesis allowed the aptamer length to be shortened to 45 and 25 bases, which formed two stable stacked G-quadruplexes. Further mutagenesis showed that these G-quadruplexes dominate the structure (Huizenga and Szostak, 1995) and later work showed that two ATP molecules intercalate into this framework as the basis for recognition and affinity (Zhang and Liu, 2018, Zhang et al., 2017b).

The observed dissociation constants (K_D) of the ATP aptamer varies with the detection method used. Initial analysis using ultrafiltration yielded an estimated K_D of 6 μM with variants giving values between 1-10 μM (Huizenga and Szostak, 1995),

supported later by isothermal titration calorimetry (ITC) which gave comparable values (Zhang et al., 2017b). Poorer affinities were observed using microscale thermophoresis (MST) and SPR techniques with K_D values of 34.4 μM and 30.98 μM , respectively (Entzian and Schubert, 2016, Chang et al., 2014).

The specificity of the ATP aptamer is dependent on its purine and ribose moieties, not by the phosphate groups. There is minimal binding with other nucleic acid bases and many diverse purines. However, the ATP aptamer does significantly bind to ADP, AMP and adenosine (Entzian and Schubert, 2016, Huizenga and Szostak, 1995) and so its application as an aptasensor for measuring ATP *in vivo* needs careful calibration.

1.4.2.2 ABA aptamer

Highly sensitive and specific ssDNA aptamers have been selected against abscisic acid (ABA) for quantitative assay development (Grozio et al., 2013). Despite being a small molecule, direct-SELEX was implemented by attaching a biotinylated linker at the C-4 position of ABA. A counter-selection step with the linker was implemented after the fourth round to avoid enriching for non-specific binders. Two aptamers, namely clone 2 and 9, were selected and K_D values were estimated at 0.98 μM and 0.80 μM , respectively using a ^3H -ABA binding assay. Displacement assays revealed a high level of aptamer specificity against the (+)2-cis, 4-trans abscisic acid enantiomer with minimal binding to the (-)2-cis, 4-trans abscisic acid enantiomer or other isomers. Although clone 9 appears to be more ABA-sensitive than clone 2, it also shows some non-specific binding to the biotinylated linker.

1.4.2.3 Trans-zeatin aptamer

Like ATP, cytokinins are purines and various researchers have been developing aptamers towards cytokinins. A modified direct-SELEX with trans-zeatin immobilised onto Sepharose (Qi et al., 2013) selected highly specific binders after 24 rounds of SELEX. Selection stringency was increased at each round, using counter-selection steps with L-histidine, increasing the number of washes, shorter elution times

with the target molecule, etc. After sequencing and secondary structure analysis, sequence truncation and mutagenesis were performed to enhance the aptamer's binding affinity, the K_D for trans-zeatin was 3.85 μM for a 35 base aptamer measured by ITC. This aptamer is highly selective for trans-zeatin with very low binding with cis-zeatin and dihydrozeatin, but some binding against trans-zeatin riboside.

As noted above, a biosensor needs the recognition event converted to a quantifiable signal and several read-out technologies have been reported for cytokinin aptamers. A graphene oxide sensor platform was developed initially, providing a 'turn-on' fluorescence measurement upon ligand-aptamer binding (Qi et al., 2013). The same aptamer was further developed as a structure-switching assay to successfully quantify trans-zeatin using another fluorescence 'turn-on' mechanism (Liu et al., 2016). A fluorescein-labelled aptamer was paired with a hybridising oligonucleotide linked to a quencher. When hybridised, the aptamer was "open" and quenched. Binding of trans-zeatin led to a conformational change as the aptamer formed a stable hairpin incorporating the target, releasing the oligo-quencher and activating fluorescence. This format of assay had a detection limit of 135 nM for trans-zeatin. An electrochemical sensor for this cytokinin aptamer with better sensitivity has also been reported, with an impressive linear response range from 0.1 to 100 nM and limit of detection of 0.03 nM (Wang et al., 2018).

1.4.3 DNA aptamer affinity maturation techniques

Identification of ligand binding site(s) gives insight to the minimal ligand binding sequences of the aptamer. Modification to the aptamer sequence accordingly can improve the ligand binding affinity and specificity, and also improve the synthesis, cost, and stability of DNA aptamers (Kalra et al., 2018, He et al., 2017, Zheng et al., 2015, Blind and Blank, 2015, Katilius et al., 2007, Odeh et al., 2019). SELEX initial library is around 80 – 120 bases long consisted of randomised region(s) flanking by conserved primer binding sites essential for amplification phase (Ruscito and DeRosa, 2016, Gopinath, 2007). However, studies have shown that only part of the aptamer sequences are involved in ligand interactions (He et al., 2017, Le et al., 2014). The primary sequence of an aptamer dictates its overall secondary structure and non-binding regions could contribute to the conformations obscuring the ligand contact

area (Hasegawa et al., 2016). Therefore, removal of those non-binding regions can facilitate ligand-induced conformational change of DNA aptamer resulting in improved binding affinity (He et al., 2017, Wang et al., 2019). Other affinity maturation techniques, including base modifications and chemical conjugations, have shown to enhance binding affinity and specificity and the stability of the aptamer within biosensor testing environment (Odeh et al., 2019, Mousivand et al., 2020, Kalra et al., 2018, Zhang and Liu, 2018, Mayer, 2016, Witt et al., 2015, Katilius et al., 2007). For instance, a PEGylated MP7 aptamer demonstrated prolonged *in vivo* stability for cancer therapy (Prodeus et al, 2015). Various affinity maturation techniques for downstream applications are discussed here.

Identification of minimal ligand binding sequences of aptamers can be performed using various techniques, including hybridisation inhibition (HI), sequence truncation, and molecular dynamics (MD) simulations (Mousivand et al., 2020, Wang et al., 2019, He et al., 2017, Gao et al., 2016, Le et al., 2014, Qi et al., 2013, Savory et al., 2013, Zhou et al., 2011, Ben Aissa et al., 2020). Binding affinity of DNA aptamer against electric eel acetylcholinesterase was improved by at least 10-fold using HI in conjunction with sequence truncation (Le et al., 2014). Instead of synthesizing each truncated variant for optimisation, HI cost-effectively utilised short complementary oligonucleotides to restrict part(s) of the aptamer sequence from ligand interaction. Binding affinities of aptamer with various restricted regions were compared to identify the regions not contributing to ligand binding. Sequence truncation was then used to confirm the minimal binding sequences obtained from HI (Le et al., 2014).

Many approaches can be used for sequence truncation of the DNA aptamers. Various studies based their sequence truncations on the predicted secondary structure features using web-based software such as mfold and RNAstructure (Ha et al., 2017, Vu et al., 2016) or a more advance MD simulations of aptamer-ligand interaction in 3-dimension (Ben Aissa et al., 2020, Gao et al., 2016). Truncations were performed according to the potential ligand binding sites predicted by these simulations. Circular dichroism (CD) was performed as a supplementary structural characterisation techniques to evaluate conformational change of each truncated variant both in presence and absence of target ligand (Wang et al., 2019). Meanwhile, some took on a more empirical ‘stepping’ approach (Reinemann et al., 2016, Le et al., 2014, He et

al., 2017). This empirical approach is more favourable when secondary structure predictions did not reveal particular structural features to further pursue (Le et al., 2014). Furthermore, in presence of target ligand, DNA aptamers are expected to undergo conformational change, and therefore, would not conform to the structural predictions (Wang et al., 2019). Regardless of the truncation approach, the consensus is that the removal of sequences not essential in binding allowed exposure of the ligand contact area(s) resulting in more readily ligand binding to occur (Hasegawa et al., 2016).

Upon identification of the minimal ligand binding sequences, DNA aptamer sequences can be further modified and optimised for enhance ligand interactions. Several techniques, including *in silico* maturation (ISM), high throughput mutagenesis microarray, and bases modification, have been used to improve binding affinities and specificities (Mousivand et al., 2020, Gao et al., 2016, Zheng et al., 2015, Witt et al., 2015, Savory et al., 2013, Katilius et al., 2007, Gao et al., 2004). ISM utilises a ‘genetic algorithm’ computational analysis to generate candidates through rounds of random pairing, cross over, and mutation of parent aptamer sequences to obtain evolved sequences with enhanced ligand binding affinity and specificity (Savory et al., 2013). Known DNA aptamer against aflatoxin B was optimised using combination of 3-D simulation, genetic algorithm, and MD simulation as *in silico* strategy to improve binding affinity from estimated K_D value of 38.5 pM to 4.0 pM (Mousivand et al., 2020). While ISM is a powerful tool, it requires in depth computational work that can be complicated and time-consuming. On the other hand, several manufacturers now offer *in situ* DNA synthesis, a high-density array could be produced for high throughput mutagenesis (Witt et al., 2015, Gao et al., 2004). Customised microarray allowed studies of aptamer binding properties through mutagenesis with single-, double- and triple- mutations (Katilius et al., 2007). This approach could offer a thorough analysis of specific nucleotides compositions that are important for ligand binding. However, *in situ* synthesis of aptamer microarrays still has some limitations while commercially available high-density microarrays can be very costly. Alternatively, site-directed mutagenesis combined with sequence truncation was used to optimise binding affinity of a DNA aptamer against saxitoxin by 30-fold (Zheng et al., 2015). Single G mutation of the small molecule aptamer was performed to enhance the formation of G-quadruplex structure to improve the aptamer structural stability.

Following sequence truncation assisted by secondary structure prediction, ELONA was used to evaluate binding affinities of aptamer variants.

Additionally, base and chemical modifications to DNA aptamers have shown to increase aptamer stability in evaluation environment (Roxo et al., 2019, Kalra et al., 2018, Pfeiffer and Mayer, 2016). Aptamer conjugation with high molecular weight compounds, such as cholesterol and polyethylene glycol (PEG), enhanced aptamer stability for both *in vitro* and *in vivo* examinations (Odeh et al., 2019, Ni et al., 2017).

1.5 Carbon-based polymer nanoparticles (CPNs) as biosensor delivery and signalling system

Signalling component of biosensor is greatly dependent on its application. While an electrochemical biosensor was successfully developed to detect cytokinin in plant (Tian et al., 2014), an optical biosensor is amongst the most popular signalling component due to ease of use and detection sensitivity (Baaske et al., 2010, Prante et al., 2019, Sadanandom and Napier, 2010, Herud-Sikimic et al., 2021, Isoda et al., 2021). Fluorescent optical biosensors using highly fluorescent proteins and nanoparticles coupled with confocal microscopy is desirable for high spatial resolution *in planta* measurements of target ligands (Bhunia et al., 2013, Brunoud et al., 2012, Chaudhuri et al., 2011, Hayashi et al., 2014, Herud-Sikimic et al., 2021, Isoda et al., 2021, Koo et al., 2015). While there is little need to compete with genetically encoded fluorescent sensors such as those developed for intracellular monitoring of phytohormones (Walia et al., 2018), the plant apoplast remains a poorly explored compartment and it is not readily amenable to most intracellular probes. Thus far, developed aptamer sensors have been used mainly on extracted samples for simple diagnostic evaluation (Komorowska et al., 2017, Qi et al., 2020). Therefore, to develop an aptamer-based biosensor, one needs to consider appropriate mechanism for sensor delivery and signalling *in planta*.

Fluorescent nanoparticles have gained popularity in recent years for their applicability for bioimaging and drug delivery (Bhunia et al., 2013, Choi and Frangioni, 2010, Koo et al., 2015). More studies are underway on the uptake and phytotoxicity of different micro- and nanoparticles in plant systems (Faisal et al.,

2018). Studies of gold nanoparticles (AuNPs) in *Arabidopsis thaliana* roots and isolated protoplasts reveals the effects the surface charges of this heavy metal particles have on the cell uptake and morphology (Milewska-Hendel et al., 2019). Studies demonstrated successful internalisation of carbon-based nanomaterials in plant tissues (Sypabekova et al., 2017). While focus has been mainly on other organic nanoparticles such as carbon nanotubes and fullerenes, carbon-based polymer nanoparticles (CPNs) is a potential aptasensor delivery and signalling system.

CPNs is one of the novel classes of nanoparticles widely studied for biomedical applications, including bioimaging, therapeutical and cancer research, and plant biology (Choi and Frangioni, 2010, Faisal et al., 2018, Frohlich, 2012). Different types of nanoparticles (NPs) demonstrated wide ranges of physicochemical properties suitable for various applications (Table 1.3; (Choi and Frangioni, 2010)). NPs are greatly fine-tuneable allowing ease of delivery mechanism. While some NPs, such as AuNPs and QDs, demonstrated smaller sizes with high photostability, potential phytotoxicity must be avoided (Choi and Frangioni, 2010, Koo et al., 2015, Milewska-Hendel et al., 2019). The introduced sensors should be non-toxic and will not stress the plant system. This is to avoid obtaining any biased manipulated data as a result of aptasensor introduction to the system. Furthermore, chosen NPs for aptasensor must allow surface functionalisation for decoration of auxin aptamer as biological recognition component.

Table 1.3. **Comparison of different types of nanoparticles developed for bioimaging application.** List adapted from (Choi and Frangioni, 2010).

NP types	Compositions	Sizes (nm)	Features	References
CPNs	Repeated units of carbon-containing monomers	1 – 1000	Organic NPs with biocompatibility. Size of CPNs can be fine-tuned through polymerisation. Variety of monomers used allows high functionalisation.	(Shakesheff et al., 1997, Sikder et al., 2021, Chan et al., 2009)
			Bioimaging of CPNs requires contrast agents or fluorescent dyes conjugated.	
AuNPs	Gold-containing nanostructures	2 – 100	Highly sensitive NPs with tuneable sizes and enhanced permeability and retention in biological samples. Compatible for near infrared imaging.	(Avellan et al., 2017, Mejac et al., 2009, O'Neal et al., 2004)
			Potential toxicity due to the gold heavy metal. Undefined available functionalisation site.	
Quantum dots (QDs)	Semiconductor core/shell arrays	5 – 50	Highly photostable and photo efficient. QDs can be fine-tuned for desired size and target.	(Allen and Bawendi, 2008, Cai et al., 2006, Smith et al., 2004)
			Physically unstable with aggregation and UV degradation. Potential toxicity.	
Silica NPs	Ceramic silica photosensitisers	5 – 100	Ease of synthesis. NPs can be fine-tuned for desired size and target.	(Burns et al., 2006, Kamata et al., 2003)
			Bioimaging of silica NPs requires contrast agent. Low mechanical stability with aggregation.	
Carbon nanotubes	Carbon-containing nanotubes	3 – 100	Durable nanotubes with tuneable sizes.	(Firme and Bandaru, 2010, Kostarelos, 2008)
			Poor water-solubility with aggregation. Not suitable for surface functionalisation. Potential toxicity.	

CPNs demonstrated the most appropriate NPs for our intended use. CPNs can be fine-tuned for desired size, surface charge, polymer chemistry, and available functionalisation site for aptamer conjugations (Bhunja et al., 2013, Canning et al., 2016, Chan et al., 2009, Yildirim et al., 2016). These physicochemical properties of CPNs shall be further investigated for suitability of *in planta* biosensor application using *A. thaliana* as a model plant. *A. thaliana* is made up of small and well-

established cell structures suitable for confocal microscopy evaluation (Meinke et al., 1998). To passively deliver this nano-sensor inside the plant system, one must consider the cell wall permeability of the studied tissues. The porosity of cell walls is not well defined and varies throughout the cell development. Mature cells contain secondary cell walls providing strength and firmness to the cell structure while younger cells are made up of mostly primary cell walls with higher flexibility (Cosgrove and Jarvis, 2012). It was previously shown that small AuNPs (12 nm Ø) and QDs with different surface polymer chemistry were readily taken up by *A. thaliana* roots (Avellan et al., 2017, Koo et al., 2015). Therefore, CPNs and nano-sensor evaluation shall focus on the primary tissues of *A. thaliana* seedlings to accomplish the auxin morphological gradient.

Upon designing a suitable signalling system, the intrinsic autofluorescence of phytochemicals must be accounted for. There are several natural plant compounds that possess autofluorescence properties, such as chlorophyll, with emission wavelength around 685 nm, and NADH around 440-470 nm (Billinton and Knight, 2001). This can severely interfere with fluorescence detection or intensities produced by the sensor itself, resulting in false positive reading. Designing the signalling component to avoid these interfering wavelengths can easily overcome this issue. Moreover, highly intense fluorescent moiety is required for high sensitivity optical sensors. Fluorescent nanoparticles are a good candidate but might be extremely difficult to completely ‘quench’ and potentially affect the ‘turn-on’ mechanism of the biosensor. To overcome this, the biosensor can be designed with a fluorophore having fluorescence emission spectrum overlapping with the excitation spectrum of the nanoparticles. This would allow fluorescence resonance energy transfer (FRET) measurements by evaluating the shift in excitation energy or the ratio of the two wavelengths (Okumoto et al., 2008). This will be extremely useful for quantitative analysis as the shift in wavelengths intensities will be proportional to auxin concentration.

Fluorescence confocal microscopy will be primary technique used for evaluation of aptasensor delivery and signalling mechanism. Unlike a traditional fluorescence microscopy, confocal microscopy is an optimal imaging technique that uses a ‘point illumination’ technique and an adjustable pinhole to control and

conjugate a focal plane allowing any signals out of focus to be eliminated (Nwaneshiudu et al., 2012). This allows any fluorescence emissions close to the focal plane to be detected and greatly help with imaging quality and resolution (Nwaneshiudu et al., 2012). Its ability to scan the specimen of interest along the horizontal plane allows spatial distribution visualisation of the fluorescence material within the specimen in three dimensional. The image resolutions might not be comparable to transmission electron microscopy, but confocal microscopy allows convenient fluorescent visualisation of living biological samples (Koo et al., 2015, Okumoto et al., 2008, Ottenschlager et al., 2003). This direct and non-invasive technique has been proven useful for visualisation of fluorescent proteins within thick organic materials such as plant roots (Brunoud et al., 2012).

1.6 Aims and objectives

The aim of this study is to develop an aptamer-based biosensor as an alternative technique for quantitative measurements of intercellular auxin distribution with high spatial and temporal distribution. To do so, DNA aptamers are selected and designed for specific auxin interaction as our biological recognition component while different CPNs are characterised for biosensor delivery and signalling systems. This study will address the following hypotheses:

- 1) SELEX process can select auxin aptamers
- 2) Affinity maturation techniques can improve auxin binding affinities and specificities of chosen aptamer candidates.
- 3) The developed auxin aptamers can be used as a biosensor recognition component in *A. thaliana* seedlings.
- 4) CPNs can be selected to target apoplast and evaluated as suitable biosensor delivery and signalling system in *A. thaliana* seedlings.
- 5) A novel nano-sensor can be devised which may map auxin gradients in *planta*.

Chapter 2 Materials and Methodology

2.1 Materials and reagents

For direct- and solution- SELEX, phosphate buffered saline (PBS) was used as selection buffer (SB) (137 mM NaCl, 2.7 mM KCl, 8.1 mM Na₂HPO₄, 1.5 mM KH₂PO₄) and was prepared in-house. Indole-3-acetic acid (IAA), indole-3-carboxylic acid (ICA), indole-3-propionic acid (IPA), indole-3-butyric acid (IBA), L-tryptophan, 1-Naphthaleneacetic acid, 2-cis-4-trans-abscisic acid (ABA), picloram, and quinclorac were purchased from Sigma-Aldrich. Acetic acid was purchased from Fisher Scientific UK. Phenylacetic acid (PAA) was purchased from Alfa Aesar. 2,4-dichlorophenoxyacetic acid (2,4-D) was from Pal Chemicals limited. All other chemicals used were of analytical grades.

2.2 PCR optimisation

Primers were synthesized and desalted by Sigma-Aldrich (Table 2.1). DNA Taq Polymerase and reaction buffer were purchased from New England Biolab (NEB). dNTP set was purchased from Invitrogen and dNTPs master mix was prepared to 10 mM final concentration of each dNTP in water. The PCR conditions tested is shown in Table 2.2.

Table 2.1. **Sequences of two SELEX libraries, primers, and capture oligos.** Randomised regions are underlined and italicised. Modifications are presented in bold.

Names	Sequences
Direct-SELEX	5'-TAGGGAAGAGAAGGACATATGAT- <u><i>N40</i></u> -TTGACTAGTACATGACCACTTGA -3'
Solution-SELEX	5'-TAGGGAAGAGAAGGACATATGAT- <u><i>N10</i></u> -TGAGGCTCGATC- <u><i>N40</i></u> -TTGACTAGTACATGACCACTTGA -3'
Capture oligos	5'- biotin – GTC – [C18 spacer] – GATCGAGCCTCA -3'
FOR	5'-TAGGGAAGAGAAGGACATATGAT -3'
REV	5'-TCAAGTGGTCATGTACTAGTCAA -3'
FAM-f	5'- fluorescein – TAGGGAAGAGAAGGACATATGAT -3'
DIGO-f	5'- digoxigenin – TAGGGAAGAGAAGGACATATGAT -3'
BIO-r	5'- biotin – TCAAGTGGTCATGTACTAGTCAA -3'
dT25-r	5'- polydT25 -[C18spacer]-TCAAGTGGTCATGTACTAGTCAA-3'
PHOS-r	5'- phosphate – TCAAGTGGTCATGTACTAGTCAA -3'

Table 2.2. Different conditions of PCR reaction optimised.

Conditions tested	Testing range
DNA concentration	50, 100, 200, and 300 pM
MgCl ₂ concentration	2, 3, 4, 5, 6, and 7 mM
Primer concentration	100, 200, 300, and 400 nM
Annealing temperature	A temperature gradient from 55 to 65°C
Number of cycles	10, 15, 20, 25, and 30 cycles

2.3 Direct-SELEX

2.3.1 Direct-SELEX library, primers, and control molecules.

Direct-SELEX library and primers were purchased from Tri-link biotechnologies. The direct-SELEX library (Table 2.1) is made of random sequences of single-stranded DNA (ssDNA) with diversity of at least 10^{15} . Control molecules used for counter-selection steps were abscisic acid, L-tryptophan, benzoic acid, N6-benzyladenine, and salicylic acid (chemical structures shown in figure 2.1). All were prepared to 100 mM stock concentration in DMSO.

2.3.2 IAA-PEG and its immobilisation onto streptavidin-coated magnetic beads.

IAA-PEG, a biotinylated IAA derivative (Figure 2.1) was a gift from Prof Ken-ichiro Hayashi (University of Kyoto, Japan) and was resuspended to 10 mg/mL final concentration with DMSO. Streptavidin-coated magnetic beads (μ Beads) and μ Columns were purchased as part of μ MACs streptavidin kit from Miltenyi Biotec.

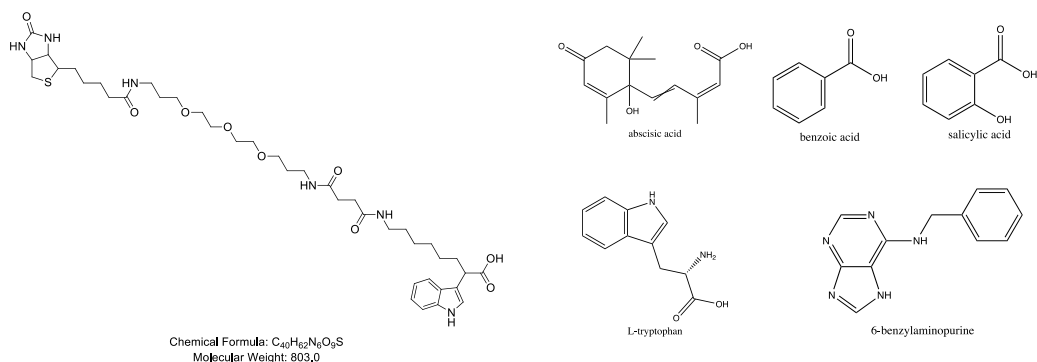


Figure 2.1. Chemical structures of biotinylated IAA-PEG derivative and control molecules used in the SELEX process.

Prior to on-column separation, a μ Column was equilibrated with the provided equilibration buffer and washed twice with SB. The appropriate amount of IAA-PEG and μ Beads were mixed (100 pmol biotinylated molecules/100 μ L μ Beads) and incubated briefly at room temperature before being washed 3 x 200 μ L to remove unbound IAA-PEG. The IAA-PEG-bead complex was eluted by plunger in 150 μ L final volume. To increase selection stringency, a lower amount of IAA-PEG was immobilised onto the μ Beads from round 5 of SELEX onwards.

2.3.3 *Direct-SELEX process.*

Prior to each selection round, direct-SELEX library, 2 nmol at first round and the total quantity in following rounds, was denatured at 95°C for 5 min and snap cooled on ice for 10 min. The library was then added to fresh, uncoated streptavidin μ Beads and the mixture was incubated at room temperature for 1 hr with mild shaking; this serves as background elimination step. The mixture was then washed with 4 x 100 μ L SB on μ Column. The non-specific sequences bound to μ Beads were held on the column while other sequences were collected in the flow-through and subjected to a further selection process. In a positive selection step, the collected ssDNA was mixed with IAA-PEG-bead complex and incubated at room temperature for 1 hr with mild shaking. From round 5 onwards, a counter-selection step was performed by addition of control molecules to the ssDNA-bead mixture at 1:1 ratio of IAA-PEG : control molecules to remove any non-specific binders. The mixture was then washed with selection buffer on μ Column. In the first 6 rounds, 2 x 100 μ L boiling water was used to elute DNA bound to IAA-PEG while 10x excess of IAA was used to specifically elute DNA in further rounds.

The SELEX products, total quantity from first round and all but 50 μ L for following rounds, were amplified via polymerase chain reaction with reaction setups as shown in Table 2.3. The PCR products were pooled and 4% agarose gel electrophoresis in TBE buffer (100 mM Tris- HCl, 100 mM Boric acid, 2 mM EDTA) was used to check successful amplifications. The pooled products were purified with a PCR purification kit (NEB) according to the manufacturer's protocol and Nanodrop was used to estimate the concentrations of purified PCR products. The positive strands were separated from biotin-tagged negative strands using fresh streptavidin-coated

μBeads. The DNA was denatured at 95°C for 5 min before snap cooled on ice for 10 min. An appropriate amount of fresh μBeads was added and the mixture was briefly incubated before being washed with 2 x 100 μL SB on a pre-conditioned μColumn. The positive strands were collected in the column flow-through.

Table 2.3. **PCR setup for products from each round of direct-SELEX.** a) The composition of primers and reagents in each PCR reaction made up to 100 μL total volume in PCR reaction buffer (0.2 M Tris-HCl pH 8.4, 0.5 M KCl). b) PCR temperature cycles.

a.

Reagents	Concentrations
MgCl ₂	3 mM
FOR	0.1 μM
BIO-r	0.1 μM
dNTPs	0.2 mM
Taq Polymerase	2.5 U

b.

Temperature	time
95°C	2 min
95°C	30 sec
56°C	30 sec
72°C	30 sec
72°C	5 min
15°C	hold

10 cycles

In total, 10 rounds of direct-SELEX process were performed. The eluted positive strands from round 10 were amplified using FOR and REV primers. 4% agarose gel electrophoresis was used to check the successful amplifications and PCR products were cleaned up using PCR purification kit (NEB) according to the manufacturer's protocol. The cleaned PCR product was further cloned and sequenced to identify aptamer candidates.

2.4 Solution-SELEX

2.4.1 *Solution-SELEX library, capture oligos, and primers.*

Solution-SELEX library and capture oligo sequences (Table 2.1) were synthesized by Microsynth AG incorporating a PAGE purification step. Primers used for amplification in solution-SELEX processes were synthesized and desalted by Sigma-Aldrich while primers used for amplification in the final round of SELEX was from Tri-Link biotechnologies.

2.4.2 Immobilisation of capture oligos onto streptavidin-coated magnetic beads.

An appropriate amount of streptavidin coated- μ Beads was added to the pre-conditioned μ Column and was washed with 2 x 200 μ L SB. Biotinylated capture oligos (100 pmol biotinylated molecules/100 μ L μ Beads) were added to the column and the mixture was incubated at room temperature for 20 min. The bead mixture was washed 3 x 200 μ L before being double-eluted by centrifugation (1000 g for 2 min) with 400 μ L final volume.

2.4.3 Solution-SELEX process.

Prior to the hybridization step, solution-SELEX library was denatured at 95°C for 8 min and immediately snap cooled on ice for 10 min. The library, 2 nmol in the first round and the total quantity in following rounds, was added to the capture oligos- μ Beads complex solution and the mixture was incubated overnight at room temperature with mild shaking. After the hybridization, the DNA-bead complex was washed with 5 x 200 μ L SB on a pre-conditioned μ Column to remove any unbound strands before eluted from μ Column by centrifugation. A further temperature step was performed to remove weakly bound oligonucleotides by incubating the DNA-bead complex at 28°C for 15 min with mild shaking and washing with 5 x 200 μ L SB. Next, as background elimination step, 1% DMSO was added to the DNA-bead complex and the mixture was incubated at room temperature with mild shaking for 1 hr. After washing the complex with 5 x 200 μ L SB, IAA was added (1 mM final concentration in SB) and the mixture was incubated at room temperature with mild shaking for 1hr. The oligonucleotides that have binding affinities to IAA were released from the hybridisation with the capture oligo. They were collected by running the mixture through a pre-conditioned μ Column and washing with 6 x 100 μ L SB.

The released oligonucleotides were amplified in 77 parallel PCR reactions in the first round and 48 PCR reactions in the following rounds (setup parameters as shown in Table 2.4). All PCR products were pooled together and 4% agarose gel electrophoresis in TBE buffer was used to determine if amplification was successful. The pooled products were ethanol precipitated in the presence of linear polyacrylamide (Gaillard and Strauss, 1989) and resuspended in 300 μ L TE buffer (10

mM Tris-HCl pH 7.4, 1 mM EDTA). The positive strands were separated from negative strands due to their unequal lengths by denaturing urea-polyacrylamide gel electrophoresis (urea-PAGE) with 13.6% polyacrylamide gel containing 8 M urea in TBE buffer. The corresponding DNA bands were excised, crushed, and ssDNA was eluted by incubating in elution buffer (2 mM EDTA, 300 mM sodium acetate, pH 7.8) at 80°C for 150 mins. After filtering the residual polyacrylamide out through GF/C filters, the ssDNA was ethanol precipitated in the presence of linear polyacrylamide and resuspended in selection buffer.

Table 2.4. **PCR setup for products from each round of solution-SELEX.** a) The composition of primers and reagents in each PCR reaction made up to 50 μ L total volume in PCR reaction buffer (0.2 M Tris-HCl pH 8.4, 0.5 M KCl). b) PCR temperature cycles.

a.	Reagents	Concentrations	b.	Temperature	time	
	MgCl ₂	3 mM		95°C	5 min	
	FAM-f	0.1 μ M		95°C	30 sec	} 15 cycles
	dT25-r	0.1 μ M		56°C	30 sec	
	dNTPs	0.2 mM		72°C	30 sec	
	Taq Polymerase	1.25 U		72°C	7 min	
				4°C	hold	

Initially, 6 rounds of solution-SELEX process were performed. The released oligonucleotides from round 6 were amplified using FOR and REV primers. 4% agarose gel electrophoresis was used to check the successful amplification and the PCR products were cleaned up using QIAGEN PCR purification kit according to the manufacturer protocol. The cleaned PCR product was further cloned and sequenced to identify aptamer candidates.

Successively, three parallel solution-SELEX processes were performed with three different initial DNA sub-libraries obtained from previous three significant rounds of solution-SELEX to further enrich IAA-specific aptamers. Sequences of aptamers from last rounds of each parallel SELEX were identified through cloning and sequencing.

2.5 Cloning and Sequencing

The clean, amplified aptamers prepared as previously described were cloned into a pCR4-TOPO vector using the TOPO TA cloning kit for sequencing (Invitrogen). The recombinant vectors were transformed into OneShot™ TOP10F' chemically competent *Escherichia coli* cells (Invitrogen) which is recommended for smaller PCR products following the product protocol (Technologies, 2014). Colony PCR of 10 positive transformants from each SELEX process were used to screen for the successful ligation and transformation of the aptamer sequences. Plasmid DNA was isolated from positive colonies using a QIAprep Spin Miniprep kit (QIAGEN) and the inserted DNA were sequenced (GATC sequencing). The total number of plasmid DNA samples sent for each SELEX process is shown in Table 2.5. Multiple sequence alignment was performed using Jalview 2.11.1.3 software while secondary structure predictions were evaluated using ViennaRNA software and G-quadruplex formation simulations were analysed using QGRS webserver software.

Table 2.5. **Summary of plasmid DNA sent for GATC sequencing.**

Sub-library	Plasmid sent	Successful sequencing
R10d	96	84
R15s	64	56
R8Bs	64	63
R10Cs	64	59

2.6 Enzyme linked oligonucleotide assay (ELONA)

2.6.1 Preparation of SELEX sub-libraries for ELONA.

Plasmid DNA obtained from cloning and sequencing were bulk amplified using DIGO-f and PHOS-r primers using PCR conditions as established above. 2.5% agarose gel electrophoresis were used to confirm successful amplifications. An appropriate amount of λ -exonuclease was added to each PCR product and incubated at 37°C for 20 min for phosphorylated negative strand digestion followed by heat inactivation at 75°C for 10 min. ssDNA aptamer candidates were ethanol-precipitated

and resuspended in ELONA binding buffers (BB; 20 mM MES, 150 mM NaCl, 2 mM KCl, 2 mM MgCl₂, 0.45% w/v glucose, 0.05% Tween-20, 0.2 µm filtered). Before ELONA experiments, ssDNA was denatured at 95°C for 8 min followed by snap cooling on ice for 10 min.

2.6.2 Reagents, instrument, and streptavidin-coated 96-well plates.

Clear flat bottom polystyrene 96-well plates were purchased from Sigma-Aldrich (Greiner). Streptavidin (VWR international) was prepared to 1 µg/mL in carbonate buffer (15 mM Na₂CO₃, 35 mM NaHCO₃, pH 9.6). For plate coating, 100 µL of streptavidin solution was added to each well and the plates were incubated overnight at 4°C. The plates were completely dried and kept at 4°C until use. Initially, three biotinylated IAA derivatives were tested on ELONA, namely IAA-PEG, IAA-C6, and b-IAA. IAA-PEG and IAA-C6 were gifted by Professor Ken-ichiro Hayashi (Okayama University of Science) with the biotin linkers conjugated through Cα-position, while b-IAA was synthesized in-house with biotin linker conjugated through C5-position (unpublished). All biotinylated IAAs and free IAA were freshly prepared to 1 µg/mL and 10 mM, respectively, in BB at the beginning of each experiment day. For enzymatic assay, anti-digoxigenin antibodies with peroxidase conjugation (anti-DIGO-POD) was purchased from Roche and prepared according to the manufacturer while TMB substrate kit was purchased from Fisher Scientific. Three anti-IAA primary antibodies raised in rabbit were SAGE, PARSLEY, and D44. CLARIOstar®Plus microplate reader was used for all absorbance measurements at 450nm with pathlength correction at 200µL.

2.6.3 ELONA positive IAA immobilisation check with anti-IAA antibodies.

Streptavidin coated 96-well plates were blocked with 200 µL/well of 2% w/v milk protein in BB by an hour incubation at 37°C. The plates were washed 3 x 200 µL BB and 100 µL/well of biotinylated IAA was added at 1 µg/mL final concentration. The plates were incubated for an hour at RT before being washed with 3 x 200 µL BB. Different dilutions (1:250, 1:500, 1:1000, 1:2000, 1:4000) of anti-IAA primary antibodies in BB were added 100 µL/well and the plates were incubated for an hour at

RT. The plates were then washed 3 x 200 μ L BB and 100 μ L of 1:1000 dilutions of anti-IgG-rabbit-POD secondary antibody in 1% w/v milk protein in BB were added to each well. The plates were incubated for an hour at RT before being washed 3 x 200 μ L BB. A colorimetric assay was developed with 100 μ L TMB substrate kit for 20 min before stopping the reaction with 100 μ L of 2 M sulfuric acid. Absorbance at 450 nm was measured immediately.

2.6.4 ELONA biotinylated IAA concentration check with anti-IAA antibodies.

Streptavidin coated 96-well plates were blocked with 200 μ L/well of 2% w/v milk protein in BB by an hour incubation at 37°C. The plates were washed 3 x 200 μ L BB and 100 μ L/well of different dilutions of biotinylated IAAs (1, 2, 4, 10, and 20 μ g/mL) were added. After an hour incubation at RT, the plates were washed 3 x 200 μ L BB and 100 μ L/well of 1:250 dilution of anti-IAA primary antibodies in BB were added. The plates were incubated for an hour at RT before being washed with 3 x 200 μ L BB. 1:1000 dilutions of anti-IgG-rabbit-POD secondary antibody in 1% w/v milk protein in BB were added 100 μ L/well and the plates were incubated for an hour at RT. The plates were washed 3 x 200 μ L BB. A colorimetric assay was developed with 100 μ L TMB substrate kit for 20 min before 100 μ L of 2 M sulfuric acid was added to stop the reaction. Absorbance at 450 nm was measured immediately.

2.6.5 ELONA.

Blocking was performed prior to ELONA experiments by adding 200 μ L of 2% w/v milk protein in BB to each streptavidin-coated well and the plates were incubated for an hour at 37°C. The plates were washed 3 x 200 μ L BB and 100 μ L/well of 1 μ g/mL biotinylated IAAs in BB was added. The plates were incubated for an hour at RT before being washed with 3 x 200 μ L BB. For competition assay, either DMSO or IAA solution (10 μ M final concentration) were added to pre-equilibrated DIGO-aptamers and the mixture was added to the appropriate wells. The plates were incubated for an hour at RT before being washed 3 x 200 μ L BB, then, 100 μ L of 1:1000 dilutions of anti-DIGO-POD in 1% w/v milk protein in BB were added to each well. After an hour incubation at RT, the plates were washed 3 x 200 μ L BB and colorimetric assay was

developed with 100 μ L of TMB substrate kit for 20mins before stopping the reaction with 100 μ L of 2M sulfuric acid. Absorbance at 450 nm was measured immediately.

2.7 Microscale Thermophoresis (MST)

2.7.1 MST instrumentation and software.

All runs were performed and analysed using MO.control and MO.analysis software, respectively, on the Monolith NT.115 instrument (NanoTemper technologies). Standard treated capillaries (NanoTemper technologies) were used for all binding assays. Stock solutions of free labelled compounds were prepared in DMSO at the beginning of each measurement day to ensure compound stability.

2.7.2 Preparation of aptamer candidates for MST.

Aptamer candidates with fluorescein conjugated at the 5-end were synthesized and desalted by Sigma-Aldrich while candidates with Cy5 conjugation were synthesized with HPLC purification by Integrated DNA technologies. Before MST experiments, ssDNA was denatured at 95°C for 8 min followed by snap cooling on ice for 10 min.

2.7.3 MST binding check experiment.

Free labelled IAA was prepared to appropriate working solution with 10% DMSO in assay buffer. An aptamer candidate solution was mixed with either buffer or IAA solution in 1:1 volume ratio in an individual PCR tube and incubated for at least 5 min at RT. After, the samples were loaded into capillaries, placed on the MST capillary tray, and MST measurement was performed using MO.control software.

2.7.4 MST binding affinity experiment.

2X dilution series of IAA were prepared from an IAA stock solution in DMSO to make 16 IAA dilutions with 10% DMSO in assay buffer. A volume ratio of 1:1 of aptamer candidate solution and each IAA dilution was carefully mixed in an individual

PCR tube and incubated for at least 5 min at RT. The samples were then loaded into capillaries, placed on the MST capillary tray, and MST measurement was performed using MO.control software.

2.7.5 Assay buffer screening.

The compositions of all buffers screened are as shown in Table 2.6. All buffers were prepared and adjusted to appropriated pH levels, and 0.2 µm filtered before use.

Table 2.6. **Compositions of all buffers used in experimental analysis.** All buffers were adjusted to appropriate pH and 0.2 µm filtered prior to use.

PBS buffer		Tris buffer		MES buffer		HEPES buffer	
8.1 mM	Na ₂ HPO ₄	50 mM	Tris-HCl	20 mM	MES	20 mM	HEPES
1.5 mM	KH ₂ PO ₄						
137 mM	NaCl	150 mM	NaCl	150 mM	NaCl	150 mM	NaCl
2.7 mM	KCl	5 mM	KCl	2 mM	KCl	2 mM	KCl
2 mM	MgCl ₂	2 mM	MgCl ₂	2 mM	MgCl ₂	2 mM	MgCl ₂
0.45%	Glucose						
0.05%	Tw-20	0.05%	Tw-20	0.05%	Tw-20	0.05%	Tw-20
pH 7.2		pH 7.4		pH 5.8 and 7.2		pH 7.2	

2.7.6 Aptamers specificity tests.

A serial dilutions of different compounds (chemical structures as shown in Figure 2.2) were tested against the chosen aptamers using MST binding affinity experiments (section 2.7.4).

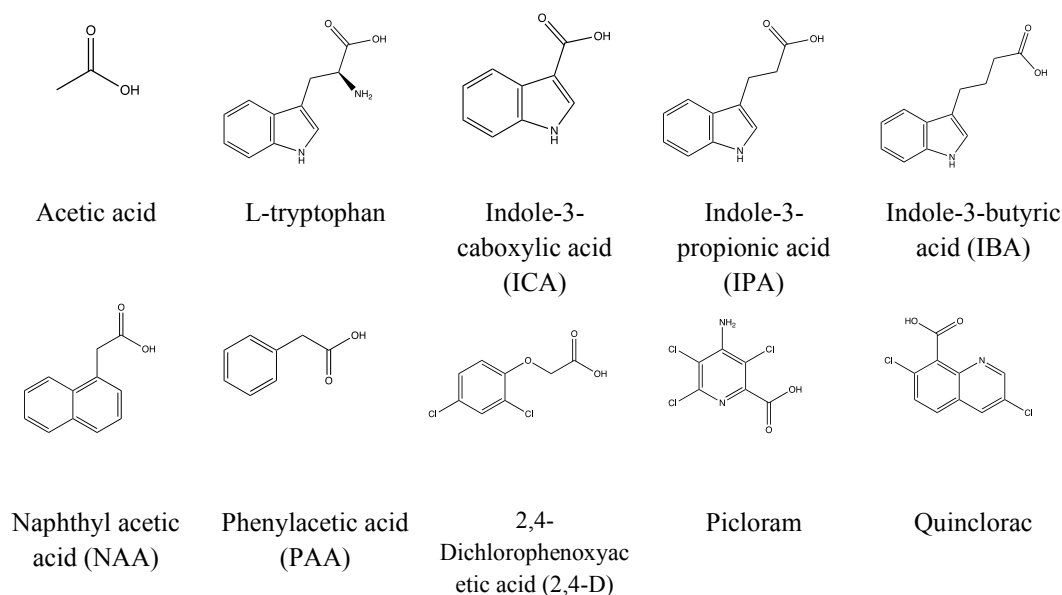


Figure 2.2. **Compounds and their chemical structures used for MST specificity tests.**

2.7.7 Alternative MST using fluorescent auxins as target.

C2-NBD-IAA, C4-NBD-IAA, 6-Bodipy-C4- triazole-C1-IAA, and C2-NBD-benzoic acid were gifted by Professor Ken-ichiro Hayashi (Hayashi et al., 2014). All fluorescent auxins and benzoic acid solutions were prepared to 10 mM stock solution in DMSO and stored at -20°C until use. The chemical structures of all IAA derivatives are as shown in Figure 2.3.

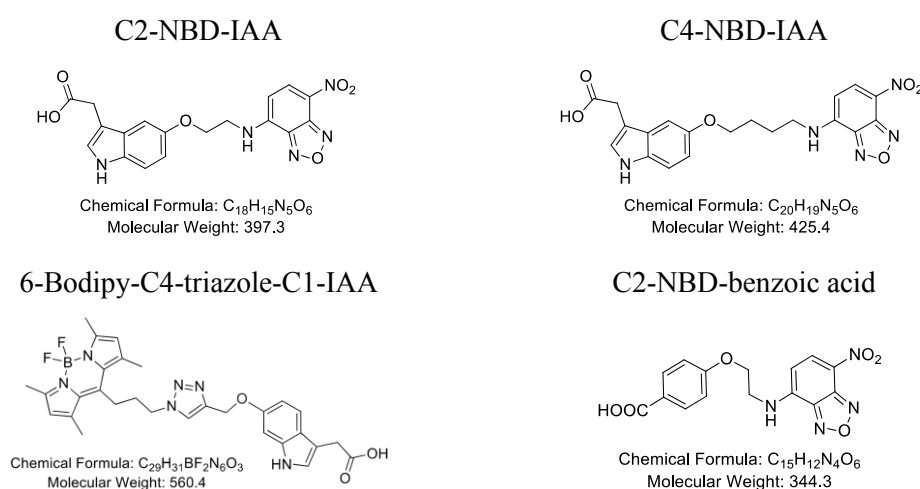


Figure 2.3. **Chemical structures of fluorescent auxins and benzoic acid used in MST secondary screening.**

2.7.7.1 Preparation of aptamer candidates for alternative MST experiments.

Plasmid DNA obtained from cloning and sequencing was bulk amplified using FOR and PHOS-r primers followed by 2.5% agarose gel electrophoresis to evaluate successful amplification. ssDNA purification from PCR products was as described above (section 2.6.1). DNA aptamers were resuspended in sterile water to 100 μ M stock solution and kept at -20°C until use. For binding affinity experiments, all aptamer candidates were synthesized and desalted by Sigma-Aldrich. Before MST experiments, ssDNA was denatured at 95°C for 8 min followed by snap cooling on ice for 10 min.

2.7.7.2 Assay optimisation.

All fluorescent compounds (Figure 2.3) were diluted to several final concentrations (20 – 1000 nM) in MES buffer with 5% DMSO. Fluorescence signals of each compound were measured using ‘pre-test’ settings on MO.Control software to determine appropriate working concentrations.

2.7.7.3 MST binding check experiment.

For each compound and each aptamer, two sets of samples were prepared, compound-only and compound-aptamer solutions. Using binding check setting, signal amplitudes and signal-to-noise ratios were compared.

2.7.7.4 Aptamer-IAA binding affinity experiments.

Binding affinity experiments were performed on C2-NBD-IAA and C2-NBD-benzoic acid with 8 aptamer candidates. Concentrations of fluorescent compounds were kept at 1 μ M final concentration in 5% DMSO. Serial dilutions of each aptamer candidate were prepared to make 16 2X dilution series with final measuring concentrations ranging from 800 pM to 25 μ M. Then, 1:1 volume ratio of fluorescent compound solutions and each aptamer candidate dilution was carefully mixed in an individual PCR tube and incubated for at least 5 min at RT. The samples were then loaded into capillaries, placed on the MST capillary tray, and MST measurement was performed on binding affinity settings.

2.8 Thioflavin T (ThT) assay

2.8.1 Thioflavin T, assay buffer, and fluorescence measurements.

Thioflavin T (ThT) was purchased from Sigma-Aldrich and was prepared to 0.1 mM stock solution in water. Tris buffer (Table 2.6) was used as assay buffer. All fluorescence measurements were performed with CLARIOstar®Plus microplate reader using black flat-bottom 96-well plates (Greiner). Excitation wavelength was set

at 425 nm with 10 nm bandwidth and fluorescence emission collected from 455 – 600 nm.

2.8.2 Preparation of aptamer candidates for ThT assay.

Unmodified aptamer candidates were synthesized and desalted by Sigma-Aldrich. Before ThT assay, all aptamer candidates were prepared to 1 μ M working solution in assay buffer and were denatured at 95°C for 8 min followed by snap cooling on ice for 10 min.

2.8.3 Assay optimisation.

Aptamer concentrations ranging from 100 nM to 800 nM final concentration were tested. In 100 μ L final volume, each aptamer concentration was added to 1 μ M ThT final concentration. The mixture was incubated for at least 5 min before being transferred to a black, flat-bottom 96-well plate and fluorescence emission was measured.

2.8.4 ATP aptamer for assay validation.

Adenosine triphosphate (ATP) was purchased from Sigma Aldrich as ATP magnesium salt. Initially, equilibrated ATP aptamer (600 nM final concentration) and ATP solution (final working concentration ranging from 250 μ M to 10 mM) were carefully mixed in assay buffer. The mixture was incubated at RT for at least 5 min before ThT solution (1 μ M final concentration) was added. After incubation at RT for at least 5 min, the mixtures were transferred to black, flat-bottom 96-well plates and fluorescence emission spectra was measured.

2.8.5 ThT assay.

For qualitative experiment, an equilibrated aptamer (100 nM final concentration) and an appropriate amount of IAA (250 μ M final concentration) or DMSO were mixed and the mixtures were incubated at RT for at least 5 min. ThT solution (1 μ M final concentration) was then added and the mixtures were incubated

for an additional 5 min before being transferred to black, flat-bottom 96-well plates and fluorescence emission spectra was measured.

For a dose response experiment, a 2X serial dilution of IAA was initially prepared from IAA stock solution to make an 11 concentration series from 250 nM to 250 μ M final concentration in assay buffer. In 100 μ L final volume, an equilibrated aptamer (100 nM final concentration) and each IAA dilution or DMSO were mixed and incubated at RT for at least 5 min. ThT solution (1 μ M final concentration) was added and the mixtures were incubated for an additional 5 min before being transferred to black, flat-bottom 96-well plates and fluorescence emission spectra was measured. Control samples of IAA or DMSO solution in buffer were used as negative controls.

2.9 Surface plasmon resonance (SPR)

2.9.1 Biacore platform and consumables.

A streptavidin coated series S (SA) sensor chip was purchased from Cytiva. Prior to immobilisation, the SA sensor chip surface was washed with 3 x 50 mM NaOH for 30 sec at 30 μ L/min to remove any contaminants and thoroughly washed with assay buffer. Samples were prepared in polypropylene (PP) plastic vials with rubber caps (Cytiva) or PP U-bottom 96-well plates (Greiner). A range of buffers (Table 2.6) were tested on the Biacore platform and were prepared and 0.2 μ m filtered at the beginning of each experimental day. The Biacore T200 system (Cytiva) was used for all SPR experiments and the system was primed with assay buffer before use. All experiments were performed at ambient temperature (25°C).

2.9.2 Biotinylated probe and poly-A tail aptamer candidates.

Biotinylated oligo(dT) probe (sequenced 5' – biotin-C14-NH-(T)25 – 3') was purchased from Promega as a 50 μ M stock solution. Aptamer sequences (Table 2.7) were designed to have a complementary poly-A tail on the 3'-end for hybridisation with dT25 probe. Before immobilisation onto SA chip, all aptamer candidates were prepared to a 1 μ M working solution in assay buffer and were denatured at 95°C for 8 min followed by snap cooling on ice for 10 min.

Table 2.7. Lists of aptamer sequences performed on Biacore platform.

Aptamer names	Sequences (5'-3')
ATP-dT ₂₅	ACCTGGGGGAGTATTGCGGAGGAAGGTAAAAAAAAAAAAAA AAAAAAAAAAAAAA
tZeatin-dT ₂₅	CGGATATGGTTAGGCAGGCATAAGAGGTTTATCCGAAAAAA AAAAAAAAAAAAAA
ST57-1-dT ₂₅	ACACGGTTTAGCTTCTACTAATCGGGGTCTTTGGCTTGACTA GTACATGACCACTTGAAAAAAAAAAAAAAAAAAAAAAAAAAAA
ST57-1-37-dT ₂₅	ACACGGTTTAGCTTCTACTAATCGGGGTCTTTGGCTGGACTA GTACATGACCACTTGAAAAAAAAAAAAAAAAAAAAAAAAAAAA
STA3-d T ₂₅	GCGGATGAAGACTGGTGTGAGGGGATGGGTAGGTGGAAAA AAAAAAAAAAAAAAAAAAAAAA
STA3-9-d T ₂₅	GCGGATGAGGACTGGTGTGAGGGGATGGGTAGGTGGAAAA AAAAAAAAAAAAAAAAAAAAAA

2.9.3 Immobilisation of aptamer candidates.

Manual runs were used for all aptamer immobilisations. Initially, 500 nM biotinylated oligo(dT) probe was immobilised on the active flow cells (Fc 2, 3, 4) of the SA chip at 5 µL/min for 10 min while the reference flow cell was left blank. Several washes with 50 mM NaOH at 30 µL/min for 30 sec were to ensure removal of any unbound biotinylated probe. Equilibrated aptamer solutions were injected on appropriate working flow cells at 4 µL/min for 15 min. The response unit (RU) was monitored to ensure appropriate immobilisation. Assay buffer was washed extensively over the surface to ensure removal of any unbound aptamers.

2.9.4 SPR assay.

SPR binding affinity experiments were performed with aptamers for ATP and trans-zeatin (tZ) used as assay validation. ATP and trans-zeatin were purchased from Sigma Aldrich and were prepared to 10 mM stock solution in DMSO. Several compounds were tested against tZ aptamer, including N6-dimethylallyl adenine, trans-zeatin-riboside, and 6-Benzylaminopurine, and were prepared to 10 mM stock solution in DMSO. Dilution series of the analytes were prepared with 2% DMSO in assay buffer. Analyte association was examined when each analyte solution was injected on the flow cells at 5 µL/min for 60 sec. Subsequent assay buffer wash for 60

sec was to allow dissociation of analytes from surface with no regeneration steps required. The assay method was set to include three start-up cycles, negative control (assay buffer with 2% DMSO), and solvent correction solutions. Binding analysis and K_D calculation were performed using built-in analysis software.

2.10 Isothermal Titration Calorimetry (ITC)

2.10.1 ITC instrumentations and assay buffer.

All ITC measurements were performed on VP-ITC (MicroCal) instrument using VPViewer and Origin 7 software. Samples were degassed and incubated at the experimental temperature using a ThermoVac unit for at least 5 min prior to sample loading. The reference cell was loaded with deionised distilled water (ddH₂O) and was cleaned periodically. The sample cell and sample auto-pipette were washed thoroughly with ddH₂O prior to each run. For extensive wash, sample cell and sample auto-pipette were flushed with 300 mL of 5% (v/v) Decon 90 (Decon) followed by 500 mL of ddH₂O. HEPES buffer (Table 2.6) was used as the assay buffer.

2.10.2 Single Injection Method (SIM) mode.

SIM mode of operation was activated in VPViewer prior to SIM experiments and the appropriate samples (Table 2.8) were loaded to the sample cell and auto-pipette. Injection and experimental parameters were set as detailed in Table 2.9.

Table 2.8. **Samples loaded on the sample cell and auto-pipette for SIM mode.**

Experiments	Samples in auto-pipette (concentration)	Samples in sample cell (concentration in μM)
Buffer-to-buffer	HEPES buffer (0 μM)	HEPES buffer (0 μM)
Trans-zeatin-to-buffer	Trans-zeatin (200 μM)	HEPES buffer (0 μM)
Trans-zeatin-to-aptamer	Trans-zeatin (200 μM)	Trans-zeatin aptamer (20 μM)
IAA-to-buffer	IAA (100 μM)	HEPES buffer (0 μM)
IAA-to-aptamer	IAA (100 μM)	STA3-9 aptamer (20 μM)

Table 2.9. **Injection (a) parameters for SIM mode experiments and experimental (b) parameters set on VPViewer for all ITC measurements except stated otherwise.**

(a) Injection parameters		(b) Experimental parameters	
Injection volume	280 μ L	Total # injections	1
Duration	2800 sec	Cell temperature	15°C
Spacing	3100 sec	Reference power	4 μ Cal/sec
Filter period	2 sec	Initial delay	60 sec
		Stirring speed	502 rpm
		Feedback gain	High
		ITC equilibration	Auto

2.10.3 Serial injection experiments.

Serial injection of water into water was used as a differential power (DP) baseline calibration. In total of 20 injections was performed for serial injection experiment with the first injection of 2 μ L for 4 sec with 200 sec spacing followed by sequential injections of 7 μ L for 14 sec with 400 sec spacing with filter period set to 2 sec. For serial injection experiments, the experimental parameters were set in accordance with the SIM mode (Table 2.9) with stirring speed adjusted to 307 rpm.

2.11 Circular Dichroism (CD)

2.11.1 Aptamer, IAA, and buffers.

HEPES buffer (Table 2.6) was used as the assay buffer for all CD measurements. STA3-9 aptamer was prepared to 10 μ M final concentration in assay buffer containing 0.1% DMSO. IAA was added to 250 μ M final concentration with 0.1% DMSO for CD spectra measurement of the aptamer in presence of auxin.

2.11.2 CD instrumentation and experimental parameters.

All CD measurements were performed at the Department of Chemistry (University of Warwick) using a J-1500 spectropolarimeter supplied with a Peltier thermally controlled cuvette holder (Jasco UK). The CD spectra were recorded at 25°C in a 1.0 mm path length cuvette (Starna). Full spectra were measured at 25°C between

210-340 nm, with a bandwidth of 2.0 nm, step resolution of 0.2 nm, scanning speed of 200 nm/min, response time of 1 s and averaged from 4 individual scans after subtraction of the solvent spectrum. Thermal melt experiments were performed by acquiring static wavelength measurements at 242 and 263 nm between temperatures of 20-85°C.

2.12 Carbon-based polymer nanoparticle (CPN) synthesis and characterisation

All carbon-based polymer nanoparticles (CPNs) investigated were synthesized and provided by the collaborating Polymer group at the Chemistry Department in the University of Birmingham. In brief, nanoparticles were synthesized using a reverse addition-fragmentation chain-transfer (RAFT) mediated polymerisation-induced self-assembly (PISA) technique (Canning et al., 2016). Dynamic light scattering (DLS), proton nuclear magnetic resonance (¹H-NMR) and spectrofluorometer analysis were used to characterise all CPNs prior to fluorescence evaluation using confocal microscopy.

2.13 Plant sample preparation

2.13.1 Arabidopsis thaliana and growth conditions.

A. thaliana ecotype Columbia-0 was used for all biosensor evaluations. The seeds were surface-sterilised using 10% bleach and 70% ethanol prior to seeding on sterile ½ MS media agar plate (2.2 g/L Murashige and Skoog medium supplemented with B5 vitamins, 1% sucrose, 1% agar, pH 5.8). Seeds were stratified on ½ MS media agar plate in the dark for two days at 4°C prior to germination for 5 days at 22°C with 12-hour light period.

2.13.2 *A. thaliana* root protoplast isolation.

2.13.2.1 Protoplast solutions and consumables.

Protoplast and enzyme solutions (Table 2.10) were prepared in-house, adjusted to pH 5.5 with Tris-HCl, 0.2 µm filtered, and stored at -20°C until use. MES hydrate and bovine serum albumin (BSA) were purchased from Sigma Aldrich. Cellulase “Onozuka” RS was purchased from Melford Biolaboratories (Duchefa) and Pectolyase was purchased from Sigma Aldrich. 35mm round Petri dishes were purchased from Falcon while 70 µm and 40 µm cell strainer meshes were purchased from VWR. Polystyrene culture tubes (STARLAB) were used for all centrifugation steps.

Table 2.10. **Buffer composition of protoplast (a) and enzyme (b) solutions used for protoplast isolation.**

(a) Protoplast solution		(b) Enzyme solution	
600 mM	Mannitol	Protoplast solution	
2 mM	MgCl ₂	1.5% (w/v)	Cellulase RS
2 mM	CaCl ₂	0.1% (w/v)	Pectolyase
10 mM	KCl		
2 mM	MES hydrate		
0.1% (w/v)	Bovine serum albumin (BSA)		

2.13.2.2 Protoplast isolation

5-day old *A. thaliana* roots (section 2.14.1) were submerged in enzyme solution and were finely chopped using a sterile blade. The solution with chopped roots was transferred to a 35 mm round Petri dish and incubated in the dark at 25°C with constant agitation for at least 2 hr. The root solution was sequentially filtered through 70 µm and 40 µm cell strainer meshes pre-soaked with enzyme solution. The filtered protoplasts in solution were carefully transferred to polystyrene culture tubes and an equal volume of protoplast solution was added. The solution was centrifuged at 300 g for 5 min at 4°C. The supernatant was discarded, and protoplasts were resuspended in equal volume of protoplast solution before being centrifuged at 300 g for 5 min at 4°C. The supernatant was discarded and protoplasts were resuspended in 500 µL protoplast solution. Isolated protoplasts were used immediately.

2.13.3 *Apoplastic fluid extraction*

Apoplastic fluid was extracted from 6 – 8 week old wild type *Nicotiana benthamiana* provided by a research colleague (University of Warwick). In short, seeds were stratified in 0.1% (w/v) agarose at 4°C for three days prior to sowing in pre-soaked compost. Leaves from 6-weeks old *Nicotiana benthamiana* were harvested and submerged in an ice-deionised water bath. Vacuum infiltration was applied to allow water intake of the leaves. Infiltrated leaves were removed from the ice-water bath and excess water was removed. Apoplastic fluid was subsequently collected by centrifugation at 2500 rpm with low acceleration and deceleration at 4°C for 25mins. Collected apoplastic fluid was placed on ice for subsequent use on the day of extraction.

2.14 **CPN evaluation in plant samples**

2.14.1 *Stability evaluation under agarose gel electrophoresis.*

For stability evaluation, 5 µL of aptamers (8 µM) or CPN samples (1 mg/mL) were added to 25 µL apoplastic fluid (section 2.14.3) and the mixture was incubated for at least 30 min. Samples were loaded onto 2% agarose gel electrophoresis in 1x TBE buffer before running at 80V for 1 hr. The gels were imaged using a Typhoon FLA 9500 biomolecular imager (Cytiva).

2.14.2 *Confocal microscopy.*

A. thaliana intact roots (section 2.13.1) and isolated protoplasts (section 2.13.2) were incubated with CPN samples (1 mg/mL) for at least an hour before visualisation under a fluorescence confocal microscope. For all confocal microscopy, plant samples were mounted on glass slides (1.0-1.2mm thick) and long glass cover slips (22x50mm, 0.16-0.19mm thick) before visualisation using a Zeiss LSM 880 instrument under 40x objective lens. The images were stacked and reconstructed by ZEN software (ZEISS) and analysed using ImageJ software.

Chapter 3 Auxin aptamer selection through SELEX processes and secondary screenings

This chapter describes the selection of IAA aptamers through a systematic evolution of ligands by exponential enrichment (SELEX) and screening additional candidates. A SELEX process starts with a ssDNA library with high diversity ($\sim 10^{15}$). An introduction of IAA to the oligonucleotide library pool allowed binding and selection of IAA-binding sequences. These binders were partitioned from the rest of the pool and subjected to amplification via polymerase chain reaction. Two types of SELEX, direct- and solution-SELEX, were performed to compare DNA sequences selected for auxin specific interactions. Whilst direct-SELEX used magnetic beads to facilitate partitioning of bound sequences, it requires immobilisation of IAA which could be problematic due to structural modifications in such a small ligand. In contrast, solution-SELEX uses unaltered ligand and can, in theory, promote selection of aptamers with active conformational change which would facilitate further assay adaptations (Blind and Blank, 2015). The latter method has been widely employed for selection of aptamers against small molecule ligands (Reinemann et al., 2016, Stoltenburg et al., 2012). Sequence analyses were used to search for aptamer candidates which have become enriched by SELEX and identify any key similarities or differences in the sub-libraries obtained from both SELEX types.

3.1 Selection of aptamers against IAA using direct-SELEX

Direct-SELEX was first performed to select auxin aptamers using biotinylated IAA immobilised on streptavidin-coated magnetic beads. To ensure a successful selection of aptamer candidates from the ssDNA library, several steps needed to be considered before SELEX was started, including PCR conditions, sub-library preparation for subsequent rounds, and selection stringency. Optimisation of PCR conditions was initially performed to ensure successful amplification of SELEX products from each round. The number of PCR cycles was monitored carefully to avoid PCR by-products or mutants. These conditions were also tested with the eluting ligand to check that it did not interfere in PCR reactions during sub-library amplifications (Figure 3.1).

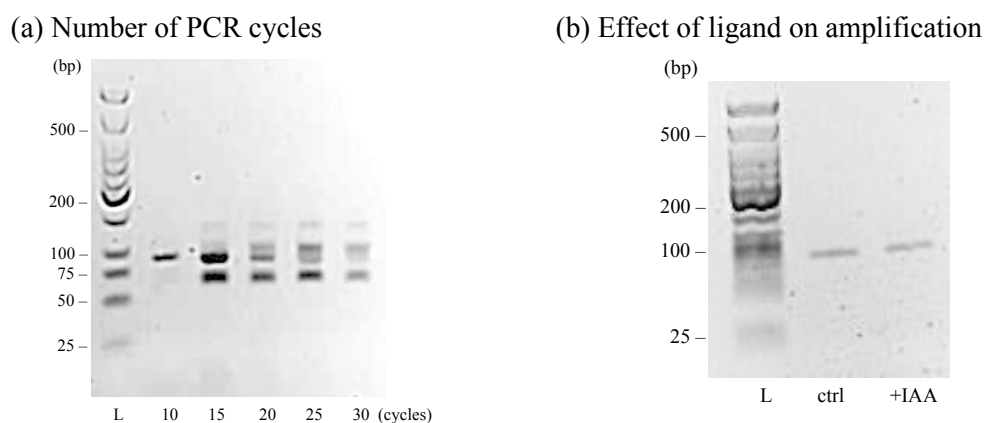


Figure 3.1. **4% agarose gel electrophoresis of PCR optimisation.** Low molecular weight DNA ladder (marked 'L', NEB) was used as DNA size standard. (a) Number of PCR cycles was optimised to 10 PCR cycles to avoid amplification of by-products. (b) IAA was added to the PCR reactions to confirm no impact of this ligand on DNA amplification.

Prior to bulk amplifications at each SELEX round, pilot PCRs were tested with various volumes of SELEX products (Figure 3.2) to ensure an appropriate amount of DNA was used for successful amplifications. In the first direct-SELEX round, after the incubation of ssDNA library with biotinylated IAA immobilised on streptavidin-coated μ Beads, the first SELEX sub-library was non-specifically eluted with hot water. In the pilot PCR, 1 μ L of eluant proved insufficient volume and resulted in an insufficient yield of amplification product, while overloading (20 μ L) saturated amplification. Bulk amplification using FOR and BIO-r primers was subsequently performed with 10 μ L of SELEX product in each PCR reaction.

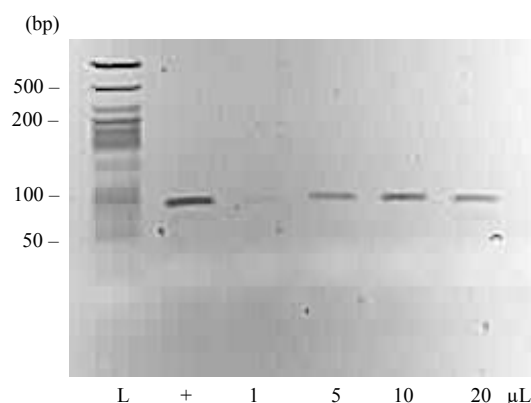


Figure 3.2. **4% agarose gel electrophoresis of PCR products using different volumes of product from first round of SELEX for IAA aptamers.** PCR products were analysed against low molecular weight DNA ladder (marked 'L') and an aliquot of library as PCR positive control (+). The optimal volume of SELEX product (10 μ L in this case) was used for bulk amplification.

Removal of unincorporated primers and PCR negative strands is essential following bulk amplifications. Any leftover primers would interfere with both product quantification using Nanodrop, and strand separation using μ Beads. Pooled bulk PCR products were purified with a standard PCR purification kit. DNA quantification then confirmed successful amplification but also allowed estimation of the volume of μ Beads required for strand separation. The purified PCR product was denatured at 95°C for 5 min before snap cooling on ice for 10 min before adding washed μ Beads. The biotin-tagged negative strands were immobilised by the strong streptavidin-biotin interaction on the μ Beads while the positive strands were collected in the flowthrough ready for the following SELEX round.

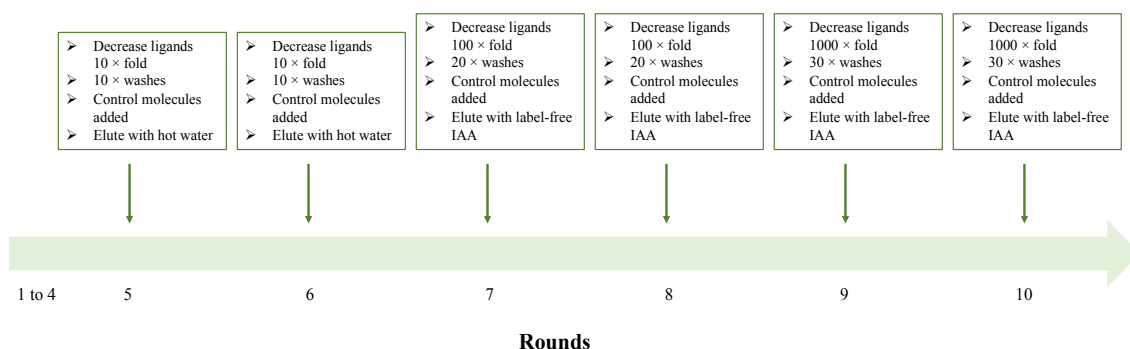


Figure 3.3. **Schematic timeline of direct-SELEX process.** The increase in stringency included lower ligand availability, introduction of control molecules to the selection process, higher number of washes, all followed by selective elution with label-free ligand.

Following five rounds of SELEX, selection stringency was gradually increased to enhance the binding affinity and specificity of the auxin aptamer selection (Figure 3.3; (Blind and Blank, 2015)). From round seven onwards, 10x excess of label-free IAA was used to compete with IAA-PEG and elute IAA-specific binders during positive selection steps. A reduced amount of immobilised IAA-PEG was used on the μ Beads for the positive selections to promote selection of aptamers with higher binding affinity. More extensive washing steps removed weak binders. Counter-selection steps with control molecules were introduced from the fifth round onwards to enhance aptamer specificity. The control molecules (Figure 3.4) were chosen for their similarities in chemical structures with IAA and are commonly found in plant. The mixture of control molecules were added at 1:1 molar ratio of each compound

with IAA-PEG to the ssDNA - μ Beads mixture and non-specific binding sequences were removed by washing.

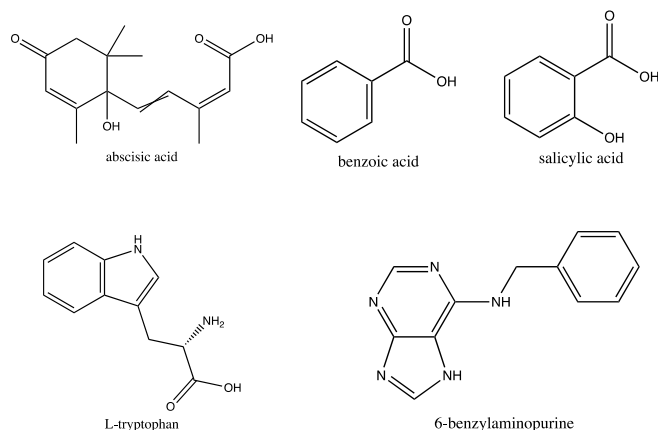


Figure 3.4 **Chemical structures of control molecules used in SELEX process.** Tryptophan, precursor for IAA, was chosen for its structural similarity while other control molecules are organic compounds commonly found in apoplast (Novak et al., 2017).

The sub-library from the tenth round of SELEX was amplified and prepared for sequence analysis through cloning and sequencing (Section 2.5). A TOPO TA cloning kit for sequencing with pCR4-TOPO vector was chosen for cloning (Reinemann et al., 2016, Stoltenburg et al., 2012, Sefah et al., 2010). Colony PCRs of 10 transformants were performed to confirm successful ligation and transformation of aptamer sequences. Subsequently, plasmid DNA was isolated from 96 positive colonies using a standard plasmid DNA purification kit and the inserted DNA was sequenced using Sanger sequencing. From all samples submitted for sequencing, 84 sequences were complete, and a full sequence analysis was performed. Only four sequences were found in duplicate while no sequences were found more than three times, suggesting little enrichment for any dominant aptamer candidate. Further, more detailed sequencing analysis was performed alongside sequencing data obtained after solution-SELEX.

3.2 Selection of aptamers against IAA using solution-SELEX

As an alternative method for auxin aptamer selection, solution-SELEX utilised biotinylated capture oligos to hybridise the ssDNA library onto streptavidin-coated magnetic beads. The general library sequence, capture oligos, and the selection

SELEX, pilot PCRs were performed prior to each bulk amplification to ensure successful amplifications.

To improve recovery of ssDNA positive strands from negative strands, a denaturing urea-PAGE technique was used instead of the streptavidin-coated μ Beads technique. During bulk amplification, FAM-f primer was used to monitor amplifications and positive strand recovery (Stoltenburg et al., 2005). A dT25-r primer was added to the amplification reaction to increase the size of negative strands over positive strands (Figure 3.6). Denaturing urea-PAGE gels were imaged under fluorescence and the fluorescent band was excised, crushed, and the DNA eluted.

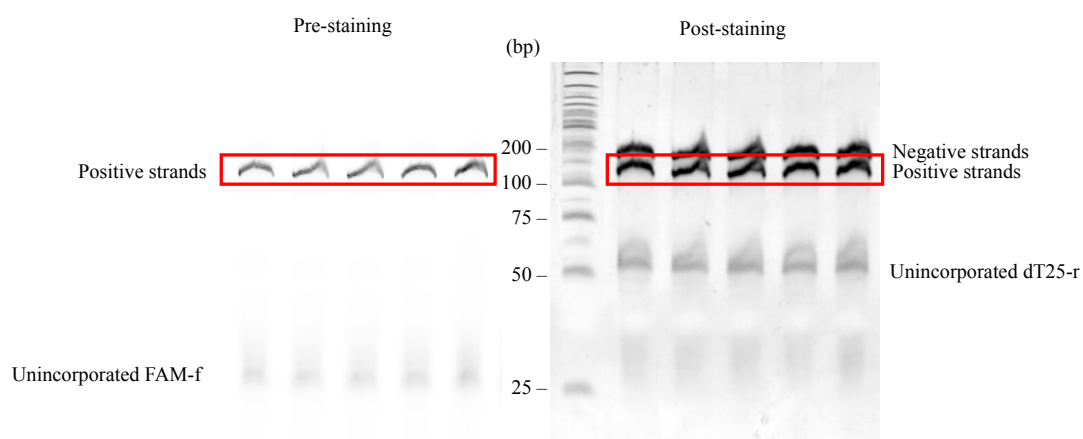


Figure 3.6. Analysis of denaturing urea-PAGE of pool PCR products from first round of solution-SELEX showing SELEX product amplification. Fluorescence image (left) revealed successful amplification of SELEX products containing fluorescein at 5'-end (red boxes). Subsequently, the gel was stained with GelRed and visualised under UV light (right) to show DNA ladder and larger bands corresponding to poly(dT₂₅) negative strands.

Initially, sub-library sequences from round 6 of solution-SELEX were cloned, sequenced, and analysed as above (Section 3.1). A total of 96 plasmid DNA samples were submitted and 82 were returned complete. At this stage, nine sequences were observed more than once suggesting improvement from previous aptamer selection with direct-SELEX. However, with no obvious enrichment of particular sequences or motif (data not shown), two additional rounds of SELEX were implemented to include counter-selection steps with control molecules (Figure 3.4) and to improve enrichment of IAA-specific binders. As previously mentioned, relative frequency of certain aptamer sequence can be observed from round 5 to 8 (Blank, 2016). Therefore, eight rounds of solution-SELEX were initially performed and a deep sequencing analysis

using next generation sequencing (NGS) was used to analyse the sub-library profiles from round two to eight. The far greater numbers of sequences available from NGS should reveal any enrichment profiling of sequences across the selection rounds and support assessments on the selection efficiency (Mayer, 2016). AptaSUIE software was used to evaluate enrichment of sequences and clustering of motifs. Only 32 copies of the most enriched cluster were found after 8 rounds, with enrichment only emerging from round 7. This accounted to less than 0.0001% of this sub-library (data not shown). While the NGS data could confirm the necessity of the additional rounds of positive and counter selections, it was clear that the selection performed so far was insufficient and further selections with various stringency were needed.

In an effort to improve the selection of auxin aptamers, three parallel solution-SELEX processes were devised starting from three different SELEX sub-libraries (Figure 3.7). Seven additional rounds of solution-SELEX with increasing stringency were performed sequentially as a direct extension of the strategy from round eight (green branch). It was hoped that auxin-specific binders would be enriched with 15 rounds of positive selection and four rounds of counter-selection. However, it was reasoned that the counter-selection steps may have overly stringent, and aptamers were lost before the positive elution step (Ruscito and DeRosa, 2016). Therefore, two branches of solution-SELEX were made from sub-libraries collected before counter-selection steps were introduced. One parallel solution-SELEX started from sub-library of first SELEX round (Figure 3.7; yellow branch). Another parallel solution-SELEX was performed from SELEX round six (Figure 3.7; blue branch) before high selection stringency had been introduced.

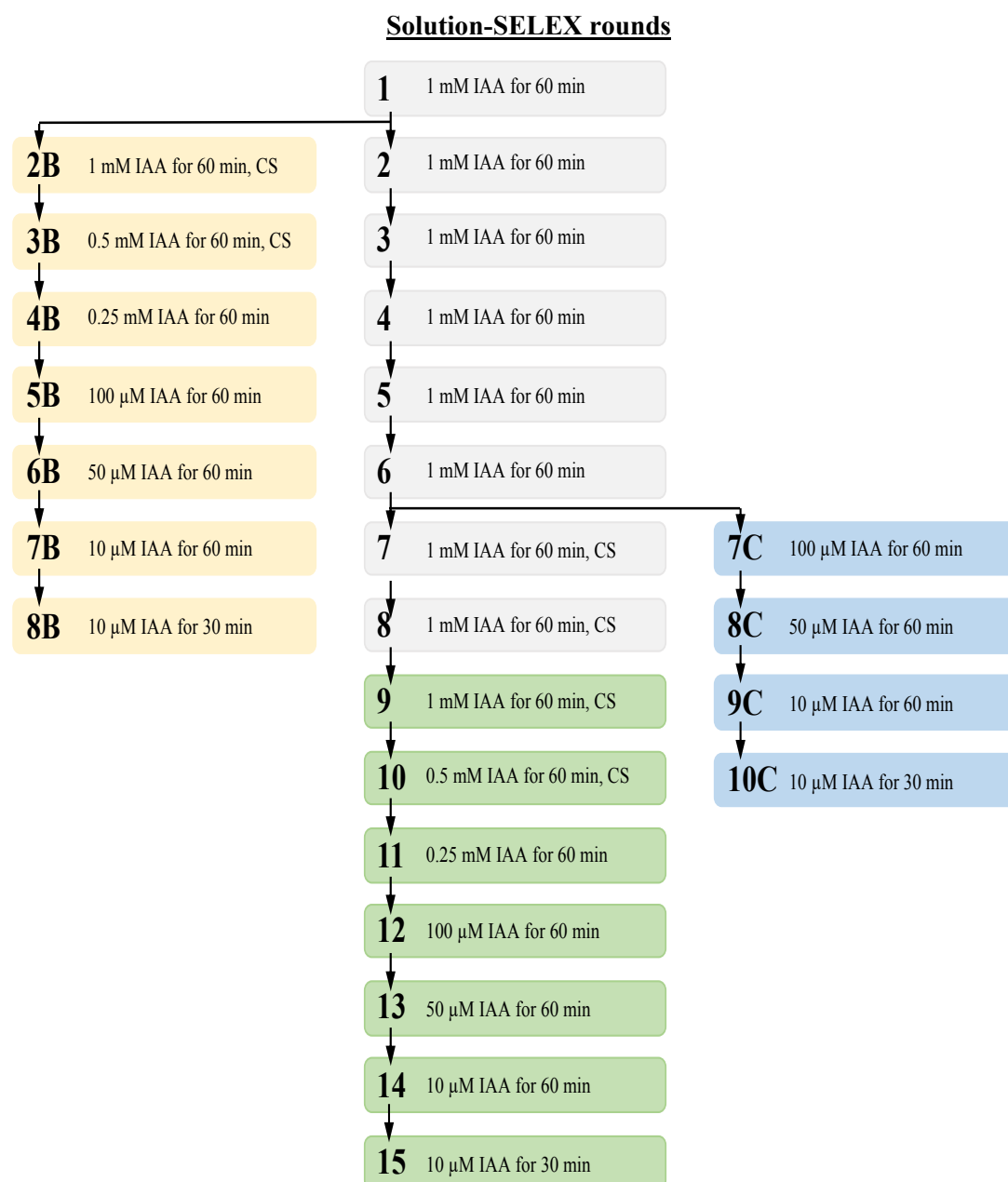


Figure 3.7. **Schematic workflow of overall solution-SELEX process.** Three parallel solution-SELEX were branched from three sub-libraries obtained from the initial eight rounds of solution-SELEX (grey). The concentration of IAA and the incubation time used in positive selection steps are listed for each round. Solution-SELEX rounds performed with counter-selection steps are noted with CS. The green branch was the continuation of the original solution-SELEX from sub-library round 8 while the B branch (yellow) started from the first SELEX product round to allow re-selection of highly diverse and low stringent sub-library. The C branch (blue) continued from SELEX product of round six where substantial selection was performed with no high stringent counter-selection introduced.

The sub-libraries from each branch of solution-SELEX (8B, 15, and 10C) were amplified and prepared for sequence analysis through cloning and sequencing. Plasmid DNA was isolated from 64 positive colonies using a standard plasmid DNA

purification kit and the inserted DNA were sequenced using Sanger sequencing. The complete sequences were subject for further analysis. Unfortunately, no predominant enrichment of particular sequences was found from the initial sequencing analysis. A more detailed analysis was performed alongside sequencing data obtained from direct-SELEX and initial solution-SELEX round six.

3.3 Comparative sequencing analysis of direct- and solution-SELEX

With the initial sequencing analysis of sub-libraries obtained from direct- and solution-SELEX showing no predominant enrichment of particular sequences, a further, more detailed sequencing analysis was performed across the sub-libraries in an attempt to identify more cryptic binding motifs or patterns and to evaluate the selection efficiency of the two SELEX techniques. A total of 384 plasmid samples were submitted for sequencing across direct- and four parallel-SELEX process (Table 3.1) with more than 87.5% complete sequences returned available for further analysis. No sequences were found more than three times suggesting little enrichment of certain sequences were reached. Comparing the data across sub-libraries, more positive selection rounds did result in more sequence duplicates. However, it can also be correlated that the number of performed counter selection steps negatively impacted the numbers of repeated sequences. The prime example is R15s where a total of 15 positive and four counter-selection rounds resulted in no identical sequences. On the other hand, three pairs of repeated sequences were observed from R10Cs with 10 positive and no counter-selection rounds. This supports the earlier hypothesis that aptamer selection could be compromised by harsh counter-selection steps (Ruscito

Table 3.1. **Summary of SELEX products sent for sequencing.** Complete sequences from sequencing were analysed for number of sequences found more than once. Total rounds of positive and counter selection steps performed are also shown here. For sub-libraries, d denotes sub-library from direct-SELEX while s represents ones from solution-SELEX.

Sub-libraries	Plasmid sent	Successful sequencing	Total positive selection performed	Total counter selection steps performed	Number of sequences found more than once
R10d	96	84	10	6	4
R6s	96	82	6	0	9
R15s	64	56	15	4	0
R8Bs	64	63	8	2	2
R10Cs	64	59	10	0	3

and DeRosa, 2016). One can argue with the result obtained from direct-SELEX where six counter selection rounds were included but repetitive sequences were obtained. One explanation to keep in mind is these aptamer candidates might have possessed binding recognition to the immobilisation linker necessary for biotinylated IAA and used for the positive selection (McKeague and DeRosa, 2012).

Multiple sequence alignments and sequence motifs analysis were performed using Jalview 2.11.1.3 software. The conserved primer binding sites were omitted from the analysis as it was shown to have no major contribution to motif analysis (Pan and Clawson, 2009, Cowperthwaite and Ellington, 2008). The sequences were initially grouped into clusters using a neighbour joining phylogenetic tree function with percentage identity distance (PID) matrix (Appendix A). Orphan sequences that do not belong to any clusters were discarded from further analysis. Consensus sequences for each cluster were generated and further aligned using Clustal Web Service (ClustalWS) highlighting nucleotides with more than 50% identity (Figure 3.8). Patterns were observed from the alignment of each sub-library suggesting that certain bases or sequences might combine for IAA binding. While each sub-library demonstrated its own distinct pattern, there was no common sequences or motifs amongst them that could be chosen for the analysis.

The secondary structures of all sequences were also predicted using ViennaRNA software (data not shown) with hope to reveal any shared structural folding of DNA that could suggest a dominant ligand binding site (Vu et al., 2016, Neves et al., 2010). Yet again, no consensus secondary folding was observed from the analysis. It is worth noting that these predictions do consider conditions including the temperature and presence of Na^+ and Mg^{2+} ions. However, aptamers can undergo complete conformational change in response to ligand binding (Liu et al., 2016, Nutiu and Li, 2003), making these predictions troublesome. At this stage, no specific sequence patterns or secondary motifs could be identified that would be useful for further aptamer development strategy. Therefore, strategies were developed for further screens to search for IAA-sensitive aptamer candidates using the sub-libraries obtained.

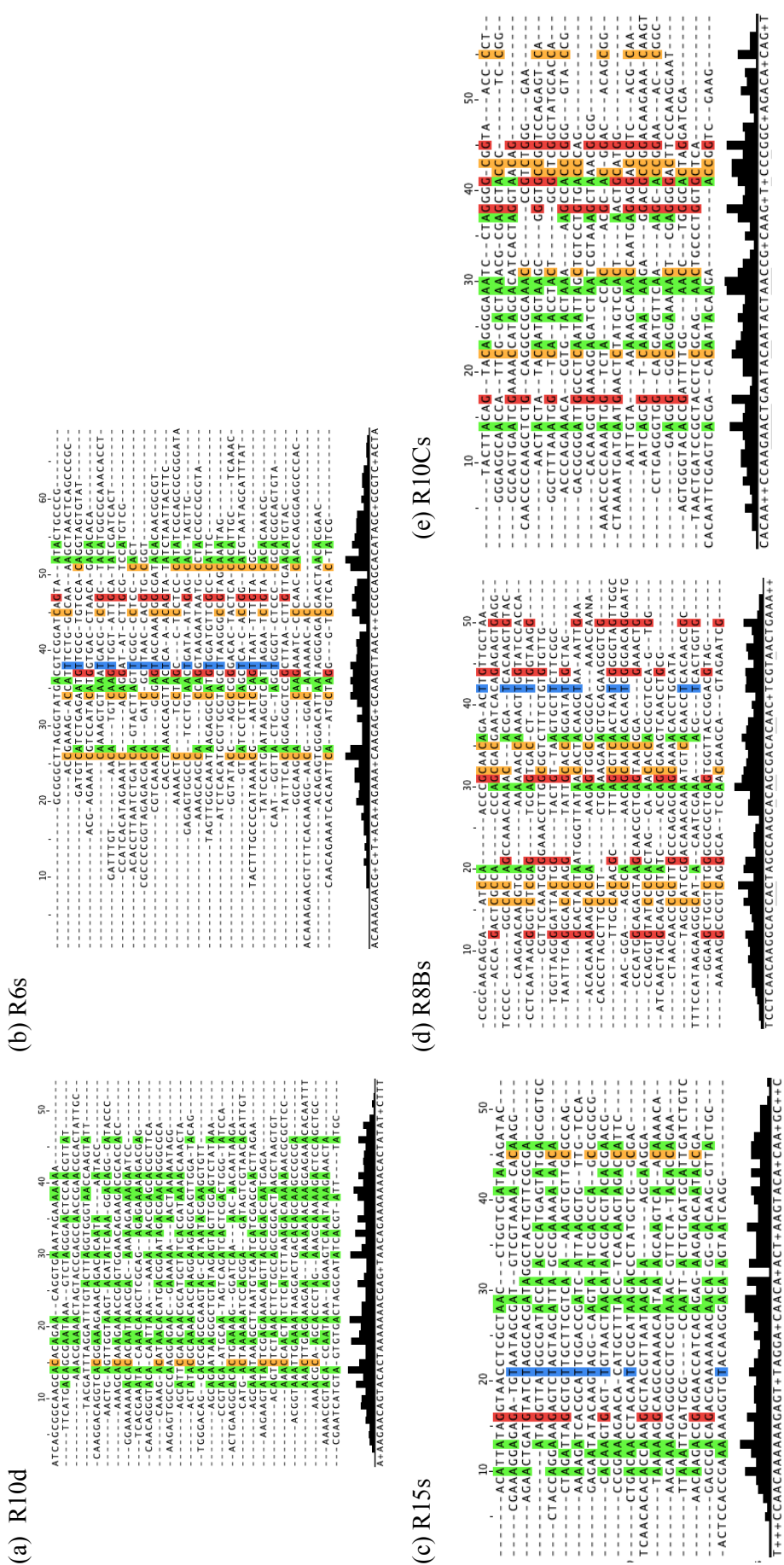


Figure 3.8. Multiple sequence alignments of consensus sequences generated from clustering of sub-libraries by phylogenetic trees. The sequences were aligned in absence of conserved regions. Bases with more than 50% identity are highlighted in green (adenine), blue (thymine), red (guanine), and orange (cytosine).

3.4 ELONA for primary screening of aptamer sub-libraries

With its simplicity and high throughput comparable to an ELISA, Enzyme-linked oligonucleotides assay (ELONA) is a suitable primary screening assay to quantify IAA interactions of aptamer candidates (Figure 3.9; (Mayer, 2016, Le et al., 2014, Kalra et al., 2018, Grozio et al., 2013).

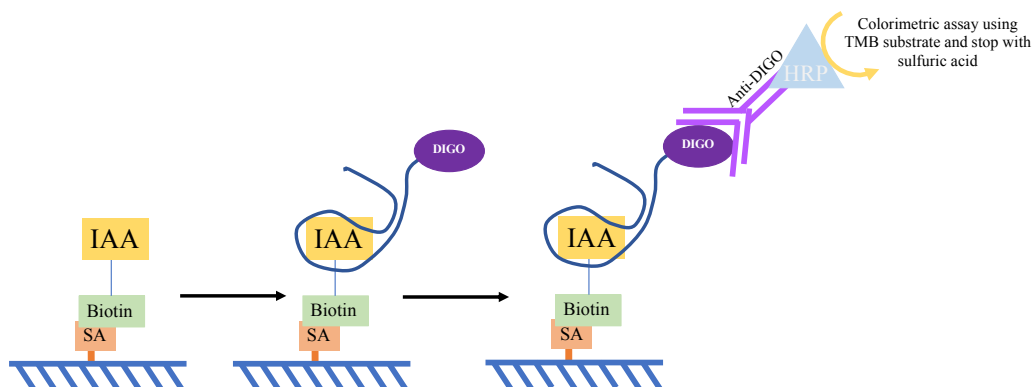
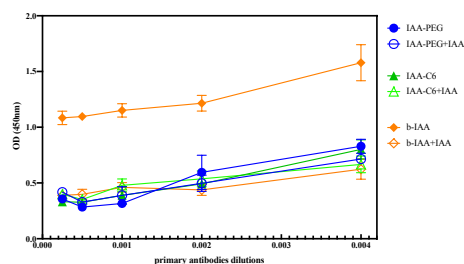


Figure 3.9. **General scheme of ELONA assay.** Biotinylated IAAs were initially immobilised onto streptavidin-coated, clear polystyrene 96-well plates. By incubating with digoxigenin tagged aptamer candidates, IAA-binding sequences interact on the surface. After extensive washes, digoxigenin-specific antibodies conjugated to peroxidase were added. After incubation and washes, TMB was added as substrate and colour change stopped with acid.

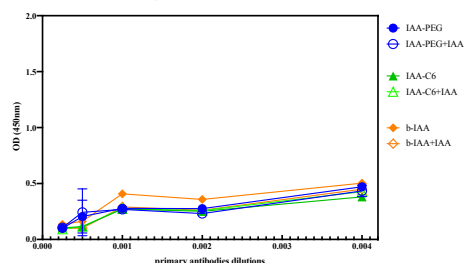
3.4.1 Assay optimisation

ELONA must be optimised and validated before it could be used to screen and evaluate auxin aptamer candidates. Several experimental parameters were validated including an appropriate and sufficient immobilisation of biotinylated IAAs. Three distinctive IAA derivatives were investigated for use in ELONA. IAA-PEG and IAA-C6, synthesized and gifted by Professor Ken-ichiro Hayashi, have biotin conjugated at C α -position through different linkers while b-IAA was synthesized (Dr Andrew Marsh, Department of Chemistry, Warwick) with a biotin tag conjugated at C5-position. These IAA conjugates and the ELONA format were investigated using three known anti-auxin antibodies, D44 (raised against indole N-conjugated IAA; (Manning, 1991), SAGE and PARSLEY (antisera raised against C5 conjugates of 1-naphthylacetic acid; Napier, unpublished).

(a) SAGE anti-IAA



(b) PARSLEY anti-IAA



(c) D44 anti-IAA

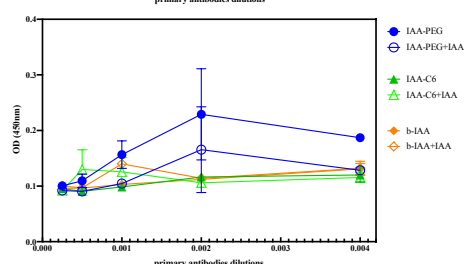


Figure 3.10. **ELONA positive immobilisation check using three different anti-IAA antibodies.** Three biotinylated IAAs, namely IAA-PEG (blue), IAA-C6 (green), and b-IAA (orange) were tested against three anti-IAAs, SAGE (a), PARSLEY (b), and D44 (c). Absorbance at 450nm was measured and recorded in OD unit. Anti-IAAs were incubated in presence (solid dots) and absence (clear dots) of 100 μ M free labelled IAA.

During the optimisation, one needed to consider the immobilisation efficiency and IAA availability once immobilised. With the binding activity and specificity of the antibodies unknown, all combinations of anti-IAAs and biotinylated IAAs were tested (Figure 3.10). A significant decrease in absorbance in the presence of 100 μ M free IAA suggested IAA-specific binding of the antibodies. Analysis of SAGE anti-IAA incubation showed a significant binding affinity and specificity to b-IAA (Figure 3.10a) confirming the complementarity of C5-conjugated auxin. On the other hand, D44 anti-IAA revealed moderate binding affinity and specificity to IAA-PEG (Figure 3.10c). This implied that IAA-PEG and b-IAA were available for binding by large molecules. No binding was observed on any anti-IAA with immobilised IAA-C6. Three possible scenarios could be that 1) none of anti-IAA antibodies have binding activity to IAA-C6, or 2) IAA-C6 was unsuccessfully immobilised onto the surface, or 3) the shorter biotin linker used for IAA-C6 might restrict the access of large molecules. From the data presented, IAA-PEG and b-IAA were chosen for ELONA.

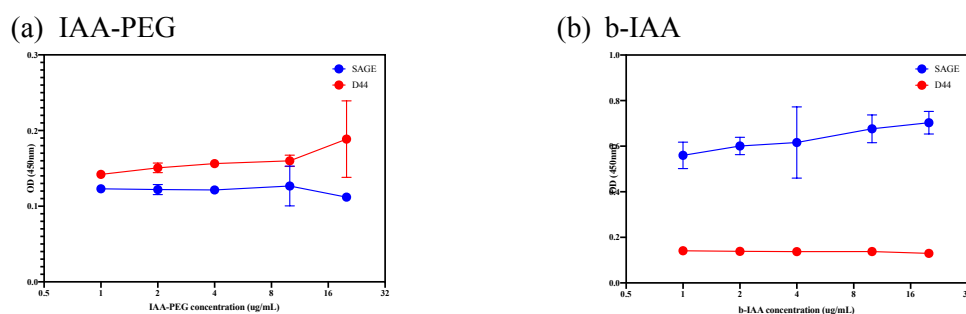


Figure 3.11. **ELONA immobilisation concentration check.** SAGE (blue) and D44 (red) were tested on dilutions of IAA-PEG (a) and b-IAA (b) immobilised on the surface. Absorbance at 450nm was measured and recorded as OD.

Another key parameter to consider is the appropriate immobilisation concentrations of biotinylated IAAs. Titrations of IAA-PEG and b-IAA were tested against a constant concentration of SAGE and D44 anti-IAAs (Figure 3.11). Absorbance readings confirmed interactions as previously discussed, D44 preferably binds IAA-PEG while SAGE to b-IAA. In both cases, no significant increases in absorbance were observed with increasing concentration of IAA conjugates suggesting that the surface had been saturated with 1 $\mu\text{g/mL}$ biotinylated IAAs. The experimental conditions for auxin aptamers screening were set.

3.4.2 ELONA assay

A total of 288 aptamer candidates were screened through ELONA, 96 from direct-SELEX (R10d) and 64 from each parallel solution-SELEX (R15s, R8Bs and R10Cs). Each aptamer was tested against both IAA-PEG and b-IAA due to the difference in biotin conjugation of the two compounds. As any modifications on small molecules can potentially hinder aptamer interaction (Ruscito and DeRosa, 2016, McKeague and DeRosa, 2012), using two different biotinylated IAAs with different conjugation positions could help recognise any aptamers specific for the core features of IAA. A set of four negative controls was tested on every ELONA plate, two of blank streptavidin coated wells and two of biotinylated IAAs immobilised exposed to no aptamer. The absorbance measured from these negative control samples served as background that could be subtracted from tested DNA samples. A competition assay was performed by testing each DNA sample in the absence and presence of 10 μM free IAA to evaluate the binding specificity of aptamer against the immobilised IAA.

IAA-sensitive aptamers would be released from binding on the ELONA surface resulting in a decrease in absorbance signal measured.

All absorbance measurements were normalised by subtracting the background absorbance. The absorbance values of samples assayed in the presence of free IAA were then subtracted from the ones measured in absence of IAA to obtain absorbance data generated purely from IAA-sensitive aptamer binding. Assays were performed in triplicate (Figure 3.12).

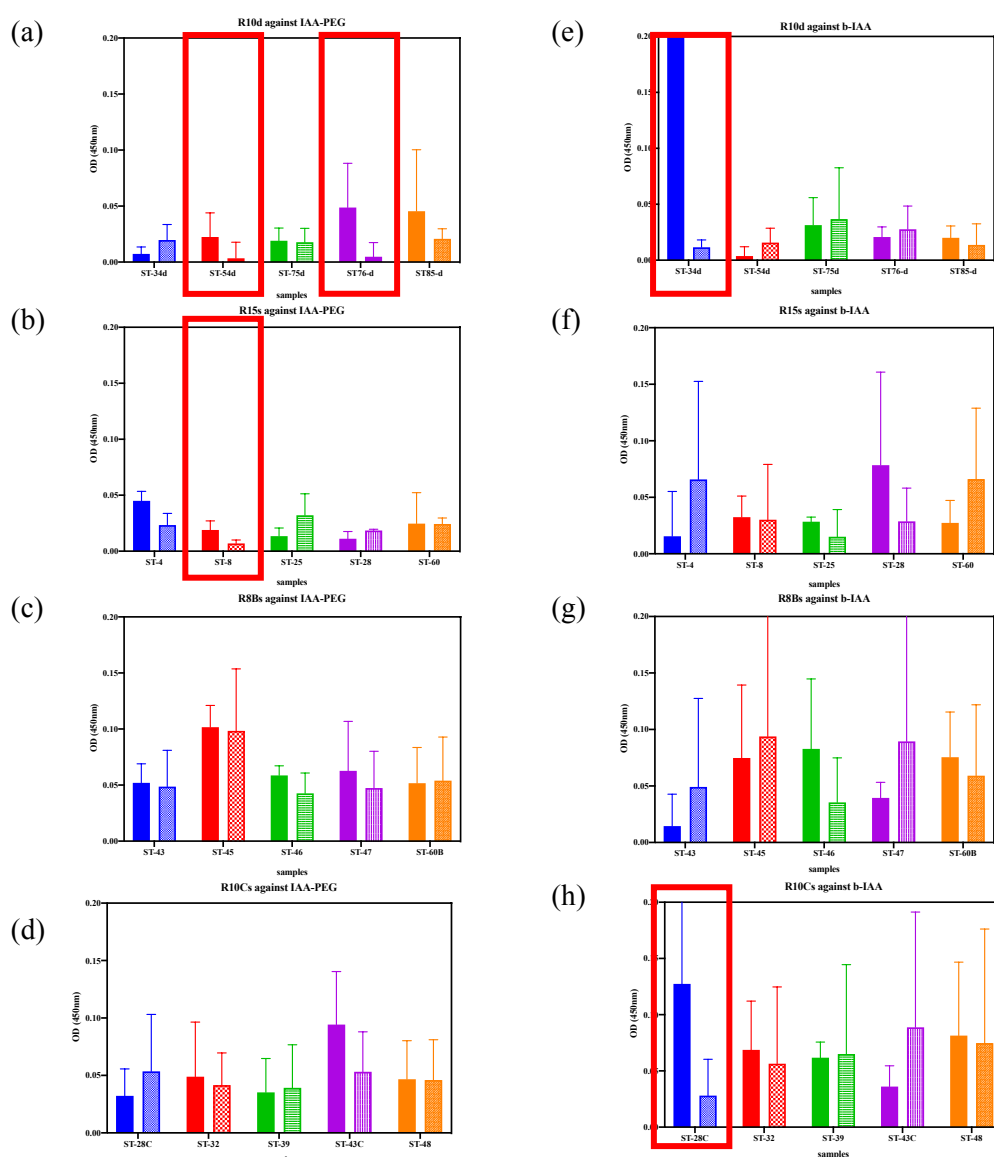


Figure 3.12. ELONA was used to select IAA sensitive aptamers. Five aptamer candidates from R10d (a, e), R15s (b, f), R8Bs (c, g), and R10Cs (d, h) were tested against IAA-PEG (a-d) and b-IAA (e-h). Each candidate was incubated in absence (filled bars) and presence (patterned bars) of free-labelled IAA. Five aptamer candidates with greatest difference in response when challenged with IAA suggesting IAA-sensitive binding were chosen (red boxes) for further secondary screening. Error bars represent standard deviations of triplicates.

From the analysed data, it is interesting to see some aptamer candidates interacted with one biotinylated IAA but not to the other. This supports the hypothesis that conjugation and linkers could contribute to binding (McKeague and DeRosa, 2012). However, the advantages of simplicity and high throughput screening with ELONA were counteracted by its low sensitivity (Kalra et al., 2018). The error bars indicate high variance between replicates and the screening should be performed with caution. Nevertheless, five aptamer candidates with IAA-sensitive binding were chosen for further secondary screening with MST (Table 3.2). Additionally, two aptamer candidates found more than once through the sequencing data were also selected to further screening using MST.

Table 3.2. Names and sequences of aptamer candidates selected for MST secondary screening. From sequencing analysis, ST-57 and ST-49 were found more than once and were chosen for secondary screening.

Names	Sequences (5'-3')	bases
ST-57	TAGGGAAGAGAAGGACATATGATCGGATCGGTGTGAGGCTCGATCTTTCAACACGGT TTAGCTTCTACTAATCGGGGTCTTTGGCTTGACTAGTACATGACCACTTGA	108
ST-49	TAGGGAAGAGAAGGACATATGATTACAGGTCTTGAGGCTCGATCGGCTTTAAATGGT CAACCTACTGCGCTCGGCTATGCACCATTGACTAGTACATGACCACTTGA	108
ST-34d	TAGGGAAGAGAAGGACATATGATACTGCCAGCAGCTCAATGATGATATCTAGGAAAA CAGCCATTGACTAGTACATGACCACTTGA	86
ST-54d	TAGGGAAGAGAAGGACATATGATATCAGTTAAGCGAAAGATATGGCAGAAGTGCTGC GTTCTATTGACTAGTACATGACCACTTGA	86
ST-76d	TAGGGAAGAGAAGGACATATGATCGAATCATGTAGTGTGACTAGGCATATCACGTAT TTATGCTTGACTAGTACATGACCACTTGA	86
ST-28	TAGGGAAGAGAAGGACATATGATCAACCGCAACTGAGGCTCGATCTACCCCCAGGCT CTGGAGGCCGCATACCCTGTGTGGTGTATTGACTAGTACATGACCACTTGA	108
ST-8	TAGGGAAGAGAAGGACATATGATGGTTACTGGATGAGGCTCGATCTGTTCTCGGGG GTACCATTGACTAGTACATGACCACTTGTGACTAGTACATGACCACTTGA	108

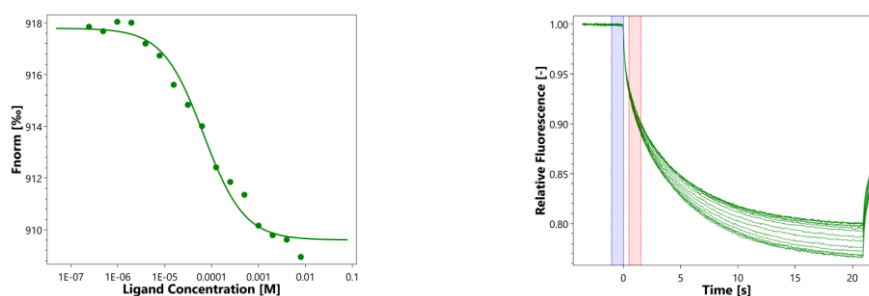
3.5 MST for secondary screening of aptamer candidates

Through SELEX and ELONA, a handful of aptamer candidates were chosen with IAA recognition properties. A secondary screening is still required to confirm the aptamer-IAA interactions and evaluate their IAA binding strengths. MST has successfully been used for the evaluation of binding affinity and specificity of small molecule aptamers such as ATP (Prante et al., 2019, Entzian and Schubert, 2016) and it was adopted for evaluating IAA binding affinity and specificity (Table 3.2).

3.5.1 Assay validation using fluorescent aptamers against ATP and ABA.

An in-house assay validation was performed using fluorescent aptamers against ATP and abscisic acid (ABA) (Figure 3.13; (Entzian and Schubert, 2016, Grozio et al., 2013). The K_D estimated for the ATP aptamer (67.2 μM) is comparable to the published value (Entzian and Schubert, 2016) and confirming that the technique is a suitable secondary screen for auxin aptamers. Other techniques do give 10-fold lower estimated K_D values for this aptamer. A similar situation was found for the ABA aptamer (Figure 3.13b) (Huizenga and Szostak, 1995, Grozio et al., 2013).

(a) ATP aptamer



(b) ABA aptamer

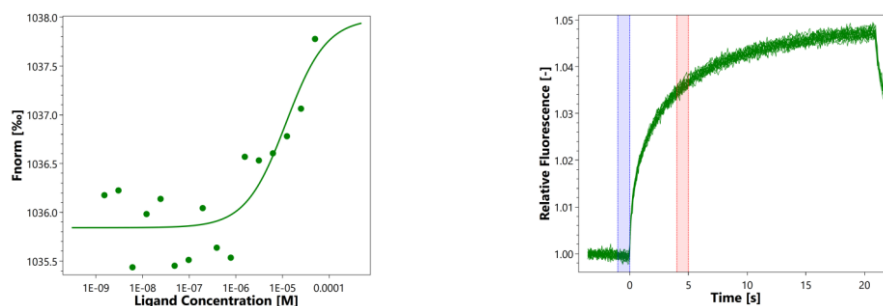


Figure 3.13. **MST technique was validated using aptamers against ATP (a) and ABA (b).** Dose response curves (left) were generated from the MST traces (right) of aptamers binding affinity experiments. K_D values were estimated at 67.2 μM and 11.9 μM for ATP and ABA aptamers, respectively.

3.5.2 Assay optimisations

A minor change in the buffer composition or a shift in pH value can greatly affect thermophoretic characteristics (Seidel et al., 2013). With the acidic nature of IAA, it must be ensured that the buffers used maintain the pH in presence of high concentration of IAA, and buffering agents can affect aptamer behaviour in MST and so a range of buffering agents was evaluated. Initially, PBS was tested against Tris buffer as recommended by the manufacturer's manual (Figure 3.14, Table 3.3). Binding affinity data generated for two aptamers was compared along with the regularity of MST traces and data repeatability. Irregularity of MST traces is often a sign of aggregation and must be avoided (NanoTemper). While no significant difference was observed when testing ATP aptamer, the buffer composition had a clear effect on ST-57. At pH 7.2, a negative thermophoresis was observed in PBS while a positive thermophoretic profile was obtained in Tris buffer (Figure 3.14b).

Additional buffering agents were investigated when PBS and Tris buffer resulted in low repeatability. ST-57 was subsequently tested in MES and Bis-Tris

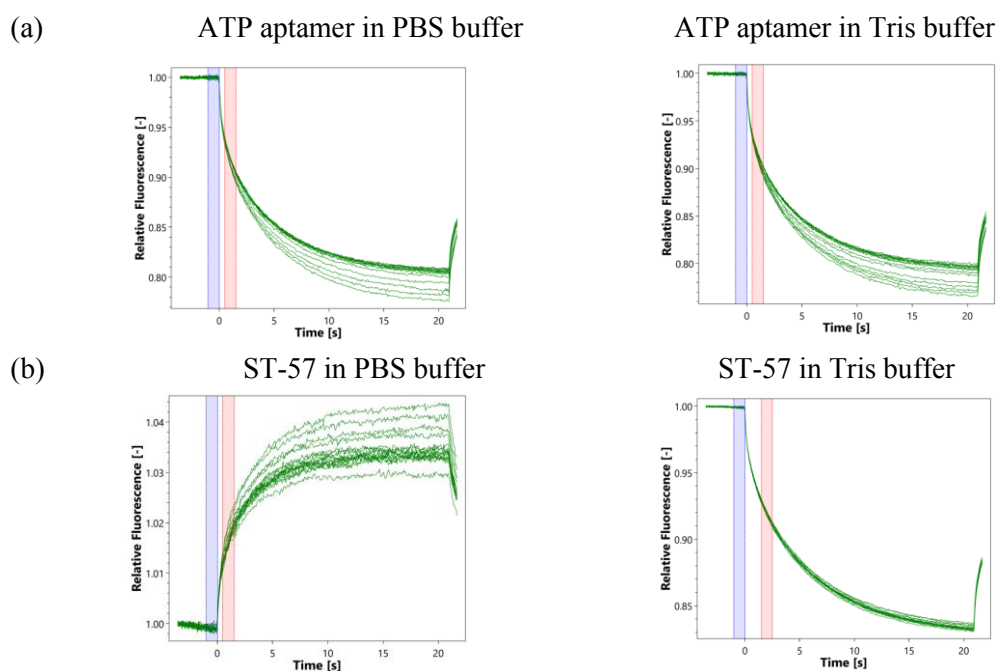


Figure 3.14. **Binding screening for MST experiments.** ATP aptamer (a) and ST-57 (b) were initially tested against PBS (left) and Tris buffer (right). Generated MST traces were compared to show no significant difference observed with ATP aptamer while ST-57 was highly dependent on buffer compositions.

buffers (Table 3.3) with repeatable MST data under both buffer conditions. The response amplitude generated using MES buffer was considerably higher than using Bis-Tris buffer. Therefore, MES buffer was chosen for all experiments onwards with this aptamer. Further, it has been observed that thermophoretic data can fluctuate between different batches of ligand and buffers used across the experiments. Therefore, only data generated on the same day was used for comparisons and analyses to avoid any inter-day variations.

Table 3.3. Buffer screening for MST experiments. Signal amplitudes (Amp) and signal-to-noise ratios (S/N) obtained from measuring aptamers in different buffers were compared. ATP aptamer and ST-57 were initially tested in PBS and Tris buffers. ST-57 was further tested in MES and Bis-Tris buffer. Data obtained from ST-57 in PBS and Tris buffers were in grey due to low repeatability.

Aptamers	PBS buffer		Tris buffer		MES buffer		Bis-Tris buffer	
	Amp	S/N	Amp	S/N	Amp	S/N	Amp	S/N
ATP	9.1	16.1	9.0	13.9	-	-	-	-
ST-57	4.9	13.3	3.3	7.6	2.3	6.3	1.0	6.5

3.5.3 Secondary screening of aptamer candidates against IAA dilution series

ST-57 and ST-49 were originally evaluated on the MST platform for their binding affinity to IAA. A constant concentration of each fluorescent aptamer candidate was incubated with an IAA dilution series from 8 nM to 250 μ M final concentration in 5% DMSO and the dose response curves were plotted (Figure 3.15). The quality of binding signals was monitored for acceptable response amplitudes and S/N ratios and K_D values were calculated (Table 3.4). While a good S/N ratio should exceed 5.0, the thresholds of acceptable response amplitudes vary depending on the MST power and MST-on time chosen in each experiment (NanoTemper, 2018), and results of dose-response experiments are plotted on the basis of the fraction of sites bound.

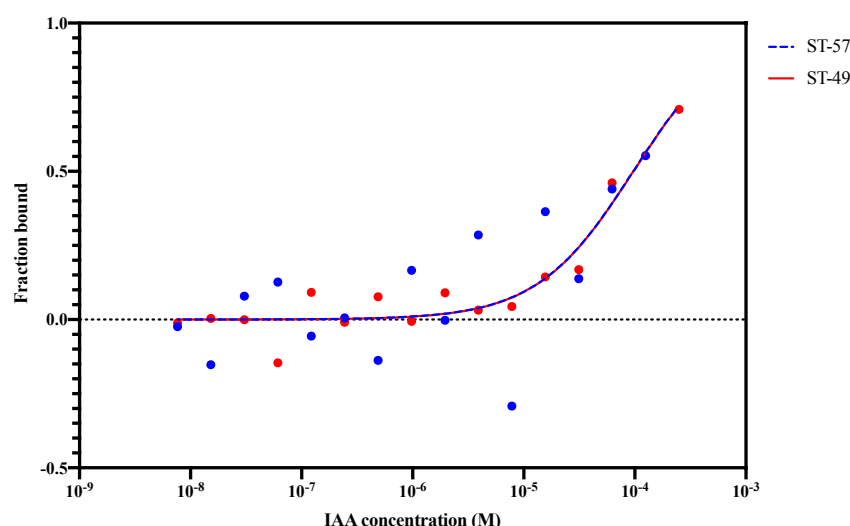


Figure 3.15. **Analysis of fitted dose response curves of ST-57 and ST-49 preliminarily showed IAA binding.** MST binding affinity experiments were performed and estimated K_D values were calculated using non-linear regression using a one-site binding model on GraphPad Prism. The estimated K_D values were 96.6 μM and 96.9 μM for ST-57 and ST-49, respectively (Table 3.4).

To calculate a K_D from dose response curves with high accuracy, there should be a good distribution of data between the bound and unbound phase (Perelson and Deeks, 2011). An increasing bound fraction observed with higher IAA concentrations did indicate dose dependent binding. However, the saturation phase was never reached over the IAA concentration range used and higher concentrations were required for more precise K_D calculation. The biggest challenge here was the solubility of IAA. Small organic molecules like IAA need to be dissolved in an organic solvent such as DMSO and its solubility in aqueous buffer limits the concentration range available for assays. Given that the K_D calculated was high, it was more useful to put more effort into the improvement of the aptamers rather than extending the assay concentration range.

Table 3.4. **MST binding affinity data of ST-57 and ST-49.**

Aptamers	Signal amplitudes	S/N ratio	Calculated K_D
ST-57	2.3	6.3	96.6 μM
ST-49	2.6	16.4	96.9 μM

3.5.4 Fluorescent auxins as alternative MST screening

As an alternative to titrating the auxin, a fluorescent auxin was tested as the MST reporter and aptamer candidates were titrated. Another major advantage of this approach is a potential improvement in binding signal quality due to a massive difference in size and surface charge between fluorescent IAA and IAA-aptamer complex. However, the modification of IAA remains the major drawback to be considered (Ruscito and DeRosa, 2016, McKeague and DeRosa, 2012). Binding interactions with aptamer candidates might be greatly affected or hindered with the fluorophores and/or linkers conjugated onto IAA even when negative controls were included to counter non-specific interactions of aptamers with the linkers.

A set of fluorescent IAAs had been previously synthesized with NBD and BODIPY dyes (Figure 3.16; (Hayashi et al., 2014). Benzoic acid was previously used as one of the control molecules in SELEX. Consequently, NBD-Benzoic acid was used as a negative control for MST specificity tests.

Optimising the fluorescence signal from each fluorescent ligand is very important for MST experiments. Different concentrations of fluorescent auxins and benzoic acid were evaluated on MST pre-test experiments to determine the appropriate

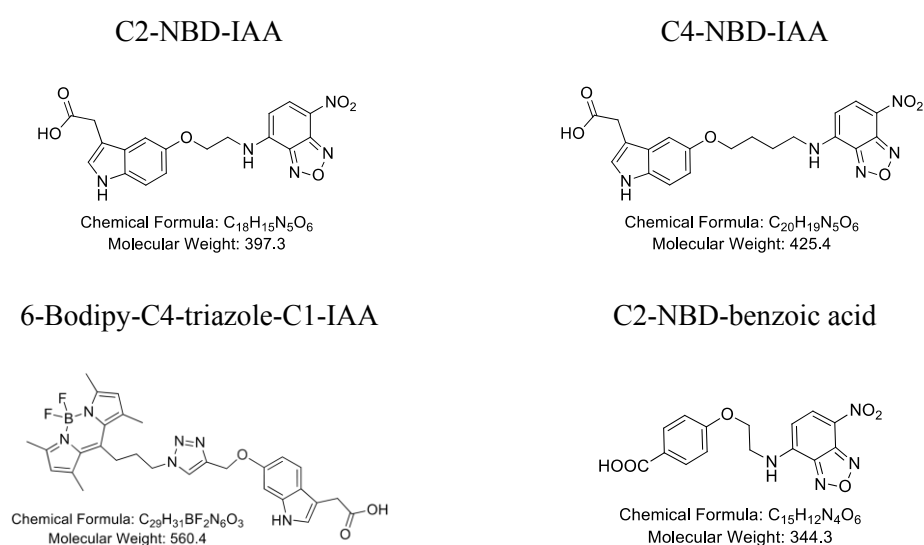


Figure 3.16. Chemical structures of fluorescent auxins and benzoic acid used in MST secondary screening.

concentrations for further analysis (Table 3.5). Fluorescence counts between 200 – 2000 units are optimal for MST experiments (Seidel et al., 2013). A very high laser power was needed for a sufficient fluorescence signal to be obtained from a high C4-NBD-IAA. This can gravely impact the stability of the fluorophore and compound during binding measurements (NanoTemper).

Table 3.5. **Optimised concentrations of fluorescent auxins and benzoic acid.** The fluorescent compounds were prepared to different concentrations in MES buffer and tested on the MST pre-test setting. Laser powers were adjusted to obtain fluorescence signals above threshold.

Compounds	Final concentrations	Fluorescence signal	Laser power
C2-NBD-IAA	1 μ M	366 \pm 2.1%	80%
C4-NBD-IAA	2 μ M	247 \pm 0.8%	100%
6-Bodipy-C4-triazole-IAA	100 nM	267 \pm 0.9%	20%
C2-NBD-benzoic acid	1 μ M	332 \pm 0.7%	20%

Once the optimal concentration and conditions for each fluorescent auxin were established, a binding check experiment was used. Any ligand-induced fluorescence change or photobleaching would be recognised during this stage. Seven aptamer candidates chosen from ELONA were screened against all fluorescent compounds (Table 3.6). Two out of seven aptamer candidates displayed a positive binding with 6-Bodipy-C4-triazole-IAA. C4-NBD-IAA was discarded due to photobleaching and fluorescence change caused by aptamer candidates. Analysis of most aptamer candidates showed positive binding to both C2-NBD-IAA and C2-NBD-benzoic acid. This proposes two possibilities; 1) aptamer candidates mainly interacted with the C2-NBD linkers or 2) aptamer candidates possessed binding affinities to both IAA and benzoic acid.

Table 3.6. **Qualitative analysis of binding interactions between aptamer candidates and fluorescent auxins and benzoic acid.** Positive bindings with signal amplitudes and S/N ratios passing thresholds were presented as YES while NO indicates no binding detected.

Compounds Aptamers	C2-NBD-IAA	C4-NBD-IAA	6-Bodipy-C4- triazole-IAA	C2-NBD- benzoic acid
ST-57	YES	Ligand induced photobleaching	NO	NO
ST-49	YES	Ligand induced photobleaching	NO	YES
ST-34d	YES	Ligand induced photobleaching	NO	NO
ST-54d	YES	YES	YES	YES
ST-76d	YES	Ligand induced photobleaching	NO	YES
ST-28	YES	NO	NO	YES
ST-8	YES	Ligand induced photobleaching	NO	YES

Subsequent binding affinity experiments were performed to analyse interactions between aptamer candidates and the two fluorescent compounds. A constant concentration of fluorescent partners (1 μM final concentration) was incubated with an aptamer dilution series (800 pM to 25 μM), and thermophoretic profiles were generated. Dose response curves (Figure 3.17) revealed some binding,

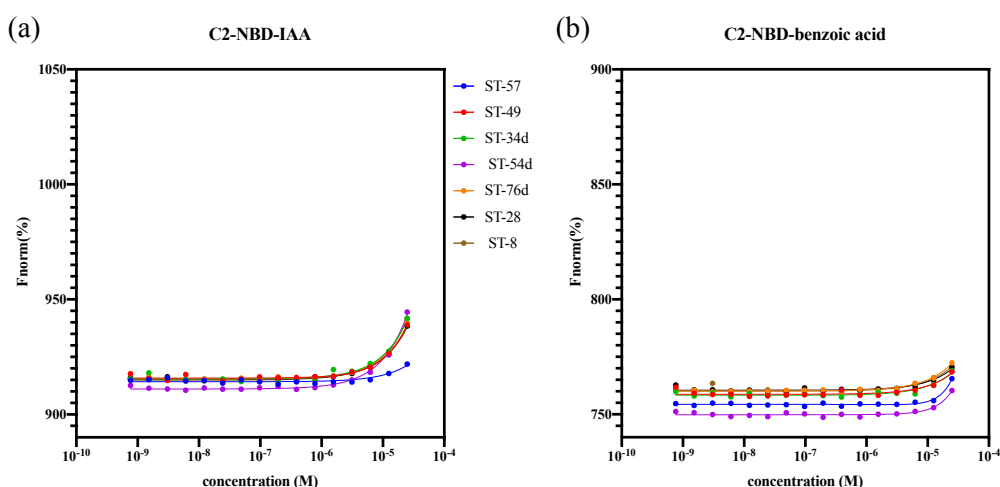


Figure 3.17. **Analysis of fitted dose response curves of aptamer candidates against C2-NBA-IAA (a) and C2-NBD-benzoic acid (b) demonstrated some IAA binidng.** The concentrations of aptamer candidates were plotted against the normalised fluorescence signal (F_{norm}).

but no binding saturation was reached making K_D estimation impractical. Minimal dose dependent signals with C2-NBD-benzoic acid suggested that observed binding activity was IAA-sensitive, but of low affinity.

3.6 Discussion

This chapter has outlined the work done to select aptamers with suitable IAA binding affinity and specificity. Two distinct SELEX methods, direct- and solution-SELEX were performed. Through the sequencing analysis and evaluation of the aptamer selection techniques, it can be suggested that the SELEX methods used were not sufficiently effective to enrich for IAA-binding aptamers. Number of SELEX rounds implemented might not be sufficient for auxin aptamers enrichment. While the sequence enrichment was typically observed from round 6 onwards, the enriched sequence could remain less than 1% of the sub-library (Blank, 2016). Meanwhile, highly specific aptamers selected against trans-zeatin were obtained after 24 rounds of SELEX (Qi et al., 2013). It was suggested that the aptamer selection against small molecules might require more SELEX rounds of positive selection steps with less selection stringency (Ruscito and DeRosa, 2016). Inclusion of highly stringent steps like counter-selection, in attempt to remove non-specific binder, could adversely affect the enrichment of auxin specific binders.

We should also consider the possible drawbacks of using conventional PCR for SELEX amplifications (Komarova and Kuznetsov, 2019). This is due to its low efficiency and the inevitable biased amplification of sequences with weaker secondary structures. A study showed lower amplifications of aptamer sequences with high sequence interactions between the randomised region and the primer binding site(s) (Wang et al, 2019). Sequences with stronger secondary structures may not be amplified properly and eventually they get lost through rounds of selection (Musheev and Krylov, 2006). Furthermore, high numbers of by-products can result from primer and product hybridisations (Tolle et al., 2014). To rectify these issues, different amplification approaches could be used, such as emulsion-PCR allowing high amplification efficiency with low by-products (Shao et al., 2011).

With no specific sequence or secondary motifs patterns useful for further aptamer development, ELONA was used as a second screen for candidates with IAA-sensitive binding. A handful of candidates were further analysed with MST to characterise and determine their binding affinities. While the results suggest that aptamer candidates were selected which did bind IAA, their affinities were low with K_D values in the high micromolar range. It was reasoned that the IAA binding affinities of these aptamers would need to improve drastically to be suitable for downstream applications as a biosensor.

Several techniques for affinity maturation have been reported, including hybridisation inhibition, sequence truncations, and mutagenesis; strategies which have been shown to greatly improve ligand binding affinity and specificity of DNA aptamers (Zheng et al., 2015, Zhang and Liu, 2018, Wang et al., 2019, Savory et al., 2013, Qi et al., 2013, Pan and Clawson, 2009, Le et al., 2014). Therefore, the two most promising candidates, ST-57 and ST-34d, were chosen for affinity maturation which is explained in the next chapter.

Chapter 4 Affinity maturation of aptamer candidates to enhance binding affinity against IAA

This chapter focuses on affinity maturation of chosen auxin aptamer candidates, ST-57 and ST-34d, to improve IAA binding affinity for downstream application. Here, sequence optimisation techniques were implemented including hybridisation inhibition (HI), sequence truncation, and single guanine (G) mutation to determine minimal and specific IAA binding sequences. An aptamer against ABA (ABAp_t) was subjected to similar affinity maturation for comparison to observe how each technique affects ligand interactions. The established MST platform was used throughout to evaluate the sequence optimisations and calculate K_D values. Subsequently, experimental conditions were also optimised to determine the optimal binding interaction between the improved aptamers and auxin.

4.1 Hybridisation inhibition (HI)

First step was to identify sequences not involved in ligand binding. Hybridisation inhibition is preferable as an initial experiment using short complementary oligonucleotides to restrict involvement of particular regions in binding (Le et al., 2014). As earlier studies have shown little influence of conserved primer binding sites (CPBS) to ligand interaction (Pan and Clawson, 2009), the CPBS were initially hybridised to determine their contributions to ligand interactions.

HI probes (Table 4.1) were designed to be complementary to the CPBS of the aptamers. A 1.25x molar of HI probe was added to each fluorescent aptamer candidate in assay buffer. The mixture was denatured at 90°C for 5 min following a temperature decrease to 56°C for 10 min for probe annealing. The mixture was brought to room temperature for at least 20 min before binding affinity evaluation.

Table 4.1. **Oligonucleotide probes used for hybridisation inhibition (HI) experiments.** HI probes were used to restrain forward (-5') and reverse (-3') primer binding sites of IAA aptamer candidates and ABA aptamer (ABAp_t).

Names	Sequences
HI-5'	5'- ATCATATGTCCTTCTCTCCCTA -3'
HI-3'	5'- TCAAGTGGTCATGTACTAGTCAA -3'
ABA-HI-5'	5'- ACACCAGTCTTCATCCGC -3'
ABA-HI-3'	5'- GTTGCTCGTATTTAGGGC -3'

4.1.1 Hybridisation inhibition of ABapt

HI of ABapt was performed to examine influence of CPBS (Figure 4.1). Good data quality and comparable dose response curves were generated from ABapt and ABapt-HI3' samples suggesting restraining the reverse CPBS did not significantly affect ABA binding and could be removed from the aptamer sequence. On the other hand, error bars of ABapt-HI5' indicated high variance between replicates. This suggested the significance of the hybridised region to aptamer stability, and therefore, should not be eliminated. This validated HI as an appropriate method for aptamer sequence optimisation, and therefore, HI was implemented on auxin aptamer candidates.

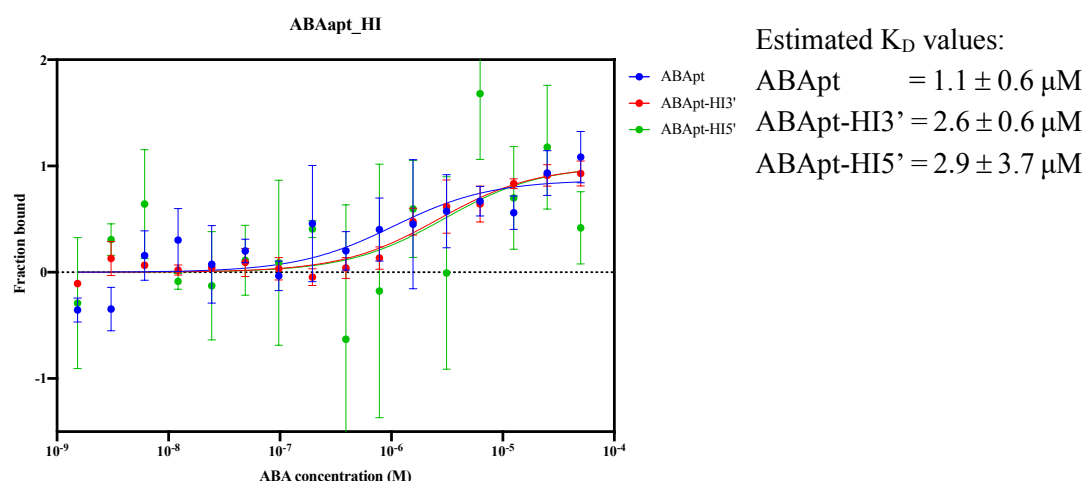


Figure 4.1. **Analysis of the fitted dose response curves of ABapt HI experiment indicating potential use of HI for sequence optimisation.** MST binding affinity experiments were performed and estimated K_D values were calculated using non-linear regression using a one-site binding model on GraphPad Prism ($n = 3$).

4.1.2 Hybridisation inhibition of ST-57

An HI experiment was performed on ST-57 and dose response curves were generated (Figure 4.2). Upon inhibition with HI-5' probe, IAA binding affinity was slightly improved implying that the forward CPBS was not necessary. In contrast, a slight decrease in binding affinity (estimated K_D values increased from $45.8 \pm 28 \mu\text{M}$ to $61.1 \pm 27 \mu\text{M}$) was observed when inhibiting with HI-3' probes, suggesting an influence on ligand binding and/or aptamer structural stability. Further investigation on sequence optimisation would confirm the importance of reverse CPBS in IAA binding.

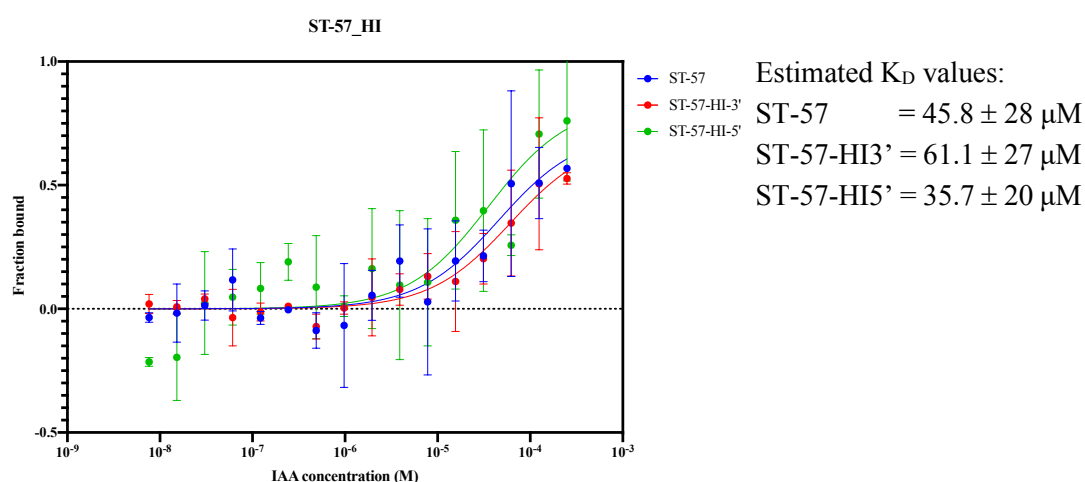


Figure 4.2. Analysis of the fitted dose response curves of ST-57 HI experiments indicated improvements in IAA binding. Estimated K_D values were calculated using non-linear regression using a one-site binding model on GraphPad Prism ($n = 3$).

4.1.3 Hybridisation inhibition of ST-34d

Fluorescent IAA (section 3.5.4) was used for an HI experiment on ST-34d. Unmodified ST-34d was incubated with 1.25x excess of HI-3' probe and the mixture was prepared and examined using MST as previously described (Figure 4.3). No significant difference was observed upon HI-3' inhibition suggesting no involvement of the region in IAA binding. With no binding saturation and K_D value likely to be in millimolar range, ST-34d was dropped from further sequence optimisation.

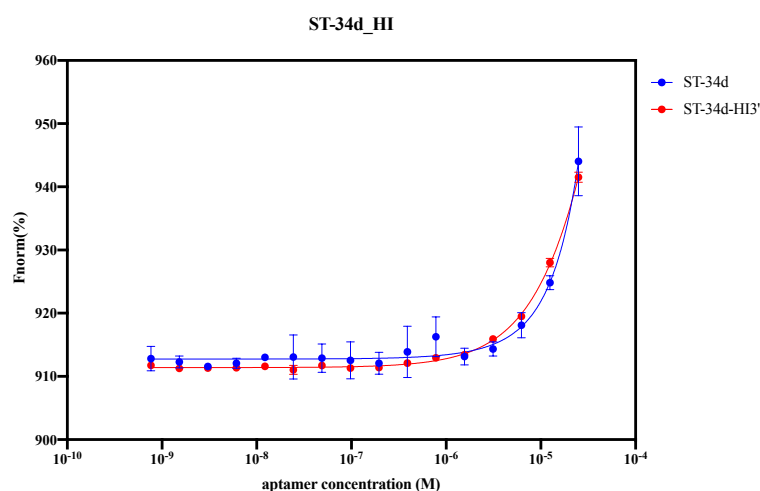


Figure 4.3. **No optimisation was observed from the analysis of ST-34d HI experiments.** Dose response curves were fitted by plotting the concentrations of ST-34d and its HI-3' variant against the normalised fluorescence signal (F_{norm}).

To conclude, the forward CPBS of ABapt was deemed important for ABA binding while the reverse CPBS was not. For ST-57, IAA binding affinity was slightly improved only when restricting the 5'-end conserved region. On the other hand, analysis of ST-34d did not show significant improvement in auxin binding and was discarded from further optimisations. Sequence truncations were further investigated to determine minimal ligand binding sequences.

4.2 Sequence truncations

Sequence truncations were performed to identify the minimal ligand binding sequences. Similar studies have used structural motif simulations as truncation guidance (Vu et al., 2016, Zheng et al., 2015), but an empirical approach was used here. The truncated variants were designed with one primer binding site removed followed by further 10 nucleotides removals (Table 4.2). Additionally, it has been hypothesized that small molecule ligands often intercalate within G-quadruplex structures (Roxo et al., 2019, Qi et al., 2013). Therefore, the QGRS Mapper webserver was implemented to identify any G-rich regions within the aptamer sequences that might form G-quadruplex.

Table 4.2. **All truncated variants of ABapt and ST-57 used in aptamer sequence optimisation.** The conserved primer binding sites and hybridisation site are underlined. Guanine bases predicted by QGRS Mapper to be involved in G-quadruplex formation are in red and green.

Aptamers	Sequences (5' – 3')	bases
ABapt	<u>GCGGATGAAGACTGGTGTGA</u> <u>GGGATGGTTA</u> <u>GGTGGAGGTGGTTAT</u> <u>CCGGGAATTCGCCCTAAATACGAGCAAC</u>	76
STA-1	<u>GCGGATGAAGACTGGTGTGA</u> <u>GGGATGGTTA</u> <u>GGTGGAGGTGGTTAT</u> <u>CCGGGAATTC</u>	58
STA-2	<u>GCGGATGAAGACTGGTGTGA</u> <u>GGGATGGTTA</u> <u>GGTGGAGGTGGTTAT</u>	48
STA-3	<u>GCGGATGAAGACTGGTGTGA</u> <u>GGGATGGTTAGGTGGA</u>	38
ST-57	<u>TAGGGAAGAGAA</u> <u>GGACATA</u> <u>TGATC</u> <u>GGATCGGTGTGA</u> <u>GGCTCGATCTTCAACAC</u> <u>GGTTTAGCTTCTACTAATC</u> <u>GGGGTCTTTGGCTTGACTAGTACATGACCACCTTGA</u>	108
ST-57-1	<u>GGACATA</u> <u>TGATC</u> <u>GGATCGGTGTGA</u> <u>GGCTCGATCTTCAACAC</u> <u>GGTTTAGCTTCTACTAATCGGGGTCTTTGGCTTGACTAGTACATGACCACCTTGA</u>	96
ST-57-2	<u>CGGATC</u> <u>GGTGTGA</u> <u>GGCTCGATCTTCAACAC</u> <u>GGTTTAGCTTCTACTAATCGGGGTCTTTGGCTTGACTAGTACATGACCACCTTGA</u>	85
ST-57-3	<u>TGA</u> <u>GGCTCGATCTTCAACAC</u> <u>GGTTTAGCTTCTACTAATC</u> <u>GGGICTTTGGCTTGACTAGTACATGACCACCTTGA</u>	75
ST-57-4	<u>TC</u> <u>TTTCAACAC</u> <u>GGTTTAGCTTCTACTAATCGGGGTCTTTGGCTTGACTAGTACATGACCACCTTGA</u>	65
ST-57-5	<u>ACAC</u> <u>GGTTTAGCTTCTACTAATCGGGGTCTTTGGCTTGACTAGTACATGACCACCTTGA</u>	58
ST-57-2'	<u>TAGGGAAGAGAA</u> <u>GGACATA</u> <u>TGATC</u> <u>GGATCGGTGTGA</u> <u>GGCTCGATCTTCAACAC</u> <u>GGTTTAGCTTCTACTAATCGGGGTCTTTGGC</u>	85
ST-57-3'	<u>TAGGGAAGAGAA</u> <u>GGACATA</u> <u>TGATC</u> <u>GGATCGGTGTGA</u> <u>GGCTCGATCTTCAACAC</u> <u>GGTTTAGCTTCTACTAATCGG</u>	75
ST-57-4'	<u>TAGGGAAGAGAA</u> <u>GGACATA</u> <u>TGATC</u> <u>GGATCGGTGTGA</u> <u>GGCTCGATCTTCAACAC</u> <u>GGTTTAGCTTCTACTAATCGG</u>	65
ST-57-5'	<u>TAGGGAAGAGAA</u> <u>GGACATA</u> <u>TGATC</u> <u>GGATCGGTGTGA</u> <u>GGCTCGATCTTCAACAC</u> <u>GGTTTAGCTTCTACTAATCGG</u>	50
ST-57-2,4'	<u>CGGATC</u> <u>GGTGTGA</u> <u>GGCTCGATCTTCAACAC</u> <u>GGTTTAGCTTCTACTAATCGG</u>	42

4.2.1 Sequence truncation of ABapt

ABapt were truncated following the HI experiment (Table 4.2) and the aptamer was only truncated from the 3'-end. The reverse CPBS was initially removed (STA-1) followed by further 10 base truncation increments to give STA-2 and STA-3. All truncated variants were synthesized with fluorescein conjugation and were examined for ABA binding (Figure 4.4). Comparable ABA binding affinities were observed between ABapt and STA-1, complementing the HI data which showed that reverse CPBS was not involved in ABA interaction. The predicted G-quadruplex of STA-1 from QGRS analysis is consistent to ABapt (table 4.2), in line with the hypothesis that ABA interaction was within the predicted tertiary quadruplex structure (Grozio et al., 2013). In contrast, a 10-fold reduction in ABA binding affinity was observed with STA-2 while STA-3 completely disrupted ABA binding (Figure 4.4), highlighting the significance of the removed sequences to the aptamer structural integrity for ligand binding.

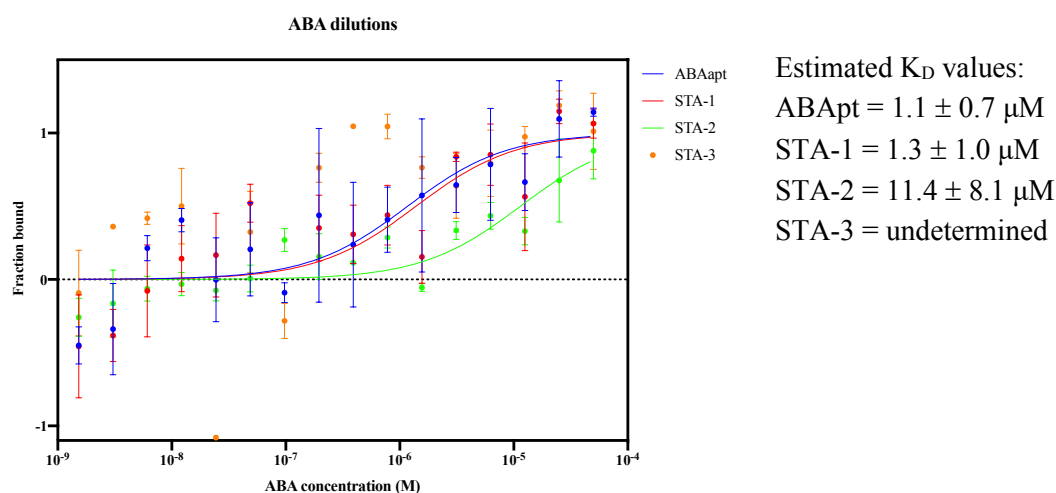


Figure 4.4. **Sequence truncation of ABapt enhanced ABA binding.** Estimated K_D values were calculated using non-linear regression using a one-site binding model on GraphPad Prism (n = 3).

A serial dilution of IAA was also tested against the fluorescent ABapt (Figure 4.5). An IAA binding affinity ($293 \pm 137 \mu\text{M}$ estimated K_D) was observed with ABapt, 300-fold lower than of ABA ($1.1 \mu\text{M}$) making ABapt considerably ABA specific. Having found that the ABapt bound IAA, against expectations, its truncated

variants were also tested (Figure 4.5). IAA binding affinity was improved by five times in STA-1 and approximately 60 times in STA-3. A low S/N ratio and high variance suggesting low data quality was obtained from STA-2 deeming it unreliable and was discarded from further analysis.

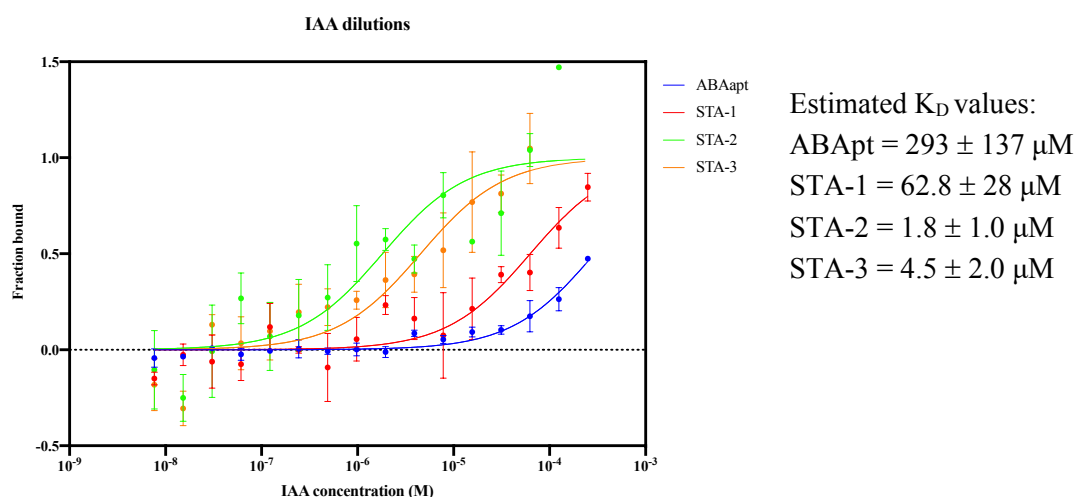


Figure 4.5. **Sequence truncation of ABapt revealed IAA binding affinity.** ABapt and truncated sequences were examined and the estimated K_D values were calculated using non-linear regression using a one-site binding model on GraphPad Prism ($n = 3$).

Truncating the ABapt sequence could have exposed an IAA binding area(s) and the alteration in predicted G-quadruplex structure of STA-3 could have promoted IAA intercalation within the aptamer. Further structural and biophysical analysis of STA-3 could confirm this hypothesis.

In summary, sequence truncation was proved useful as a sequence optimisation technique. ABapt sequence truncation to STA-1 improved ABA binding affinity to an estimated K_D of $1.3 \pm 1.0 \mu\text{M}$. Whilst removing ABA binding activity, STA-3 bound IAA ($4.5 \pm 2.0 \mu\text{M}$ estimated K_D) making it the most promising auxin aptamer candidate thus far.

4.2.2 *Sequence truncation of ST-57*

A total of ten truncated variants of ST-57 were synthesized and examined for improved IAA binding affinity (Table 4.2); five from 5'-end, four from 3'-end and one from both ends seeking minimal IAA binding sequences.

MST binding experiments were performed on ST-57 and its truncated variants and dose response curves were generated (Figure 4.6). At first glance, only ST-57-5 (purple curve) demonstrated improved IAA binding in comparison to its full sequence (black curve). Analysis of some variants showed no significant difference in IAA binding while others lost ligand recognition. A non-linear regression using a one-site specific binding model was used to estimate K_D values of each truncated aptamer with R-squared determining the goodness of fit (Table 4.3; (McKeague et al., 2015)). ST-57-2, -3, and -4 were discarded from further analysis.

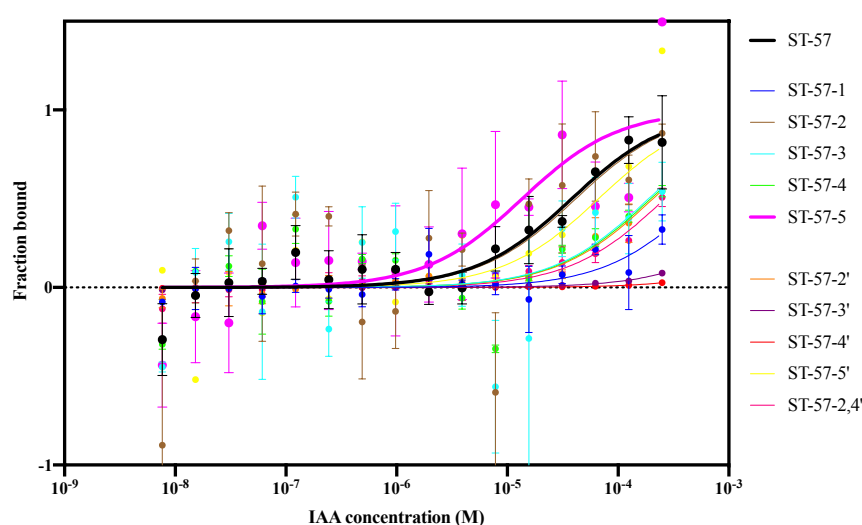


Figure 4.6. **Detailed sequence truncation of ST-57 slightly improved IAA binding affinity.** The dose response curves of ST-57 (black) and ST-57-5 (purple) are in bold to highlight improved IAA binding through sequence truncation. The estimated K_D values of all truncated variants were calculated using non-linear regression using a one-site binding model on GraphPad Prism (Table 4.3).

IAA binding of the aptamer was hypothesized to be within one of the predicted G-quadruplexes (Table 4.2; in green). All 3'-end truncated variants disrupted the quadruplex and demonstrated at least 10-fold reductions in IAA binding. On the other hand, truncation of ST-57 to ST-57-5 allowed the quadruplex to remain intact and resulted in improved IAA binding affinity (decreased estimated K_D values from $38.1 \pm 16 \mu\text{M}$ to $13.6 \pm 11 \mu\text{M}$). Again, structural and biophysical analysis would help elaborate this theory.

Table 4.3. **Estimated K_D values of ST-57 and its truncated variants from MST binding experiments.** The estimated K_D values were calculated using non-linear regression using a one-site binding model on GraphPad Prism with R-squared indicating goodness of fit ($n = 3$). Truncated variants with R-squared below threshold (in grey) were deemed unreliable and discarded from further analysis. (N/A = not applicable R-squared from undetermined K_D value).

Aptamers	Calculated K_D (μM)	R-squared
ST-57	38.1 ± 16	0.8853
ST-57-1	567 ± 1472	0.5856
ST-57-2	41.5 ± 63	0.3889
ST-57-3	188 ± 585	0.2418
ST-57-4	197 ± 373	0.4701
ST-57-5	13.6 ± 11	0.6471
ST-57-2'	206 ± 175	0.9024
ST-57-3'	2869 ± 7211	0.9561
ST-57-4'	Undetermined	N/A
ST-57-5'	498 ± 717	0.7876
ST-57-2,4'	264 ± 162	0.9124

The sequence truncation of ST-57 combined with QGRS mapper analysis suggested IAA binding site(s) of the aptamer to be within one of the predicted G-quadruplexes of the aptamer (Table 4.2, marked green). The hypothesis was supported by the MST binding affinity experiment. Truncated variants without the expected predicted G-quadruplex (i.e. G-tetrads marked green in Table 4.2) demonstrated reduced IAA binding affinities (Table 4.3).

To conclude, a 50-base truncation of ST-57 to ST-57-5 demonstrated improvement in IAA binding affinity with estimated K_D value of $13.6 \pm 11 \mu\text{M}$.

4.3 Single G-mutations to improve IAA binding affinity

To further investigate aptamer sequence optimisation, G-mutation was chosen as the subsequent technique. As ST-57 and STA-3 demonstrated good IAA binding affinity, single G-mutation was performed on both aptamers. Single guanine substitutions were designed given the known importance of G-quadruplex structures

for ligand intercalations (Zheng et al., 2015). For each single-site variant, a non-guanine (G) base adjacent to an existing guanine (G) was substituted with G base to promote a G-tetrad and G-quadruplex formation.

4.3.1 *Single G-mutations on ST-57-5*

A total of 14 mutated variants were generated from ST-57-5 (Table 4.4). Predicted quadruplexes were identified using QGRS Mapper. Some mutations indeed influenced the predicted quadruplex and the QGRS Mapper analysis offered a scoring system to evaluate the tendency of forming stable G-quadruplexes; a higher G-score indicates higher structural stability (Kikin et al., 2006). All mutated variants were predicted with elevated G-scores suggesting more stable G-quadruplexes.

Table 4.4. **ST-57-5 and its mutated variants for sequence optimisation experiments.** All substituted guanines are marked in red. From QGRS analysis, G-tetrads predicted to form G-quadruplex structures are underlined and in bold.

Names	Sequences (5'-3')	Predicted G-scores
ST-57-5	ACAC <u>GG</u> TTTAGCTTCTACTAATC <u>GGGG</u> TCTTT <u>GG</u> CTTGACTAGTACATGACCACTTGA	12
ST-57-5-4	ACA <u>GG</u> TTTAGCTTCTACTAATC <u>GGGG</u> TCTTT <u>GG</u> CTTGACTAGTACATGACCACTTGA	19
ST-57-5-7	ACAC <u>GG</u> TTTAGCTTCTACTAATC <u>GGGG</u> TCTTT <u>GG</u> CTTGACTAGTACATGACCACTTGA	20
ST-57-5-10	ACAC <u>GG</u> TTT <u>GG</u> CTTCTACTAATC <u>GGGG</u> TCTTT <u>GG</u> CTTGACTAGTACATGACCACTTGA	27
ST-57-5-12	ACAC <u>GG</u> TTTAG <u>GG</u> TCTACTAATC <u>GGGG</u> TCTTT <u>GG</u> CTTGACTAGTACATGACCACTTGA	29
ST-57-5-23	ACAC <u>GG</u> TTTAGCTTCTACTAAT <u>GGGG</u> TCTTT <u>GG</u> CTTGACTAGTACATGACCACTTGA	21
ST-57-5-28	ACAC <u>GG</u> TTTAGCTTCTACTAATC <u>GGGG</u> <u>G</u> TCTTT <u>GG</u> CTTGACTAGTACATGACCACTTGA	20
ST-57-5-32	ACAC <u>GG</u> TTTAGCTTCTACTAATC <u>GGGG</u> TCTTT <u>GG</u> CTTGACTAGTACATGACCACTTGA	19
ST-57-5-35	ACAC <u>GG</u> TTTAGCTTCTACTAATC <u>GGGG</u> TCTTT <u>GG</u> <u>G</u> TTGACTAGTACATGACCACTTGA	19
ST-57-5-37	ACACGGTTTAGCTTCTACTAATC <u>GGGG</u> TCTTT <u>GG</u> CT <u>GG</u> ACTAGTACATGACCACTTGA	31
ST-57-5-39	ACACGGTTTAGCTTCTACTAATC <u>GGGG</u> TCTTT <u>GG</u> CTT <u>GG</u> CTAGTACATGACCACTTGA	31
ST-57-5-42	ACACGGTTTAGCTTCTACTAATC <u>GGGG</u> TCTTT <u>GG</u> CTTGACT <u>GG</u> TACATGACCACTTGA	29
ST-57-5-44	ACACGGTTTAGCTTCTACTAATC <u>GGGG</u> TCTTT <u>GG</u> CTTGACTAG <u>G</u> ACATGACCACTTGA	28
ST-57-5-48	ACAC <u>GG</u> TTTAGCTTCTACTAATC <u>GGGG</u> TCTTT <u>GG</u> CTTGACTAGAC <u>GG</u> ACCACTTGA	26
ST-57-5-50	ACACGGTTTAGCTTCTACTAATC <u>GGGG</u> TCTTT <u>GG</u> CTTGACTAGTACAT <u>GG</u> CCACTTGA	22

A binding check experiment was performed to qualitatively screen for IAA binders (Table 4.5). Good response amplitudes (>1.0) and S/N ratios (>5.0) indicated positive IAA binders. With this threshold, seven ST-57-5 mutated variants were selected and evaluated further with MST binding affinity experiments.

Table 4.5. MST qualitative binding to determine positive IAA binding of ST-57-5 and its mutated variants. YES was used to denote positive IAA binding variants. The non-binding variants are presented in grey.

Aptamers	Signal amplitudes	S/N ratios	Positive binding
ST-57-5	1.6	5.2	YES
ST-57-5-4	1.2	1.7	-
ST-57-5-7	1.1	3.3	-
ST-57-5-10	1.1	6.9	YES
ST-57-5-12	1.6	7.4	YES
ST-57-5-23	1.1	9.4	YES
ST-57-5-28	1.2	4.4	-
ST-57-5-32	0.6	1.3	-
ST-57-5-35	0.7	1.3	-
ST-57-5-37	1.1	5.5	YES
ST-57-5-39	1.1	6.4	YES
ST-57-5-42	1.2	5.7	YES
ST-57-5-44	0.5	0.6	-
ST-57-5-48	0.9	5.0	-
ST-57-5-50	1.4	7.3	YES

Positive binders were evaluated on the MST platform for enhanced IAA binding affinity (Figure 4.7). At a glance, G-mutations improved IAA recognition with exceptions of ST-57-5-42 and ST-57-5-50 (Table 4.6). The two mutants were discarded from further analysis.

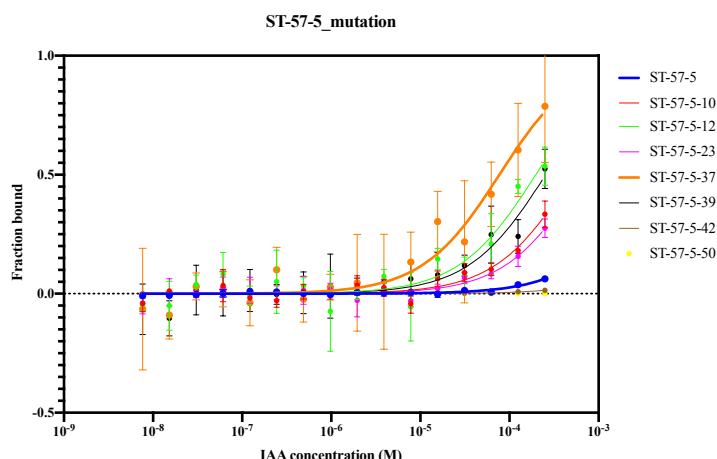


Figure 4.7. **G-mutation experiments on ST-57-5 improved IAA binding affinity by 50-fold.** Dose response curves of ST-57-5 (blue) and ST-57-5-37 (orange) are in bold to highlight improvement in IAA binding through single G mutation. The estimated K_D values of all mutated variants were calculated using non-linear regression using a one-site binding model on GraphPad Prism (Table 4.6).

Other mutants illustrated improved binding affinities; notably ST-57-5-12 and ST-57-5-37, two mutants with over 20-fold decrease in estimated K_D values. Correlating the sequence and structural analyses (Table 4.4), both variants were predicted doubled G-scores suggesting a greater structural stability that could further facilitate ligand intercalations. Moreover, the quadruplexes of the two mutants were predicted to form with ‘bigger’ guanine tetrads and shorter, equal loops implying more stable tertiary structures (Kikin et al., 2006). This MST analysis confirmed using G-mutation was an appropriate approach for sequence optimisation. The effect of G-mutation to the IAA binding affinity was evaluated through the G-quadruplex prediction in conjunction

Table 4.6. **Estimated K_D of ST-57-5 and its mutated variants from MST binding experiments.** K_D was calculated using nonlinear regression one-site specific binding model on GraphPad Prism 8 with R-squared indicating goodness of fit ($n = 3$).

Aptamers	Calculated K_D (μ M)	R-Square
ST-57-5	3717 ± 1883	0.8966
ST-57-5-10	510.1 ± 430	0.9203
ST-57-5-12	197.4 ± 116	0.8967
ST-57-5-23	661.4 ± 612	0.9321
ST-57-5-37	77.1 ± 25	0.9438
ST-57-5-39	255.3 ± 156	0.9096
ST-57-5-42	Undetermined	N/A
ST-57-5-50	Undetermined	N/A

with the MST binding affinity experiments. The increased G-scores of the mutated variants combined with improved binding affinities of mutated variants suggested IAA binding likely to involve G-quadruplex intercalation.

To conclude, ST-57-5-37 exhibited the optimal IAA binding sequence optimised from ST-57, the aptamer candidate selected through solution-SELEX, with an estimated K_D value of $77.1 \pm 25 \mu\text{M}$.

4.3.2 Single G-mutations on STA-3

A total of 16 mutated variants were generated from STA-3 (Table 4.7). QGRS analysis of the mutants revealed a significant change in the predicted tertiary structures but not G-scores.

Table 4.7. **Mutated variants of STA-3 synthesized for sequence optimisation experiments.** All substituted guanines were marked in red. From QGRS Mapper, G-tetrads predicted to form G-quadruplex structures are underlined and in bold.

Names	Sequences (5'-3')	Predicted G-scores
STA-3	GCGGATGAAGACT <u>GG</u> TGTGAG <u>GGG</u> GAT <u>GG</u> GTTA <u>GG</u> TGGA	28
STA-3-2	G <u>G</u> GGATGAAGACT <u>GG</u> TGTGAG <u>GGG</u> GAT <u>GG</u> GTTA <u>GG</u> TGGA	28
STA-3-5	GCG <u>G</u> GATGAAGACT <u>GG</u> TGTGAGG <u>GG</u> ATGGGTTA <u>GG</u> TGGA	28
STA-3-6	GCGGA <u>G</u> GAAGACT <u>GG</u> TGTGAG <u>GGG</u> GAT <u>GG</u> GTTA <u>GG</u> TGGA	28
STA-3-8	GCGGAT <u>GG</u> AGACT <u>GG</u> TGTGAG <u>GGG</u> GAT <u>GG</u> GTTAGGTGGA	29
STA-3-9	GCGGATGA <u>G</u> AGACT <u>GG</u> TGTGAG <u>GGG</u> GAT <u>GG</u> GTTAGGT <u>GG</u> A	28
STA-3-11	GCGGATGAAG <u>G</u> CT <u>GG</u> TGTGAG <u>GGG</u> GAT <u>GG</u> GTTA <u>GG</u> TGGA	28
STA-3-13	G <u>GG</u> ATGAAGAC <u>G</u> <u>GG</u> TGTGAGG <u>GG</u> ATGGGTTA <u>GG</u> TGGA	29
STA-3-16	GCGGATGAAGACTG <u>GG</u> <u>G</u> GTGAG <u>GGG</u> GAT <u>GG</u> GTTA <u>GG</u> TGGA	29
STA-3-18	GCGGATGAAGACTGGTG <u>GG</u> AGG <u>GG</u> AT <u>GG</u> GTTA <u>GG</u> TGGA	29
STA-3-20	GCGGATGAAGACT <u>GG</u> TGTG <u>G</u> <u>GGG</u> GAT <u>GG</u> GTTA <u>GG</u> TGGA	28
STA-3-25	GCGGATGAAGACT <u>GG</u> TGTGAG <u>GGG</u> G <u>T</u> <u>GG</u> GTTA <u>GG</u> TGGA	28
STA-3-26	GCGGATGAAGACT <u>GG</u> TGTGAG <u>GGG</u> GA <u>GGG</u> GTTAGGT <u>GG</u> A	28
STA-3-30	GCGGATGAAGACT <u>GG</u> TGTGAG <u>GGG</u> GAT <u>GG</u> <u>G</u> TAGGT <u>GG</u> A	28
STA-3-32	GCGGATGAAGACT <u>GG</u> TGTGAG <u>GGG</u> GAT <u>GG</u> GTT <u>G</u> <u>GG</u> TGGA	28
STA-3-35	GCGGATGAAGACT <u>GG</u> TGTGAG <u>GGG</u> GAT <u>GG</u> GTTAGG <u>G</u> <u>G</u> A	29
STA-3-38	GCGGATGAAGACT <u>GG</u> TGTGAG <u>GGG</u> GAT <u>GG</u> GTTAGGT <u>GG</u> <u>G</u>	28

The mutants were screened through an MST binding check experiment for IAA positive binders (Table 4.8). A total of seven mutated variants with good signal amplitudes and S/N ratios were chosen for further evaluation. Interestingly, binding checks on mutations towards the 3'-end of the sequence (STA-3-18 to STA-3-35) generated low signal amplitudes and/or S/N ratios.

Table 4.8. **MST qualitative binding to determine positive IAA binding of STA-3 and its mutated variants.** Positive IAA binding variants are denoted YES. The non-binding variants are presented in grey.

Aptamers	Signal amplitudes	S/N ratios	Positive binding
STA-3	1.0	7.5	YES
STA-3-2	2.2	7.3	YES
STA-3-5	1.3	2.8	-
STA-3-6	1.5	6.1	YES
STA-3-8	2.4	3.3	-
STA-3-9	1.4	11.6	YES
STA-3-11	1.7	6.9	YES
STA-3-13	1.7	10.8	YES
STA-3-16	1.7	6.1	YES
STA-3-18	1.0	2.3	-
STA-3-20	0.7	1.9	-
STA-3-25	(ligand induced photobleaching)		
STA-3-26	0.6	2.0	-
STA-3-30	0.3	0.8	-
STA-3-32	1.0	5.6	-
STA-3-35	1.7	2.5	-
STA-3-38	2.3	7.2	YES

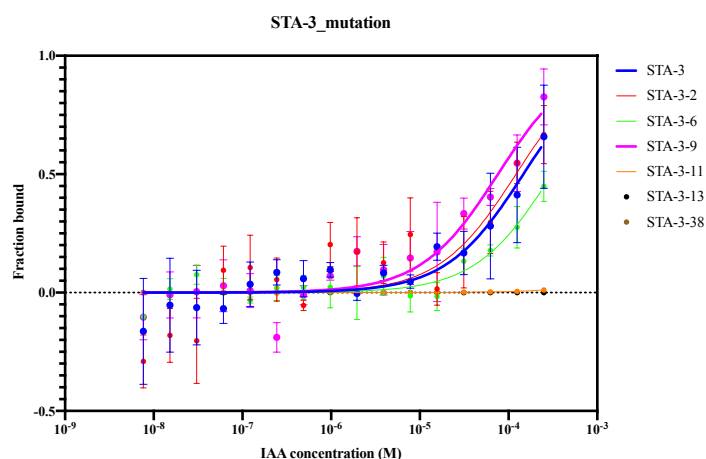


Figure 4.8. **Single G-mutation variants of STA-3 improved IAA binding.** Dose response curves of STA-3 (blue) and STA-3-9 variant (purple) are in bold to highlight improvement in IAA binding through single G mutation.

MST binding affinity experiments were performed on the positive binders and dose response curves were generated (Figure 4.8, Table 4.9). STA-3-2 could marginally enhance IAA binding and STA-3-9 demonstrated an improvement in IAA binding with the estimated K_D value lowered by half. In contrast, no IAA interaction was found on STA-3-11, STA-3-13 and STA-3-38.

Table 4.9. **Estimated K_D of STA-3 and its mutated variants from MST binding experiments.** The estimated K_D values of all mutated variants were calculated using non-linear regression using a one-site binding model on GraphPad Prism (Table 4.10) with R-squared indicating goodness of fit.

Aptamers	Calculated K_D (μ M)	R-Square
STA-3	146.7 ± 84	0.8806
STA-3-2	121.2 ± 122	0.6793
STA-3-6	310.5 ± 228	0.8939
STA-3-9	75.9 ± 32	0.9076
STA-3-11	Undetermined	N/A
STA-3-13	Undetermined	N/A
STA-3-38	Undetermined	N/A

With all the data considered, the single G-mutation technique was effective at improving IAA binding affinity, and STA-3-9 exhibited an estimated K_D value of $75.9 \pm 32 \mu$ M.

4.4 Optimisation of experimental conditions

At this point, only modest IAA binding affinities could be reached after several sequence optimisation methods under current experimental conditions. Ligand binding interactions can vary greatly in different buffer and pH conditions (Baaske et al., 2010). Therefore, further optimisation on the buffer conditions was performed on MST to establish the optimal aptamer-IAA binding conditions. Different buffering agents, including MES and HEPES, were investigated. To evaluate the aptamer-IAA binding under apoplastic pH of 5.5 – 6.0, additional MES buffer at pH 5.8 was investigated. A buffer screening was performed on the optimised STA-3-9 to compare signal amplitudes and S/N ratios (Table 4.10).

Table 4.10. **Buffer screening of 5'-FAM-STA-3-9.** Signal amplitudes (Amp) and signal-to-noise ratios (S/N) obtained from different buffers were compared. MES buffer was prepared to pH 5.8 while other buffers were prepared to pH 7.2.

Aptamer	PBS buffer		Tris buffer		MES buffer (pH 5.8)		MES buffer (pH 7.2)		HEPES buffer	
	Amp	S/N	Amp	S/N	Amp	S/N	Amp	S/N	Amp	S/N
STA-3-9	1.7	5.3	5.4	18.4	5.3	1.6	2.3	6.3	7.4	11.1

A good signal strength (i.e. high S/N ratio) was obtained from Tris and HEPES buffers better than PBS and MES buffer at both pH levels. As Tris buffer previously demonstrated low repeatability (Section 3.5.2), HEPES buffer was chosen for further investigation. During close examination, we recognised the failed S/N ratio from MES buffer at pH 5.8 (Table 4.10) was potentially due to the pH dependence of the fluorescein dye used. Fluorescein dye is highly pH dependent and exhibits a significant decrease in fluorescence intensity when diluted in acidic buffers (Slyusareva and Gerasimova, 2014). To overcome this, Cy-5 dye was chosen for its stability in different pH and salt conditions as an alternative fluorophore (Chen et al., 2008). STA-3 and STA-3-9 were synthesized with Cy-5 conjugation on the 5'-end before re-screening in different buffer compositions (Table 4.11).

Table 4.11. **Additional buffer screening of 5'-Cy5 aptamers.** Signal amplitudes (Amp) and signal-to-noise ratios (S/N) obtained in different buffers were compared. MES/sap buffer (20 mM MES, 10 mM KCl, 0.4 mM CaCl₂, 0.2 mM MgCl₂, 0.05% Tween-20) was additionally tested as a reflection of apoplastic fluid salt compositions. All buffers were prepared in-house and 0.2 µm filtered prior to use.

Aptamer	Tris buffer		HEPES buffer		MES buffer (pH 5.8)		MES/sap buffer (pH 5.8)	
	Amp	S/N	Amp	S/N	Amp	S/N	Amp	S/N
STA-3	0.5	2.4	0.4	1.3	4.8	10.6	1.1	2.0
STA-3-9	1.2	3.1	5.1	16.6	1.4	4.2	undetermined	

With high fluorescent stability, only 5 nM final concentration of Cy-5 aptamers were sufficient to obtain good fluorescence signals. Analysis of STA-3-9 demonstrated a strong binding strength in HEPES buffer but not in MES buffer at lower pH. Interestingly, significant IAA binding was observed upon evaluation of STA-3 under MES buffer at pH 5.8.

MST binding affinity experiments were performed to evaluate IAA binding interactions of these two aptamers. Good signal amplitudes and acceptable S/N ratios were obtained from the experiments (Figure 4.9). STA-3-9 exhibited optimal IAA binding in HEPES buffer at pH 7.2 with an estimated K_D value at 21.9 ± 10.6 nM, more than a thousand-fold improvement from previous conditions. In contrast, the binding analysis of STA-3 demonstrated a very good binding with IAA ($K_D = 172.2 \pm 64.3$ nM) in MES buffer at pH 5.8. These high IAA binding affinities could support potential applications *in planta*, as an aptamer-based biosensor is expected to experience an apoplastic matrix with a pH range between 5.5 – 6.0 (Sattelmacher, 2001). Further investigation on buffer and salt compositions would further benefit aptamer characterisation.

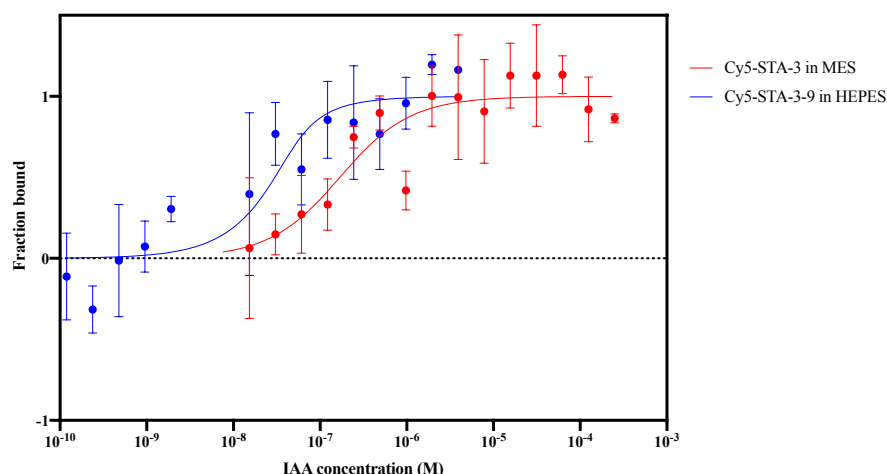


Figure 4.9. **Analysis of fitted dose response curves of Cy-5 aptamers in different buffers showed optimal IAA binding.** Cy5-STA-3 (red) were tested in MES buffer at pH 5.8 while Cy5-STA-3-9 (blue) was tested in HEPES buffer at pH 7.2. The estimated K_D values were calculated using non-linear regression using a one-site binding model on GraphPad Prism to be 172.2 ± 64.3 nM and 21.9 ± 10.6 nM for STA-3 and STA-3-9, respectively.

4.5 Discussion

To conclude, this chapter has demonstrated that aptamers are amenable to engineering to enhance ligand binding affinity. Several sequence optimisation approaches were employed to establish the optimal ligand binding sequences. ABAPt was initially used to validate the optimisation techniques. Hybridisation inhibition and sequence truncation were used to establish the minimal sequences required for optimal ligand binding affinity. Single G-mutation was subsequently performed to obtain the optimal IAA binding aptamer sequences.

The non-binding regions within the aptamer sequences were identified using HI and further eliminated through sequence truncations. It was observed that, while the conserved primer binding sites (CPBS) contributed to the overall secondary structures of the aptamer (Yang et al., 2018), they usually did not involve in ligand-specific interactions (Pan and Clawson, 2009, Komarova and Kuznetsov, 2019, Cowperthwaite and Ellington, 2008). While HI and sequence truncation of ABAPt sequence did not drastically improve ABA binding affinity, the shorten aptamer sequences could be useful for downstream biosensor application (Pan and Clawson, 2009).

Subsequently, single G-mutations were performed on ST-57-5 and STA-3 to achieve specific IAA binding sequences. Moderate IAA binding affinities were observed with estimated K_D values of $77.1 \pm 25 \mu\text{M}$ and $75.9 \pm 32 \mu\text{M}$ for ST-57-5-37 and STA-3-9, respectively. Notably, STA-3 originally optimised for ABA binding, but upon binding analysis with IAA, it showed excellent binding to IAA. The similarity in the chemical structures of ABA and IAA could explain this. The ligand binding site(s) of STA-3 could involve interactions with the carboxyl group and the aromatic ring, existing in both compounds. A comparable situation is cocaine-binding aptamers with more than 30-fold higher binding affinity against quinine (Slavkovic et al., 2015). An extensive study with isothermal titration calorimetry (ITC) and nuclear magnetic resonance (NMR) revealed that the aptamer interacted with both compounds at the same binding site (Reinstein et al., 2013). It was suggested that the overlap in the ligand bindings of these aptamers was due to the similarities in their chemical structures (Slavkovic et al., 2015, Reinstein et al., 2013).

Experimental conditions were further optimised on STA-3 and STA-3-9 for additional affinity maturation. Ultimately, STA-3 was optimised for IAA binding in MES buffer at pH 5.8 with estimated K_D at $172.2 \pm 64.3 \text{ nM}$ while STA-3-9 was optimised under HEPES buffer at pH 7.2 with estimated K_D at $21.9 \pm 10.6 \text{ nM}$.

To fully understand the biophysics of aptamer-IAA interaction, further characterisations of aptamers STA-3 and STA-3-9 are explored in the next chapter. This would paint a clearer picture of the aptamer-IAA binding mechanism. This would be highly beneficial for further assay development for IAA quantification and *in planta* biosensor development.

Chapter 5 Binding and biophysical characterisation of auxin aptamers

This chapter focuses on further characterisation of the two optimised auxin aptamers, STA-3 and STA-3-9, to assess them for development of suitable quantification assays. As part of the developed biosensor, it is important that the aptamers used provide a specific and robust auxin measurement. Therefore, the aptamers were first characterised for their auxin specificity against other small plant analytes. The aptamer binding affinities were also characterised in different salt compositions to evaluate the effect sodium (Na^+) and potassium (K^+) salts have on aptamer binding quality. Subsequently, several techniques, including a fluorescence Thioflavin T (ThT) assay and surface plasmon resonance (SPR), were performed to characterise and develop suitable quantification assays using these aptamers. Finally, aptamer characterisation using isothermal titration calorimetry (ITC) and circular dichroism (CD) allowed first glimpse into aptamer tertiary structure and auxin binding mechanism.

5.1 Auxin aptamer binding specificities

A set of small molecule compounds were chosen to evaluate IAA binding specificity of STA-3 and STA-3-9 (Figure 5.1). L-tryptophan (Figure 5.1b) was chosen as auxin chemical precursor. To examine the possible binding site(s) within auxin chemical structures, indole derivatives with distinctive carboxyl side chains (Figure 5.1c-e) were tested against acetic acid with various aromatic rings (Figure 5.1f-g). Three widely used auxin analogue herbicides (Figure 5.1h-j) were also chosen for specificity evaluation. Previously, the binding conditions of these two aptamers were evaluated (Section 4.5) for optimal auxin binding recognition and, therefore, STA-3 were tested on MES buffer at pH 5.8 while STA-3-9 were tested on HEPES buffer at pH 7.2.

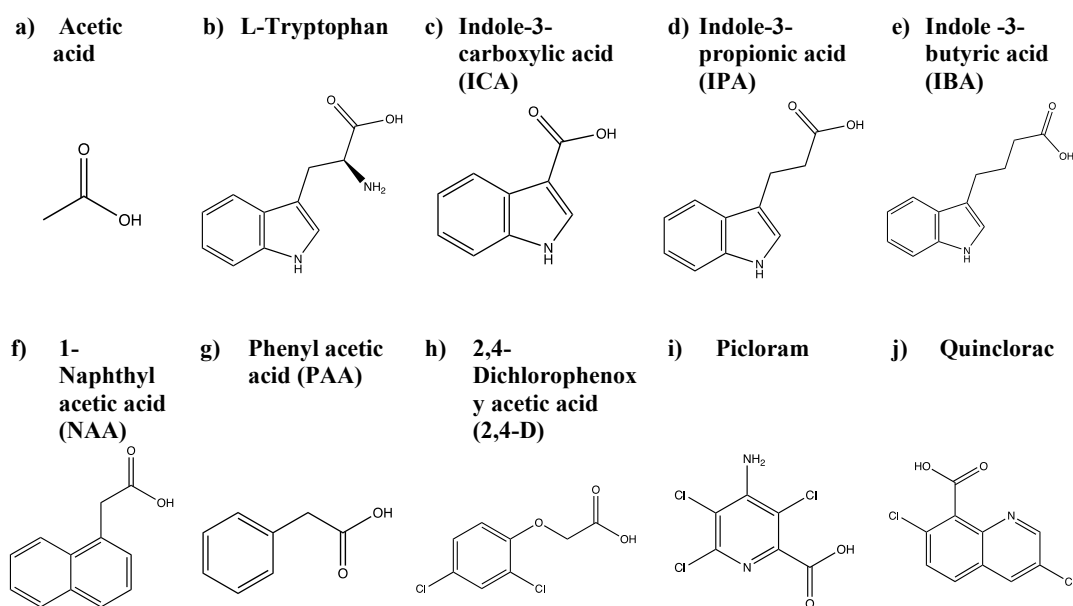


Figure 5.1. Chemical structures of compounds used for auxin aptamers specificity evaluations.

5.1.1 Binding specificity of STA-3

Serial dilutions of IAA and small molecules were tested against fluorescent STA-3 in MES buffer at pH 5.8 and dose response curves were generated (Figure 5.2, left panel). At first glance, STA-3 demonstrated degrees of binding affinities with the

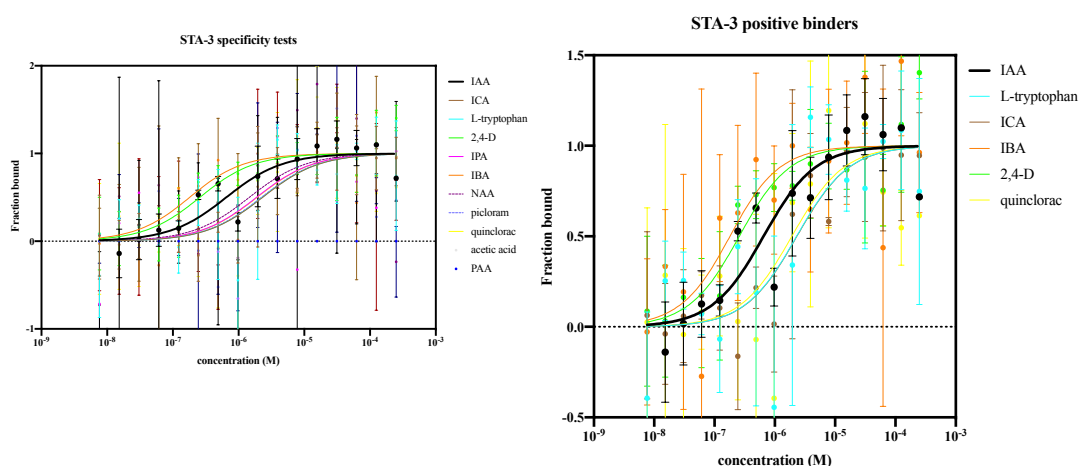


Figure 5.2. Analysis of fitted dose response curves revealed moderate auxin binding specificity of STA-3. Dose response curves of all small molecules tested were compared (left) with only IAA, ICA, and 2,4-D showing significant binding affinities (right). Dose response curves of compounds with R-squared values below threshold (<0.5) are in dashed lines. The estimated K_D values were calculated using non-linear regression using a one-site binding model on GraphPad Prism (Table 5.1). The error bars represent standard deviation of the measurements ($n = 3$).

compounds tested while no binding was observed with acetic acid, IPA and PAA. A non-linear regression using a one-site specific binding model was used to estimate K_D values with R-squared determining the goodness of fit (Table 5.1). The low R-squared values (in grey) suggested poor K_D fit correlating to the large error bars in dose response curves suggesting low binding data quality (Figure 5.2, left panel). Using the R-squared threshold, NAA and picloram binding data were deemed unreliable and discarded from further analysis.

Table 5.1. Estimated K_D values of STA-3 from auxin binding specificity evaluations. The estimated K_D values were calculated using non-linear regression using a one-site binding model on GraphPad Prism with R-squared indicating goodness of fit ($n = 3$). Compounds with R-squared below threshold (in grey) were discarded from further analysis. (N/A = not applicable R-squared from undetermined K_D value).

Compounds	Calculated K_D (nM)	R-squared
IAA	645 ± 290	0.8279
Acetic acid	Undetermined	N/A
L-Tryptophan	2303 ± 1878	0.6394
ICA	2333 ± 869	0.8949
IPA	Undetermined	N/A
IBA	185 ± 127	0.6310
NAA	1460 ± 2145	0.3447
PAA	Undetermined	N/A
2,4-D	262 ± 96	0.8660
Picloram	2236 ± 3627	0.3524
quinclorac	1923 ± 1803	0.5696

Dose response curves of positive binders with good R-squared values were extracted for further analysis (Figure 5.2, right panel). In comparison to IAA, approximately 3-fold decrease in binding affinities were observed upon binding with L-Tryptophan, ICA, and quinclorac. On the other hand, significantly enhanced binding affinities were observed with IBA and 2,4-D (Table 5.1). This binding data suggested that the ligand intercalation and complex structural stability depended on the specific length of the carboxyl side chains. Similar comparison was demonstrated with cocaine aptamers with enhanced binding affinity with quinine analogues (Slavkovic et al., 2015). It has been observed that 2,4-D can mimic auxin both structurally and functionally in plants and is believed to behave like IAA in the

molecular level (Song, 2014). Further structural analyses would help elaborate this theory.

To conclude, STA-3 demonstrated moderate binding specificity with binding interactions with IBA and 2,4-D but low affinities towards L-Tryptophan, ICA, and quinclorac.

5.1.2 Binding specificity of STA-3-9

Fluorescent STA-3-9 was tested against serial dilutions of IAA and small molecules in HEPES buffer at pH 7.2 for binding specificity evaluation and dose response curves were generated (Figure 5.3, left panel). At first glance, STA-3-9 demonstrated superior auxin binding specificity to STA-3 with no binding observed with acetic acid, ICA, IPA, PAA, and quinclorac.

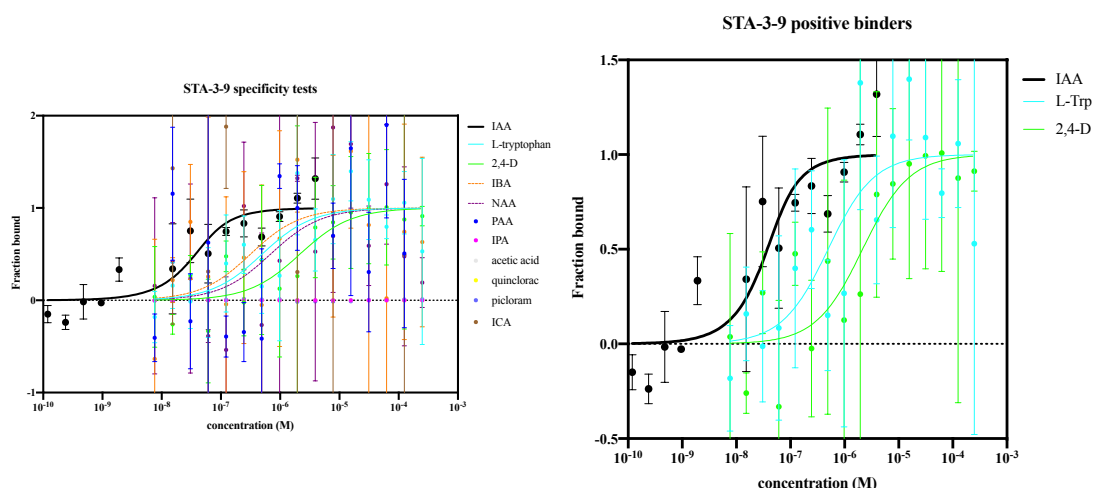


Figure 5.3. **Enhanced binding specificity was observed with STA-3-9.** Dose response curves of all small molecules tested were compared (left) with only IAA, L-Trp and 2,4-D showing significant binding affinities (right). Dose response curves of compounds with R-squared values below threshold (<0.5) are in dashed lines. The estimated K_D values were calculated using non-linear regression using a one-site binding model on GraphPad Prism (Table 5.2). The error bars represent standard deviation of the measurements ($n = 3$).

A non-linear regression using a one-site specific binding model was used to estimate K_D values with R-squared determining the goodness of fit (Table 5.2). Large error bars indicating high variance between triplicates supported by low R-squared values indicating unreliable binding data resulted in exclusion of IBA, NAA, and picloram from further analysis (Table 5.2, in grey). STA-3-9 demonstrated

interactions to L-Tryptophan and 2,4-D (Figure 5.3, right panel). However, the estimated K_D values significantly decreased by 20- and 70-fold in L-Trp and 2,4-D, respectively, (Table 5.2). Notably, higher data variance resulting in lower R-squared demonstrated lower goodness of fit in STA-3-9 binding with L-Trp and 2,4-D in comparison to IAA.

Table 5.2. **Estimated K_D values of STA-3-9 from auxin binding specificity evaluation.** The estimated K_D values were calculated using non-linear regression using a one-site binding model on GraphPad Prism with R-squared indicating goodness of fit ($n = 3$). Compounds with R-squared below threshold (in grey) were discarded from further analysis. (N/A = not applicable).

Compounds	Calculated K_D (nM)	R-squared
IAA	29.0 ± 15.4	0.8525
Acetic acid	Undetermined	N/A
L-Tryptophan	489.3 ± 358.6	0.6499
ICA	Undetermined	N/A
IPA	Undetermined	N/A
IBA	307.8 ± 461.4	0.2904
NAA	692.0 ± 996.9	0.3342
PAA	Undetermined	N/A
2,4-D	2155 ± 1187	0.7948
Picloram	40.6 mM	0.1094
quinclorac	Undetermined	N/A

All in all, STA-3-9 demonstrated high auxin binding affinity and specificity. In addition, this could also suggest that the sequence optimisation of STA-3 to STA-3-9 by single G-mutation can enhance both binding affinity (over 20-fold reduction in estimated K_D value) and specificity (increase in IAA-specific binding of STA-3-9).

5.2 Salt composition effects on aptamer-IAA binding quality

Until now, the developed auxin aptamers have demonstrated excellent auxin binding affinities and specificities in assay buffers containing high monovalent cation concentrations (150 mM Na^+ and 2 mM K^+). Several studies have demonstrated the significant impact Na^+ and K^+ have on aptamer structural stability and ligand interactions (Zhou et al., 2011, Qi et al., 2013, Baaske et al., 2010). However, it is desirable to employ these aptamers for auxin binding in acidic apoplasmic fluid which has low ionic strength (Sattelmacher, 2001). Therefore, these aptamers were evaluated

for their IAA binding affinities in different salt compositions ranging from 0 to 150 mM NaCl and 0 to 10 mM KCl using MST.

5.2.1 STA-3 auxin binding quality in different salt compositions

An IAA binding check experiment was performed on STA-3 to qualitatively screen for positive binding conditions (Table 5.3). High signal amplitudes and some aggregations were observed with high salt combinations, but no clear correlations or pattern were determined at this point. The aggregation observed at higher concentration of sodium could be suggested to be due to the interaction of Na⁺ ions with the G-quadruplex structure of STA-3 forming weak complexes that could interfere with its structural stability (Hianik et al., 2007). Good response amplitudes (>1.0) and S/N ratios (>5.0) indicated positive IAA binders. With this threshold, three buffering conditions were selected and evaluated further with MST binding affinity experiments.

Table 5.3. **MES buffer salt concentration screenings with STA-3.** Signal amplitudes (Amp) and signal-to-noise ratios (S/N) obtained in MES buffers prepared with different final concentration of NaCl and KCl at pH 5.8. Positive binders with good Amp and S/N are in bold.

KCl \ NaCl	0 mM	50 mM	100 mM	150 mM
0 mM	Amp = 2.0 S/N = 0.9	Aggregation	Amp = 3.9 S/N = 1.0	Aggregation
1 mM	Amp = 1.3 S/N = 5.3	Amp = 1.9 S/N = 3.2	Amp = 1.7 S/N = 1.2	Amp = 1.4 S/N = 3.1
2 mM	Amp = 5.9 S/N = 3.3	Amp = 1.8 S/N = 5.7	Amp = 4.3 S/N = 1.1	Amp = 4.8 S/N = 10.6
5 mM	Amp = 3.9 S/N = 2.6	Amp = 1.1 S/N = 3.6	Amp = 1.9 S/N = 2.2	Aggregation
10 mM	Amp = 14.7 S/N = 1.4	Aggregation	Amp = 7.4 S/N = 2.4	Aggregation

MST binding affinity experiments were performed using conditions conducive to binding, dose response curves generated (Figure 5.4) and K_D values estimated using a non-linear regression using a one-site specific binding model with R-squared determining the goodness of fit (Table 5.4). The IAA dose response curve at 50 mM

NaCl + 2 mM KCl demonstrated high variance between triplicates with low R-squared value and, therefore, was discarded from further analysis.

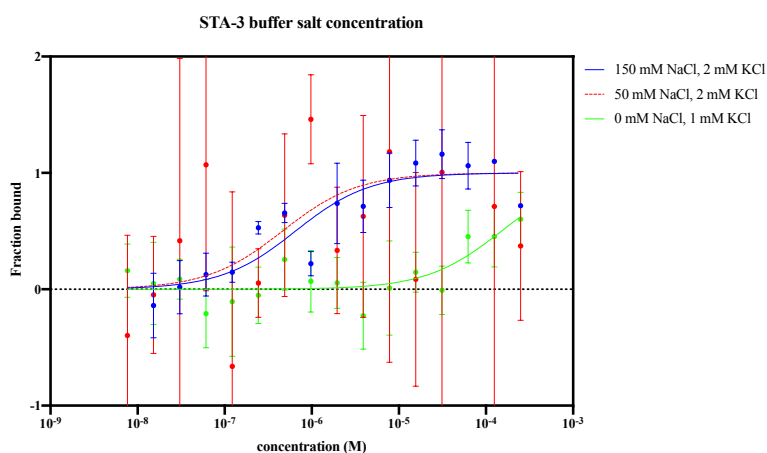


Figure 5.4. **Analysis of fitted dose response curves of STA-3 showed different IAA binding ability in different salt compositions.** The estimated K_D values were calculated using non-linear regression using a one-site binding model on GraphPad Prism (Table 5.4).

In comparison to binding in 150 mM NaCl + 2 mM KCl, IAA binding affinity was reduced by three orders of magnitude in 0 mM NaCl + 1 mM KCl. It was clear that appropriate Na^+ and K^+ concentrations are essential for proper aptamer folding and ligand binding (Ponzo et al., 2019). With studies suggested that Na^+ and K^+ significant affect G-quadruplex structural stability, the absence of Na^+ salt could affect the stability of STA-3 predicted G-quadruplex structure (Section 4.4.2) resulting in reduced IAA binding affinity.

Table 5.4. **Estimated K_D values of STA-3 auxin binding affinities in different salt conditions.** Estimated K_D values were calculated using nonlinear regression one-site specific binding model on GraphPad Prism 8 with R-squared indicating goodness of fit ($n = 3$). IAA binding experiment with R-squared below threshold is in grey.

Salt compositions	Calculated K_D (nM)	R-squared
150 mM NaCl + 2mM KCl	645 ± 290	0.8279
50 mM NaCl + 2 mM KCl	461 ± 791	0.2496
0 mM NaCl + 1 mM KCl	(150000 ± 175000)	0.6478

To conclude, IAA binding properties of STA-3 in MES buffer was highly dependent on the salt composition. The optimal salt composition for STA-3 is 150 mM NaCl + 2 mM KCl in MES buffer.

5.2.2 STA-3-9 auxin binding quality in different salt compositions

Different salt conditions were evaluated on MST binding check experiment to identify STA-3-9 positive binding conditions (Table 5.5). Interestingly, low signal amplitudes were observed across all salt conditions with highest at 5.1 in 150 mM NaCl + 2 mM KCl. In this case, any salt conditions with S/N ratio above 5.0, regardless of the signal amplitudes, were further evaluated with MST binding affinity experiments.

Table 5.5. **HEPES buffer salt concentration screenings with STA-3-9.** Signal amplitudes (Amp) and signal-to-noise ratios (S/N) obtained in HEPES buffers prepared with different final concentration of NaCl and KCl at pH 7.2. Positive binders with good S/N are in bold.

NaCl KCl	0 mM	50 mM	100 mM	150 mM
0 mM	Amp = 0.7	Amp = 1.0	Amp = 1.4	Amp = 1.7
	S/N = 5.1	S/N = 1.1	S/N = 0.9	S/N = 2.5
1 mM	Amp = 0.4	Amp = 0.5	Amp = 0.5	Amp = 0.9
	S/N = 0.8	S/N = 6.5	S/N = 4.0	S/N = 4.0
2 mM	Amp = 0.1	Amp = 0.9	Amp = 0.4	Amp = 5.1
	S/N = 1.1	S/N = 12.7	S/N = 0.8	S/N = 16.6
5 mM	Amp = 0.6	Amp = 0.4	Amp = 3.3	Amp = 0.6
	S/N = 1.8	S/N = 2.3	S/N = 3.7	S/N = 2.7
10 mM	Amp = 0.4	Amp = 0.8	Amp = 0.7	Amp = 0.9
	S/N = 1.0	S/N = 4.8	S/N = 2.8	S/N = 1.9

MST binding affinity experiments were performed on (a) 150 mM NaCl + 2 mM KCl, (b) 0 mM NaCl + 0 mM KCl, (c) 50 mM NaCl + 2 mM KCl, and (d) 50 mM NaCl + 1 mM KCl. Dose response curves were generated (Figure 5.5) and estimated K_D values were calculated using a non-linear regression using a one-site specific binding model with R-squared determining the goodness of fit (Table 5.6).

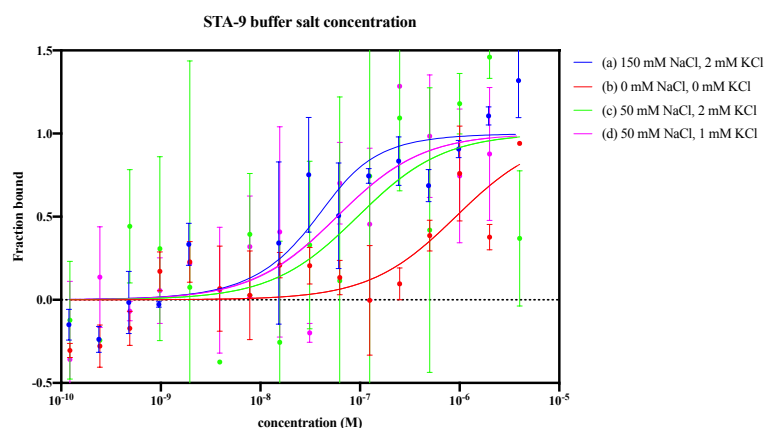


Figure 5.5. **Analysis of fitted dose response curves of STA-3-9 indicated salt composition effects on IAA binding.** The estimated K_D values were calculated using non-linear regression using a one-site binding model on GraphPad Prism (Table 5.6).

Lower but comparable IAA binding affinities were observed upon evaluation of STA-3-9 in (c) and (d) while a 30-fold decrease in IAA affinity was observed in (b). This reiterated the importance of Na^+ and K^+ in STA-3-9 IAA binding and/or G-quadruplex structural stability (Qi et al., 2013, Ponzo et al., 2019). All in all, STA-3-9 has an optimal IAA binding at 150 mM NaCl + 2 mM KCl.

Table 5.6. **Estimated K_D values of STA-3-9 auxin binding affinities in various salt conditions.** Estimated K_D values were calculated using a non-linear regression using a one-site binding model on GraphPad Prism with R-squared indicating goodness of fit ($n = 3$).

Salt compositions	Calculated K_D (nM)	R-squared
(a) 150 mM NaCl + 2mM KCl	29.0 ± 15.4	0.8525
(b) 0 mM NaCl + 0 mM KCl	916 ± 830	0.6635
(c) 50 mM NaCl + 2 mM KCl	95.3 ± 96.8	0.5483
(d) 50 mM NaCl + 1 mM KCl	58.8 ± 44.4	0.6938

Both STA-3 and STA-3-9 demonstrated optimal IAA binding affinities in buffers containing 150 mM NaCl and 2 mM KCl posing a potential challenge for *in planta* application due to their low IAA sensitivity at low ionic strength. Meanwhile, it has been observed with numerous developed aptamers that their binding properties can greatly vary between different analytical techniques and platforms (McKeague et al., 2015, Kalra et al., 2018). Therefore, while STA-3 and STA-3-9 did not demonstrate optimal binding for *in planta* application through MST, it was deemed worthwhile investigating their IAA binding characteristics under other biophysical

techniques. Consequently, additional assays were developed and evaluated, including a fluorescence Thioflavin T (ThT) assay and surface plasmon resonance (SPR), to characterise and develop IAA quantification assays using the optimised aptamers.

5.3 Thioflavin T assay as fluorescence IAA quantification assay

Thioflavin T (ThT) is one of benzothiazole fluorescent dyes widely used for biophysical studies of specific quadruplex probes including telomeric motifs (Zhao et al., 2019, Roxo et al., 2019). Enhanced fluorescence emission is observed upon specific ThT intercalation within G-quadruplex DNA structures (Renaud de la Faverie et al., 2014) and has been used as fluorescent ‘turn-off’ probe for small molecule *in situ* quantification (Wu et al., 2018). Therefore, taking advantage of the predicted G-quadruplex structures of IAA aptamers (Section 4.4.2; Table 4.8), ThT assay was optimised for potential IAA quantification.

5.3.1 Assay validation using an aptamer against ATP

An in-house assay validation was performed using unmodified ATP aptamer in synthetic sap buffer (10 mM KCl, 0.4 mM CaCl₂, 0.2 mM MgCl₂, 1.5 mM sucrose, 0.05% Tween-20, pH 5.8). A constant concentration of ATP aptamer (100 nM final concentration) was incubated with an ATP dilution series from 4 µM to 250 µM final concentration for 10 mins before adding ThT (1 µM final concentration). After 10 mins of incubation, fluorescence intensity was measured using 425 nm excitation and emission collected from 455 – 600 nm (Figure 5.6a). The fluorescence intensities at emission maximum (490 nm) were plotted against the ATP concentrations to generate dose response curves (Figure 5.6b). The K_D estimated for ATP aptamer (65.6 ± 39.3 µM) is comparable to the K_D previously estimated using MST (Section 3.5.1) suggesting the suitability of this assay for small molecule ligand *in vitro* quantification.

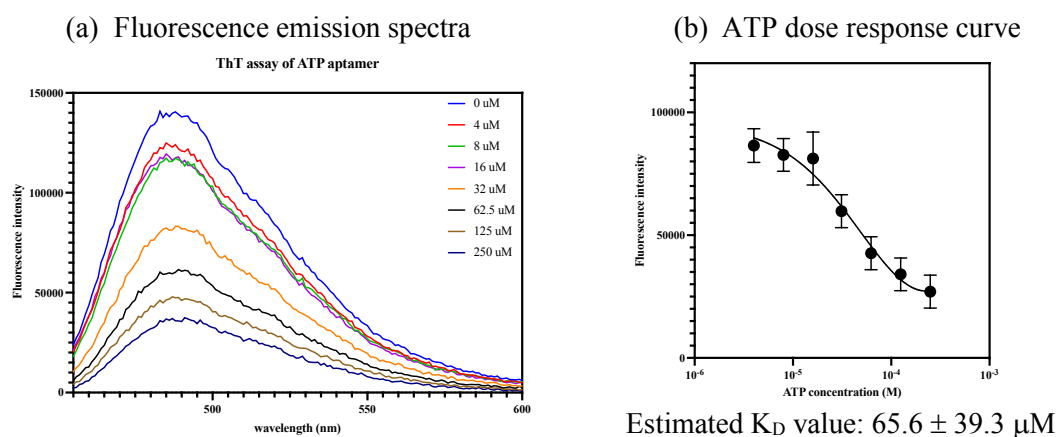


Figure 5.6 **ThT assay was validated with aptamer against ATP.** (a) A mean fluorescence emission spectra of ATP aptamer incubated with ATP serial dilution ($n = 3$). (b) Fluorescence intensities at emission maxima (490 nm) was plotted against ATP concentrations to generate a dose response curve. The estimated K_D value was calculated using non-linear regression using a one-site binding model on GraphPad Prism ($n = 3$).

5.3.2 Auxin quantification using STA-3 and STA-3-9 on ThT assay

In absence of buffering agents in synthetic sap buffer, the addition of acidic IAA could greatly alter the pH of the solution affecting the fluorescence intensity. Therefore, STA-3 and STA-3-9 were evaluated on ThT assay using their respective optimal buffer conditions, MES buffer at pH 5.8 for STA-3 and HEPES buffer at pH 7.2 for STA-3-9. A constant concentration (100 nM final concentration) of unmodified aptamers was incubated with IAA serial dilution ranging from 6.25 – 200 μM for 10 mins before adding ThT. After 10 mins, fluorescence emission intensity was collected from 455 – 600 nm and dose response curves were generated from the fluorescence intensities at 490 nm (Figure 5.7).

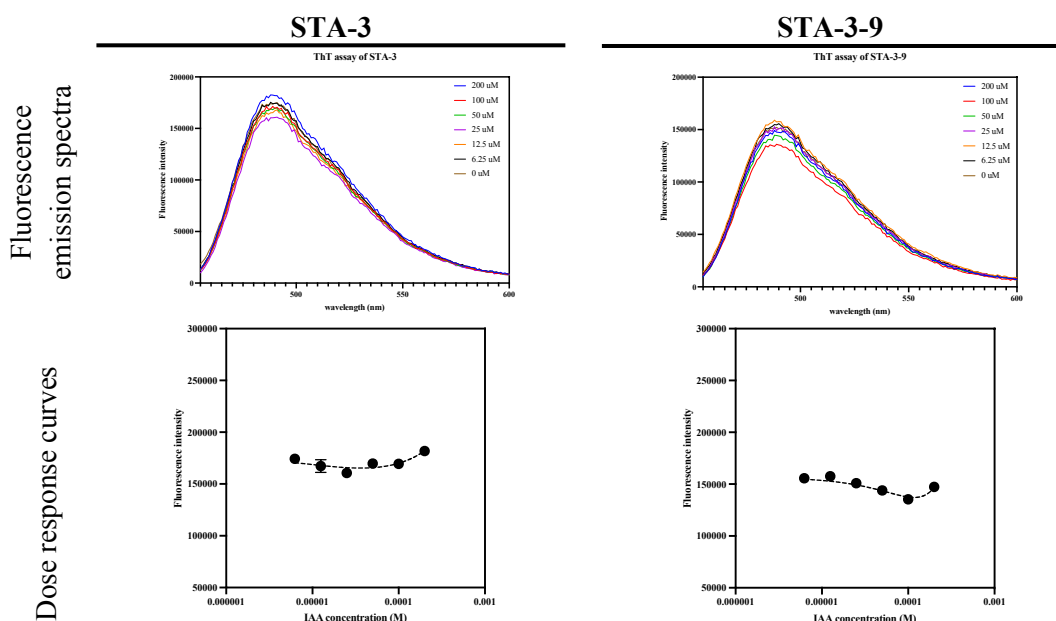


Figure 5.7. **Analysis of ThT assay of STA-3 and STA-3-9 showed no dose dependent fluorescence change.** The fluorescence emission spectra (top) of STA-3 incubated with IAA serial dilution was measured and intensity at emission maxima (490 nm) was collected to generate a dose response curve (bottom). The estimated K_D values were undetermined from the dose response curves generated.

No significant dose dependent fluorescence change was observed upon evaluation of STA-3 or STA-3-9 using ThT assay (Figure 5.7, bottom panel). While ThT intercalation is towards any G-quadruplex structure, the ThT intercalation might involve a stronger interaction than that of IAA resulting in no IAA dependent signal.

In conclusion, while assay validation deemed ThT suitable for ligand measurement using aptamers with G-quadruplex structure, it could not be used with the developed IAA aptamers for auxin measurement in solution.

5.4 SPR platform for IAA quantification assay

Surface plasmon resonance (SPR) has been successfully used to evaluate the binding properties of aptamers and as a sensing platform to detect and quantify target small molecules in samples (McKeague et al., 2015, Chang et al., 2014). With a practical lower limit of detection for analyte around 100 Da molecular weight (Healthcare, 2012), it should be sufficiently sensitive for detection of small molecules

such as IAA. Therefore, it was evaluated as a potential sensing platform for auxin quantification.

5.4.1 Assay validation using an aptamer against trans-zeatin

An in-house validation of SPR was performed using an aptamer developed against the cytokinin trans-zeatin (tZ) (219.24 Dalton molecular weight; (Qi et al., 2013). tZ aptamer was designed with 3' poly (A) tail for hybridisation on the biotinylated poly dT probe immobilised on an SPR sensor chip. A serial dilution of tZ from 390 nM to 50 μ M was evaluated in Tris buffer. Binding sensorgrams were generated with a blank flow cell as reference (Figure 5.8a) and the relative binding responses (black arrow) were plotted against tZ concentrations to generate a dose response curve (Figure 5.8b). The estimated K_D value for tZ aptamer ($2.37 \pm 0.43 \mu$ M) was comparable to the published value (Qi et al., 2013).

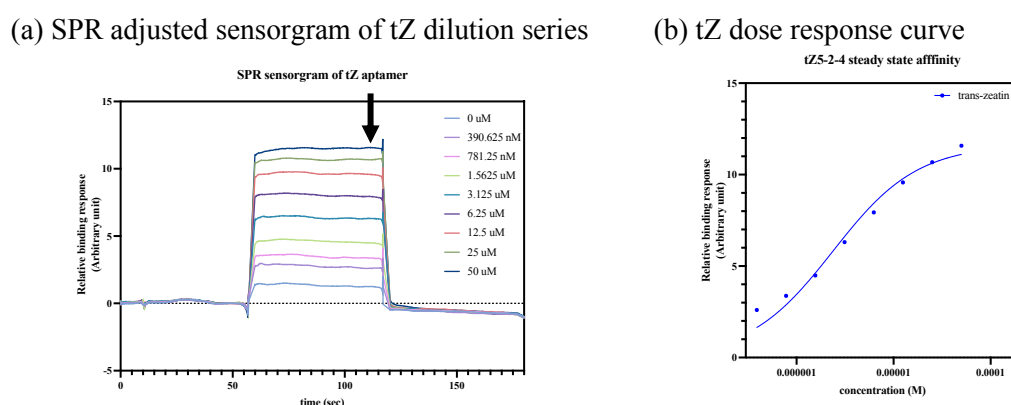


Figure 5.8 **SPR platform was validated using tZ aptamer against tZ dilution series.** Dose dependent sensorgrams were generated (a) and the relative binding responses were plotted against tZ concentrations (b). The K_D value was estimated at $2.37 \pm 0.43 \mu$ M using non-linear regression using a one-site binding model on GraphPad Prism.

To further evaluate the binding specificity of tZ aptamer, serial dilutions of several compounds were tested on SPR. Relative binding sensorgrams were generated (Figure 5.9a-g) and dose response curves were compared (Figure 5.9h). The estimated K_D values of each compound were calculated using non-linear regression one-site binding model on GraphPad Prism to compare the aptamer binding affinities (Table 5.7). Upon analysis, the saturation of the relative binding response along the lowest and highest concentrations (Figure 5.8b) indicated the bound and unbound phases

saturation of the dose response curve. This correlated to the lower and higher limit of quantification of tZ using SPR platform. In comparison to tZ, lower binding affinities were observed with dimethylallyladenine (15.6 μ M), benzylaminopurine (140 μ M), and trans-zeatin riboside (1998 μ M) while no binding was observed when testing IAA, ABA, or salicylic acid.

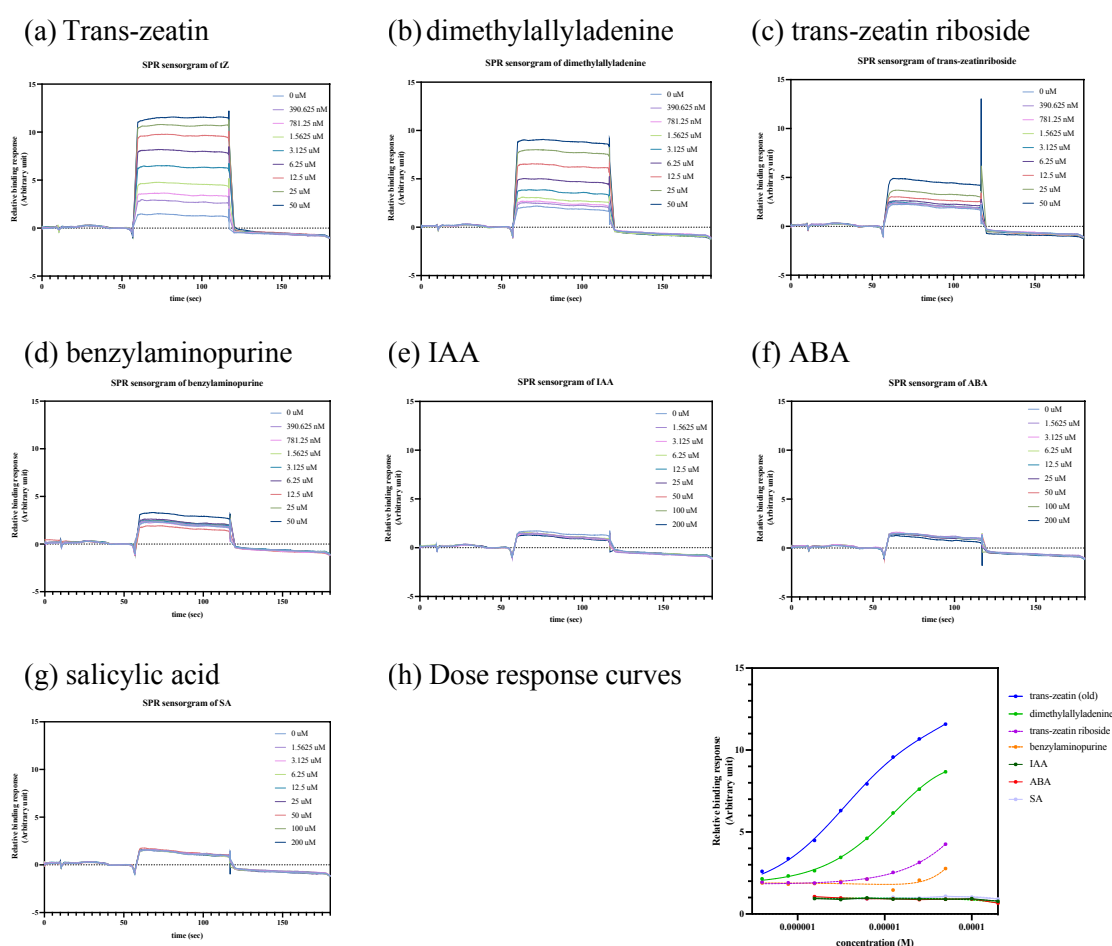


Figure 5.9. Binding specificity tZ aptamer could be evaluated through SPR platform. Relative binding sensorgrams (a-g) of tZ aptamer with several compounds (Table 5.7) were generated. Binding responses were plotted against compounds concentrations to compare binding affinities (h).

The observed ‘square-pulse’ sensorgrams (Figure 5.9) resembled steady state responses common with rapid kinetics bindings (Liu and Wilson, 2010). While it is useful for binding affinity evaluation, binding kinetics could not be calculated.

Table 5.7. **List of compounds evaluated for binding specificity of tZ aptamer using SPR platform and their estimated K_D values.** The estimated K_D values were calculated using non-linear regression using a one-site binding model on GraphPad Prism with R-squared indicating goodness of fit.

Compounds	Calculated K_D (μ M)	R-squared
Trans-zeatin	3.38 ± 0.28	0.9993
Dimethylallyladenine	15.61 ± 1.81	0.9996
Trans-zeatin riboside	1998	0.9958
Benzylaminopurine	140 ± 1512	0.7473
IAA	Undetermined	N/A
ABA	Undetermined	N/A
Salicylic acid	Undetermined	N/A

All in all, tZ aptamer confirmed SPR as a promising sensing platform for aptamers binding small molecule ligands revealing a high binding affinity and specificity of the aptamer for tZ.

5.4.2 Auxin quantification by STA-3 and STA-3-9 on SPR platform

STA-3 and STA-3-9 were initially evaluated on SPR in Tris buffer. A serial dilution of IAA from 1.56 to 200 μ M was evaluated against IAA aptamers with a blank flow cell as reference. Binding sensorgrams analysis did not show any IAA binding with the aptamers (data not shown). As previously mentioned, buffers can greatly affect the binding analysis (Baaske et al., 2010), and so MES and HEPES buffers were evaluated on SPR alongside PBS which is recommended for low molecular weight analyte evaluation (Figure 5.10; (GE Healthcare, 2012)).

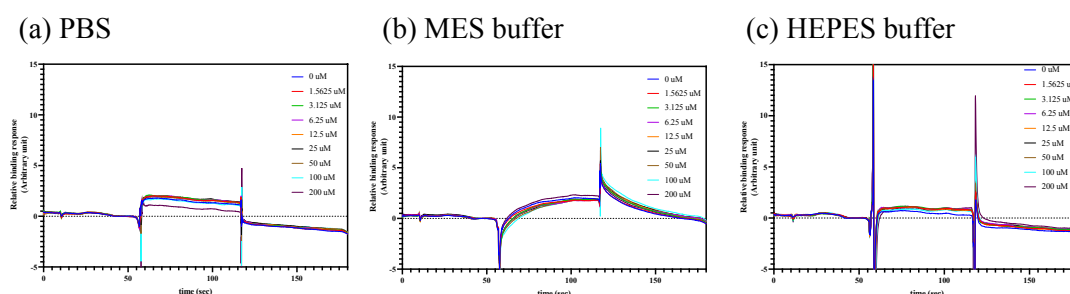


Figure 5.10. **SPR buffer screening analysis of STA-3-9 did not show positive IAA binding.** No dose dependent response was observed from any buffer system.

A minimal square pulse binding sensorgram was observed from PBS and HEPES buffer indicating no auxin concentration dependent response. On the other

hand, while slower binding kinetics were observed in MES buffer, no dose-dependent response could be determined (Figure 5.10b). As no dose dependent response could be observed in any buffer conditions, a potential pitfall could be the immobilisation of DNA aptamers on the sensor surface at the 5'-end. While the immobilisation did not involve the aptamer binding sequences, anchoring of aptamer close to the surface could hinder the formation of aptamer tertiary conformation (Urmann et al., 2017). Furthermore, higher immobilisation levels of DNA aptamers are required to clearly see the binding response from a low molecular weight analyte. The immobilisation level of tZ aptamer (35 bases long; ~2000 response unit) yielded a dose dependent binding response with maximum response (R_{max}) less than 15 RU (Figure 5.8). Therefore, a higher immobilisation level STA-3-9 (58 bases long) would be necessary to detect any IAA binding. This, however, could crowd the sensor surface and, again, hinder the proper aptamer folding required for IAA intercalation (Oberhaus et al., 2020). Therefore, the absence of dose-dependent binding sensorgrams of STA-3-9 could correspond to the immobilisation STA-3-9 affecting IAA binding and/or the insufficient aptamer immobilisation for IAA-dependent refractive index change.

In conclusion, while SPR is a powerful sensing platform to characterise and detect binding interactions of aptamers and small molecule analytes, no IAA binding was detected using STA-3-9.

5.5 Further IAA aptamer characterisation

Whilst the optimised fluorescence ThT assay and SPR platforms were able to evaluate aptamers against ATP and tZ, they were unsuccessful for auxin. Therefore, further studies using isothermal titration calorimetry (ITC) and circular dichroism (CD) were set out in attempts to obtain a better understanding on the IAA binding mechanism of STA-3-9.

5.5.1 *Isothermal titration calorimetry (ITC)*

ITC has been widely used to study the binding interactions between macromolecules (proteins or oligonucleotides) and a wide range of analytes. A major advantage of using ITC is no modifications or labelling of either binding partners are

required to evaluate the interaction (Slavkovic and Johnson, 2018, Reinstein et al., 2013).

5.5.1.1 Assay validation using an aptamer against *trans*-zeatin

An in-house validation of ITC was performed using tZ aptamer. The experimental parameters were extensively optimised for appropriate thermodynamics evaluation of tZ – tZ aptamer interaction (Table 5.8). Various buffer conditions were evaluated to show no significant difference in enthalpic change (data not shown). Therefore, HEPES buffer was chosen to allow consistency with other characterisation techniques. The cell temperature was adjusted to 15°C to enhance any enthalpy signal (Slavkovic and Johnson, 2018) while the reference power was also adjusted to 4 µCal/sec to allow good thermogram reading.

Table 5.8 **Optimisation of ITC experimental parameters.** Each experimental parameter was adjusted on VPViewer software of the ITC instrument to improve ITC thermograms. The optimised parameters are in bold.

Parameters	Optimisation variables
Buffers	Tris buffer at pH 7.2 MES buffer at pH 5.8 HEPES buffer at pH 7.2
Cell temperature	25°C 15°C
Reference power	10 µCal/sec 4 µCal/sec

Initially, buffer-to-buffer titration was used to confirm a stable baseline. An ITC thermogram of tZ-to-aptamer single injection was compared to one of tZ-to-buffer (Figure 5.11a) and thermodynamic binding parameters were calculated using Origin software (Figure 5.11b).

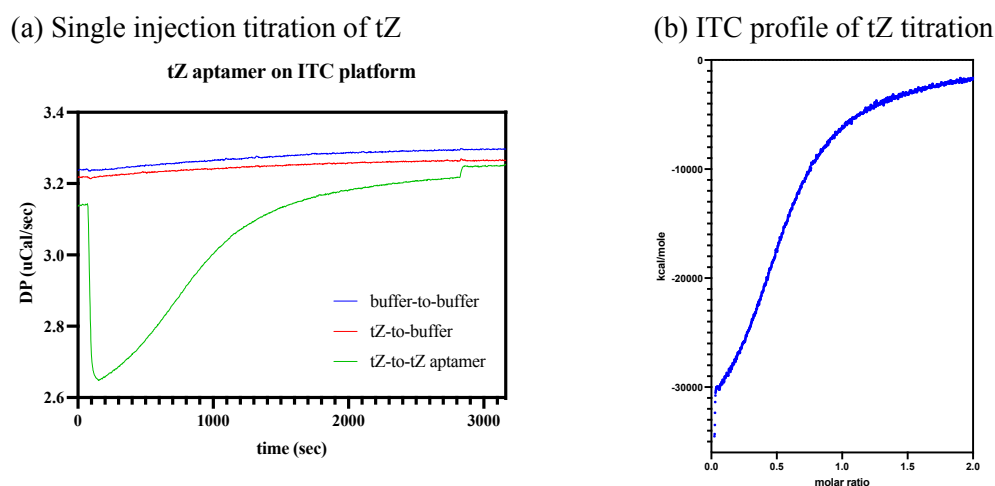


Figure 5.11. **tZ binding of tZ aptamer could be evaluated using ITC.** (a) ITC thermograms for the tZ-aptamer binding interaction (green) in comparison to heat of dilution of tZ in buffer (red) with buffer-to-buffer injection as reference baseline (blue). (b) The injection enthalpy was plotted against the tZ-aptamer molar ratio and Origin software was used to obtain an estimated K_D value of 1.73 μM .

A large negative spike was observed upon injection of tZ into the sample cell (Figure 5.11a, green curve) suggesting exothermal interaction between tZ and the aptamer. This exothermal interaction corresponded to the previous studies on the complete conformational change of the aptamer upon tZ interaction (Liu et al., 2016). Origin software was used to plot the enthalpy against the molar ratio in the sample cell and thermodynamic binding parameters were calculated. The K_D value estimated (1.73 μM) was comparable to the published value using the same technique (Qi et al., 2013).

This confirmed the suitability of ITC under optimised experimental parameters to evaluate the binding interaction of aptamer and small molecule ligand.

5.5.1.2 STA-3-9 IAA binding characterisation using ITC

The ITC experimental parameters optimised with tZ aptamer were applied to the evaluation of IAA interaction with STA-3-9. A single injection of IAA (200 μM) was titrated to 20 μM of STA-3-9 in the ITC sample cell and the thermogram was monitored (Figure 5.12).

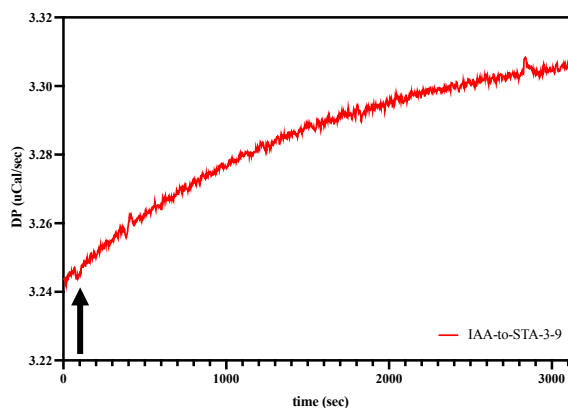


Figure 5.12 The analysis of ITC thermogram of IAA to STA-3-9 single injection showed no significant enthalpy change due to IAA binding interaction. No shift in differential power was observed upon IAA injection (black arrow).

The upward shift in the baseline over very small differential power (0.06 $\mu\text{Cal/sec}$) was consistent. This shift was considered insignificant and could be ignored. However, no peak was detected in response to injection of IAA into STA-3-9 (Figure 5.12, black arrow). While IAA interaction of this aptamer was consistent by MST, the IAA binding mechanism might not involve a significant conformational change of STA-3-9. Instead, if IAA were to intercalate into an already stable G-quadruplex, there would be no significant conformational change of STA-3-9 contributing to the new hydrogen bonds and major enthalpic change upon IAA injection. This could explain the absence of isothermal peak at the injection time.

In conclusion, ITC data analysis suggested the IAA binding mechanism as ligand intercalation of the existing G-quadruplex rather than large conformational change of the aptamer.

5.5.2 CD for G-quadruplex structure characterisation

Circular dichroism has been extensively used to evaluate the tertiary structures of oligonucleotides including DNA aptamers and to distinguish different G-quadruplex conformations (Wang et al., 2019, Qi et al., 2013, Grozio et al., 2013). Therefore, CD spectra of unmodified STA-3-9 (10 μ M final concentration) was monitored in different assay buffers (Figure 5.13). The CD spectra was analysis to show a positive elliptic maximum at 263 nm and negative elliptic minimum at 242 nm corresponding to those of a parallel G-quadruplex structure (Małgowska et al., 2012, Del Villar-Guerra et al., 2018). The high elliptic intensities at these wavelengths also suggested a uniformity of the parallel G-quadruplex structure in the sample. No significant difference in the spectra was observed upon evaluation in different buffers. For consistency with previous binding optimisation using MST, HEPES buffer was, therefore, chosen as assay buffer for further binding analysis.

Next, CD spectra of STA-3-9 was measured both in absence (red) and presence (blue) of 250 μ M IAA (Figure 5.14) to examine any effect IAA had on STA-3-9 structural conformation. Identical CD spectra of STA-3-9 were observed in absence and presence of IAA suggesting no conformational change upon IAA binding of STA-3-9. This supported previous hypothesis on IAA binding mechanism of STA-3-9 from

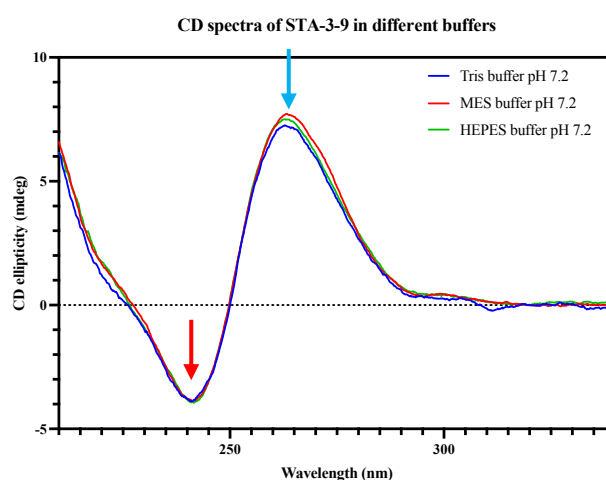


Figure 5.13. **No buffer effect was observed in the analysis of CD spectra of STA-3-9.** CD spectra of STA-3-9 (10 μ M) was collected at 25°C in different buffers at pH 7.2. A positive elliptic maximum at 264 nm (blue arrow) and negative elliptic minimum at 240 nm (red arrow) was observed corresponding to a parallel G-quadruplex structure.

ITC data that IAA intercalates rather than triggers a large conformational change of the DNA aptamer.

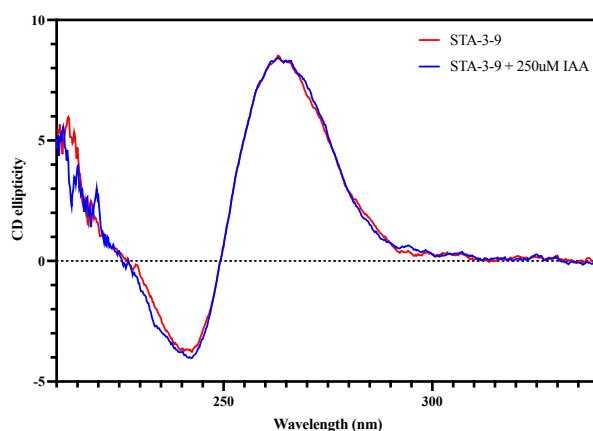


Figure 5.14. CD spectra analysis of STA-3-9 in absence (red) and presence (blue) of 250 μ M IAA revealed no conformational change of aptamer upon IAA interaction. The CD spectra were collected at 25°C in HEPES buffer at pH 7.2. There was no significant difference in the CD ellipticity observed.

Further, to evaluate the stability effect of IAA on the tertiary structure of STA-3-9, a thermal melt experiment was performed. The CD signal was monitored at the elliptic peaks (242 nm minimum and 263 nm maximum) between 20 – 85°C to establish the melting temperature (Figure 5.15). Upon rising the temperature, the CD ellipticities at the two wavelengths tended towards zero corresponding to the melting of the G-quadruplex structure. However, there was no significant shift in the melting curves observed in presence of IAA at both wavelengths. The melting temperature was observed between 30 – 50°C suggesting that the aptamer structure was not highly stable. However, a study showed a 13-mer oligonucleotide with melting temperature at 25°C could stabilise in final duplex state upon an enthalpic force (Vesnaver and Breslauer, 1991). The intercalation of IAA within the parallel G-quadruplex structure of STA-3-9 could slightly improve the structural stability resulting in an increase in the ellipticity at 263 nm between 20 – 30°C (Figure 5.15b). However, experimental replicates are required to confirm the hypothesis.

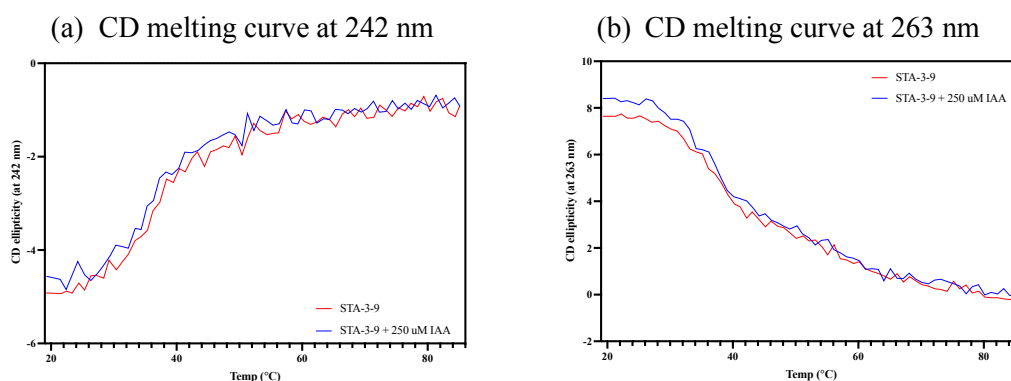


Figure 5.15. The analysis of CD thermal melt experiments of STA-3-9 in absence (red) and presence (blue) of 250 μ M IAA did not show significant shift in melting temperature of the aptamer upon IAA binding. A slight increase in ellipticity was observed around 20 – 30°C at 263 nm (b).

5.6 Discussion

This chapter has presented several techniques used to further characterise aptamers and assay formats which could be applied for ligand quantification. While the established aptamers for ATP and tZ were proven valuable for validating the suitability of ThT and SPR assays for ligand quantification, we were not able to employ the techniques to quantify IAA binding or concentrations using STA-3 and STA-3-9. Additional aptamer characterisation was, therefore, performed using ITC and CD to further investigate the IAA – STA-3-9 interaction.

CD spectral evaluation suggested that STA-3-9 was parallel G-quadruplex, and this structure was inherent – present without and with IAA. This may explain why ThT assay failed to recognise IAA binding. ThT assay relies on the aptamer conformational change upon ligand binding and the competition with ligand to intercalate within the G-quadruplex structure (Zhao et al., 2019, Wu et al., 2018). On the other hand, the use of SPR platform was validated by tZ aptamer but was not able to detect an auxin dose dependent response. It becomes of a significant challenge to evaluate binding of small molecule analytes (~100 Daltons) (GE Healthcare, 2012) and measuring auxin binding of STA-3-9 is hitting the limit of detection.

ITC data suggested no large enthalpic change could be observed upon IAA titration to STA-3-9 indicating to conformational change upon IAA binding. Notably, the ITC experimental parameters were optimised based on the success of tZ aptamer.

However, studies have shown that this tZ aptamer undergoes major conformational change upon tZ binding (Wang et al., 2018, Qi et al., 2013, Liu et al., 2016). To allow proper thermodynamics evaluation of IAA intercalation within STA-3-9, further optimisation of ITC experimental parameters is necessary.

Taking all the data into account, it was suggested that the ligand binding mechanism of STA-3-9 is through IAA intercalation within the existing G-quadruplex structure of the aptamer rather than inducing a conformational change. Controversially, the failure to quantify auxin binding using ThT assay and SPR and the insignificant enthalpic change from ITC could be interpreted as STA-3-9 possessing a low auxin binding affinity, contradicting the MST data with IAA binding at nanomolar range. However, more advanced techniques, such as nuclear magnetic resonance (NMR) or crystallography, would be able to confirm this (Małgowska et al., 2012, McKeague and DeRosa, 2012, Pfeiffer and Mayer, 2016). As it stands, STA-3-9 would not be suitable as biosensor recognition for *in planta* application as the binding was only detectable using MST platform.

Next step is to establish *in planta* application of STA-3-9 for IAA detection. To do so, stability and suitability of STA-3-9 in plants are evaluated in the next chapter. Furthermore, the delivery system of developed aptamer-based biosensor is assessed to explore the mechanism of which IAA can be quantify in plant system.

**Chapter 6 Aptamers and biosensor delivery and signalling system
evaluation *in planta***

In previous chapters, sequential processes were performed to select, optimise, and characterise aptamers with high IAA binding affinity and specificity. In this chapter, we explored and evaluated the applicability of the aptamers as sensing tools *in planta*. Many aptamer sensing platforms have been developed for measurements on extracted samples making aptamers amenable for rapid, facile diagnostic kits (Qi et al., 2020, Komorowska et al., 2017). However, for measurements *in planta*, a fluorescent optical biosensor coupled with confocal microscopy is desirable to give high spatial resolution and sensitivity (Walia et al., 2018, Sadanandom and Napier, 2010, Herud-Sikimic et al., 2021, Brunoud et al., 2012). Both *A. thaliana* intact primary roots and isolated root protoplasts were studied for sensor evaluation. Aptamers were first evaluated for their stability in apoplastic fluid, and fluorescent STA-3-9 was evaluated for accumulation in isolated protoplasts. The protoplast system removed the cell wall barriers to allow evaluation of accumulation and penetrance of the aptamers and CPNs through cell's plasma membrane. Novel CPNs were investigated as a plausible biosensor delivery and signalling system due to their small size and low cytotoxicity (Bhunja et al., 2013). The particles were evaluated for permeation within the apoplastic matrix and whether or not they remain outside the plasma membrane or are able to pass inside the cells.

6.1 Aptamer stability evaluation in apoplastic fluid

For a robust and reliable intercellular measurement of IAA, aptasensors must be stable in acidic apoplastic fluid with low ionic strength and can withstand possible exposure to nucleases (Sattelmacher, 2001). It is also unclear how cells might respond to the introduction of aptasensors. While minimal nuclease is present in apoplast, it was shown that mechanical injuries or infiltration can induce nuclease secretion and activity in the apoplast (Mittler and Lam, 1997). Therefore, a set of unmodified and fluorescently labelled aptamers was examined for their stability in apoplast. Each aptamer (5 μ L) was denatured at 95°C for 5 min followed by snap cooling on ice for 10 min before adding to either 25 μ L extracted apoplastic fluid or distilled water. The mixtures were incubated for 30 min at room temperature before stability evaluation on 2% agarose gel electrophoresis (Figure 6.1).

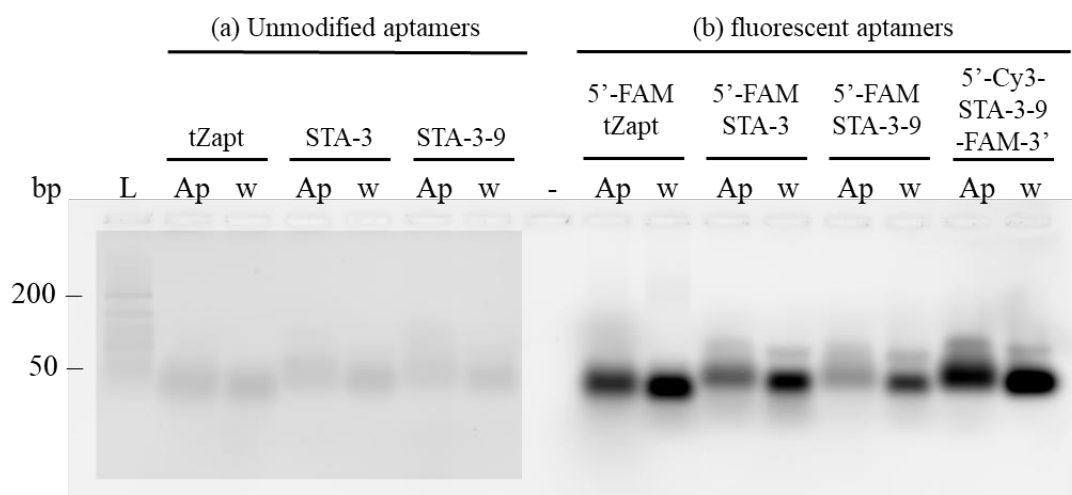


Figure 6.1. **Stability of unmodified (a, left panel) and fluorescent (b, right panel) aptamers was reduced upon incubation in extracted apoplastic fluid from *Nicotiana benthamiana* leaves (Ap) in comparison to those incubated in distilled water (w).** 2% agarose gel electrophoresis was performed with NEB low Mw DNA ladder (L) as size standard. A negative control of apoplastic fluid (-) confirmed no background bands. Brightness and contrast of unmodified aptamers was manually adjusted for improved visualisation using ImageJ software.

A Typhoon FLA 9500 biomolecular imager was used to visualise the 2% agarose gel using 473 nm excitation laser and LPB filter. The image was adjusted for brightness and contrast using ImageJ software to enhance visualisation without affecting raw intensity values. ImageJ software was also used to evaluate the integrated density values of each aptamer band (Figure 6.2). While less than 10% decrease in integrated density was observed upon incubation in apoplastic fluid compared to those in water (Figure 6.2a), the bands appeared to be diffused possibly

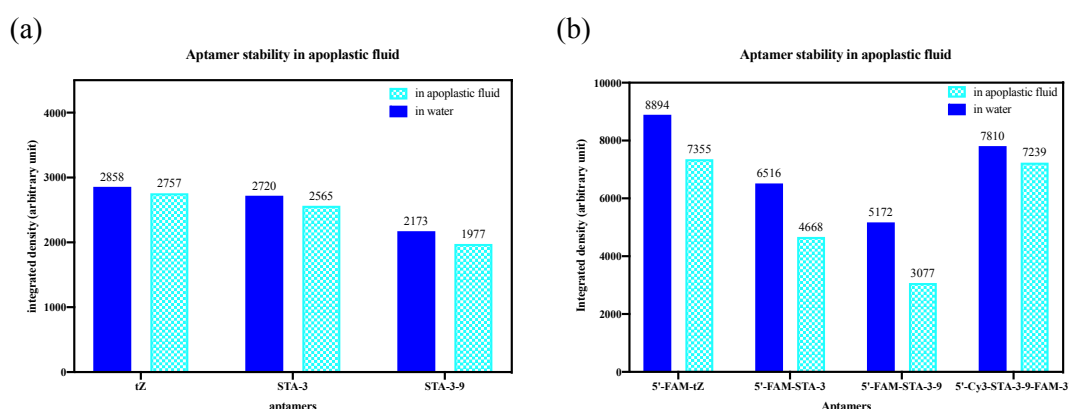


Figure 6.2. **Integrated density of unmodified (a) and fluorescent (b) aptamers suggested degradation in apoplastic fluid (pattern cyan) in comparison to those in water (solid blue).** ImageJ software was used to analyse the integrated density of the aptamers from 2% agarose gel electrophoresis image (Figure 6.1).

corresponding to degradation or the lower pH or higher salt concentration. As aptasensor will be conjugated with signalling compounds, evaluation was focused on fluorescent aptamers. Conjugated fluorophore(s) allowed more reliable quantification under a fluorescence scanner (Figure 6.2b). All 5'-FAM aptamers demonstrated a significant reduction in integrated densities upon incubation in apoplastic fluid, with 5'-FAM-STA-3-9 displaying more than 40% decrease. This suggested an insufficient protection of conjugated fluorophore against degradation. In contrast, around 7% reduction in the integrated density was observed for 5'-Cy5-STA-3-9-FAM-3' incubated in apoplastic fluid. This implied conjugations on both ends of the aptamer could slow down DNA degradation (Odeh et al., 2019). While extensive base modifications could further provide protections against nucleases degradation (Odeh et al., 2019, Ni et al., 2017), it appeared that the overall structures of unmodified and fluorophore-conjugated aptamers were affected in presence of apoplastic fluid. Further investigations will be necessary once aptamers are conjugated to CPNs to ensure they are suitable as a sensing tool *in planta*.

6.2 Aptamer evaluation in *A. thaliana* protoplasts

Fluorescent STA-3-9 was evaluated in protoplasts for its penetrance and accumulation behaviour within plant cells. 5'-Cy5-STA-3-9-3' aptamer (8 μ M final concentration) was denatured at 95°C for 5 min followed by snap cooling on ice for 10 min before mixing with protoplasts isolated from 5-days old *A. thaliana* roots (Section 2.13.2). The mixture was incubated at room temperature for one hour before visualisation by laser scanning microscopy using 633 nm excitation laser and emission

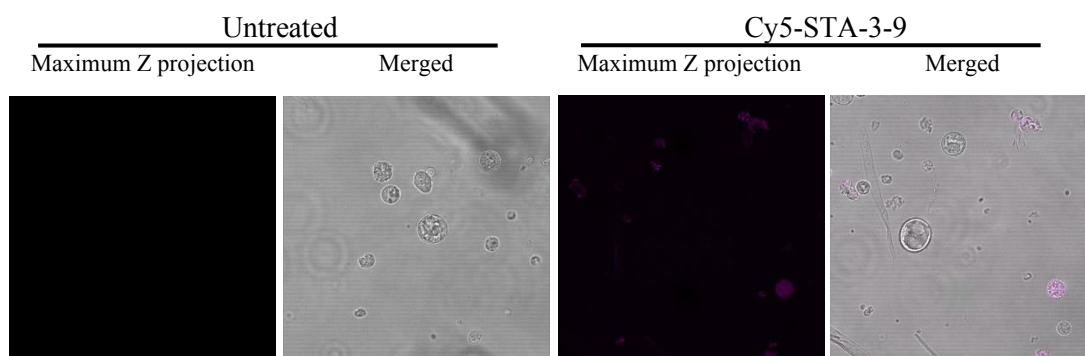


Figure 6.3. **High accumulation of Cy5-STA-3-9 in cell debris while no penetration was observed in protoplasts.** ImageJ software was used to generate maximum Z projections for optimal fluorescence visualisation and superimposition of brightfield images for structural reference.

collected from 638 – 759 nm, corresponding to magenta Cy5 emission. ZEN software was used to generate Z-stack images of the protoplasts before using ImageJ software to create corresponding maximum Z-projections for optimal visualisation. Brightfield images were superimposed for structural references (Figure 6.3, merged). An untreated protoplast solution was visualised under the same settings as a negative control to check for background autofluorescence (Figure 6.3, left panel). No fluorescence emission was observed in untreated protoplasts confirming no interfering background autofluorescence at Cy5 microscopy settings.

After an hour incubation with Cy5-STA-3-9, fluorescence was only observed associated with cell debris and dying cells (Figure 6.3, right panel) which could account for an electrostatic interaction with cell components. However, no fluorescence was detected inside or around healthy (round and spherical) protoplasts implying that aptamers were not taken up by the cells and nor did they accumulate around the cell surface. A repulsive force between the DNA strand and the phospholipid headgroups of the plasma membrane could account for the aptamer failing to access the membrane surface (Nagata and Melchers, 1978).

Taking all the data into account, ‘naked’ fluorescent aptamers were not found to be suitable as sensing tool in plants. It is proposed that novel CPNs could serve as a suitable delivery and signalling system for plant aptasensors.

6.3 CPNs design and synthesis

A series of CPNs with different hydrodynamic sizes and surface charges were investigated. In short, a reverse addition-fragmentation chain-transfer (RAFT) mediated polymerisation-induced self-assembly (PISA) approach was designed to synthesize thermodynamically stable co-polymer nanoparticles (Yildirim et al., 2016, Canning et al., 2016). Two monomers, dimethyl acrylamide (DMA) and diacetone acrylamide (DAA), were used to form neutral corona core co-polymers at different sizes. The developed synthetic pathway allowed refinements of CPNs with adjustable physicochemical properties. In the first instance, different surface charges were investigated by adding different compounds to the core corona.

Subsequent conjugation with a suitable dye was necessary for fluorescence visualisation. Chosen fluorophores must be fluorescently stable in various pH and ion concentration to allow robust measurements in acidic apoplastic matrix (Chen et al., 2008). Moreover, excitation/emission spectra of chosen fluorophores should not overlap with plant compound autofluorescence (Billinton and Knight, 2001). BODIPY dye was chosen due to its pH independent properties and suitable excitation/emission spectra. BODIPY was covalently conjugated onto the core CPNs through a crosslinking chemistry. Synthesized CPNs were suspended in distilled water at 1 mg/mL final concentration and were characterised under dynamic light scattering (DLS) to determine average sizes (Table 6.1).

Table 6.1 CPN samples synthesized and evaluated for accumulation and permeation into plants. The average sizes of CPNs were determined using dynamic light scattering (DLS) and overall surface charges were evaluated from polymer chemistry.

CPN samples	Polymers	Average sizes (number size distribution; nm)	Overall surface charges	CPN abbreviations
SP-1-076	PDMAm-PDAAm ₅₀	20	Neutral	N ₁ (20 nm)
SP-1-077	PDMAm-PDAAm ₁₀₀	32	Neutral	N ₁ (32 nm)
SP-1-078	PDMAm-PDAAm ₂₀₀	71	Neutral	N ₁ (71 nm)
SP-1-086	P(DMAm+DMAEA)-PDAAm ₅₀	19	Neutral	N ₂ (19 nm)
SP-2-16B	PDMAm ₇₀ -PDAAm ₃₀	19	Neutral (zwitterionic)	N ₂ (19 nm)
SP-1-082	P(DMAm+AA)-PDAAm ₅₀	25	Negative	⊖(25 nm)
SP-1-083	P(DMAm+AA)-PDAAm ₁₀₀	45	Negative	⊖(45 nm)
SP-1-084	P(DMAm+AA)-PDAAm ₂₀₀	78	Negative	⊖(78 nm)
SP-2-007B	PQDMAEMA-PDAAm ₁₀₀	20	Positive	+(20 nm)
SP-2-007A	PQDMAEMA-PDAAm ₂₀₀	30	Positive	+(30 nm)
SP-2-001B	P(DMAm+QDMAEMA)-PDAAm ₁₀₀	34	Positive	+(34 nm)
SP-2-001C	P(DMAm+QDMAEMA)-PDAAm ₂₀₀	45	Positive	+(45 nm)
SP-2-29A	PDMAm-PDAAm ₅₀ with 5'-ATPapt-Cy3-3'	Data not available	Neutral	N ₁ (ATPapt)
SP-2-29B	PQDMAEMA-PDAAm ₁₀₀ with 5'-ATPapt-Cy3-3'	Data not available	Positive	+(ATPapt)

In total, 14 CPN samples with various surface charges, sizes and polymer composition were submitted for evaluation (Table 6.1, Figure 6.4). Most CPNs contained a (PDMAm-PDAAm) core with adjusted DAA monomer to fine-tune the particle sizes. Acrylic acid (AA) as $\text{CH}_2=\text{CHCOO}^-$ form (Wisniewska et al., 2017) was co-polymerised to create CPNs with negatively charged surface while a cationic polymer, poly quaternised dimethyl aminoethyl methacrylate (PQDMAEMA; (Du and Zhao, 2004), was integrated as part of the corona core to generate permanently positively charged CPNs. These CPNs with different surface charges were synthesized to different sizes. To investigate the effect of polymer composition on cell penetration and accumulation in plants, an additional dimethyl aminoethyl acrylamide (DMAEA) monomer was used to create additional neutral CPN. Moreover, a poly-3-dimethyl (methacryloyloxyethyl) ammonium propane sulfonate (PDMAPS) was used to synthesize zwitterionic CPNs to investigate its influence in accumulation and penetrance into plant tissues (Tian et al., 2013).

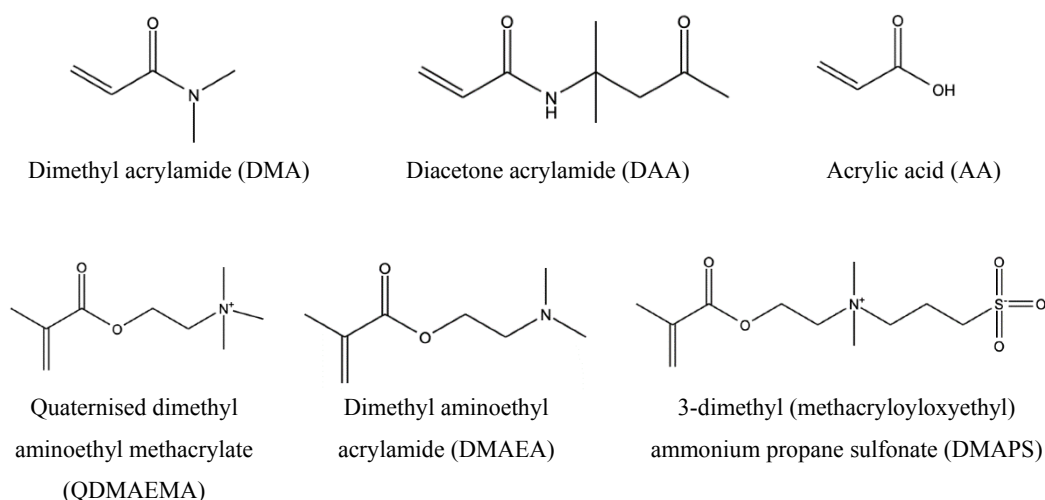


Figure 6.4. **Chemical structures of monomers used for the synthesis of various CPNs (Table 6.1).**

To further evaluate the delivery system of aptamer-based biosensor in plants, two aptamer-conjugated CPNs were synthesized and assessed. The established aptamer against ATP (ATPapt) was chosen for CPN conjugation. A 5'-primary amine-ATPapt-Cy3-3' were conjugated on N₁(20nm) and +(20nm) through 1-ethyl-3-(3-dimethyl aminopropyl)carbodiimide (EDC) coupling (Farokhzad et al., 2004) and the CPNs were evaluated for the root penetrance and cell uptake. As previously mentioned, a suitable optical aptasensor can be designed with fluorescence resonance

energy transfer (FRET) properties for auxin quantification. Therefore, ATPapt was synthesized with Cy3 dye at the 3'-end. The overlap of CPN's BODIPY 'donor' fluorescence emission with the Cy3 'acceptor' fluorescence excitation spectrum would allow FRET measurements by evaluating the shift in excitation energy or the ratio of the two wavelengths (Okumoto et al., 2008).

Prior to evaluation under fluorescence confocal microscopy, CPNs were visualised using a UV light box (365nm excitation wavelength) to confirm and compare their fluorescence (Figure 6.5). All tested CPNs exhibited bright green fluorescence corresponding to the conjugated BODIPY dye, and no significant difference in brightness or transparency between different CPNs suspensions was observed.

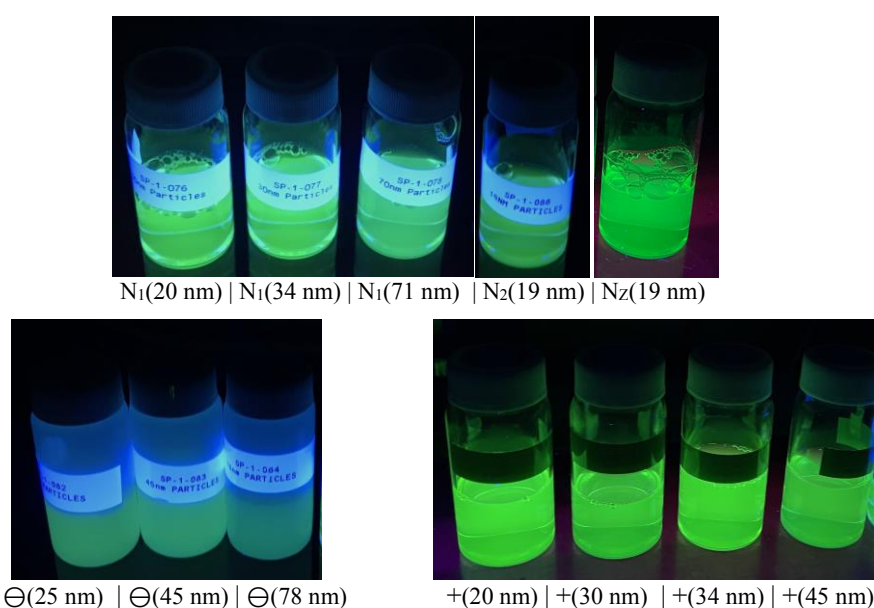


Figure 6.5. **Preliminary fluorescence evaluation of BODIPY-CPNs under UV light showed no visual difference in the fluorescence intensities between samples.**

6.4 Stability evaluation of CPNs samples in apoplastic fluid

CPNs were initially investigated for their stability in apoplastic fluid by mixing each CPN (5 μ L) with either 25 μ L extracted apoplastic fluid or distilled water. The mixtures were incubated for 30 min at room temperature prior to visualisation using 2% agarose gel electrophoresis (Figure 6.6). Negatively charged CPNs migrated down

the gel towards the anode while no migration was observed for neutral CPNs (Figure 6.6). It was impractical to run and analyse positively charged CPNs on the same gel as they would migrate in the opposite direction.

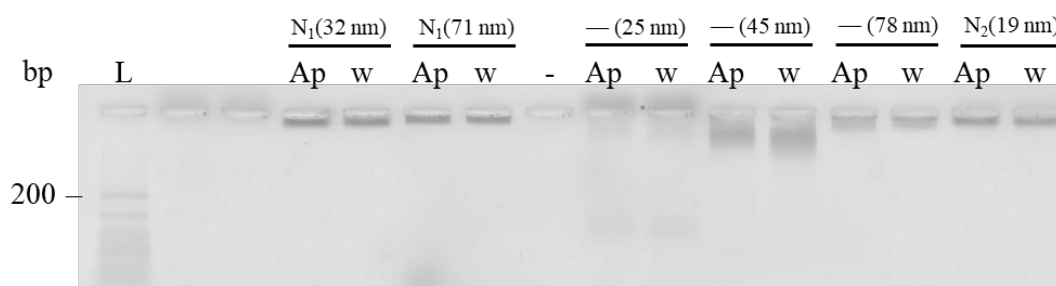


Figure 6.6. **Comparable stability of CPNs upon incubation in extracted apoplastic fluid from *Nicotiana benthamiana* leaves (Ap) in comparison to those incubated in distilled water (w).** 2% agarose gel electrophoresis was performed with low Mw DNA ladder (L) as size standard. A negative control of apoplastic fluid (-) confirmed no background bands.

No significant difference in band thickness was observed between the samples incubated in apoplastic fluid (Ap) and in distilled water (w) indicating the integrity of CPNs in lower pH and higher ionic strength (Figure 6.6). ImageJ software was used to quantify the integrated densities of each band (Figure 6.7). Comparable integrated densities were observed between CPN samples incubated in water and in apoplastic fluid confirming their stability in apoplastic fluid with lower pH.

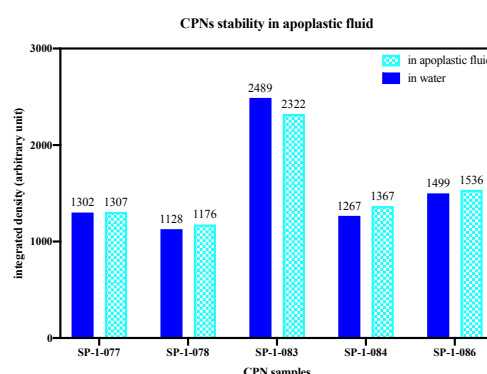


Figure 6.7. **Neutral and negatively charged CPNs were stable in apoplastic fluid (pattern cyan) and in water (solid blue).** ImageJ software was used to analyse the integrated density of the bands corresponded to CPNs from the image of a 2% agarose gel after electrophoresis (Figure 6.6).

To summarise, neutral and negatively charged CPNs were stable upon incubation with apoplastic fluid allowing further investigations into their penetrance and accumulation in plant samples.

6.5 CPN evaluation in intact roots of *A. thaliana*

CPN samples were first evaluated in intact roots for their penetrance and accumulation. Five-days old *A. thaliana* seedling roots were carefully transferred from ½ MS plates into 1 mg/mL CPN suspensions. The roots were incubated at room temperature for at least one hour before fluorescence visualisation by laser scanning microscopy using 488 nm laser and emission collected from 493 – 577 nm, corresponding to green BODIPY emission. ZEN software was used to generate Z-stack images of root tips and hair zones before using ImageJ software to create corresponding maximum Z-projections for optimal visualisation. Brightfield images were superimposed for root structural references (denoted in figures as merged). An untreated root was visualised under the same settings to check for the absence or influence of background autofluorescence (Figure 6.8). Only very minimal green emission was observed, confirming BODIPY as an appropriate dye choice for CPNs.

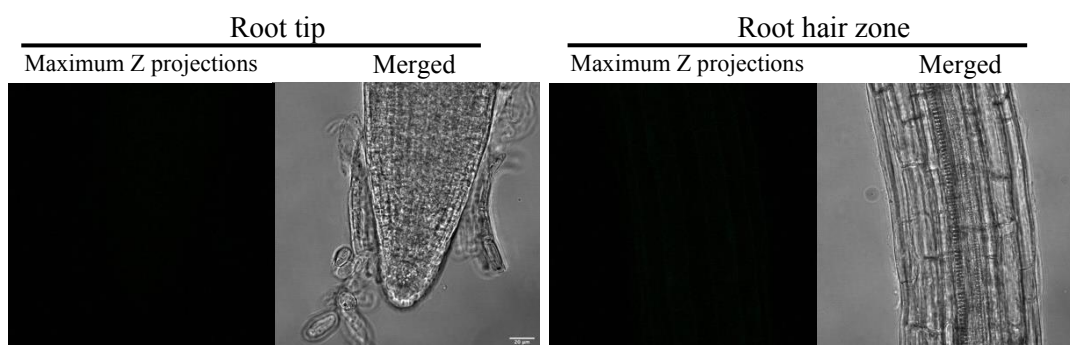


Figure 6.8. **No autofluorescence of plant compounds detected in untreated *A. thaliana* roots using BODIPY settings.** ImageJ software was used to generate maximum Z projections and brightfield superimposed images (denoted as Merged). Scale bar, 20 µm.

6.5.1 CPN surface charge effects on root penetrance and accumulation

In medical applications, several studies have shown charge-dependency on the cell uptake and cytotoxicity of nanoparticles in different cell types (Frohlich, 2012, Faisal et al., 2018, Choi and Frangioni, 2010, Mondini et al., 2015). It was considered essential that we evaluated each parameter for our novel CPNs.

The maximum Z projections revealed a significant accumulation of $N_1(20\text{ nm})$ inside the lateral root cap, columella, and epidermal cells (Figure 6.9a & 6.10a) corresponding to a successful penetration through plant cell walls. A moderate fluorescence emission was also observed along the xylem files (Figure 6.10b, inset) suggesting a possible particle uptake in the plant system. On the other hand, it was shown from the analysis that $\Theta(25\text{ nm})$ could penetrate the cell walls but were not taken up by the root system. At root tip, the accumulation of $\Theta(25\text{ nm})$ was reduced

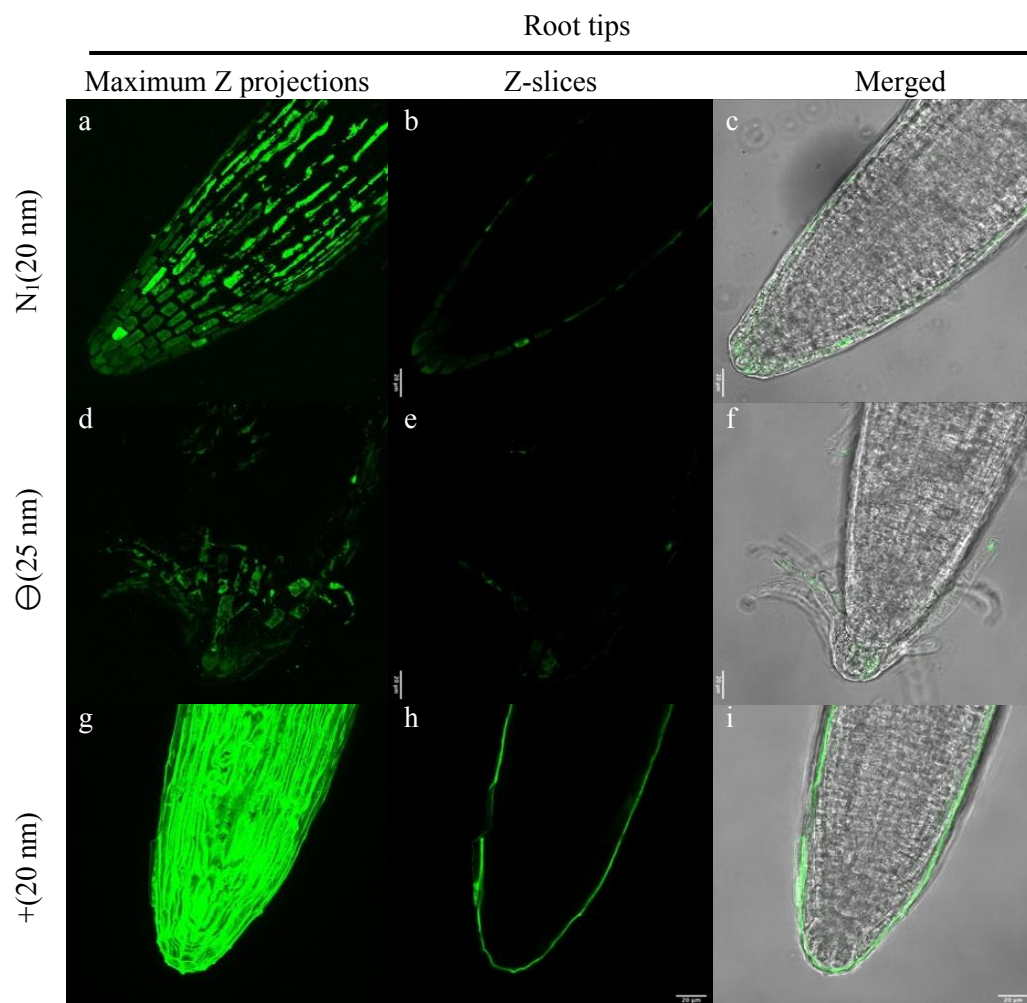


Figure 6.9. Surface charges of small CPNs significantly affected penetrance and accumulation in *A. thaliana* root tips. Penetrance and accumulation of (a-c) $N_1(20\text{ nm})$, (d-f) $\Theta(25\text{ nm})$, and (g-i) $+(20\text{ nm})$ were evaluated using a ZEISS 880 LSM. Maximum Z projections in 488 nm laser channel were analysed alongside the Z-slices and merged with brightfield images using ImageJ software. Scale bar, $20\text{ }\mu\text{m}$. The images are representatives of experimental replicates ($n=3$).

to mostly in shedding lateral root cap cells (Figure 6.9d) in contrast to a significant fluorescence detected in the epidermal cells along the root hair zone (Figure 6.10d). However, no fluorescence was detected along the xylem files in the vascular system of roots (Figure 6.10e) indicating no particle uptake. Meanwhile, an interesting behaviour was observed with roots treated with $+(20\text{ nm})$ (Figure 6.9g & 10g). Whilst no penetrance detected, there was a significant sheet-like accumulation around the surface of the whole root.

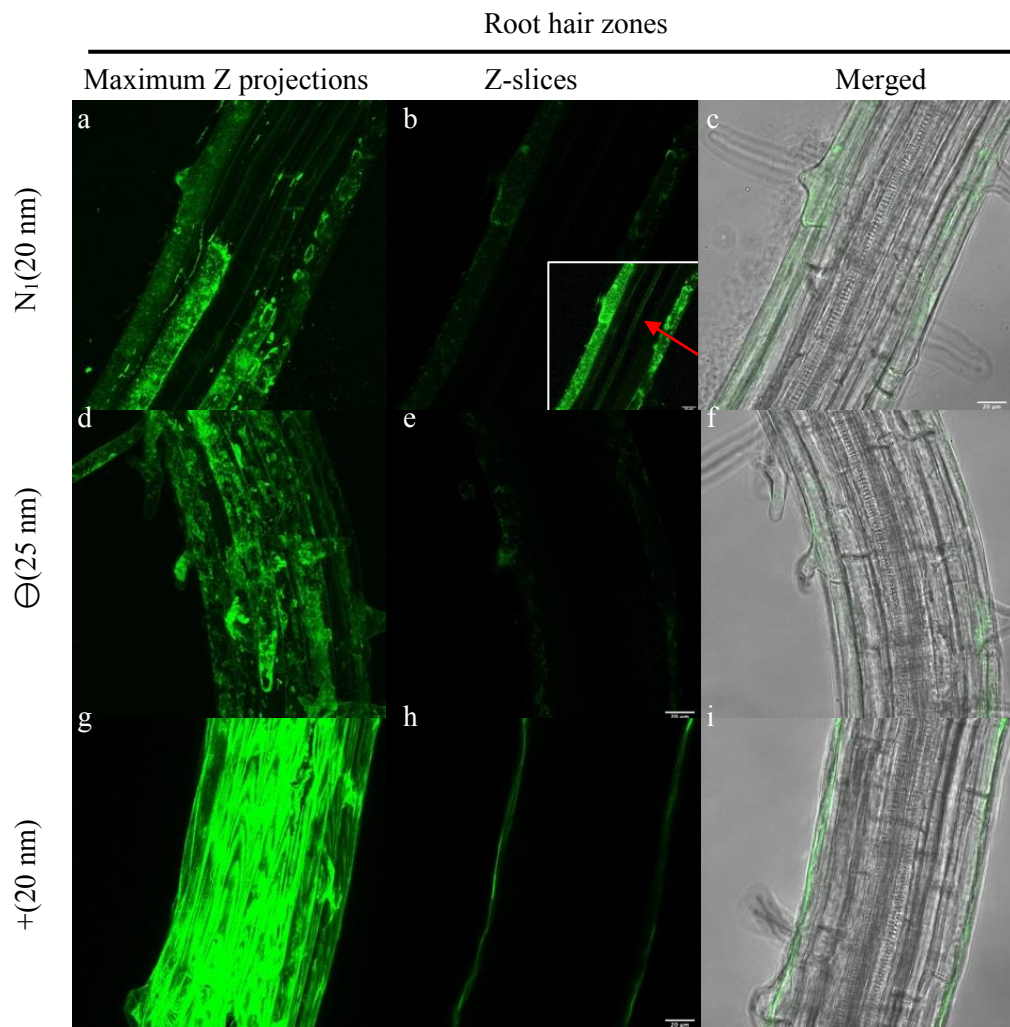


Figure 6.10. **Surface charges of small CPNs significantly affected penetrance and accumulation in *A. thaliana* root hair zones.** Penetrance and accumulation of (a-c) N₁(20 nm), (d-f) Θ(25 nm), and (g-i) +(20 nm) were evaluated under ZEISS 880 LSM. Maximum Z projections in 488 nm laser channel were analysed alongside the Z-slices and merged with brightfield images using ImageJ software. The image contrast was adjusted to enhance visualisation of N₁(20nm) uptake in xylem files (b, inset with red arrow). Scale bar, 20 μm. The images are representatives of experimental replicates (n=3).

To assess the level of cell penetration and root uptake of the CPNs, an orthogonal view of the Z-images was constructed using ImageJ software (Figure 6.11). Propidium iodide (PI) cell staining was used to achieve a higher resolution of cellular structures (Herrera-Ubaldo and de Folter, 2018).

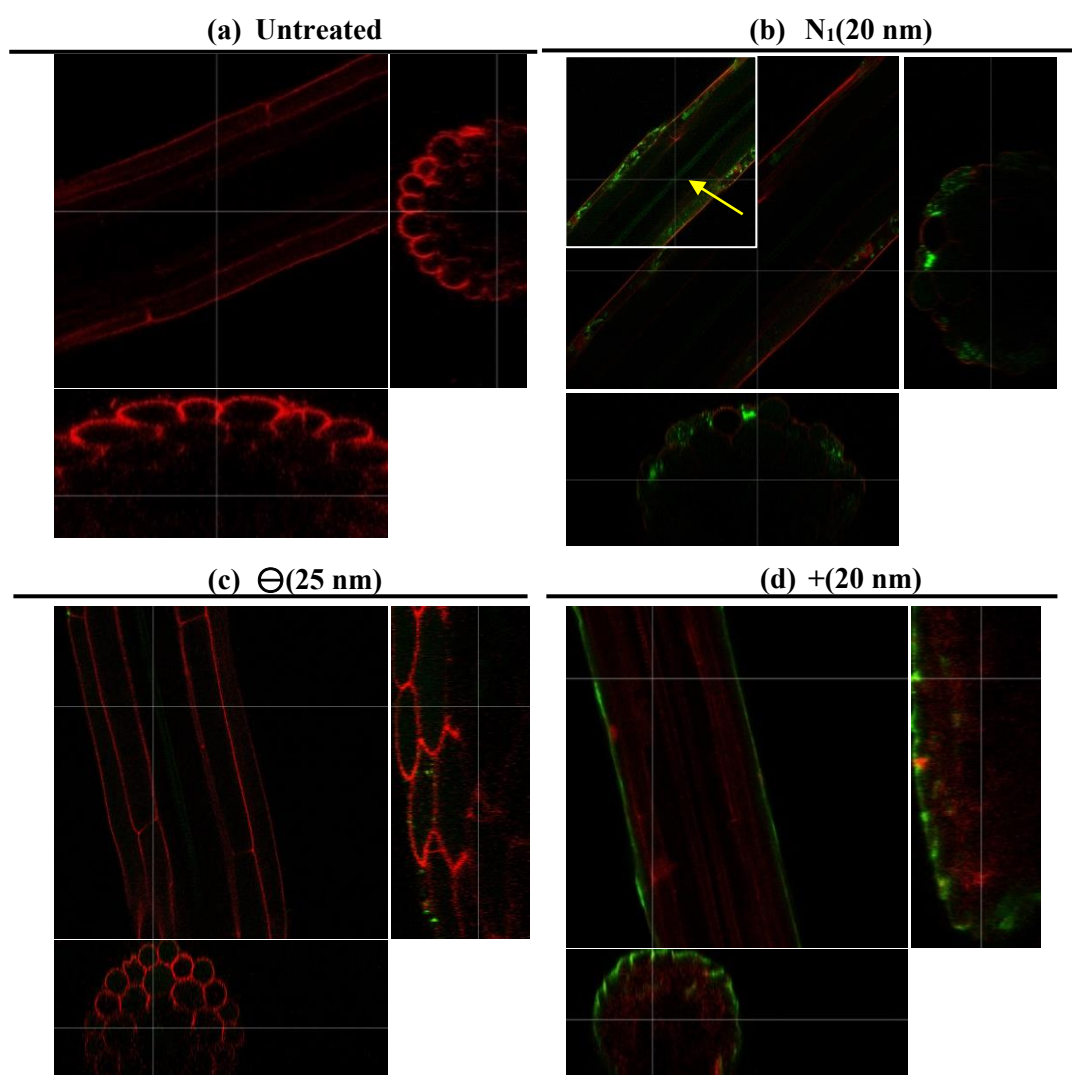


Figure 6.11. **Cross-section images of root hair zones revealed different level of the cell penetrance and uptake of small CPNs with different surface charges.** Propidium iodide staining was used to outline the cellular structure of the root hair zone (red). ImageJ software was used to generate the orthogonal views of the Z-stack images of root treated with (b) $N_1(20\text{ nm})$, (c) $\Theta(25\text{ nm})$, and (d) $+(20\text{ nm})$ in comparison to the untreated root (a). The image contrast was adjusted to enhance visualisation of $N_1(20\text{ nm})$ uptake in xylem files (b, inset with yellow arrow). The images are representatives of experimental replicates ($n=3$).

After an hour incubation with CPN samples, roots were stained with PI for 10 min prior to fluorescence evaluation. An additional fluorescence channel for PI

visualisation was used with 561 nm excitation laser and emission collected from 580 – 718 nm, corresponding to red PI emission. An untreated root was visualised as a reference showing a clear outline of cells in root hair zone with no background autofluorescence observed with the 561 nm laser (Figure 6.11a). The orthogonal view suggested possible uptake of $N_1(20\text{ nm})$ in root vascular system with green emission observed along the xylem files (Figure 6.11b, inset with yellow arrow). It was also observed penetrating the cell walls and significantly accumulating inside the epidermal cells (Figure 6.11b). Corresponding with the previous observations, a reduced accumulation $\ominus(25\text{ nm})$ was observed inside the epidermal cells (Figure 6.11c) and a sheet-like layer of $+(20\text{ nm})$ was detected covering the surface of the root hair zone (Figure 6.11d).

To conclude, there was a significant surface charge effect on the penetration and accumulation of CPN samples in *A. thaliana* roots with a neutral surface charge preferably taken up by the plant system but positively charge highly accumulated around the root surface.

6.5.2 CPNs size effect on root penetrance and accumulation

Cell penetration and uptake also have been reported to be highly influenced by the particle size (Faisal et al., 2018, Choi and Frangioni, 2010, Bhunia et al., 2013, Wisniewska et al., 2017, Shang et al., 2014, He et al., 2010). Therefore, neutral CPN samples with different hydrodynamic sizes were evaluated (Figure 6.12 & 6.13). In comparison to $N_1(20\text{ nm})$, there was a marked reduction in penetrance and accumulation as the CPN size increases. A moderate fluorescence corresponding to $N_1(32\text{ nm})$ and $N_1(71\text{ nm})$ was detected in shedding lateral root cap (Figure 6.12d & g) and epidermal layer (Figure 6.13d & g). Further, larger CPNs were not detected within the xylem files indicating unsuccessful uptake into the plant system (Figure 6.13).

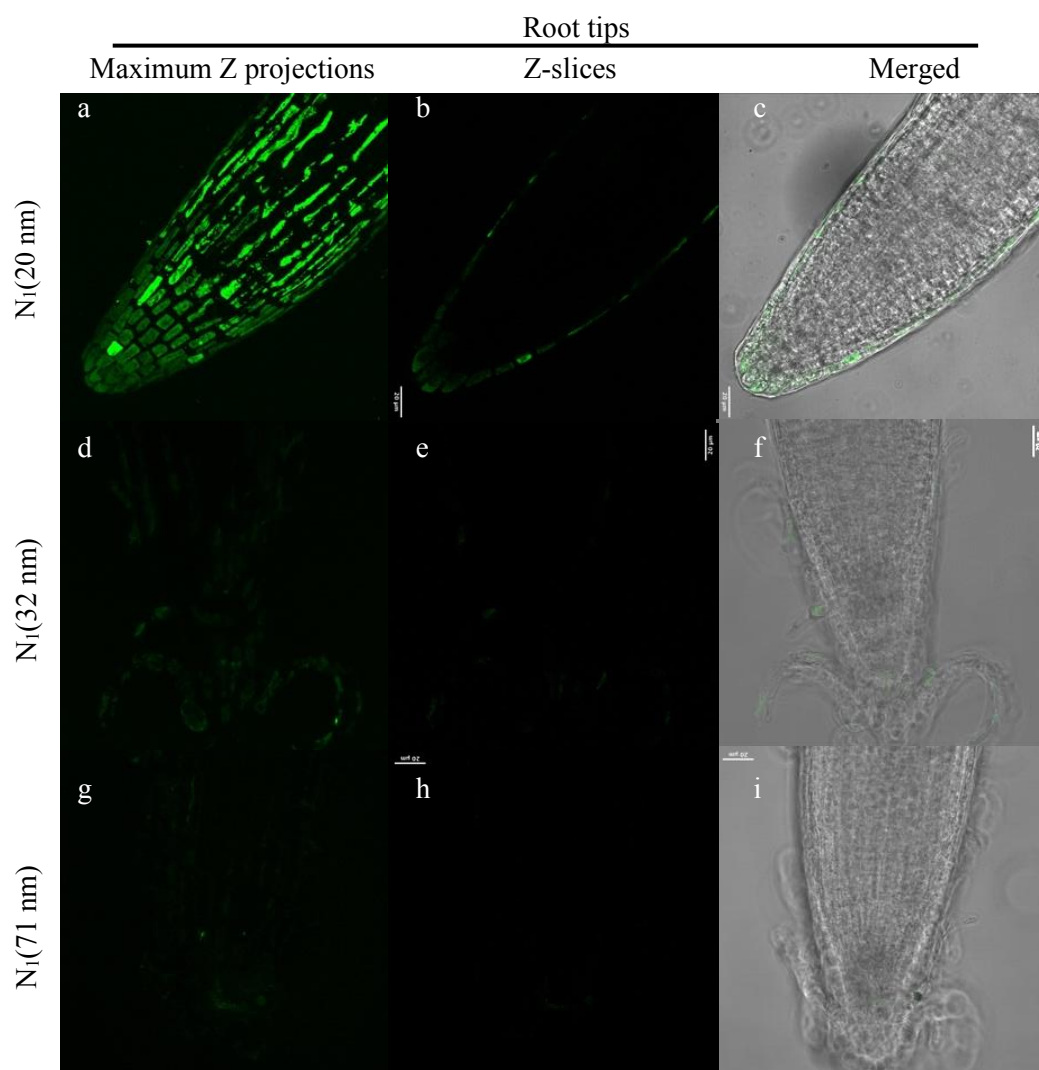


Figure 6.12. **Significant influence of CPN size on penetrance in *A. thaliana* root tips.** Penetrance and accumulation of (a-c) N₁(20 nm), (d-f) N₁(32 nm), and (g-i) N₁(71 nm) were evaluated under ZEISS 880 LSM. Maximum Z projections were analysed alongside the Z-slices and merged with brightfield images using ImageJ software. Scale bar, 20 μm. The images are representatives of experimental replicates (n=3). Same figure panels representing the penetration of N₁(20 nm) are reused from Figure 6.9 (a-c).

Negatively charged CPNs with different sizes were also evaluated to reveal a similar trend (Appendix B) with the penetration and accumulation inside the epidermal cells drastically decreased as the particle size increased. On the other hand, a sheet-like accumulation was observed around the surface of the whole root treated with all positively charged CPNs regardless of their sizes (Appendix C) consistent with the previous observation (Section 6.5.1).

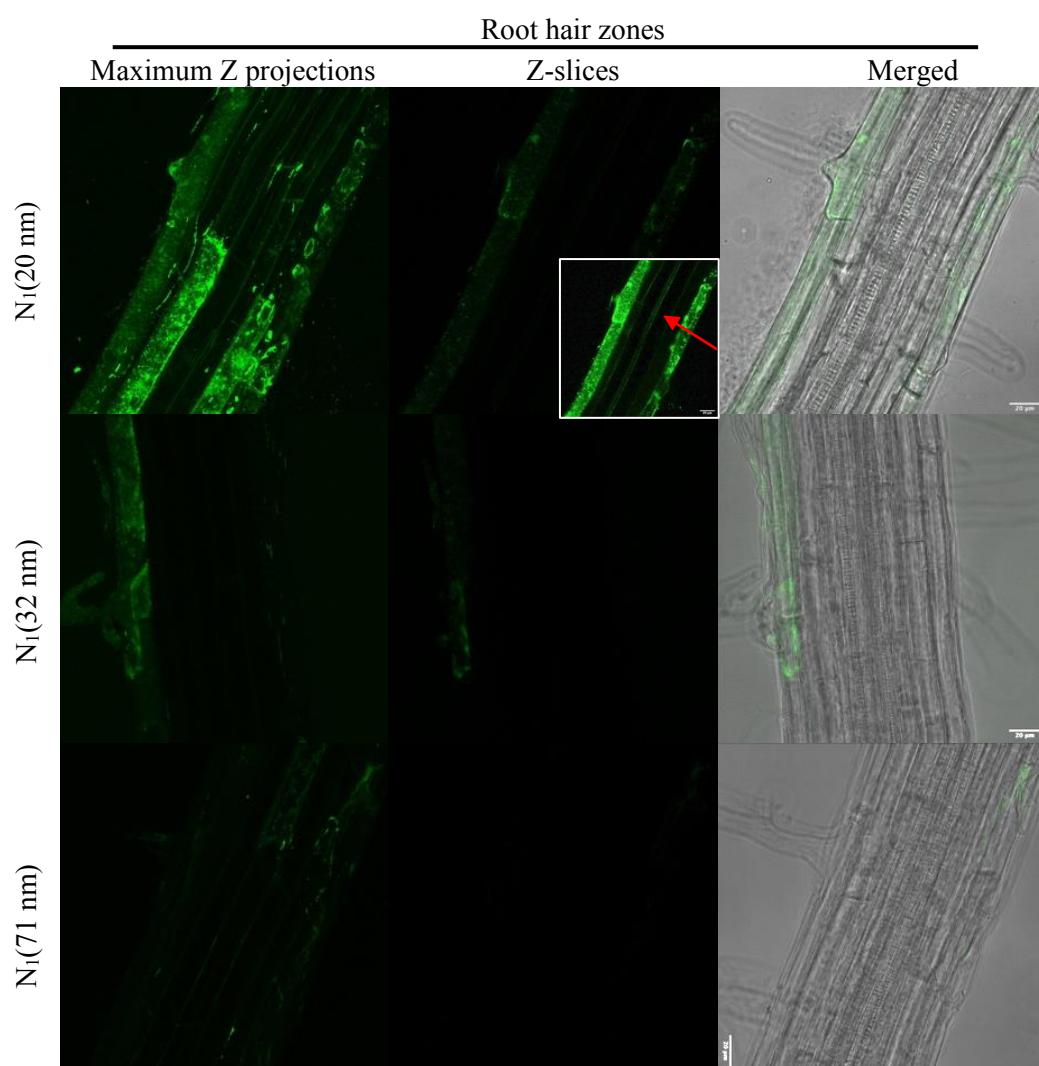


Figure 6.13. **CPN size significantly affected penetration in *A. thaliana* root hair zones.** Penetrance and accumulation of (a-c) $N_1(20 \text{ nm})$, (d-f) $N_1(32 \text{ nm})$, and (g-i) $N_1(71 \text{ nm})$ were evaluated under ZEISS 880 LSM. Maximum Z projections were analysed alongside the Z-slices and merged with brightfield images using ImageJ software. The image contrast was adjusted to enhance visualisation of $N_1(20\text{nm})$ uptake in xylem files (b, inset with red arrow). Scale bar, $20 \mu\text{m}$. The images are representatives of experimental replicates ($n=3$). Same figure panels representing the penetration of $N_1(20 \text{ nm})$ are reused from Figure 6.10 (a-c).

To conclude, particle sizes played a significant role in root penetration and accumulation with only small CPNs ($20 \text{ nm } \varnothing$) demonstrated total root uptake.

6.5.3 CPNs polymer chemistry effect on root penetrance and accumulation

Polymer chemistry of nanoparticles has shown significant effect in cell interaction and accumulation (Smith et al., 2004, Ou et al., 2018, Koo et al., 2015, Bhunia et al., 2013, Avellan et al., 2017). Therefore, small neutral CPNs (20 nm \varnothing) with different polymer compositions were investigated for cell penetration and root uptake (Figure 6.14 & 6.15). In comparison to N₁(20 nm), the accumulation of N₂(19 nm) was only observed in the shedding lateral root cap (Figure 6.14d) and epidermal cells in the root hair zone (Figure 6.15d). No fluorescence was detected along the xylem files suggesting no particle uptake by the vascular system (Figure 6.15e).

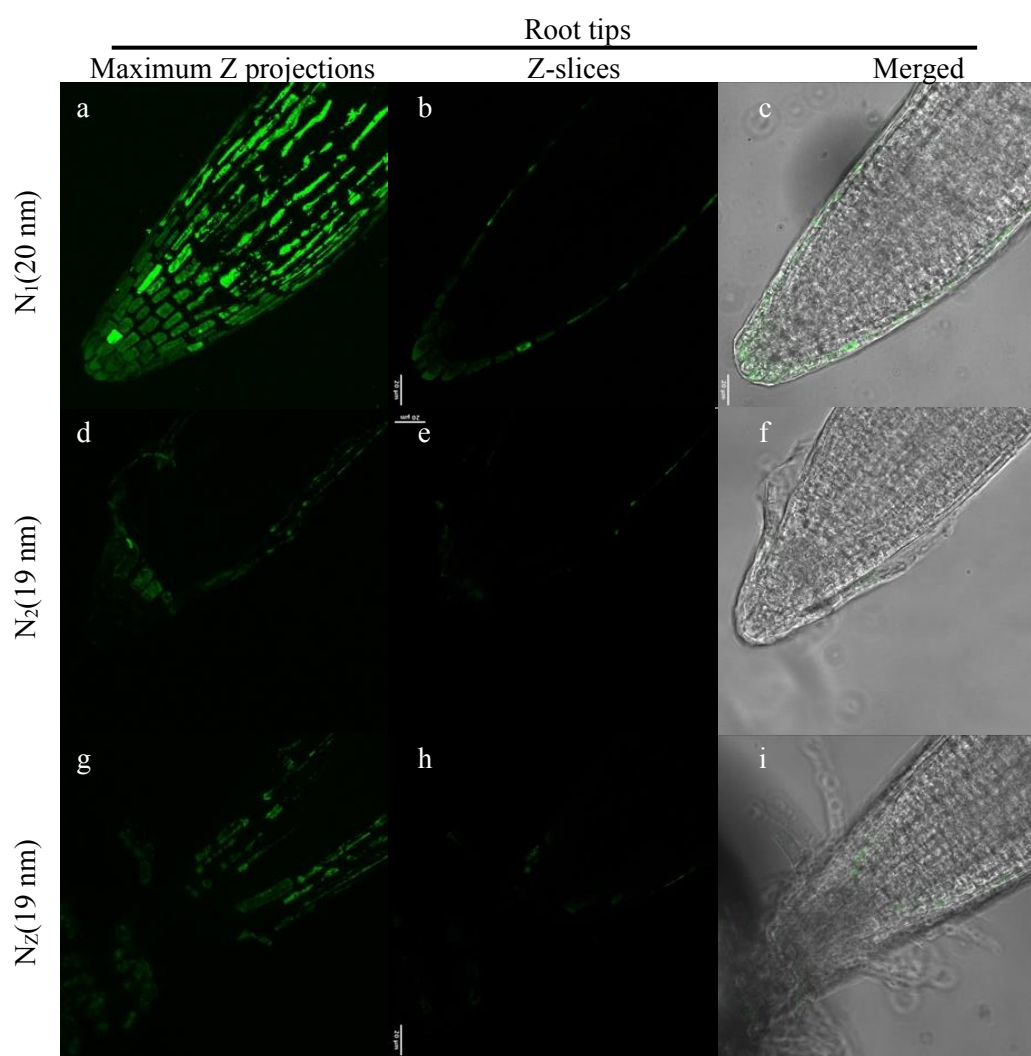


Figure 6.14. **Polymer compositions of neutral CPNs demonstrated an effect on penetration in different root tip cell types.** Penetrance and accumulation of (a-c) N₁(20 nm), (d-f) N₂(19 nm), and (g-i) N_z(19 nm) were evaluated. Maximum Z projections were analysed alongside Z-slices and merged with brightfield images using ImageJ software. The images are representatives of experimental replicates (n=3). Same figure panels representing the penetration of N₁(20 nm) are reused from Figure 6.9 (a-c).

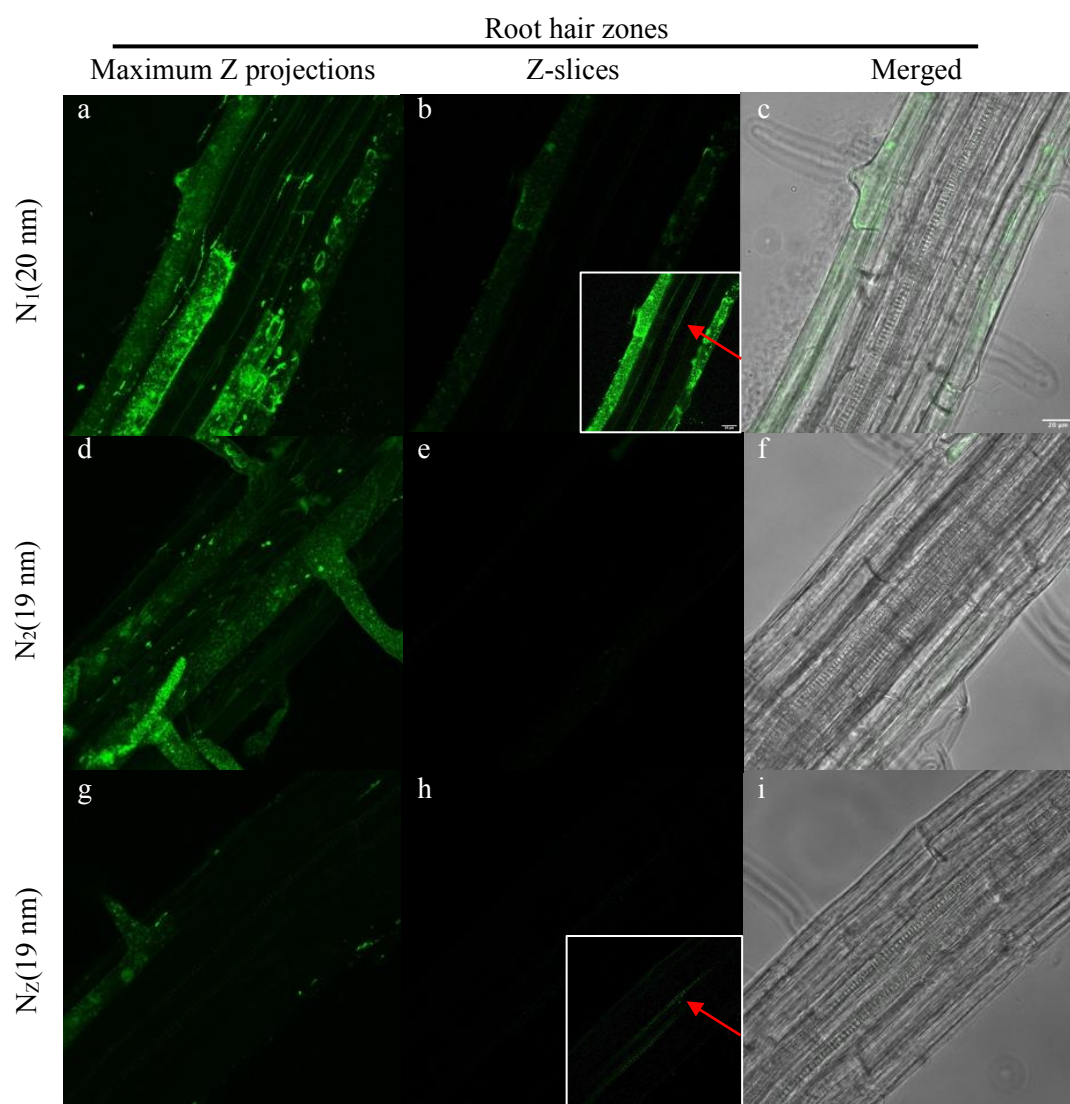


Figure 6.15. **Polymer compositions of neutral CPNs revealed a cell-specific accumulation and penetrance in root hair zones.** Penetrance and accumulation of (a-c) $N_1(20\text{ nm})$, (d-f) $N_2(19\text{ nm})$, and (g-i) $N_Z(19\text{ nm})$ were evaluated. Maximum Z projections were analysed alongside Z-slices and merged with brightfield images using ImageJ software. Scale bar, $20\text{ }\mu\text{m}$. The image contrast was adjusted to enhance uptake visualisation in xylem files (b and h, inset with red arrows). The images are representatives of experimental replicates ($n=3$). Same figure panels representing the penetration of $N_1(20\text{ nm})$ are reused from Figure 6.10 (a-c).

However, a moderate accumulation of $N_Z(19\text{ nm})$ was observed in shedding lateral root cap and early epidermal cells (Figure 6.14g). While there was a minimal uptake in the epidermal cells along the root hair zone (Figure 6.15g), some fluorescence was observed along the xylem files (Figure 6.15h, inset red arrow).

To compare the level of penetrance and uptake of $N_z(19\text{ nm})$ to that of $N_1(20\text{ nm})$, an orthogonal view of the Z-images was constructed using ImageJ software (Figure 6.16). The fluorescence corresponding to $N_1(20\text{ nm})$ was observed both accumulating inside the epidermal cells and possibly along xylem files (Figure 6.16a, inset).

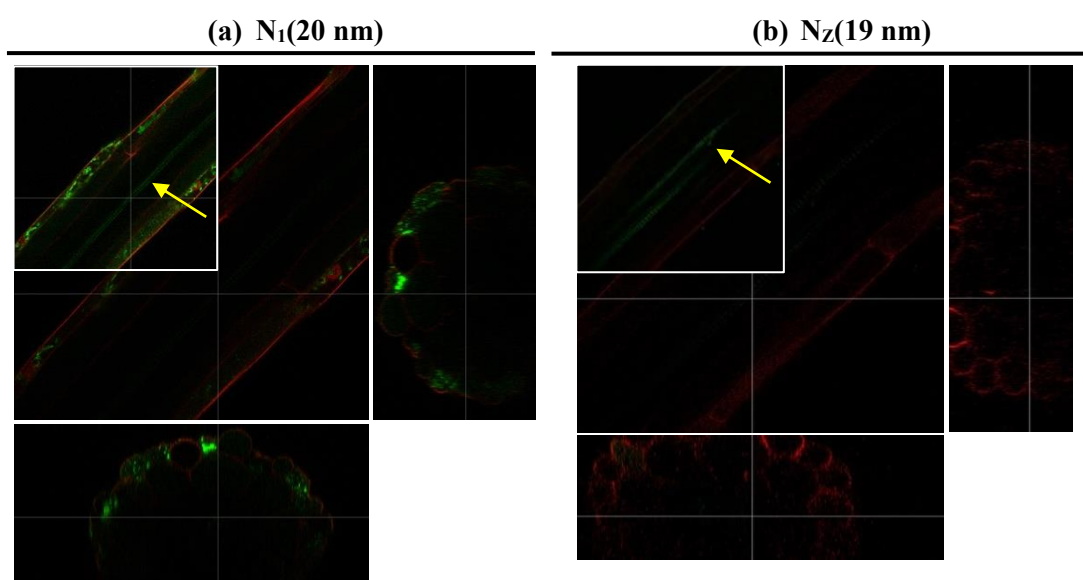


Figure 6.16. **Cross-section images of root hair zones revealed a cell-specific penetrance and uptake of $N_1(20\text{ nm})$ and $N_z(19\text{ nm})$.** Propidium iodide staining was used to outline the cellular structure of the root hair zone (red). The orthogonal views of the Z-stack images of root treated with (b) $N_z(19\text{ nm})$ was generated by ImageJ software and compared to those of (a) $N_1(20\text{ nm})$. The image contrast was adjusted to enhance visualisation of CPNs uptake in xylem files (insets with yellow arrows). The images are representatives of experimental replicates ($n=3$). Same figure representing the penetration of $N_1(20\text{ nm})$ is reused from Figure 6.11b.

To conclude, the polymer chemistry of CPNs was proven influence the cell-specificity of the penetration and uptake level in root system. $N_1(20\text{ nm})$ still demonstrated the highest level of cell accumulation and uptake level while $N_z(19\text{ nm})$ showed a degree of root uptake with no cell accumulation. Therefore, $N_1(20\text{ nm})$ was chosen for further evaluation.

6.5.4 Aptamer conjugated CPNs on root penetrance and accumulation

To assess the delivery of aptamer-based biosensor in the root system, *A. thaliana* roots were incubated in $N_1(\text{ATPapt})$ and $+(\text{ATPapt})$ suspensions for one hour before fluorescence visualisation by laser scanning microscopy to generate Z-stack images of root tips and root hair zones for cell penetration and root uptake evaluation (Figure 6.17 & 6.18). In addition to the green BODIPY emission, an additional fluorescence channel was used to visualise Cy3 dye conjugated on ATPapt using 561

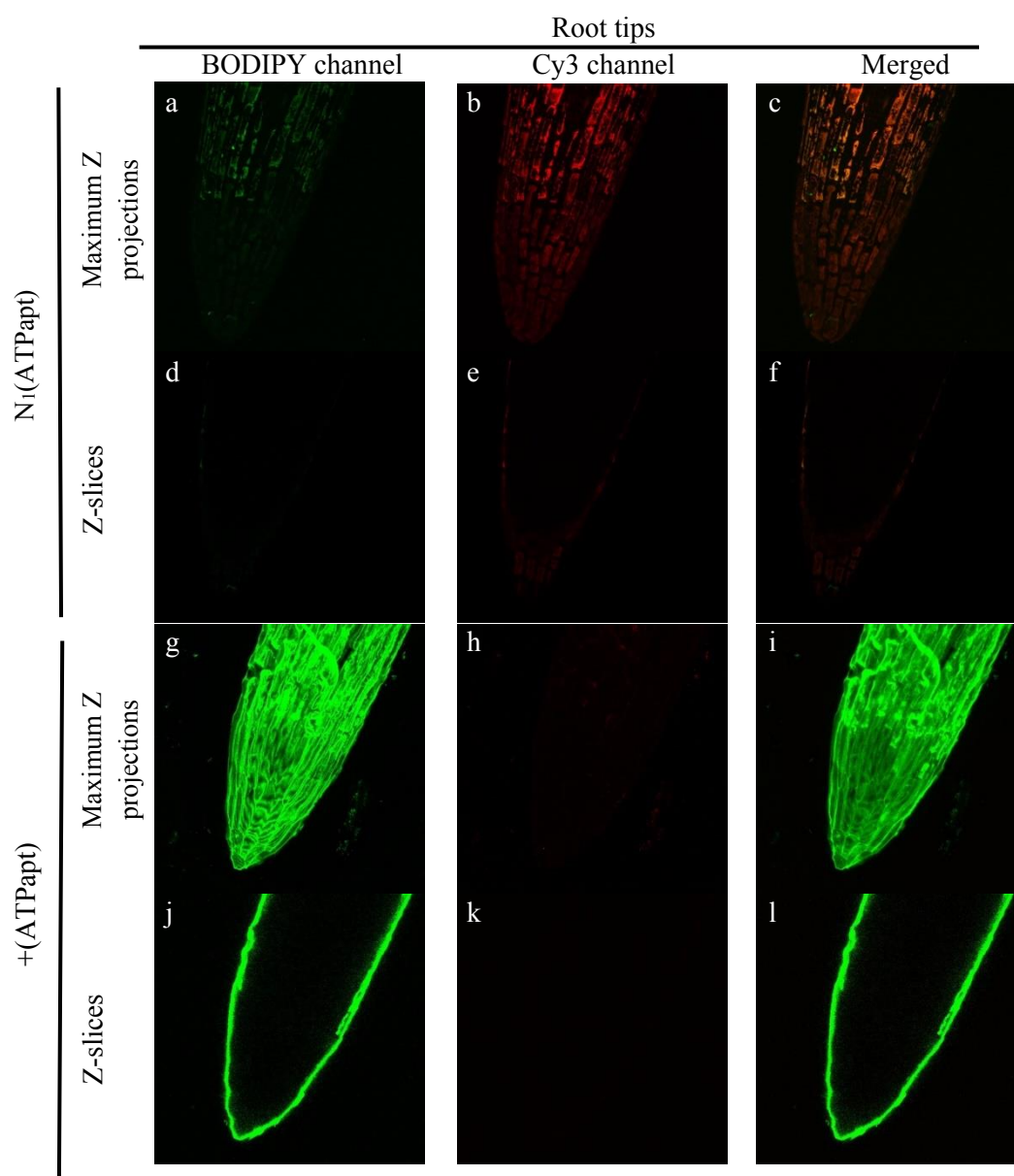


Figure 6.17. **Aptamer conjugated CPNs demonstrated similar uptake and penetrance behaviours as their core CPNs in root tips.** Penetrance and accumulation of (a-f) $N_1(\text{ATPapt})$ and (g-l) $+(\text{ATPapt})$ were evaluated under ZEISS 880 LSM. Maximum Z projections at both channels were analysed alongside the Z-slices using ImageJ software.

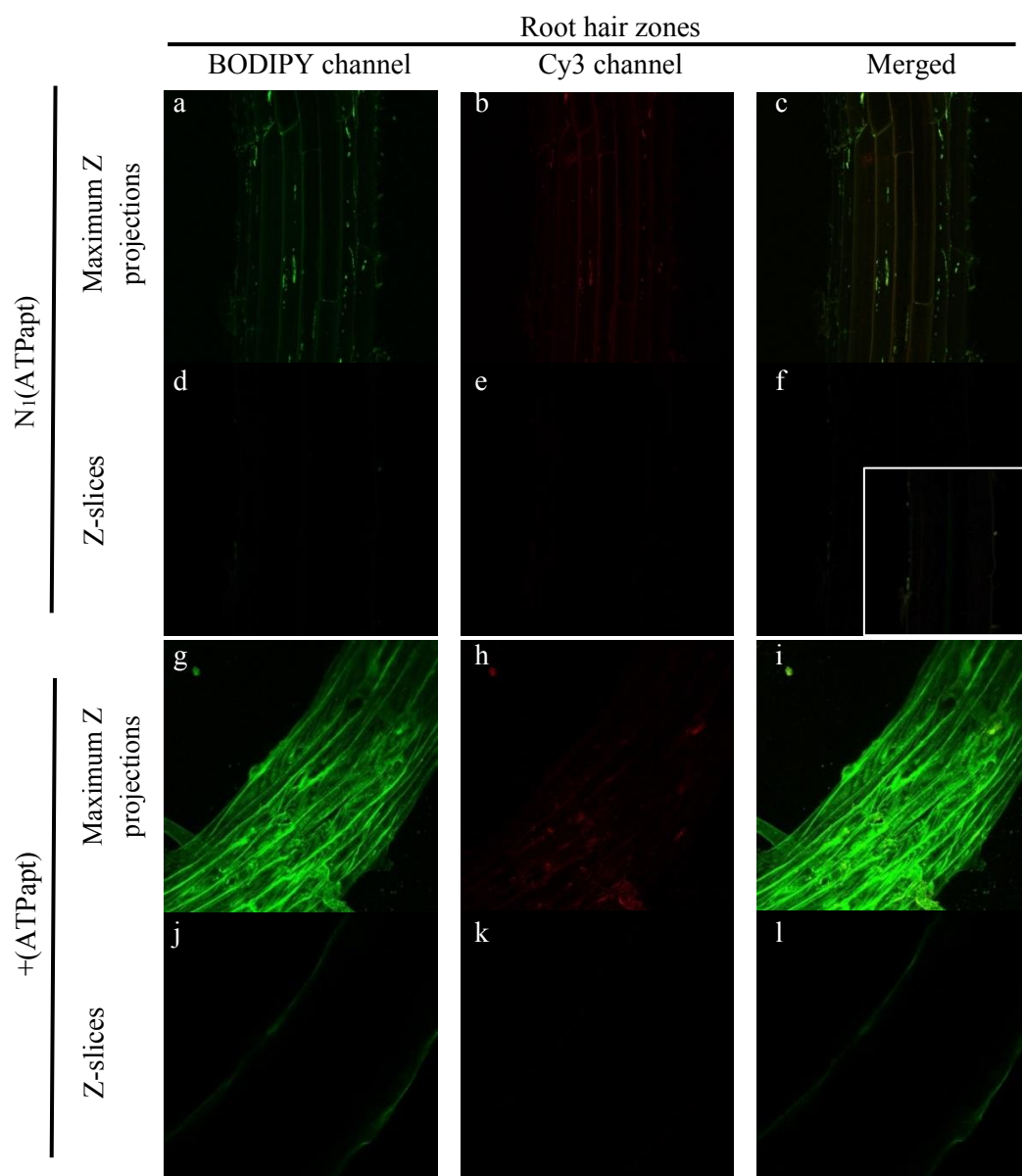


Figure 6.18. **Aptamer conjugated CPNs demonstrated similar uptake and penetrance behaviours as their core CPNs in root hair zones.** Penetrance and accumulation of (a-f) N₁(ATPapt) and (g-l) +(ATPapt) were evaluated under ZEISS 880 LSM. Maximum Z projections at both channels were analysed alongside the Z-slices using ImageJ software. The image contrast was adjusted to enhance visualisation of N₁(ATPapt) uptake in xylem files (f, inset).

nm laser and emission collected from 580 – 718 nm, corresponding to red Cy3 emission.

Upon evaluation of maximum Z-projections and Z-slice images, the penetrance and uptake level of aptamer conjugated CPNs reflected the behaviours of their core CPNs (Figure 6.17 & 6.18). In BODIPY channel, N₁(ATPapt) was analysed to show a moderate accumulation in the lateral root cap cells (Figure 6.17a) and the

epidermal cells along the root hair zones (Figure 6.18a) corresponding to the penetration of N₁(20 nm) (Figure 6.9a & 6.10a). Some green fluorescence emission was also detected along the xylem files indicating a successful uptake of N₁(ATPapt) into the vascular system (Figure 6.18f, inset). Moreover, fluorescence in Cy3 channel suggested that Cy3 is present in the lateral root cap cells (Figure 6.17b) and the epidermal cells in root hair zones (Figure 6.18b). This could indicate the penetrance of the intact 5'-Cy3-ATPapt within the cells and the successful delivery of aptamer-based biosensor past epidermal cell wall. However, the Z-slice image of the xylem files revealed only green BODIPY emission in absence of Cy3 emission (Figure 6.18f, inset). This suggested that, whilst the neutral particles could enter the plant vascular system, the particles along the xylem files were either unconjugated N₁(20 nm) or ones with degraded ATPapt.

A green fluorescence emission corresponding to +(ATPapt) was observed as a sheet-like accumulation surrounding the surface of the whole root (Figure 6.17g & 6.18g) resembling the sheet-like accumulation of +(20 nm) (Figure 6.9g & 6.10g). However, a minimal Cy3 fluorescence was detected at the root tip (Figure 6.17h) suggested low level of Cy3-ATPapt present.

N₁(ATPapt) was further evaluated for potential fluorescence energy transfer from BODIPY to Cy3 corresponding to the FRET properties (Figure 6.19). FRET was evaluated using fluorescence laser scanning microscopy with only 488 nm laser for excitation and collecting emission from 493 – 577 nm (BODIPY channel) and 580 – 718 nm (Cy3 channel). Theoretically, any red Cy3 fluorescence observed would result from a fluorescence energy transfer through the fluorescence spectra overlap of BODIPY and Cy3 confirming FRET properties of N₁(ATPapt) (Ishikawa-Ankerhold et al., 2012).

No fluorescence was detected in the Cy3 channel when evaluating the accumulated N₁(ATPapt) in root tip (Figure 6.19b) and root hair zone Figure 6.19e). This suggested that there was no significant fluorescence energy transfer from the BODIPY at the N₁(20 nm) core to the Cy3 at the 3'-end of the ATPapt.

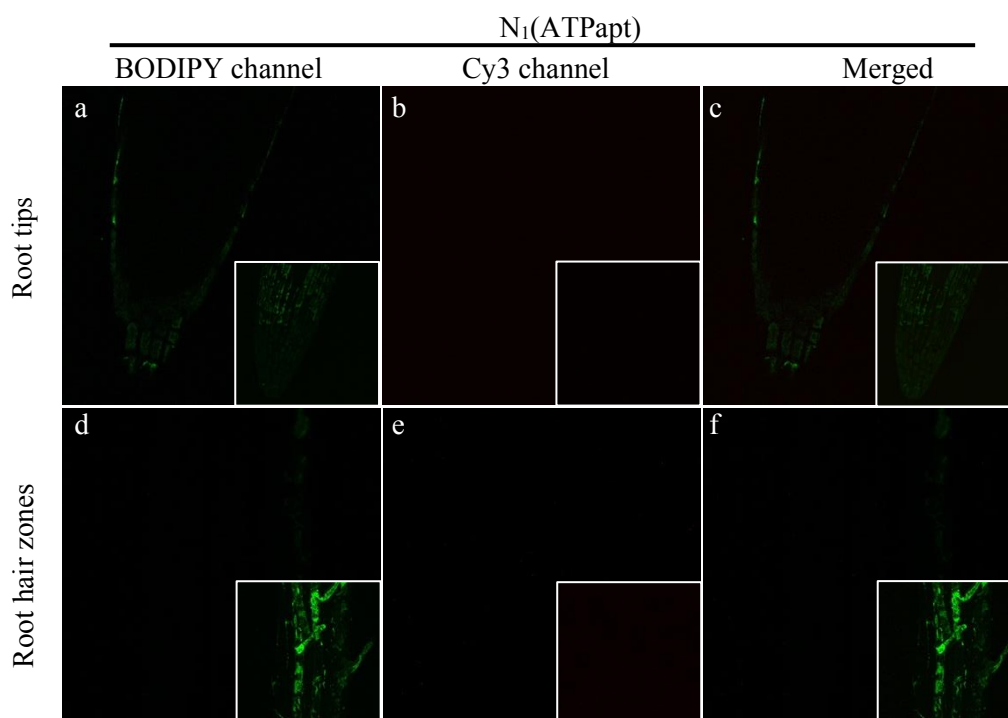


Figure 6.19. **N₁(ATPapt) did not demonstrate FRET.** The accumulated N₁(ATPapt) in (a-c) root tips and (d-f) root hair zones was evaluated for FRET properties under ZEISS 880 LSM. The Z-slice images were analysed alongside the maximum Z projections (insets) at both channels using ImageJ software. No fluorescence was detected in Cy3 channel suggested that there was no energy transferred from BODIPY to Cy3.

All in all, aptamer conjugated CPNs, N₁(ATPapt) and +(ATPapt), demonstrated a similar cellular penetrance and root uptake pattern to the corresponding CPNs. In current experimental setup, N₁(20 nm) successfully penetrated the epidermal cells but did not demonstrate FRET properties to be useful for ligand binding measurement. Further characterisation and optimisation of N₁(20 nm) could improve the application of aptamer-based biosensor in plants.

6.6 CPN time dependent evaluation in intact roots of *A. thaliana*

The penetration and accumulation of nanoparticles in different cell types has been shown to greatly depend on the incubation time (Koo et al., 2015, Avellan et al., 2017). Therefore, five-days old *A. thaliana* seedling roots were incubated in CPN suspensions at room temperature for various times and fluorescence evaluation was performed as previously described (Section 6.5.1). ImageJ software was used to create the corresponding maximum Z projections and to enhance the contrast of Z-slice images for optimal visualisation of green BODIPY emission. Brightfield images was

superimposed on the Z-slice images with focal planes along the xylem files for structural references (denoted as merged).

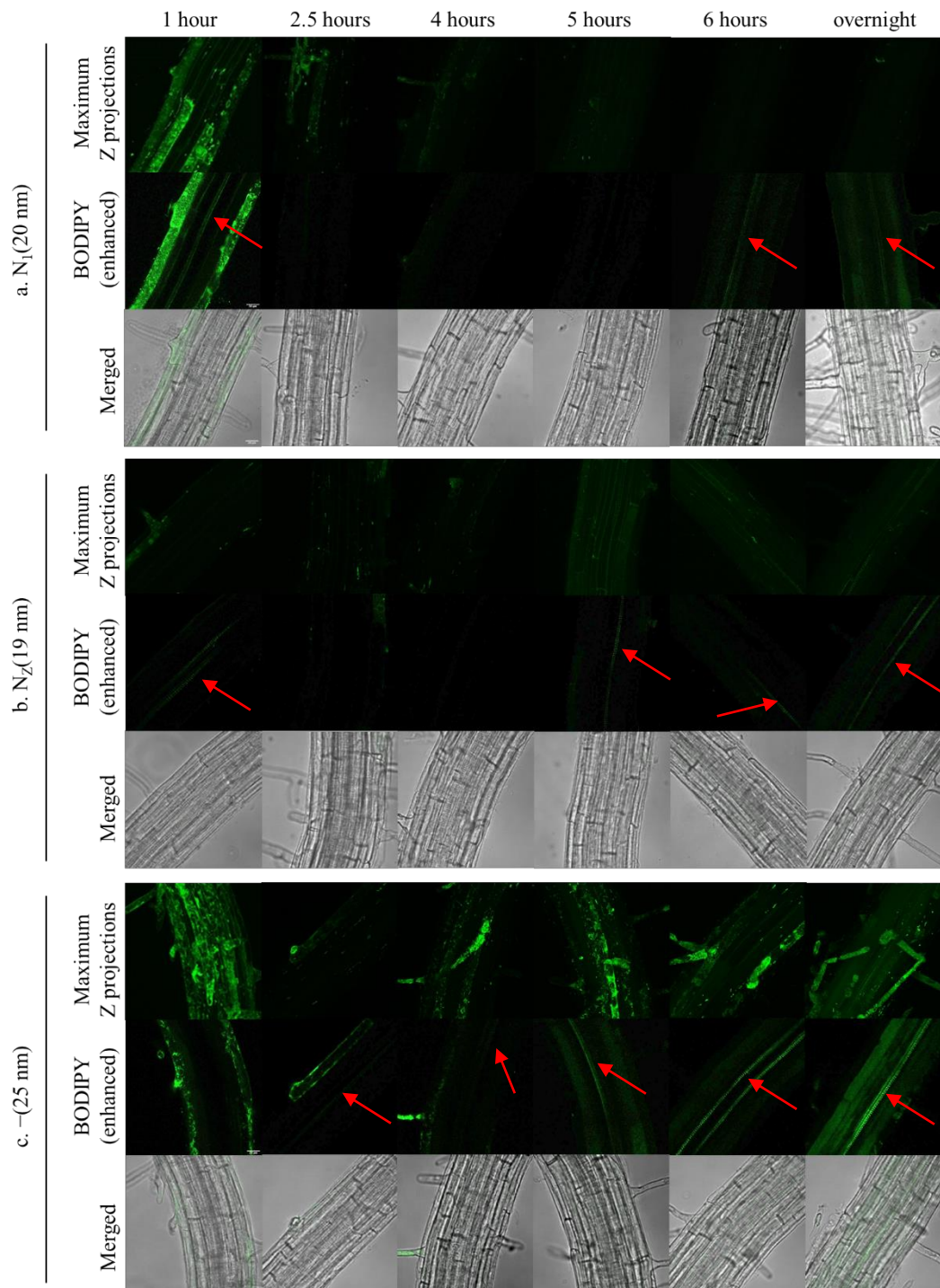


Figure 6.20. **Cell penetrance and root uptake of $\ominus(25\text{ nm})$ was time dependent in contrast to the accumulation of $N_1(20\text{ nm})$ and $N_z(19\text{ nm})$.** Penetrance and accumulation of (a) $N_1(20\text{ nm})$, (b) $N_z(19\text{ nm})$, and (c) $\ominus(25\text{ nm})$ were evaluated under ZEISS 880 LSM. Maximum Z projections were analysed. The contrast of Z-slice images was adjusted to enhance visualisation of green BODIPY emission along the xylem files (red arrows).

The time dependent experiment was initially performed with the smallest CPNs (20 nm \varnothing) at time point ranging from one hour to overnight (Figure 6.20). The cell penetration and root uptake of all CPNs except \ominus (25 nm) were independent of the incubation time. The fluorescence intensity corresponding to N_1 (20 nm) and N_z (19 nm) did not significantly change over time suggesting the accumulation saturated at an hour incubation. The CPNs diffused to all layers but no specific accumulation was observed in any cell type. Additionally, a saturated sheet-like accumulation of $+$ (20 nm) around the roots was also observed at all time points (Appendix D). However, a significant increase in accumulation of \ominus (25 nm) was observed along the epidermal cells over time (Figure 6.20c). Green fluorescence emission was also detected along the xylem files from 2.5 hours incubation onwards.

N_1 (ATPapt) was also evaluated for time-dependent accumulation in root hair zones (Figure 6.21). Analysis of the maximum Z projections showed slight increase in the CPN accumulation inside the epidermal cell along the root hair zones. The enhanced Z-slice images also revealed both green and red fluorescence along the xylem files from 5 hours incubation onwards. This suggested successful uptake of N_1 (ATPapt) with intact Cy3-ATPapt into the vascular system over time.

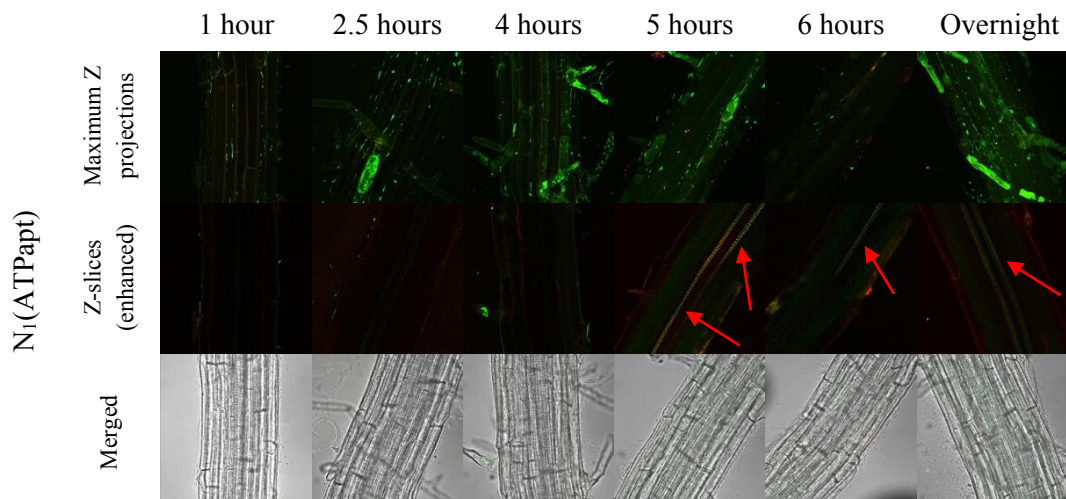


Figure 6.21. **N_1 (ATPapt) revealed time-independent accumulation in root hair zones.** Penetrance and accumulation of N_1 (ATPapt) was evaluated under ZEISS 880 LSM. Maximum Z projections were analysed. The contrast of Z-slice images was adjusted to enhance visualisation of green BODIPY and red Cy3 emission along the xylem files (red arrows).

The cell accumulation and root uptake of Θ (25 nm) and N_1 (ATPapt) significantly enhanced over time. Meanwhile, the smallest neutral CPNs, N_1 (20 nm) and N_Z (19 nm), did not demonstrate a time-dependent accumulation.

6.7 CPN evaluation in isolated protoplasts from *A. thaliana*

In addition to penetrance and uptake evaluation in intact roots, the CPN samples were also evaluated for the cell uptake and cytotoxicity in protoplasts isolated from five-days old *A. thaliana* roots (Section 2.13.2). Each CPN sample (0.1 mg/mL final concentration) was added to isolated protoplast solution and incubated for one

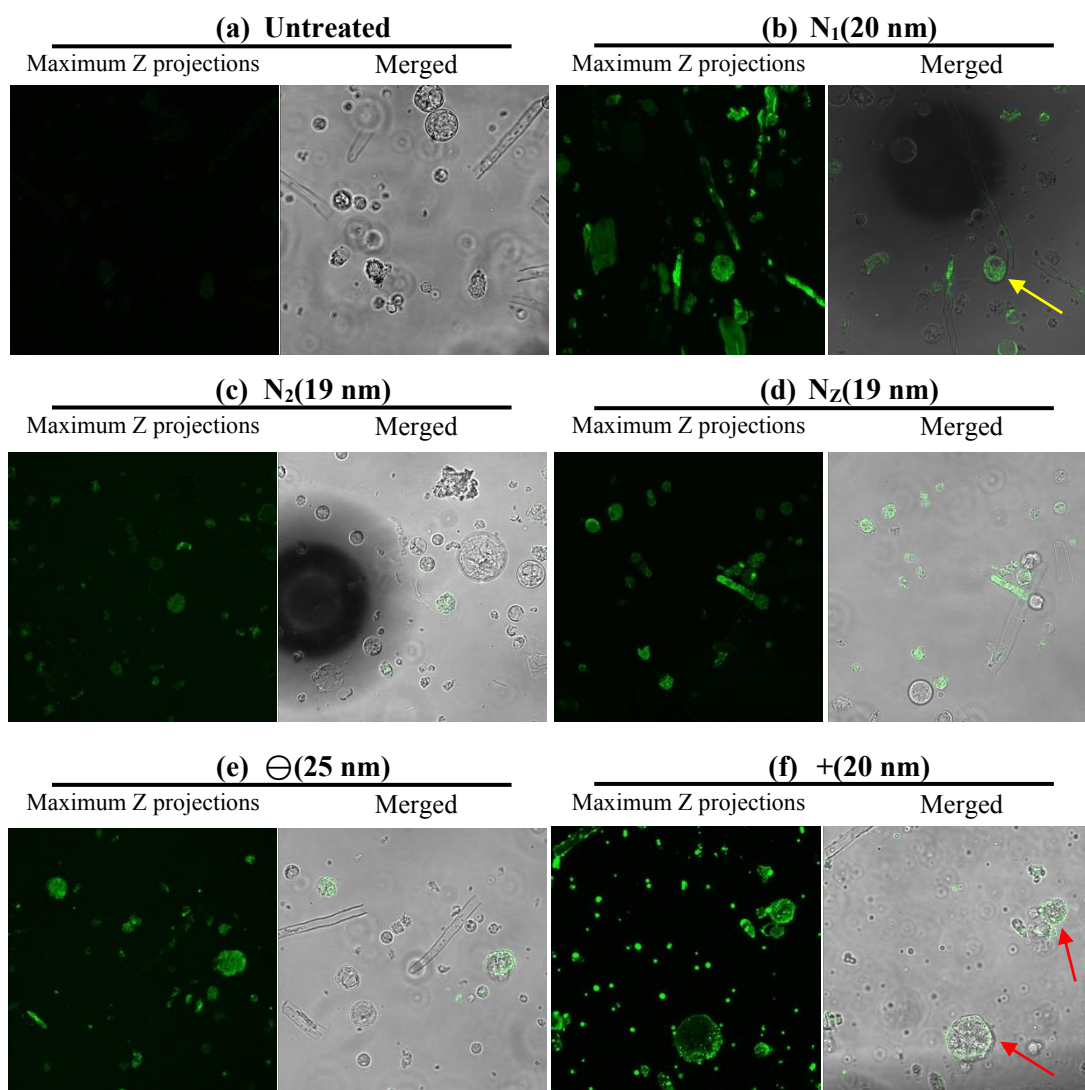


Figure 6.22. Surface charges of small CPN samples (20 nm Ø) influenced accumulation and toxicity in protoplasts. ImageJ software was used to generate maximum Z projections for enhanced visualisation and brightfield superimposed images for cellular references. The images are representatives of experimental replicates (n=3).

hour before fluorescence laser scanning microscopy evaluation as previously described (Section 6.5). ZEN software was used to generate Z-stack images of the protoplasts before using ImageJ software to create corresponding maximum Z-projections for optimal visualisation. Brightfield images were superimposed for cellular references (denoted as merged). An untreated protoplast solution was visualised under the same settings as a negative control to check for background autofluorescence (Figure 6.22a). Minimal green fluorescence emission was observed in untreated protoplasts confirming no interfering background autofluorescence at the settings used.

The small CPNs (20 nm \varnothing) with different polymer chemistries and surface charges were evaluated for effects on protoplasts penetrance and accumulation (Figure 6.22). At a glance, green fluorescence emission was observed in all cell debris regardless of the surface charge of CPNs suggesting a non-specific interaction of particles to cell components. Interestingly, only N₁(20 nm) demonstrated a successful penetration inside the healthy (round and spherical) protoplasts (Figure 6.22b, yellow arrow). No fluorescence emission was observed inside the healthy protoplasts treated with N₂(19 nm) or N_z(19 nm). Meanwhile, charged CPNs did not demonstrate any penetration through the plasma membrane of healthy protoplasts. Analysis of protoplast incubated with \ominus (25 nm) showed a reduced interaction with cell debris (Figure 6.22e) while +(20 nm) posed cytotoxic effect with more visible cell debris and rough, asymmetrical cells (Figure 6.22f, red arrows).

Further, different sizes of neutral CPNs were investigated for effects on cell penetration (Figure 6.23). A moderate green BOIDPY emission corresponding to $N_1(32\text{ nm})$ was observed in all cell types while the analysis of protoplast incubated with $N_1(71\text{ nm})$ showed no penetrance inside the protoplasts with a significant decrease in debris accumulation (Figure 6.23). This suggested a significant size effect on cell components interactions with only smaller CPNs (20 – 30 nm) readily passing through the plasma membrane.

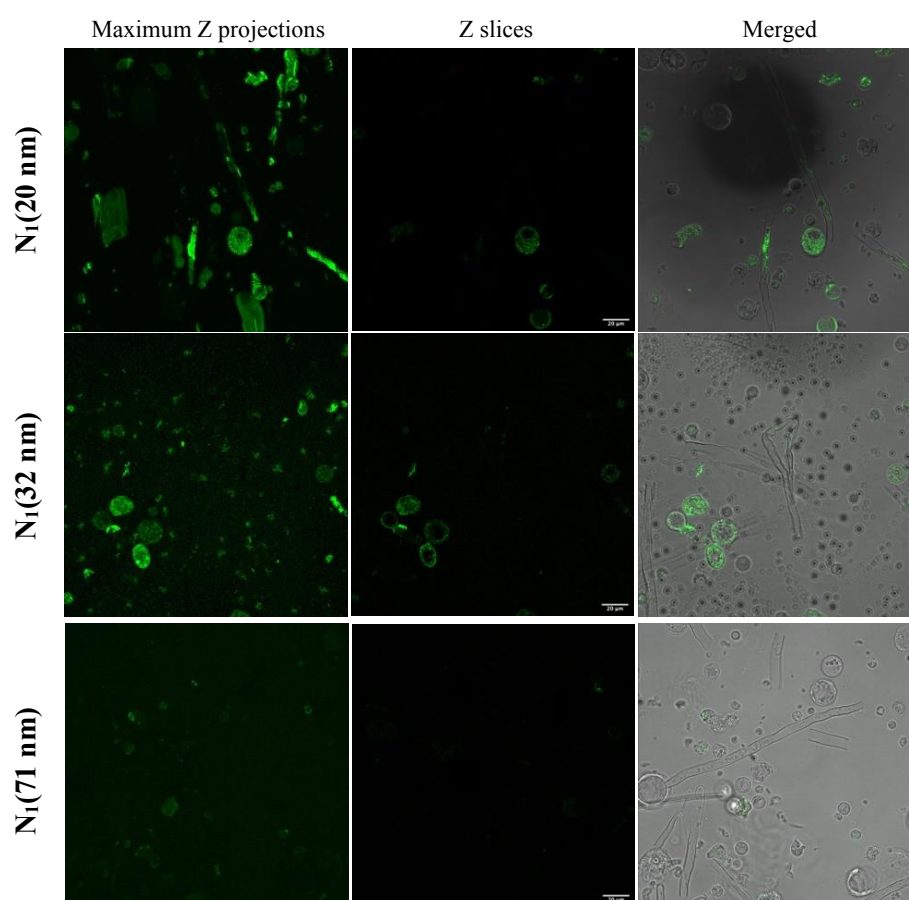


Figure 6.23. **Sizes of neutral CPNs influenced penetrance in protoplasts and accumulation in cell debris.** ImageJ software was used to generate maximum Z projections, Z slice images and their brightfield superimposed images for penetration evaluation. The images are representatives of experimental replicates (n=3). Same figure panels representing the cell penetration of $N_1(20\text{ nm})$ are reused from Figure 6.22b.

With $+(20\text{ nm})$ analysis showed a degree of toxicity towards protoplasts, different sizes of positively charged CPNs were evaluated for the size effect on cytotoxicity (Figure 6.24). There was no increase in cell debris or unhealthy

protoplasts visible in the solutions treated in bigger CPNs. This suggested no size effect on the cytotoxicity level observed.

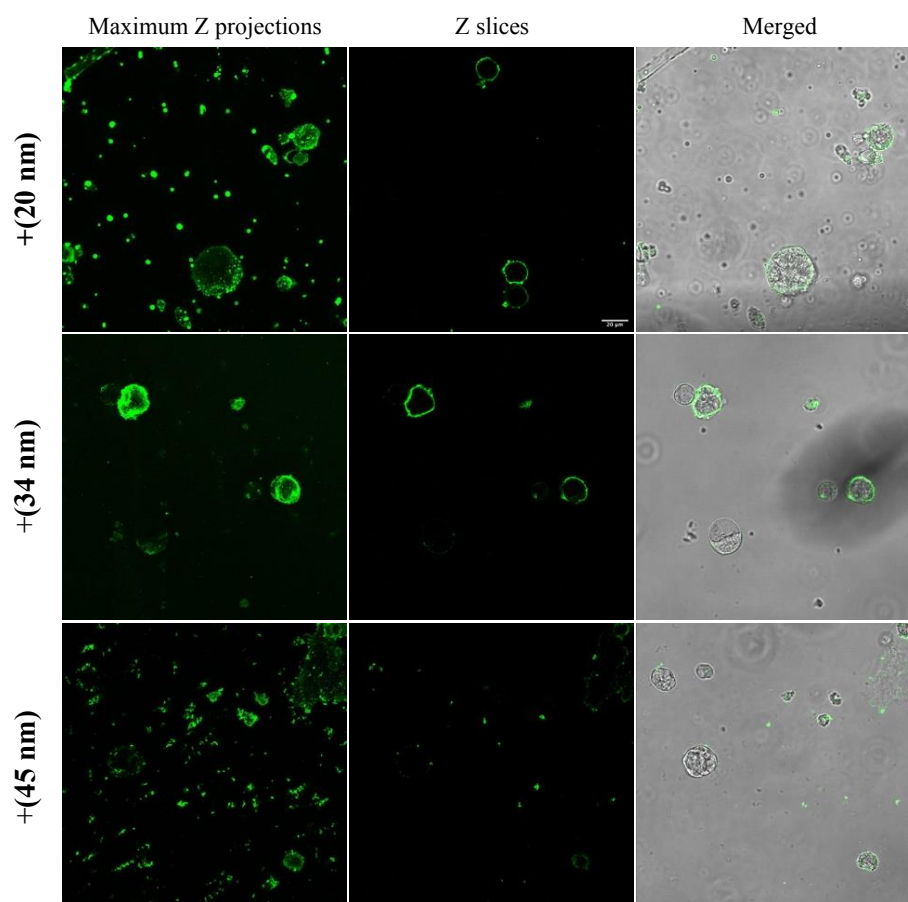


Figure 6.24. **Sizes of positively charged CPNs did not adversely affect the cytotoxicity level in protoplasts.** ImageJ software was used to generate maximum Z projections for enhanced visualisation. Z slice images and their brightfield superimposed images were used for penetration evaluation. The images are representatives of experimental replicates (n=3). Same figure panels representing the cell penetration of +(20 nm) are reused from Figure 6.22f.

To conclude, surface charge, polymer composition, and size all had a significant effect on plasma membrane penetrance and accumulation in protoplasts. Meanwhile, negatively charged CPNs were cytotoxic regardless of their sizes.

6.8 Discussion

This chapter has demonstrated an in-depth investigation into the development for aptamer-based biosensor suitable for *in planta* application. ‘Naked’ aptamers were evaluated and deemed unsuitable for *in situ* measurements. Therefore, a set of CPNs was introduced and investigated as the biosensor delivery and signalling system. CPNs varied in surface charge, size, and polymer chemistry were evaluated in both intact roots (Table 6.2) and isolated root protoplasts (Table 6.3). These physicochemical properties were assessed to all play significant roles in cell penetration and accumulation including root uptake.

Table 6.2. A summary table of CPNs evaluation for cell penetration and accumulation and uptake of *A. thaliana* intact roots.

			GOOD	MODERATE	POOR
CPNs	Surface charges	Surface accumulation	Cell penetration	Cell accumulation	Root uptake in xylem files
N ₁ (20 nm)	Neutral				
N ₁ (32 nm)	Neutral				
N ₁ (71 nm)	Neutral				
N ₂ (19 nm)	Neutral				
N ₂ (19 nm)	Zwitterionic				
Θ(25 nm)	Negative				
Θ(45 nm)	Negative				
Θ(78 nm)	Negative				
+(20 nm)	Positive				
+(30 nm)	Positive				
+(34 nm)	Positive				
+(45 nm)	Positive				
N ₁ (ATPapt)	Neutral				
+(ATPapt)	Positive				

Plant cell wall is mainly made up of polysaccharide cellulose crosslinked with pectin rich in galacturonic acid (Herrera-Ubaldo and de Folter, 2018) making plant cell wall net negatively charged. Nonetheless, some positively charged proteins are also present in cell walls (Shomer et al., 2003). While different types of nanoparticles

have been studied for their interactions and uptake in different cell types, little has been known on CPNs behaviour in plant. While the entering mechanism of CPNs is unclear, it has been proven that roots could passively uptake different types of nanoparticles into the system through osmotic pressure, endocytosis, and passive diffusion (Tripathi et al., 2017, Rico et al., 2011, Milewska-Hendel et al., 2019, Banerjee et al., 2019).

The accumulation of CPNs was inversely proportional to the nanoparticle sizes. It has been shown that small nanoparticles (20 nm \varnothing) could cross the cell wall barrier and taken up by the root hair cells (Tripathi et al., 2017). It is essential that CPNs chosen for the developed aptamer-based biosensor are small as there was a significant reduction in cell penetration and accumulation of neutral CPNs as size increased.

The surface charge and polymer chemistry of CPNs also significantly affected the penetration and uptake into roots. Neutral CPNs do not have electrostatic interactions with plant components and could passively diffuse into the cell and travel through the vascular system (Frohlich, 2012). N₁(20 nm) demonstrated the highest-level cell penetration and accumulation with uptake by the vascular system. The addition of longer side chain of DMAEA monomer in N₂(19 nm) increased the hydrophobicity of the CPNs affecting the surface chemistry of the CPNs and adversely defecting the ability to penetrate the meristem cells. This finding, however, contradicted previous studies showing higher hydrophobicity allowed higher cell uptake (He et al., 2010, Frohlich, 2012). On the other hand, the N_Z(19 nm) demonstrated cell-specific penetration which could be due to the interaction between a zwitterionic polymer and cell components allowing uptake by the vascular system (Ou et al., 2018, Mondini et al., 2015). A study of zwitterionic polypeptide effect in BY-2 cell culture revealed interaction of the polypeptide to the cellulose nanocrystal resulting in a dissociation of cellulose microfibril network and the polysaccharide layers (Tsuchiya et al., 2020). This could suggest a mode of entry for zwitterionic CPN. However, a study showed a low cell uptake of zwitterionic-coated iron in comparison to other iron oxide nanoparticles (Mondini et al., 2015). This correlated to the low uptake of N_Z(19 nm) in epidermal cells along the root hair zone. The

positive and negative charges on $N_z(19\text{ nm})$ could interact with various root components affecting the surface chemistry of $N_z(19\text{ nm})$ (Milewska-Hendel et al., 2019). While the PDMAPS polymer used is considered permanently zwitterionic and unlikely to gain/lose charges (Tian et al., 2013), further investigation of $N_z(19\text{ nm})$ in different ionic environments would be beneficial. Additionally, a time-dependent analysis of neutral CPNs showed no significant difference in time-dependent cell accumulation. As neutral CPNs do not possess any electrostatic interaction with cell components, it was possible that $N_1(20\text{ nm})$ could non-specifically diffuse in and out of the cells through time.

In contrast, a moderate accumulation of $\ominus(25\text{ nm})$ was observed at an hour incubation. Negatively charged CPNs could exhibit a repulsive electrostatic interaction with acidic polysaccharides in the cell wall affecting the particle's accumulation and uptake (Shomer et al., 2003, Milewska-Hendel et al., 2019). A further time-dependent experiment revealed a significant effect incubation time had on the cell accumulation and root uptake. An enhanced accumulation and positive root uptake of $\ominus(25\text{ nm})$ was observed over time could result from a slow ion exchange between $\ominus(25\text{ nm})$ and cell wall proteins and components that allowed passage into the plant system. As mentioned, there are some positively charged proteins present in cell walls. Interactions with these positively charged proteins over time would allow penetration and uptake of the CPN in the vascular system (Shomer et al., 2003, He et al., 2010, Zhu et al., 2012).

Meanwhile, a sheet-like accumulation of positively charged CPNs was observed around the root surface. It was potentially due to the attractive electrostatic interaction between the plant cell wall and $+(20\text{ nm})$ (Shomer et al., 2003, Cosgrove and Jarvis, 2012). While studies on mammalian cells demonstrated a successful penetration of cationic nanoparticles through plasma membrane (Frohlich, 2012), the extra cell wall of plants could prohibit nanoparticle penetration.

Biosensor delivery and signalling system was further investigated by ATPapt conjugation onto the surfaces of CPNs. $N_1(20\text{ nm})$ and $+(20\text{ nm})$ were chosen for aptamer conjugation according to the previous experimental observations. $N_1(20\text{ nm})$

demonstrated the highest level of cell penetration and accumulation with a successful root uptake and was chosen for aptamer conjugation. Meanwhile, a strategic plan was made to mimic the cell-specific accumulation of N_z (19 nm). Therefore, +(20 nm) was chosen to compensate the negatively charged DNA backbone and mimic the successful uptake of zwitterionic particles.

The aptamer conjugated CPNs demonstrated cell penetrance and root uptake behaviours comparable to their core CPNs counterpart. The fluorescence emission of both channels and the presence of Cy3 emission inside the roots suggested CPNs could shield aptamers against nuclease degradation whilst acting as an aptamer delivering mechanism into the root system (Odeh et al., 2019). The negatively charged DNA aptamer did not affect the interaction of CPNs with the cell wall components. The relative sizes of CPNs and ATPapt and percentage aptamer conjugation were the possible factors. The size of DNA aptamers is approximately 3 – 5 nm in length equating to approximately a quarter of the CPNs (Zhou and Rossi, 2017). While the conjugated aptamer could introduce negative charges to the CPNs, the conjugation level might not be sufficient to significantly alter the CPN surface chemistry. Further characterisation of $N_1(\text{ATPapt})$ could not determine the amount of ATPapt conjugated on the surface. The detected Cy3 emission (Figure 6.17b & 6.18b) confirmed the presence of ATPapt, although it was hypothesized that ATPapt was not covalently conjugated but rather interacted on the surface of +(20 nm) through a strong attractive electrostatic interaction. This was reflected by the minimal Cy3 emission detected on the surface of root tip (Figure 6.17h) and root hair zone (Figure 6.18h). The change in pH and ionic environment around the root surface could lead to ATPapt leaving from +(20 nm) surface.

$N_1(\text{ATPapt})$ demonstrated an interesting accumulation and uptake behaviour over time. Following an hour incubation, the accumulation and uptake of this aptamer-conjugated CPN corresponded to $N_1(20 \text{ nm})$. However, an increase in fluorescence was detected along the xylem files as the incubation time increased coinciding with $\ominus(25 \text{ nm})$ accumulation pattern. Only green BODIPY emission was detected along the xylem files in one- and 2.5-hours incubations corresponding to the unconjugated $N_1(20 \text{ nm})$ in the CPN suspension (Figure 6.21). However, significant green BODIPY and red Cy3 emissions were observed from five hours onwards. The negatively

charged DNA aptamers on N₁(ATPapt) could interact with positively charged proteins over time, like Θ (25 nm), allowing enhanced cell accumulation and root uptake. A low level of aptamer conjugation could explain the delay in accumulation and uptake of N₁(ATPapt) at five hours in comparison to 2.5 hours of Θ (25 nm).

A signalling mechanism corresponding to ligand binding must be in place in order to measure the ligand-aptamer interaction. Many aptamer-based biosensors designed the signalling mechanism based on the conformational change of DNA aptamer upon ligand binding, including ‘turn-on’ fluorescence and FRET measurements (Zhang et al., 2013, Wang et al., 2019, Liu et al., 2016, Ben Aissa et al., 2020). FRET measurement can be very useful for intercellular auxin quantification. The ratio of the two wavelength intensities can be measured quantitatively in proportion to auxin concentration (Okumoto et al., 2008). A recently developed genetically encoded biosensor successfully used FRET for auxin distribution *in planta* (Herud-Sikimic et al., 2021). As BODIPY was already established as an appropriate dye for CPNs visualisation, it was chosen as FRET donor. Cy3 was chosen as FRET acceptor and conjugated on the other end of the aptamer. ATPapt has been reported to have a hairpin secondary structure (Zhang et al., 2017b) and this would position Cy3 in proximity to the CPN surface promoting the chance of FRET.

Upon FRET evaluation of N₁(ATPapt), the absence of Cy3 emission suggested an inefficient energy transfer between the FRET partners. Studies showed significant effects of the environment, including pH and ionic buffer strength, on the secondary structures of DNA aptamers (Smestad and Maher, 2013, Baaske et al., 2010). The structural stability of the ATPapt could be affected by the low ionic condition in the CPN suspension and root system. Additionally, one should also consider the distance between the 3'-Cy3 and the BODIPY conjugated on the CPN surface. FRET partners must be within 8 – 10 nm proximity for a successful energy transfer (Ishikawa-Ankerhold et al., 2012, Karpova et al., 2003). The exact positions of BODIPY and Cy3-aptamer on the CPN surface is undetermined by current characterisation techniques. Further in-depth characterisation of N₁(ATPapt) would help determine the amount of aptamer conjugation and the positions of the FRET dye partners.

Additional studies on CPN uptake in isolated root protoplasts allowed further investigation into the CPNs behaviours in absence of the plant cell wall barrier Table 6.3). As observed in intact roots, nanoparticles' surface charge, polymer chemistry, and size all played a significant role in the penetration and accumulation in the isolated root protoplasts. Only N₁(20 nm) demonstrated accumulation in intact cells. Minimal accumulation of zwitterionic N_z(19 nm) could correspond to its cell-specific behaviour observed in intact roots. Interestingly, +(20 nm) analysis showed level of toxicity evidenced by more visible broken cell debris. The studies with other types of nanoparticles, the cytotoxicity has been ranked as positively charged > negatively charged > neutral CPNs (Frohlich, 2012, Firme and Bandaru, 2010). It is believed that the cytotoxicity could result from the electrostatic adsorption of positively charged CPNs onto the negatively charged plasma membrane (Frohlich, 2012). This could explain the observed cytotoxicity of +(20 nm).

Table 6.3. A summary table of CPNs evaluation for cell penetration and cytotoxicity level in *A. thaliana* isolated protoplasts.

			GOOD	MODERATE	POOR
CPNs	Surface charges	Cell debris accumulation	Cell surface accumulation	Healthy cell penetration	Cytotoxicity level
N ₁ (20 nm)	Neutral				
N ₁ (32 nm)	Neutral				
N ₁ (71 nm)	Neutral				
N ₂ (19 nm)	Neutral				
N _z (19 nm)	Zwitterionic				
⊖(25 nm)	Negative				
⊖(45 nm)	Negative				
⊖(78 nm)	Negative				
+(20 nm)	Positive				
+(30 nm)	Positive				
+(34 nm)	Positive				
+(45 nm)	Positive				

Taking all the data into account, small CPNs (20 nm Ø) with different surface charge and polymer chemistry demonstrated various degrees of cell penetration and root uptake. The designed aptamer-based biosensor should be positioned in the apoplastic matrix between cell walls for intercellular auxin quantification, one of the

original aims for the combined project. While some CPNs might not be fit-for-purpose for this project, they could be beneficial for different auxin measurement applications. The analysis of N₁(20 nm) and N₁(ATPapt) demonstrated the highest level of cell accumulation and a successful uptake in intact roots from an hour incubation while that of Θ (25 nm) showed enhanced accumulation and uptake over time. This could be useful as a complementary tool to the genetically encoded biosensor for intracellular auxin quantification (Herud-Sikimic et al., 2021, Walia et al., 2018, Brunoud et al., 2012). On the other hand, +(20 nm) form a sheet-like accumulation around the surface of the root. While it might be deemed unsuitable for *in planta* measurement, it could be further developed to measure the flux of different analytes in and out of the root system (Ghestem et al., 2011).

Undoubtedly, further studies on the development of aptamer conjugated CPNs, including the conjugation level, system characterisation and uptake mechanism of CPNs are required to achieve a better understanding on their behaviours in plants. Conventional techniques, like DLS and fluorometry, might not be sufficient for in-depth characterisation. Fluorescence evaluation under the alternative fluorescence-lifetime imaging microscopy (FLIM) can be applied for CPNs nanostructure, photostability in plants, and FRET evaluation for binding signal (Ishikawa-Ankerhold et al., 2012, Trautmann et al., 2013, Santra et al., 2006). The fluorescence lifetime of the fluorophores is greatly dependent on the local environment, including pH and ion concentration (Trautmann et al., 2013). It was used to successfully determine the nanostructure of the dye conjugated nanoparticles and its photostability in different environments (Santra et al., 2006). FRET can also be measured and quantified by using time-correlated single photon counting (Ishikawa-Ankerhold et al., 2012). This can be used to evaluate the fluorescence lifetime of the FRET partners and FRET efficiency (Zhang et al., 2017a, Ishikawa-Ankerhold et al., 2012). FLIM allows critical analysis of the stability and performances of aptamer conjugated CPNs as aptamer-based biosensor in plants as well as allowing evaluation of the environment in which the sensor is deployed.

Chapter 7 Conclusion and future work

This study has focused on the development of an aptamer-based biosensor as an alternative tool to map intercellular auxin gradients *in planta* with high spatial and temporal resolution. To do so, the scopes of this study have focused on addressing the following hypotheses: (1) SELEX processes can select auxin aptamers; (2) affinity maturation techniques can improve auxin binding affinities and specificities of the chosen aptamer candidates; (3) the developed auxin aptamers can be used as biosensor recognition component; (4) CPNs can be selected to target the apoplast and evaluated as a suitable biosensor delivery and signalling system; and (5) a novel nano-sensor may map auxin gradients *in planta*. Table 7.1 summarises the key achievements towards the research hypotheses.

Table 7.1. A summary table of the achievements towards the project objectives.

	COMPLETE	PARTIAL	NO
	Achieved?	Further works?	
1. SELEX processes can select for auxin aptamers.		-	
2. Affinity maturation techniques can improve auxin binding affinities and specificities of the chosen aptamer candidates.		-	
3. The developed auxin aptamers can be used as biosensor recognition components in <i>A. thaliana</i> seedlings		Further aptamer characterisation and sequence modification is required.	
4. CPNs can be selected to target apoplast and evaluated as a suitable biosensor delivery and signalling system in <i>A. thaliana</i> seedlings		Further CPNs characterisation using FLIM and FLIM-FRET system.	
5. A novel nano-sensor can be devised which may map auxin gradient <i>in planta</i> .		Conjugation of optimised IAA aptamer to well characterised CPNs to create suitable auxin mapping tool.	

7.1 SELEX processes can select for auxin aptamers

The study showed that while SELEX processes were successful in the selection of aptamers with auxin binding recognition, they were not sufficiently effective in enriching specific aptamer sequences. Two types of SELEX, direct- and solution-SELEX, were performed to select suitable aptamer candidates with auxin binding affinities. Through an extensive comparative sequence analysis, basic patterns of nucleotides and repeated sequences were obtained from each sub-library (Figure 3.8). However, no pattern consensus was observed across sub-libraries restricting further aptamer selection. It was hypothesized that this ineffective aptamer enrichment was due to the insufficient number of SELEX rounds performed combined with some overly stringent counter-selection steps. Aptamer enrichment has often been observed after five rounds of SELEX (Blank, 2016). The repeated sequences observed in sub-libraries from the tenth and sixth rounds of direct- and solution-SELEX, respectively, could indicate that this project successfully achieve some degrees of sequence enrichment (Table 3.1), but it was insufficient to advance in the aptamer selection process. It is noted that a study of an aptamer developed against trans-zeatin required a total of 24 rounds of SELEX to obtain highly specific aptamer sequences (Qi et al., 2013). It can also be correlated that the number of performed counter selection steps negatively impacted the numbers of repeated sequences (Table 3.1). Potential auxin aptamers could have been lost through successive rounds of harsh counter-selection steps (Ruscito and DeRosa, 2016, McKeague and DeRosa, 2012, McKeague et al., 2015).

To advance in the auxin aptamer selection process, ELONA was adopted as a high-throughput screen to select for auxin positive binders across the sub-libraries (Le et al., 2014, Chumphukam et al., 2014). While it was not the most sensitive technique, it allowed a quick screen for sequences with auxin recognition (Figure 3.12, Table 3.2). MST was subsequently used to characterise the chosen aptamer candidates which gave us access to auxin binding affinity data. Ultimately, ST-57 and ST-34d, aptamer candidates from SELEX processes, were selected for auxin binding affinity with K_D values in the high micromolar range.

7.2 Affinity maturation techniques can improve auxin binding affinities and specificities of the chosen aptamer candidates

To be suitable for downstream *in planta* application, sequence optimisation was necessary to enhance the auxin binding affinity and specificity of the aptamers. It is common for aptamer sequences obtained from SELEX processes to go through various modifications to improve their target sensitivities and specificities and facilitate downstream biosensor synthesis (Zhang et al., 2017b, Zhang and Liu, 2018, Wang et al., 2019, Reinemann et al., 2016, Le et al., 2014, He et al., 2017, Hasegawa et al., 2016). For example, the aptamer with high ATP binding affinity was selected after 8 rounds of SELEX, and affinity maturation was performed for the optimal ATP binding sequence in the micromolar range (Zhang et al., 2017b, Zhang and Liu, 2018). It was confirmed in this study, that the affinity maturation techniques, including hybridisation inhibition (HI), sequence truncation, and single G-mutations, can improve auxin binding affinities and specificities of the chosen aptamer candidates.

HI and sequence truncation were used to identify the minimal ligand binding sequences of the aptamers while single G-mutations were used to optimise binding sequences. Studies showed the conserved primer binding sites (CPBS) of aptamer sequences do not participate in ligand-specific interactions (Pan and Clawson, 2009, Cowperthwaite and Ellington, 2008). The removal of the 3'-end CPBS of ABAPt did not affect its ABA binding affinity (Figure 4.1) while truncation of ST-57 from 5'-end CBPS improved IAA binding affinity (Figure 4.2). Interestingly, further truncation of ABAPt to STA-3 demonstrated decreased ABA affinity but an excellent binding to IAA (Figure 4.5). The similarity in the chemical structures between these compounds could be accounted for the overlap in the ligand bindings (Slavkovic et al., 2015, Reinstein et al., 2013).

Further single G-mutation of STA-3 to STA-3-9 demonstrated enhanced IAA binding affinity (Figure 4.8, Table 4.9). Additional optimisation of the experimental conditions and characterisation confirmed STA-3 and STA-3-9 as two optimal auxin aptamer candidates, having high binding affinities and specificities against IAA with estimated K_D values of 172.2 ± 64.3 nM and 21.9 ± 10.6 nM, respectively (Figure 4.9).

7.3 The developed auxin aptamers can be used as biosensor recognition components in *A. thaliana* seedlings

The two developed aptamers, STA-3 and STA-3-9 demonstrated high IAA binding affinities and specificities in the nanomolar range using MST. While MST is a powerful tool to determine K_D associated with the auxin binding of aptamers, the nature of MST experimental set up does not allow for *in vitro* nor *in planta* auxin quantification. Therefore, several techniques were developed to further characterise these aptamers and assay formats which could be used for IAA quantification. However, these techniques suggested that the developed aptamers would not be suitable as the recognition component of an aptasensor for *in planta* application.

Neither of the aptamers could recognise auxin at low ionic strength, conditions reflecting the apoplastic environment. Indeed, auxin binding analysis to STA-3-9 was shown to greatly depend on the environment. Its optimal auxin binding was observed in HEPES buffer with 150 mM NaCl and 2 mM KCl at pH 7.2 (Figure 5.5, Table 5.6). While STA-3 demonstrated good auxin binding at pH 5.8, high Na^+ and K^+ ions were required for this ligand interaction (Figure 5.4, Table 5.4). No auxin interaction could be detected upon evaluation of these aptamers at lower salt and pH conditions reflecting the apoplastic environment (Sattelmacher, 2001). This will be a challenge to adapt these aptamers for auxin recognition in a low ionic, acidic apoplastic matrix. Further sequence modifications, such as chemical conjugations and/or modifications to the nucleotides including alterations to the ribose ring, phosphodiester linkage or the bases themselves, could increase aptamer stability in apoplastic-like environment (Odeh et al., 2019, Ni et al., 2017, Elskens et al., 2020). A ribose modification has shown to improve aptamer stability in serum (Odeh et al., 2019) while polyethylene glycol (PEG) conjugation has been suggested to enhance aptamer stability for both *in vitro* and *in vivo* examinations (Elskens et al., 2020).

Techniques, including the Thioflavin (ThT) assay, surface plasmon resonance (SPR), isothermal titration calorimetry (ITC), and circular dichroism (CD), were evaluated to further characterise STA-3-9 as assay formats for a potential auxin quantification method. However, these techniques failed to detect auxin binding to the

aptamer. A CD structural study of STA-3-9 revealed no significant auxin-induced conformational change of the aptamer (Figure 5.14). This suggested the binding mechanism of auxin with STA-3-9 as ligand intercalation within the aptamer's stable G-quadruplex structure rather than a ligand-induced conformational change. This revelation may help explain the failure of the ThT assay (Figure 5.7) to recognise auxin binding because the assay relies on conformational change and ThT intercalation in competition with the ligand (Wu et al., 2018, Renaud de la Faverie et al., 2014).

Furthermore, while SPR was able to recognise specific trans-zeatin binding to tZ aptamer (Figure 5.9), no auxin response was observed for STA-3-9 (Figure 5.10). The latest generation of SPR was developed as a highly sensitive technique with the limit of detection of small analytes around 100 Dalton in size (Healthcare, 2012). The molecular weight (Mw) of trans-zeatin is 219.24 g/mol which is considerably larger than IAA with 175.18 g/mol Mw. The lack of auxin binding detection could be due to analysis close to the limit of detection resulting in no observed auxin dose-dependent response. The square-pulse sensorgram observed is common with fast kinetics binding (Liu and Wilson, 2010). This would suggest low auxin binding affinity, but this would then contradict the previous MST data. To resolve this, more advanced techniques, including nuclear magnetic resonance (NMR) or crystallography, could be developed to confirm the auxin intercalation with STA-3-9 structure (Neves et al., 2017, Sakamoto, 2017, Ruigrok et al., 2012).

The trans-zeatin aptamer was also used to optimise and validate ITC as a method to evaluate the K_D and other thermodynamic parameters corresponding to small molecule aptamer bindings, including aptamers against adenosine (507.18 g/mol Mw) and cocaine (303.353 g/mol Mw) (Zhang et al., 2017b, Slavkovic et al., 2015, Reinstein et al., 2013). However, these aptamers underwent major conformational changes in the presence of their ligands and large enthalpic changes were observed. STA-3-9, on the other hand, did not demonstrate any measurable change upon IAA injection. This suggested two possibilities: (1) the auxin intercalation of STA-3-9 was at low affinity resulting no detectable binding; or (2) the ITC experimental conditions were not optimal for measuring auxin intercalation of STA-3-9.

Taking all the evidence into account, the mechanism of STA-3-9 is suggested to be intercalation of auxin within the already stable G-quadruplex of the aptamer. This is consistent with the failure to quantify auxin binding using ThT assay and SPR and the insignificant changes in the CD spectra and ITC enthalpy upon IAA injection. Consequently, the aptamer was deemed not suitable as a biosensor recognition element for auxin measurements *in planta* as it stands.

7.4 CPNs can be selected to target apoplast and evaluated as a suitable biosensor delivery and signalling system in *A. Thaliana* seedlings

The physicochemical properties of different CPNs have been extensively evaluated for their effects on the uptake and penetration into plants. While no CPNs have yet been observed specifically in the apoplast, several of the CPNs studied could be used as biosensor delivery and signalling vehicles for *in planta* application. As the biosensor delivery system, various CPNs demonstrated degrees of penetration and uptake in intact roots. $N_1(20\text{nm})$ (Figure 6.9 and 6.10) and $N_1(\text{ATPapt})$ (Figure 6.17 and 6.18), the smallest neutral CPN and its aptamer-conjugated form, demonstrated the highest penetration and accumulation in both *A. thaliana* intact roots and isolated protoplasts while $\Theta(25\text{ nm})$ demonstrated enhanced root uptake over time (Figure 6.20). These may allow successful measurement of analytes throughout the vascular system. On the other hand, $+(20\text{ nm})$ (Figure 6.8 and 6.9) and $+(\text{ATPapt})$ (Figure 6.17 and 6.18) formed a sheet-like accumulation around the root surface and suggesting a potential application for flux measurement of analytes across the root tip surface (McLamore et al., 2010). Regarding CPNs as signalling system, a bright fluorescence emission was observed upon confocal microscopic evaluation with no interference from autofluorescence in plants (Figure 6.8). This is highly suitable for *in planta* visualisation. Preliminary evaluation of CPNs conjugated to ATPapt-Cy3 to quantify auxin recorded no FRET (Figure 6.19). However, this is most likely a limitation of the current aptamer.

7.5 A novel nano-sensor can be devised which may map auxin gradient *in planta*.

By evaluating N₁(ATPapt), a neutral CPNs with conjugated ATPapt-Cy3, the data suggested that there is potential for this aptamer conjugated CPNs to measure ATP *in planta* (Figure 6.17). Microscopy evaluation revealed successful uptake of intact N₁(ATPapt) inside *A. thaliana* vascular system. Upon time-dependence evaluation of N₁(ATPapt), presence of Cy3 emission corresponding to intact ATPapt suggested CPN successfully shielded aptamer from degradation by nucleases (Figure 6.21). However, FRET was not observed within the N₁(ATPapt) system (Figure 6.19). Further evaluation with added exogenous ligand might allow optimisation of FRET in this system (Isoda et al., 2021). Nevertheless, the nano-sensor system is the first step towards a mapping tool for intercellular auxin gradients.

7.6 Future work

Undoubtedly, all the works established within this study have demonstrated potential for a successful nano-sensor to map auxin gradient *in planta*. STA-3-9 was developed with high auxin binding affinity and specificity as demonstrated using MST while 20 nm Ø CPNs with different surface charges allowed delivery of such a biosensor to different compartments of *A. thaliana* seedlings. Nonetheless, both components of this novel biosensor require further optimisation to be fully functional and applicable for intercellular auxin gradient mapping.

7.6.1 Further development of auxin aptamer as biosensor recognition component

To be suitable as biosensor recognition component and for *in planta* auxin measurements, further characterisation and sequence modification is necessary. Determination of auxin binding site(s) within STA-3-9 will allow structure-led modification of the sequence for suitable auxin binding. This can be done computationally and/or experimentally. Molecular dynamics (MD) simulations will allow tertiary structure predictions of the aptamers in presence and absence of ligand.

To date, well established simulation algorithms allowed tertiary structure predictions only of RNA sequences. Most studies on DNA aptamers provide only secondary structure predictions (Zhou et al., 2011, Vu et al., 2016, Qi et al., 2013, Grozio et al., 2013, Zhang et al., 2017b). The simulation of DNA aptamer tertiary structure would involve sequence conversion to RNA analogue, simulate the tertiary structure of the RNA analogue, followed by manually converting uracil bases to thymine bases (Ben Aissa et al., 2020). Some MD simulations using in-house developed algorithms have been done (Song et al., 2020, Gao et al., 2016).

Further CD analysis and additional techniques like nuclear magnetic resonance (NMR) and crystallography will experimentally allow an in-depth understanding of the auxin binding mechanism and identify the ligand binding site(s) of STA-3-9. CD spectra of an aptamer and its mutated variants in the presence and absence of ligand ochratoxin A (OTA) allowed in-depth evaluation of the variants and illustrated a ligand-induced conformational change (Wang et al., 2019). The G-quadruplex structures of oligonucleotides with modified guanine bases have been successfully evaluated using CD coupled with NMR (Esposito et al., 2004).

Once the auxin binding site(s) of STA-3-9 is established, a more direct optimisation can take place. Further sequence truncation to the minimal binding sequence could improve binding affinity (Gao et al., 2016). Alternatively, sequence modification can be performed with MD simulation as guidelines to ‘force’ the sequence undergoes conformational change upon auxin binding. This will also facilitate downstream FRET application of the nano-sensor.

An interesting application might be an electrochemical biosensor for auxin quantification using STA-3-9 as probe. An electrochemical biosensor was previously developed for cytokinin measurement using cytokinin oxidase as probe (Tian et al., 2014). Aptamer-based electrochemical biosensors have been successfully developed for detection of both proteins and small molecules such as ATP (Li et al., 2009, Han et al., 2016, Deng et al., 2009). In these cases, major conformational changes are not necessary and the ligand intercalation within the immobilised DNA strand can restrict the aptamer mobility sufficiently to allow a ligand-dependent redox measurement (Prante et al., 2020).

7.6.2 Further development of CPNs as biosensor delivery and signalling system

Further characterisation and studies on the uptake mechanism of CPNs are required to achieve a better understanding on their behaviours in plants. Fluorescence-lifetime imaging microscopy (FLIM) can provide a more in-depth fluorescence analysis of the CPN's nanostructure and their stability in plants, the environment in which they sit (Trautmann et al., 2013). The intrinsic fluorescence of the control CPN samples can be measured and set as baseline. The fluorescence decay constants of CPN samples can indicate any adverse effects the acidic apoplast has on CPNs stability (Santra et al., 2006).

Moreover, signalling system can utilise the combination of fluorescence resonance energy transfer (FRET) and FLIM to evaluate auxin binding (Orthaus et al., 2009, Berezin and Achilefu, 2010). The fluorescence lifetime of FRET donor and acceptor will be monitored. In principle, auxin binding would alter the proximity of the FRET partners leading to significant change in the fluorescence lifetime of the FRET donor (Orthaus et al., 2009). This change can be monitored and correlate directly to the auxin bound to aptasensor. FLIM-FRET system will analyse CPNs as suitable and stable biosensor delivery and signalling system (Zhang et al., 2017a, Orthaus et al., 2009, Ishikawa-Ankerhold et al., 2012). An appropriate experimental set up will need to be established for high temporal and spatial measurement of auxin gradient in *A. thaliana* roots.

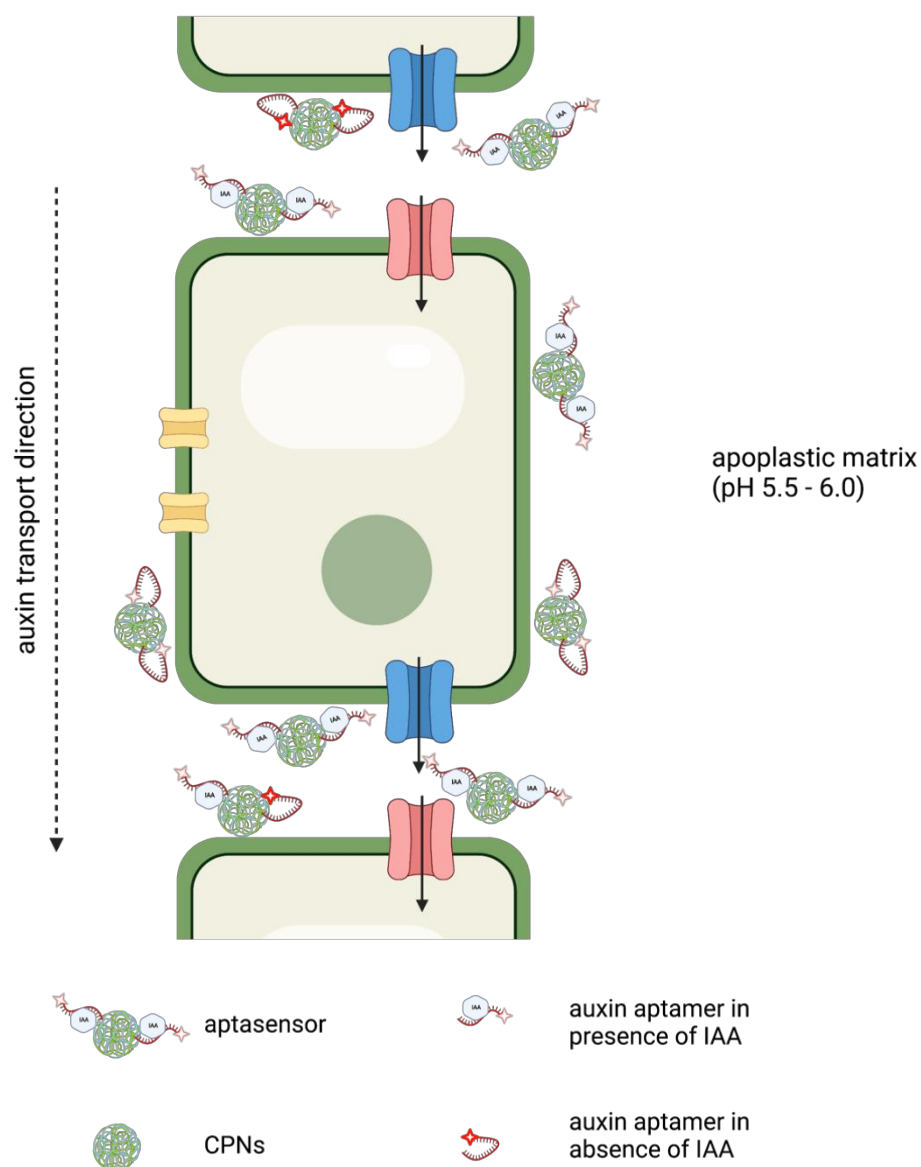


Figure 7.1. **Schematic illustration of the optimal aptasensor deployed in apoplastic matrix as suitable tool to map intercellular auxin gradient *in planta*.** Scheme created with BioRender.com

Once the optimised auxin aptamer is established, it will be conjugated on the well characterised CPN surface to create the novel aptasensor as a suitable tool to map auxin gradient *in planta* using fluorescence microscopy such as FLIM-FRET system (Figure 7.1).

References

- ALLEN, P. M. & BAWENDI, M. G. 2008. Ternary I-III-VI quantum dots luminescent in the red to near-infrared. *Journal of the American Chemical Society*, 130, 9240-9241.
- ARMENGOT, L., MARQUES-BUENO, M. M. & JAILLAIS, Y. 2016. Regulation of polar auxin transport by protein and lipid kinases. *Journal of Experimental Botany*, 67, 4015-4037.
- AVELLAN, A., SCHWAB, F., MASION, A., CHAURAND, P., BORSCHNECK, D., VIDAL, V., ROSE, J., SANTAELLA, C. & LEVARD, C. 2017. Nanoparticle Uptake in Plants: Gold Nanomaterial Localized in Roots of *Arabidopsis thaliana* by X-ray Computed Nanotomography and Hyperspectral Imaging. *Environmental Science & Technology*, 51, 8682-8691.
- BAASKE, P., WIENKEN, C. J., REINECK, P., DUHR, S. & BRAUN, D. 2010. Optical thermophoresis for quantifying the buffer dependence of aptamer binding. *Angewandte Chemie International Edition in English*, 49, 2238-41.
- BANERJEE, K., PRAMANIK, P., MAITY, A., JOSHI, D. C., WANI, S. H. & KRISHNAN, P. 2019. Methods of Using Nanomaterials to Plant Systems and Their Delivery to Plants (Mode of Entry, Uptake, Translocation, Accumulation, Biotransformation and Barriers). *Advances in Phytotechnology*. 123-152.
- BEN AISSA, S., MASTOURI, M., CATANANTE, G., RAOUAFI, N. & MARTY, J. L. 2020. Investigation of a Truncated Aptamer for Ofloxacin Detection Using a Rapid FRET-Based AptA-Assay. *Antibiotics*, 9, 860.
- BEREZIN, M. Y. & ACHILEFU, S. 2010. Fluorescence lifetime measurements and biological imaging. *Chemical Reviews*, 110, 2641-2684.
- BHUNIA, S. K., SAHA, A., MAITY, A. R., RAY, S. C. & JANA, N. R. 2013. Carbon nanoparticle-based fluorescent bioimaging probes. *Scientific Reports*, 3, 1473.
- BILLINTON, N. & KNIGHT, A. W. 2001. Seeing the wood through the trees: a review of techniques for distinguishing green fluorescent protein from endogenous autofluorescence. *Analytical Biochemistry*, 291, 175-197.
- BLANK, M. 2016. Next-Generation Analysis of Deep Sequencing Data: Bringing Light into the Black Box of SELEX Experiments. In: Günter Mayer (ed.), Nucleic Acid Aptamers: Selection, Characterization, and Application, *Methods in Molecular Biology*, 1380, 85-95.
- BLIND, M. & BLANK, M. 2015. Aptamer Selection Technology and Recent Advances. *Molecular Therapy-Nucleic Acids*, 4, e223.
- BRUNOUD, G., WELLS, D. M., OLIVA, M., LARRIEU, A., MIRABET, V., BURROW, A. H., BEECKMAN, T., KEPINSKI, S., TRAAS, J., BENNETT, M. J. & VERNOUX, T. 2012. A novel sensor to map auxin response and distribution at high spatio-temporal resolution. *Nature*, 482, 103-106.
- BURNS, A., SENGUPTA, P., ZEDAYKO, T., BAIRD, B. & WIESNER, U. 2006. Core/Shell fluorescent silica nanoparticles for chemical sensing: towards single-particle laboratories. *Small*, 2, 723-726.
- CAI, W., DONG-WOON, CHEN, S., GHEYSENS, O., CAO, Q., WANG, S. X., GAMBHIR, S. S. & CHEN, X. 2006. Peptide-Labeled Near-Infrared Quantum Dots for Imaging Tumor Vasculature in Living Subjects. *American Chemical Society*, 6, 669-676.

- CANNING, S. L., SMITH, G. N. & ARMES, S. P. 2016. A Critical Appraisal of RAFT-Mediated Polymerization-Induced Self-Assembly. *Macromolecules*, 49, 1985-2001.
- CHAN, J. M., ZHANG, L., YUET, K. P., LIAO, G., RHEE, J. W., LANGER, R. & FAROKHZAD, O. C. 2009. PLGA-lecithin-PEG core-shell nanoparticles for controlled drug delivery. *Biomaterials*, 30, 1627-1634.
- CHANG, A. L., MCKEAGUE, M. & SMOLKE, C. D. 2014. Facile characterization of aptamer kinetic and equilibrium binding properties using surface plasmon resonance. *Methods in Enzymology*, 549, 451-466.
- CHAPMAN, E. J. & ESTELLE, M. 2009. Mechanism of auxin-regulated gene expression in plants. *Annual Review of Genetics*, 43, 265-285.
- CHAUDHURI, B., HORMANN, F. & FROMMER, W. B. 2011. Dynamic imaging of glucose flux impedance using FRET sensors in wild-type *Arabidopsis* plants. *Journal of Experimental Botany*, 62, 2411-2417.
- CHEN, A. K., CHENG, Z., BEHLKE, M. A. & TSOURKAS, A. 2008. Assessing the sensitivity of commercially available fluorophores to the intracellular environment. *Analytical Chemistry*, 80, 7437-7444.
- CHIVASA, S., NDIMBA, B. K., SIMON, W. J., LINDSEY, K. & SLABAS, A. R. 2005. Extracellular ATP functions as an endogenous external metabolite regulating plant cell viability. *The Plant Cell*, 17, 3019-3034.
- CHOI, H. S. & FRANGIONI, J. V. 2010. Nanoparticles for Biomedical Imaging: Fundamentals of Clinical Translation. *Molecular Imaging*, 9, 291-310.
- CHUMPHUKAM, O., LE, T. T. & CASS, A. E. 2014. High efficiency acetylcholinesterase immobilization on DNA aptamer modified surfaces. *Molecules*, 19, 4986-4996.
- COSGROVE, D. J. & JARVIS, M. C. 2012. Comparative structure and biomechanics of plant primary and secondary cell walls. *Frontier in Plant Science*, 3, 204.
- COWPERTHWAIT, M. C. & ELLINGTON, A. D. 2008. Bioinformatic analysis of the contribution of primer sequences to aptamer structures. *Journal of Molecular Evolution*, 67, 95-102.
- DALE, N. 2020. Real-time measurement of adenosine and ATP release in the central nervous system. *Purinergic Signal*, 17, 109-115.
- DEL VILLAR-GUERRA, R., TRENT, J. O. & CHAIRES, J. B. 2018. G-Quadruplex Secondary Structure Obtained from Circular Dichroism Spectroscopy. *Angewandte Chemie International Edition in English*, 57, 7171-7175.
- DENG, C., CHEN, J., LIHUA NIE, Z. N. & YAO, S. 2009. Sensitive Bifunctional Aptamer-Based Electrochemical Biosensor for Small Molecules and Protein. *Analytical Chemistry*, 81, 9972-9978.
- DU, R. & ZHAO, J. 2004. Positively Charged Composite Nanofiltration Membrane Prepared by Poly(N,N-dimethylaminoethyl methacrylate)/ Polysulfone. *Journal of Applied Polymer Science*, 91, 2721-2728.
- ELLINGTON, A. D. & SZOSTAK, J. W. 1990. *In vitro* selection of RNA molecules that bind specific ligands. *Nature*, 346, 818-822.
- ELSKENS, J. P., ELSKENS, J. M. & MADDER, A. 2020. Chemical Modification of Aptamers for Increased Binding Affinity in Diagnostic Applications: Current Status and Future Prospects. *International Journal of Molecular Science*, 21, 4522.
- ENDERS, T. A. & STRADER, L. C. 2015. Auxin activity: Past, present, and future. *American Journal of Botany*, 102, 180-196.

- ENTZIAN, C. & SCHUBERT, T. 2016. Studying small molecule-aptamer interactions using MicroScale Thermophoresis (MST). *Methods*, 97, 27-34.
- ESPOSITO, V., RANDAZZO, A., PICCIALI, G., PETRACONE, L., GIANCOLA, C. & MAYOL, L. 2004. Effects of an 8-bromodeoxyguanosine 161 incorporation on the parallel quadruplex structure [d(TGGGT)]₄. *Organic & Biomolecular Chemistry*, 2, 313-318.
- FAISAL, M., SAQUIB, Q., ALATAR, A. A. & ABDULAZIZA.AL-KHEDHAIRY 2018. *Phytotoxicity Of Nanoparticles*. Springer, Cham.
- FAROKHZAD, O. C., JON, S., KHADEMHOSEINI, A., TRAN, T.-N. T., LAVAN, D. A. & LANGER, R. 2004. Nanoparticle-Aptamer Bioconjugates: A New Approach for Targeting Prostate Cancer Cells. *Cancer Research*, 64, 7668-7672.
- FIRME, C. P., 3RD & BANDARU, P. R. 2010. Toxicity issues in the application of carbon nanotubes to biological systems. *Nanomedicine: Nanotechnology, Biology, and Medicine*, 6, 245-256.
- FROHLICH, E. 2012. The role of surface charge in cellular uptake and cytotoxicity of medical nanoparticles. *International Journal of Nanomedicine*, 7, 5577-5591.
- GAILLARD, C. & STRAUSS, F. 1989. Ethanol precipitation of DNA with linear polyacrylamide as carrier. *Nucleic Acids Research*, 18, 378.
- GAO, S., HU, B., ZHENG, X., LIU, D., SUN, M., QIN, J., ZHOU, H., JIAO, B. & WANG, L. 2016. Study of the binding mechanism between aptamer GO18-T-d and gonyautoxin 1/4 by molecular simulation. *Physical Chemistry Chemical Physics*, 18, 23458-23461.
- GAO, X., GULARI, E. & ZHOU, X. 2004. *In situ* synthesis of oligonucleotide microarrays. *Biopolymers*, 73, 579-596.
- GHESTEM, M., SIDLE, R. C. & STOKES, A. 2011. The Influence of Plant Root Systems on Subsurface Flow: Implications for Slope Stability. *BioScience*, 61, 869-879.
- GOOCH, J., DANIEL, B., PARKIN, M. & FRASCIONE, N. 2017. Developing aptasensors for forensic analysis. *Trends in Analytical Chemistry*, 94, 150-160.
- GOPINATH, S. C. 2007. Methods developed for SELEX. *Analytical and Bioanalytical Chemistry*, 387, 171-182.
- GRENNAN, K., STRACHAN, G., PORTER, A. J., KILLARD, A. J. & SMYTH, M. R. 2003. Atrazine analysis using an amperometric immunosensor based on single-chain antibody fragments and regeneration-free multi-calibrant measurement. *Analytica Chimica Acta*, 500, 287-298.
- GROZIO, A., GONZALEZ, V. M., MILLO, E., STURLA, L., VIGLIAROLO, T., BAGNASCO, L., GUIDA, L., D'ARRIGO, C., DE FLORA, A., SALIS, A., MARTIN, E. M., BELLOTTI, M. & ZOCCHI, E. 2013. Selection and characterization of single stranded DNA aptamers for the hormone abscisic Acid. *Nucleic Acid Therapeutics*, 23, 322-331.
- HA, N. R., JUNG, I. P., LA, I. J., JUNG, H. S. & YOON, M. Y. 2017. Ultra-sensitive detection of kanamycin for food safety using a reduced graphene oxide-based fluorescent aptasensor. *Scientific Reports*, 7: 40305.
- HAN, K., LIU, T., WANG, Y. & MIAO, P. 2016. Electrochemical aptasensors for detection of small molecules, macromolecules, and cells. *Reviews in Analytical Chemistry*, 35, 201-211.
- HASEGAWA, H., SAVORY, N., ABE, K. & IKEBUKURO, K. 2016. Methods for Improving Aptamer Binding Affinity. *Molecules*, 21, 421.

- HAYASHI, K., NAKAMURA, S., FUKUNAGA, S., NISHIMURA, T., JENNESS, M. K., MURPHY, A. S., MOTOSE, H., NOZAKI, H., FURUTANI, M. & AOYAMA, T. 2014. Auxin transport sites are visualized *in planta* using fluorescent auxin analogs. *Proceedings of the National Academy of Sciences*, 111, 11557-11562.
- HE, C., HU, Y., YIN, L., TANG, C. & YIN, C. 2010. Effects of particle size and surface charge on cellular uptake and biodistribution of polymeric nanoparticles. *Biomaterials*, 31, 3657-3666.
- HE, X., GUO, L., HE, J., XU, H. & XIE, J. 2017. Stepping Library-Based Post-SELEX Strategy Approaching to the Minimized Aptamer in SPR. *Analytical Chemistry*, 89, 6559-6566.
- GE HEALTHXCARE BIO-SCIENCES, 2012. Biacore™ Assay Handbook. 29-0194-00 Edition AA
- HERRERA-UBALDO, H. & DE FOLTER, S. 2018. Exploring Cell Wall Composition and Modifications During the Development of the Gynoecium Medial Domain in *Arabidopsis*. *Frontier in Plant Science*, 9, 454.
- HERUD-SIKIMIC, O., STIEL, A. C., KOLB, M., SHANMUGARATNAM, S., BERENDZEN, K. W., FELDHAUS, C., HOCKER, B. & JURGENS, G. 2021. A biosensor for the direct visualization of auxin. *Nature*, 592, 768-772.
- HIANIK, T., OSTATNA, V., SONLAJTNEROVA, M. & GRMAN, I. 2007. Influence of ionic strength, pH and aptamer configuration for binding affinity to thrombin. *Bioelectrochemistry*, 70, 127-133.
- HOINKA, J., BACKOFEN, R. & PRZYTYCKA, T. M. 2018. AptaSUIE: A Full-Featured Bioinformatics Framework for the Comprehensive Analysis of Aptamers from HT-SELEX Experiments. *Molecular Therapy - Nucleic Acids*, 11, 515-517.
- HUIZENGA, D. E. & SZOSTAK, J. W. 1995. A DNA Aptamer That Binds Adenosine and ATP. *Biochemistry*, 34, 656-665.
- ISHIKAWA-ANKERHOLD, H. C., ANKERHOLD, R. & DRUMMEN, G. P. 2012. Advanced fluorescence microscopy techniques--FRAP, FLIP, FLAP, FRET and FLIM. *Molecules*, 17, 4047-132.
- ISODA, R., YOSHINARI, A., ISHIKAWA, Y., SADOINE, M., SIMON, R., FROMMER, W. B. & NAKAMURA, M. 2021. Sensors for the quantification, localization and analysis of the dynamics of plant hormones. *The Plant Journal*, 105, 542-557.
- JONES, A. M., DANIELSON, J., MANOJKUMAR, S. N., LANQUAR, V., GROSSMANN, G. & FROMMER, W. B. 2014. Absciscic acid dynamics in roots detected with genetically encoded FRET sensors. *eLife*, 3: e01741
- KALRA, P., DHIMAN, A., CHO, W. C., BRUNO, J. G. & SHARMA, T. K. 2018. Simple Methods and Rational Design for Enhancing Aptamer Sensitivity and Specificity. *Frontier in Molecular Biosciences*, 5, 41.
- KAMATA, K., LU, Y. & XIA, Y. 2003. Synthesis and Characterization of Monodispersed Core-Shell Spherical Colloids with Movable Cores. *Journal of American Chemical Society*, 125, 2384-2385.
- KARPOVA, T. S., BAUMANN, C. T., HE, L., WU, X., GRAMMER, A., LIPSKY, P., HAGER, G. L. & NALLY, J. G. M. C. 2003. Fluorescence resonance energy transfer from cyan to yellow fluorescent protein detected by acceptor photobleaching using confocal microscopy and a single laser. *Journal of Microscopy*, 209, 56-70.

- KATILIUS, E., FLORES, C. & WOODBURY, N. W. 2007. Exploring the sequence space of a DNA aptamer using microarrays. *Nucleic Acids Research*, 35, 7626-7635.
- KIKIN, O., D'ANTONIO, L. & BAGGA, P. S. 2006. QGRS Mapper: a web-based server for predicting G-quadruplexes in nucleotide sequences. *Nucleic Acids Research*, 34, W676-82.
- KIM, S., LEE, S. & LEE, H. J. 2018. An aptamer-aptamer sandwich assay with nanorod-enhanced surface plasmon resonance for attomolar concentration of norovirus capsid protein. *Sensors and Actuators B: Chemical*, 273, 1029-1036.
- KOMAROVA, N. & KUZNETSOV, A. 2019. Inside the Black Box: What Makes SELEX Better? *Molecules*, 24, 3598.
- KOMOROWSKA, B., HASIOW-JAROSZEWSKA, B. & MINICKA, J. 2017. Application of nucleic acid aptamers for detection of Apple stem pitting virus isolates. *Molecular and Cellular Probes*, 36, 62-65.
- KOO, Y., WANG, J., ZHANG, Q., ZHU, H., CHEHAB, E. W., COLVIN, V. L., ALVAREZ, P. J. & BRAAM, J. 2015. Fluorescence reports intact quantum dot uptake into roots and translocation to leaves of *Arabidopsis thaliana* and subsequent ingestion by insect herbivores. *Environmental Science & Technology*, 49, 626-632.
- KOSTARELOS, K. 2008. The long and short of carbon nanotube toxicity. *Nature Biotechnology*, 26, 774-776.
- LAUTNER, G., BALOGH, Z., BARDOCZY, V., MESZAROS, T. & GYURCSANYI, R. E. 2010. Aptamer-based biochips for label-free detection of plant virus coat proteins by SPR imaging. *Analyst*, 135, 918-926.
- LE, T. T., CHUMPHUKAM, O. & CASS, A. E. G. 2014. Determination of minimal sequence for binding of an aptamer. A comparison of truncation and hybridization inhibition methods. *RSC Advances*, 4, 47227-47233.
- LI, W., NIE, Z., XU, X., SHEN, Q., DENG, C., CHEN, J. & YAO, S. 2009. A sensitive, label free electrochemical aptasensor for ATP detection. *Talanta*, 78, 954-958.
- LIAO, C.-Y., SMET, W., BRUNOUD, G., YOSHIDA, S., VERNOUX, T. & WEIJERS, D. 2015. Reporters for sensitive and quantitative measurement of auxin response. *Nature Methods*, 12, 207-210.
- LIU, C., CHEN, J., MAO, G., SU, C., JI, X. & HE, Z. 2016. Target-induced structure switching of a hairpin aptamer for the fluorescence detection of zeatin. *Analytical Methods*, 8, 5957-5961.
- LIU, Y. & WILSON, W. D. 2010. Quantitative analysis of small molecule-nucleic acid interactions with a biosensor surface and surface plasmon resonance detection. *Methods in Molecular Biology*, 613, 1-23.
- LOFKE, C., LUSCHNIG, C. & KLEINE-VEHN, J. 2013. Posttranslational modification and trafficking of PIN auxin efflux carriers. *Mechanism of Development*, 130, 82-94.
- LU, Q., ZHANG, L., CHEN, T., LU, M., PING, T. & CHEN, G. 2008. Identification and quantitation of auxins in plants by liquid chromatography/electrospray ionization ion trap mass spectrometry. *Rapid Communication in Mass Spectrometry*, 22, 2565-2572.
- MAŁGOWSKA, M., GUDANIS, D., TEUBERT, A., DOMINIAK, G. & GDANIEC, Z. 2012. How to study G-quadruplex structures. *BioTechnologia*, 4, 381-390.

- MANNING, K. 1991. Heterologous enzyme immunoassay for the determination of free indole-3-acetic acid (IAA) using antibodies against ring-linked IAA. *Journal of Immunological Methods*, 136, 61-68.
- MAYER, G. 2016. Nucleic Acid Aptamers: Selection, Characterization, and Application. *Methods in Molecular Biology*, 1380.
- MAYER, G. & HOVER, T. 2009. In vitro selection of ssDNA aptamers using biotinylated target proteins. *Methods in Molecular Biology*, 535, 19-32.
- MCKEAGUE, M., DE GIROLAMO, A., VALENZANO, S., PASCALE, M., RUSCITO, A., VELU, R., FROST, N. R., HILL, K., SMITH, M., MCCONNELL, E. M. & DEROSA, M. C. 2015. Comprehensive analytical comparison of strategies used for small molecule aptamer evaluation. *Analytical Chemistry*, 87, 8608-8612.
- MCKEAGUE, M. & DEROSA, M. C. 2012. Challenges and opportunities for small molecule aptamer development. *Journal of Nucleic Acids*, 2012, 748913.
- MCKEAGUE, M., VELU, R., HILL, K., BARDOCZY, V., MESZAROS, T. & DEROSA, M. C. 2014. Selection and characterization of a novel DNA aptamer for label-free fluorescence biosensing of ochratoxin A. *Toxins*, 6, 2435-2452.
- MEINKE, D. W., CHERRY, J. M., DEAN, C., ROUNSLEY, S. D. & KOORNNEEF, M. 1998. *Arabidopsis thaliana*: A Model Plant for Genome Analysis. *Science*, 282, 662-682.
- MEJAC, I., BRYAN, W. W., LEE, T. R. & TRAN, C. D. 2009. Visualizing the Size, Shape, Morphology, and Localized Surface Plasmon Resonance of Individual Gold Nanoshells by Near-Infrared Multispectral Imaging Microscopy. *Analytical Chemistry*, 81, 6687-6694.
- MENDONSA, S. D. & BOWSER, M. T. 2004. In Vitro Evolution of Functional DNA Using Capillary Electrophoresis. *Journal of American Chemical Society*, 126, 20-21.
- MILEWSKA-HENDEL, A., ZUBKO, M., STROZ, D. & KURCZYNSKA, E. U. 2019. Effect of Nanoparticles Surface Charge on the *Arabidopsis thaliana* (L.) Roots Development and Their Movement into the Root Cells and Protoplasts. *International Journal of Molecular Sciences*, 20, 1650.
- MITTLER, R. & LAM, E. 1997. Characterization of nuclease activities and DNA fragmentation induced upon hypersensitive response cell death and mechanical stress. *Plant Molecular Biology*, 34, 209-221.
- MONDINI, S., LEONZINO, M., DRAGO, C., FERRETTI, A. M., USSEGLIO, S., MAGGIONI, D., TORNESE, P., CHINI, B. & PONTI, A. 2015. Zwitterion-Coated Iron Oxide Nanoparticles: Surface Chemistry and Intracellular Uptake by *Hepatocarcinoma* (HepG2) Cells. *Langmuir*, 31, 7381-7390.
- MORITA, T., KATO, H., IWANAGA, S., TAKADA, K., KIMURA, T. & SAKAKIBARA, S. 1977. New Fluorogenic Substrates for α -Thrombin, Factor Xa, Kallikreins, and Urokinase. *Journal of Biochemistry*, 82, 1495-1498.
- MOUSIVAND, M., ANFOSSI, L., BAGHERZADEH, K., BARBERO, N., MIRZADI-GOHARI, A. & JAVAN-NIKKHAH, M. 2020. In silico maturation of affinity and selectivity of DNA aptamers against aflatoxin B1 for biosensor development. *Analytica Chimica Acta*, 1105, 178-186.
- MULLER, A., DUCHTING, P. & WEILER, E. W. 2002. A multiplex GC-MS/MS technique for the sensitive and quantitative single-run analysis of acidic phytohormones and related compounds, and its application to *Arabidopsis thaliana*. *Planta*, 216, 44-56.

- MUSHEEV, M. U. & KRYLOV, S. N. 2006. Selection of aptamers by systematic evolution of ligands by exponential enrichment: addressing the polymerase chain reaction issue. *Analytica Chimica Acta*, 564, 91-96.
- NAGATA, T. & MELCHERS, G. 1978. Surface Charge of Protoplasts and their Significance in Cell-Cell Interaction. *Planta*, 142, 235-238.
- NANOTEMPER TECHNOLOGIES 2018. User Manual Monolith® NT.115. V24_2018-04-05.
- NEVES, M. A. D., REINSTEIN, O., SAAD, M. & JOHNSON, P. E. 2010. Defining the secondary structural requirements of a cocaine-binding aptamer by a thermodynamic and mutation study. *Biophysical Chemistry*, 153, 9-16.
- NEVES, M. A. D., SLAVKOVIC, S., CHURCHER, Z. R. & JOHNSON, P. E. 2017. Salt-mediated two-site ligand binding by the cocaine-binding aptamer. *Nucleic Acids Research*, 45, 1041-1048.
- NGUYEN, B., TANIOUS, F. A. & WILSON, W. D. 2007. Biosensor-surface plasmon resonance: quantitative analysis of small molecule-nucleic acid interactions. *Methods*, 42, 150-61.
- NI, S., YAO, H., WANG, L., LU, J., JIANG, F., LU, A. & ZHANG, G. 2017. Chemical Modifications of Nucleic Acid Aptamers for Therapeutic Purposes. *International Journal of Molecular Sciences*, 18, 1683.
- NOVAK, O., NAPIER, R. & LJUNG, K. 2017. Zooming In on Plant Hormone Analysis: Tissue- and Cell-Specific Approaches. *Annual Reviews in Plant Biology*, 68:18, 1-18.26.
- NUTIU, R. & LI, Y. 2003. Structure-Switching Signaling Aptamers. *Journal of American Chemical Society*, 125, 4771-4778.
- NWANESHIUDU, A., KUSCHAL, C., SAKAMOTO, F. H., ANDERSON, R. R., SCHWARZENBERGER, K. & YOUNG, R. C. 2012. Introduction to confocal microscopy. *Journal of Investigative Dermatology*, 132, e3.
- O'NEAL, D. P., HIRSCH, L. R., HALAS, N. J., PAYNE, J. D. & WEST, J. L. 2004. Photo-thermal tumor ablation in mice using near infrared-absorbing nanoparticles. *Cancer Letters*, 209, 171-6.
- OBERHAUS, F. V., FRENSE, D. & BECKMANN, D. 2020. Immobilization Techniques for Aptamers on Gold Electrodes for the Electrochemical Detection of Proteins: A Review. *Biosensors*, 10, 45.
- ODEH, F., NSAIRAT, H., ALSHAER, W., ISMAIL, M. A., ESAWI, E., QAQISH, B., BAWAB, A. A. & ISMAIL, S. I. 2019. Aptamers Chemistry: Chemical Modifications and Conjugation Strategies. *Molecules*, 25, 3.
- OKUMOTO, S., TAKANAGA, H. & FROMMER, W. B. 2008. Quantitative imaging for discovery and assembly of the metabo-regulome. *New Phytologist*, 180, 271-295.
- ORTHAUS, S., BUSCHMANN, V., BÜLTER, A., FORE, S., KÖNIG, M. & ERDMANN, R. 2009. Quantitative *in vivo* imaging of molecular distances using FLIM-FRET. Application Note, PicoQuant.
- OTTENSCHLAGER, I., WOLFF, P., WOLVERTON, C., BHALERAU, R. P., SANDBERG, G., ISHIKAWA, H., EVANS, M. & PALME, K. 2003. Gravity-regulated differential auxin transport from columella to lateral root cap cells. *Proceedings of the National Academy of Sciences*, 100, 2987-2991.
- OU, H., CHENG, T., ZHANG, Y., LIU, J., DING, Y., ZHEN, J., SHEN, W., XU, Y., YANG, W., NIU, P., LIU, J., AN, Y., LIU, Y. & SHI, L. 2018. Surface-adaptive zwitterionic nanoparticles for prolonged blood circulation time and enhanced cellular uptake in tumor cells. *Acta Biomaterialia*, 65, 339-348.

- PAN, W. & CLAWSON, G. A. 2009. The shorter the better: reducing fixed primer regions of oligonucleotide libraries for aptamer selection. *Molecules*, 14, 1353-1369.
- PARK, J. W., TATAVARTY, R., KIM, D. W., JUNG, H. T. & GU, M. B. 2012. Immobilization-free screening of aptamers assisted by graphene oxide. *Chemical Communications*, 48, 2071-2073.
- PERELSON, A. S. & DEEKS, S. G. 2011. Drug effectiveness explained: the mathematics of antiviral agents for HIV. *Science Translational Medicine*, 3, 91ps30.
- PFEIFFER, F. & MAYER, G. 2016. Selection and Biosensor Application of Aptamers for Small Molecules. *Frontiers in Chemistry*, 4, 25.
- PIETROWSKA-BOREK, M., DOBROGOJSKI, J., SOBIESZCZUK-NOWICKA, E. & BOREK, S. 2020. New Insight into Plant Signaling: Extracellular ATP and Uncommon Nucleotides. *Cells*, 9, 345.
- PONZO, I., MOLLER, F. M., DAUB, H. & MATSCHEKO, N. 2019. A DNA-Based Biosensor Assay for the Kinetic Characterization of Ion-Dependent Aptamer Folding and Protein Binding. *Molecules*, 24, 2877.
- PORFIRIO, S., GOMES DA SILVA, M. D. R., PEIXE, A., CABRITA, M. J. & AZADI, P. 2016. Current analytical methods for plant auxin quantification--A review. *Analytica Chimica Acta*, 902, 8-21.
- PRANTE, M., SCHULING, T., ROTH, B., BREMER, K. & WALTER, J. 2019. Characterization of an Aptamer Directed against 25-Hydroxyvitamin D for the Development of a Competitive Aptamer-Based Assay. *Biosensors*, 9, 134.
- PRANTE, M., SEGAL, E., SCHEPER, T., BAHNEMANN, J. & WALTER, J. 2020. Aptasensors for Point-of-Care Detection of Small Molecules. *Biosensors*, 10, 108.
- PRODEUS, A., ABDUL-WAHID, A., FISCHER, N. W., HUANG, E. H., CYDZIK, M. & GARIEPY, J. 2015. Targeting the PD-1/PD-L1 Immune Evasion Axis With DNA Aptamers as a Novel Therapeutic Strategy for the Treatment of Disseminated Cancers. *Molecular Therapy-Nucleic Acids*, 4, e237.
- QI, C., BING, T., MEI, H., YANG, X., LIU, X. & SHANGGUAN, D. 2013. G-quadruplex DNA aptamers for zeatin recognizing. *Biosensors and Bioelectronics*, 41, 157-162.
- QI, Y., CHEN, Y., XIU, F.-R. & HOU, J. 2020. An aptamer-based colorimetric sensing of acetamiprid in environmental samples: Convenience, sensitivity and practicability. *Sensors and Actuators B: Chemical*, 304, 127359.
- REINEMANN, C., FREIIN VON FRITSCH, U., RUDOLPH, S. & STREHLITZ, B. 2016. Generation and characterization of quinolone-specific DNA aptamers suitable for water monitoring. *Biosensors and Bioelectronics*, 77, 1039-1047.
- REINSTEIN, O., YOO, M., HAN, C., PALMO, T., BECKHAM, S. A., WILCE, M. C. & JOHNSON, P. E. 2013. Quinine binding by the cocaine-binding aptamer. Thermodynamic and hydrodynamic analysis of high-affinity binding of an off-target ligand. *Biochemistry*, 52, 8652-8662.
- RENAUD DE LA FAVERIE, A., GUEDIN, A., BEDRAT, A., YATSUNYK, L. A. & MERGNY, J. L. 2014. Thioflavin T as a fluorescence light-up probe for G4 formation. *Nucleic Acids Research*, 42, e65.
- RICO, C. M., MAJUMDAR, S., DUARTE-GARDEA, M., PERALTA-VIDEA, J. R. & GARDEA-TORRESDEY, J. L. 2011. Interaction of nanoparticles with edible plants and their possible implications in the food chain. *Journal of Agricultural and Food Chemistry*, 59, 3485-3498.

- ROXO, C., KOTKOWIAK, W. & PASTERNAK, A. 2019. G-Quadruplex-Forming Aptamers-Characteristics, Applications, and Perspectives. *Molecules*, 24, 3781.
- RUIGROK, V. J., LEVISSON, M., HEKELAAR, J., SMIDT, H., DIJKSTRA, B. W. & VAN DER OOST, J. 2012. Characterization of aptamer-protein complexes by X-ray crystallography and alternative approaches. *International Journal of Molecular Science*, 13, 10537- 10552.
- RUSCITO, A. & DEROSA, M. C. 2016. Small-Molecule Binding Aptamers: Selection Strategies, Characterization, and Applications. *Frontiers in Chemistry*, 4, 14.
- RŮŽIČKA, K. & HEJÁTKO, J. 2017. Auxin transport and conjugation caught together. *Journal of Experimental Botany*, 68, 4409-4412.
- SADANANDOM, A. & NAPIER, R. M. 2010. Biosensors in plants. *Current Opinion in Plant Biology*, 13, 736-743.
- SAKAMOTO, T. 2017. NMR study of aptamers. *Aptamers*, 1, 13-18.
- SANTRA, S., LIESENFELD, B., BERTOLINO, C., DUTTA, D., CAO, Z., TAN, W., MOUDGIL, B. M. & MERICLE, R. A. 2006. Fluorescence lifetime measurements to determine the core-shell nanostructure of FITC-doped silica nanoparticles: An optical approach to evaluate nanoparticle photostability. *Journal of Luminescence*, 117, 75-82.
- SATTELMACHER, B. 2001. The apoplast and its significance for plant mineral nutrition. *New Phytologist*, 149, 167-192.
- SAVORY, N., LEDNOR, D., TSUKAKOSHI, K., ABE, K., YOSHIDA, W., FERRI, S., JONES, B. V. & IKEBUKURO, K. 2013. *In silico* maturation of binding-specificity of DNA aptamers against *Proteus mirabilis*. *Biotechnology and Bioengineering*, 110, 2573-2580.
- SCHWIEBERT, E. M. & ZSEMBERY, A. 2003. Extracellular ATP as a signaling molecule for epithelial cells. *Biochimica et Biophysica Acta*, 1615, 7-32.
- SEFAH, K., SHANGGUAN, D., XIONG, X., O'DONOGHUE, M. B. & TAN, W. 2010. Development of DNA aptamers using Cell-SELEX. *Nature Protocols*, 5, 1169-1185.
- SEIDEL, S. A., DIJKMAN, P. M., LEA, W. A., VAN DEN BOGAART, G., JERABEK-WILLEMSSEN, M., LAZIC, A., JOSEPH, J. S., SRINIVASAN, P., BAASKE, P., SIMEONOV, A., KATRITCH, I., MELO, F. A., LADBURY, J. E., SCHREIBER, G., WATTS, A., BRAUN, D. & DUHR, S. 2013. Microscale thermophoresis quantifies biomolecular interactions under previously challenging conditions. *Methods*, 59, 301-315.
- SHAKESHEFF, K. M., EVORA, C., SORIANO, I. & LANGER, R. 1997. The Adsorption of Poly(vinyl alcohol) to Biodegradable Microparticles Studied by X-Ray Photoelectron Spectroscopy (XPS). *Journal of Colloid and Interface Science*, 185, 538-547.
- SHANG, L., NIENHAUS, K. & NIENHAUS, G. U. 2014. Engineered nanoparticles interacting with cells: size matters. *Journal of Nanobiotechnology*, 12:5.
- SHAO, K., DING, W., WANG, F., LI, H., MA, D. & WANG, H. 2011. Emulsion PCR: a high efficient way of PCR amplification of random DNA libraries in aptamer selection. *Public Library of Science One*, 6, e24910.
- SHOMER, I., NOVACKY, A. J., PIKE, S. M., YERMIYAHU, U. & KINRAIDE, T. B. 2003. Electrical potentials of plant cell walls in response to the ionic environment. *Plant Physiology*, 133, 411-422.

- SIKDER, A., PEARCE, A. K., PARKINSON, S. J., NAPIER, R. & O'REILLY, R. K. 2021. Recent Trends in Advanced Polymer Materials in Agriculture Related Applications. *ACS Applied Polymer Materials*, 3, 1203-1217.
- SLAVKOVIC, S., ALTUNISIK, M., REINSTEIN, O. & JOHNSON, P. E. 2015. Structure-affinity relationship of the cocaine-binding aptamer with quinine derivatives. *Bioorganic & Medicinal Chemistry*, 23, 2593-2597.
- SLAVKOVIC, S. & JOHNSON, P. E. 2018. Isothermal titration calorimetry studies of aptamer-small molecule interactions: practicalities and pitfalls. *Aptamers*, 2, 45-51.
- SLYUSAREVA, E. A. & GERASIMOVA, M. A. 2014. pH-Dependence of the Absorption and Fluorescent Properties of Fluorone Dyes in Aqueous Solutions. *Russian Physics Journal*, 56, 1370-1377.
- SMESTAD, J. & MAHER, L. J., 3RD 2013. Ion-dependent conformational switching by a DNA aptamer that induces remyelination in a mouse model of multiple sclerosis. *Nucleic Acids Research*, 41, 1329-1342.
- SMITH, A. M., GAO, X. & NIE, S. 2004. Quantum Dot Nanocrystals for *In Vivo* Molecular and Cellular Imaging. *Photochemistry and Photobiology*, 80, 377-385.
- SONG, Y. 2014. Insight into the mode of action of 2,4-dichlorophenoxyacetic acid (2,4-D) as an herbicide. *Journal of Integrative Plant Biology*, 56, 106-113.
- SONG, Y., SONG, J., WEI, X., HUANG, M., SUN, M., ZHU, L., LIN, B., SHEN, H., ZHU, Z. & YANG, C. 2020. Discovery of Aptamers Targeting the Receptor-Binding Domain of the SARS-CoV-2 Spike Glycoprotein. *Anal Chem*, 92, 9895-9900.
- STOLTENBURG, R., NIKOLAUS, N. & STREHLITZ, B. 2012. Capture-SELEX: Selection of DNA Aptamers for Aminoglycoside Antibiotics. *Journal of Analytical Methods in Chemistry*, 2012, 415697.
- STOLTENBURG, R., REINEMANN, C. & STREHLITZ, B. 2005. FluMag-SELEX as an advantageous method for DNA aptamer selection. *Analytical and Bioanalytical Chemistry*, 383, 83-91.
- SYPAJEKOVA, M., BEKMURZAYEVA, A., WANG, R., LI, Y., NOGUES, C. & KANAYEVA, D. 2017. Selection, characterization, and application of DNA aptamers for detection of *Mycobacterium tuberculosis* secreted protein MPT64. *Tuberculosis*, 104, 70-78.
- TANAKA, K., CHOI, J., CAO, Y. & STACEY, G. 2014. Extracellular ATP acts as a damage-associated molecular pattern (DAMP) signal in plants. *Frontiers in Plant Science*, 5, 446.
- TANAKA, K., GILROY, S., JONES, A. M. & STACEY, G. 2010. Extracellular ATP signaling in plants. *Trends in Cell Biology*, 20, 601-608.
- LIFE TECHNOLOGIES, 2014. TOPO® TA Cloning® Kit for Sequencing. MAN0000109 revision A.0.
- TIAN, F., GREPLOVA, M., FREBORT, I., DALE, N. & NAPIER, R. 2014. A highly selective biosensor with nanomolar sensitivity based on cytokinin dehydrogenase. *Public Library of Science One*, 9, e90877.
- TIAN, M., WANG, J., ZHANG, E., LI, J., DUAN, C. & YAO, F. 2013. Synthesis of agarose-graft-poly[3-dimethyl (methacryloyloxyethyl) ammonium propanesulfonate] zwitterionic graft copolymers via ATRP and their thermally-induced aggregation behavior in aqueous media. *Langmuir*, 29, 8076-8085.

- TIVENDALE, N. D., ROSS, J. J. & COHEN, J. D. 2014. The shifting paradigms of auxin biosynthesis. *Trends in Plant Science*, 19, 44-51.
- TOLLE, F., WILKE, J., WENGEL, J. & MAYER, G. 2014. By-product formation in repetitive PCR amplification of DNA libraries during SELEX. *Public Library of Science One*, 9, e114693.
- TRAUTMANN, S., BUSCHMANN, V., SANDRA ORTHAUS, F. K., ORTMANN, U. & ERDMANN, R. 2013. Fluorescence Lifetime Imaging (FLIM) in Confocal Microscopy Applications: An Overview. Application Note, PicoQuant.
- TRIPATHI, D. K., SHWETA, SINGH, S., SINGH, S., PANDEY, R., SINGH, V. P., SHARMA, N. C., PRASAD, S. M., DUBEY, N. K. & CHAUHAN, D. K. 2017. An overview on manufactured nanoparticles in plants: Uptake, translocation, accumulation and phytotoxicity. *Plant Physiology and Biochemistry*, 110, 2-12.
- TSUCHIYA, K., YILMAZ, N., MIYAMOTO, T., MASUNAGA, H. & NUMATA, K. 2020. Zwitterionic Polypeptides: Chemoenzymatic Synthesis and Loosening Function for Cellulose Crystals. *Biomacromolecules*, 21, 1785-1794.
- URMANN, K., MODREJEWSKI, J., SCHEPER, T. & WALTER, J.-G. 2017. Aptamer-modified nanomaterials: principles and applications. *BioNanoMaterials*, 18(1-2): 20160012.
- VESNAVER, G. & BRESLAUER, K. J. 1991. The contribution of DNA single-stranded order to the thermodynamics of duplex formation. *Proceedings of the National Academy of Sciences*, 88, 3569-3573.
- VU, C. Q., TANTIRUNGROTECHAI, Y. & SOONTORNWORAJIT, B. 2016. Truncation of PDGF-BB Aptamer by Secondary Structural Analysis and Immunoassay. *International Journal of Pharma Medicine and Biological Sciences*, 5, 86-90.
- WALIA, A., WAADT, R. & JONES, A. M. 2018. Genetically Encoded Biosensors in Plants: Pathways to Discovery. *Annual Review of Plant Biology*, 69, 497-524.
- WANG, X., GAO, X., HE, J., HU, X., LI, Y., LI, X., FAN, L. & YU, H. Z. 2019. Systematic truncating of aptamers to create high-performance graphene oxide (GO)-based aptasensors for the multiplex detection of mycotoxins. *Analyst*, 144, 3826-3835.
- WANG, Y., ZHOU, Y., XU, L., HAN, Z., YIN, H. & AI, S. 2018. Photoelectrochemical apta-biosensor for zeatin detection based on graphene quantum dots improved photoactivity of graphite-like carbon nitride and streptavidin induced signal inhibition. *Sensors and Actuators B: Chemical*, 257, 237-244.
- WANG, T., CHEN, C., LARCHER, L. M., BARRERO, R. A. & VEEDU, R. N. 2019. Three decades of nucleic acid aptamer technologies: Lessons learned, progress and opportunities on aptamer development. *Biotechnology Advances*, 37, 28-50.
- WISNIEWSKA, M., NOSAL-WIERCINSKA, A., OSTOLSKA, I., STERNIK, D., NOWICKI, P., PIETRZAK, R., BAZAN-WOZNIAK, A. & GONCHARUK, O. 2017. Nanostructure of Poly(Acrylic Acid) Adsorption Layer on the Surface of Activated Carbon Obtained from Residue After Supercritical Extraction of Hops. *Nanoscale Research Letters*, 12:2.
- WITT, M., WALTER, J. G. & STAHL, F. 2015. Aptamer Microarrays-Current Status and Future Prospects. *Microarrays*, 4, 115-132.

- WOODWARD, A. W. & BARTEL, B. 2005. Auxin: regulation, action, and interaction. *Annals of Botany*, 95, 707-735.
- WU, K., MA, C., ZHAO, H., HE, H. & CHEN, H. 2018. Label-Free G-Quadruplex Aptamer Fluorescence Assay for Ochratoxin A Using a Thioflavin T Probe. *Toxins*, 10, 198.
- YANG, D.-K., CHOU, C.-F. & CHEN, L.-C. 2018. Selection of aptamers for AMACR detection from DNA libraries with different primers. *RSC Advances*, 8, 19067-19074.
- YILDIRIM, T., TRAEGER, A., PREUSSGER, E., STUMPF, S., FRITZSCHE, C., HOEPPENER, S., SCHUBERT, S. & SCHUBERT, U. S. 2016. Dual Responsive Nanoparticles from a RAFT Copolymer Library for the Controlled Delivery of Doxorubicin. *Macromolecules*, 49, 3856-3868.
- YOSHITOMI, T., HAYASHI, M., OGURO, T., KIMURA, K., WAYAMA, F., FURUSHO, H. & YOSHIMOTO, K. 2020. Binding and Structural Properties of DNA Aptamers with VEGF-A-Mimic Activity. *Molecular Therapy Nucleic Acids*, 19, 1145-1152.
- ZHANG, M., LE, H. N. & YE, B. C. 2013. Graphene oxide-based fluorescent "on/off" switch for visual bioassay using "molecular beacon"-hosted Hoechst dyes. *ACS Applied Materials & Interfaces*, 5, 8278-8282.
- ZHANG, Y., CHEN, Y., YU, J. & BIRCH, D. J. S. 2017a. 'Endosytosis study of gold nanoparticles through FRET-FLIM approach', 2017 13th IASTED International Conference on Biomedical Engineering, Innsbruck, Austria, 20-21 February.
- ZHANG, Z. & LIU, J. 2018. An engineered one-site aptamer with higher sensitivity for label-free detection of adenosine on graphene oxide. *Canadian Journal of Chemistry*, 96, 957-963.
- ZHANG, Z., ONI, O. & LIU, J. 2017b. New insights into a classic aptamer: binding sites, cooperativity and more sensitive adenosine detection. *Nucleic Acids Research*, 45, 7593-7601.
- ZHAO, H., MA, C. & CHEN, M. 2019. A novel fluorometric method for inorganic pyrophosphatase detection based on G-quadruplex-thioflavin T. *Molecular and Cellular Probes*, 43, 29-33.
- ZHENG, X., HU, B., GAO, S. X., LIU, D. J., SUN, M. J., JIAO, B. H. & WANG, L. H. 2015. A saxitoxin-binding aptamer with higher affinity and inhibitory activity optimized by rational site-directed mutagenesis and truncation. *Toxicon*, 101, 41-47.
- ZHOU, J. & ROSSI, J. 2017. Aptamers as targeted therapeutics: current potential and challenges. *Nature Reviews Drug Discovery*, 16, 181-202.
- ZHOU, J., SOONTORNWORAJIT, B., SNIPES, M. P. & WANG, Y. 2011. Structural prediction and binding analysis of hybridized aptamers. *Journal of Molecular Recognition*, 24, 119-126.
- ZHU, Z. J., WANG, H., YAN, B., ZHENG, H., JIANG, Y., MIRANDA, O. R., ROTELLO, V. M., XING, B. & VACHET, R. W. 2012. Effect of surface charge on the uptake and distribution of gold nanoparticles in four plant species. *Environmental Science & Technology*, 46, 12391-12398.

Appendices

Appendix A: Phylogenetic trees of SELEX sub-libraries

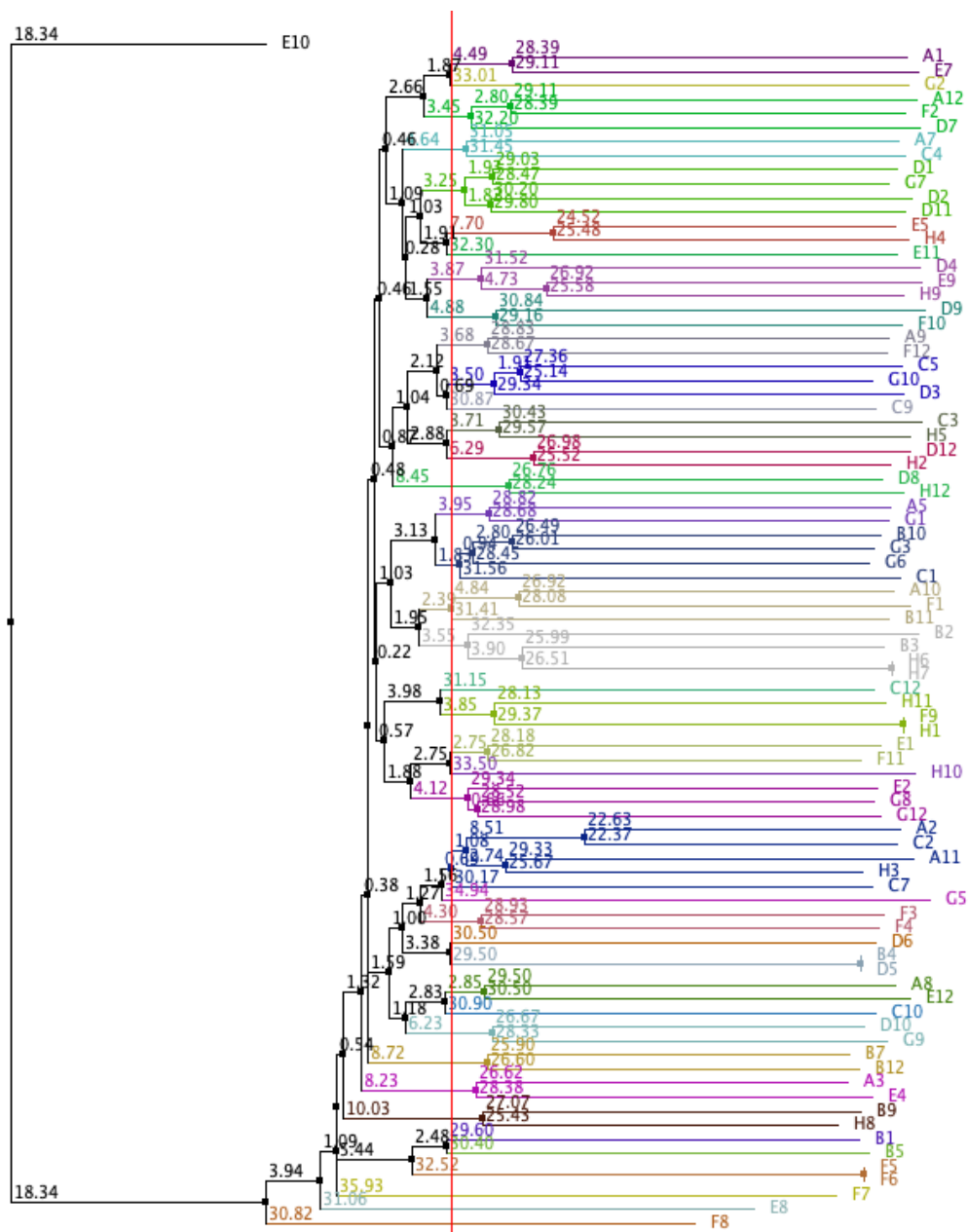


Figure A.1 **Phylogenetic tree of R10d sub-library generated by Jalview 2.11.1.3 software using a neighbour joining algorithm.** The threshold for sequence clustering is indicated by the red vertical line and each group is colour-coded.

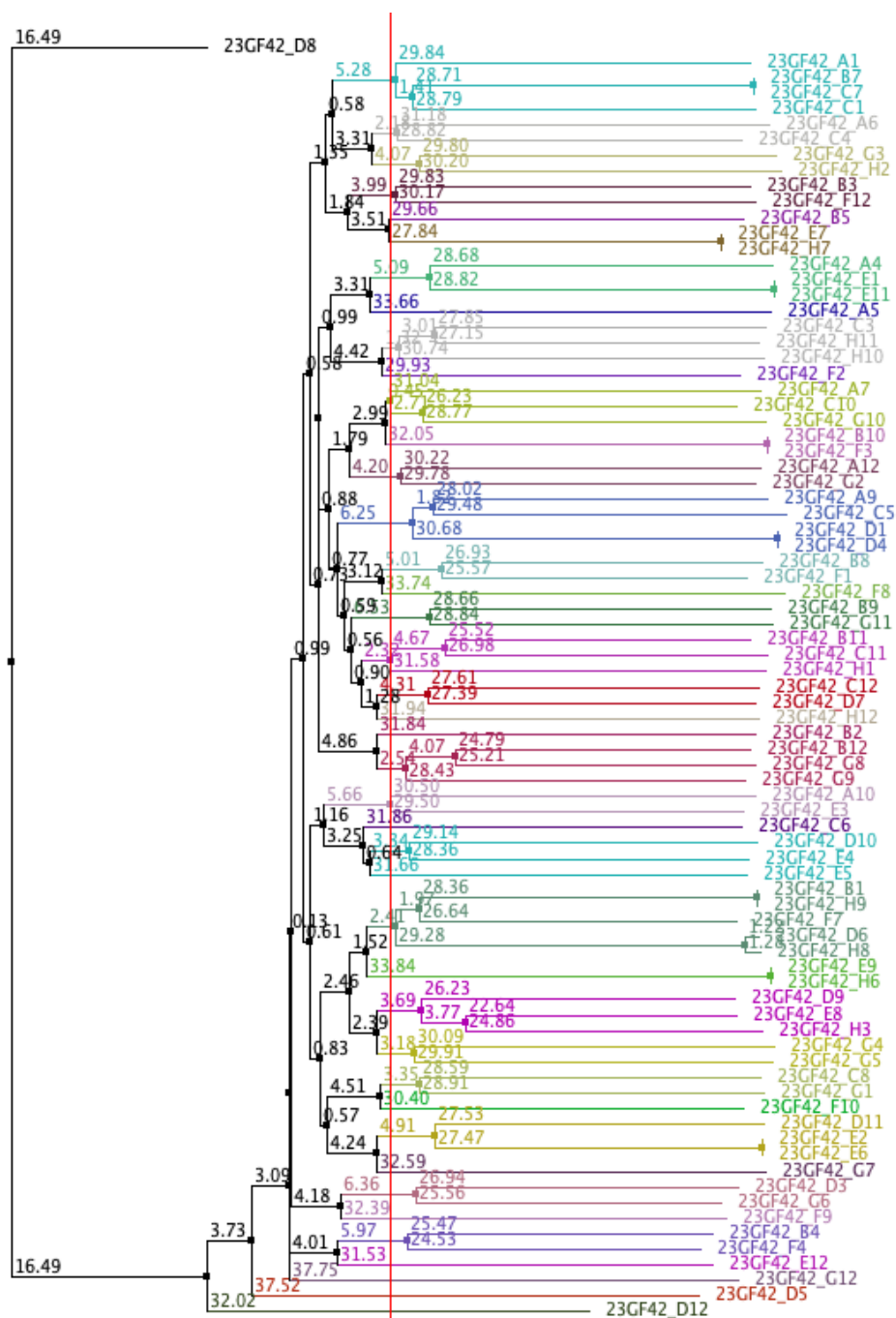


Figure A.2 Phylogenetic tree of R6s sub-library generated by Jalview 2.11.1.3 software using a neighbour joining algorithm. The threshold for sequence clustering is indicated by the red vertical line and each group is colour-coded.

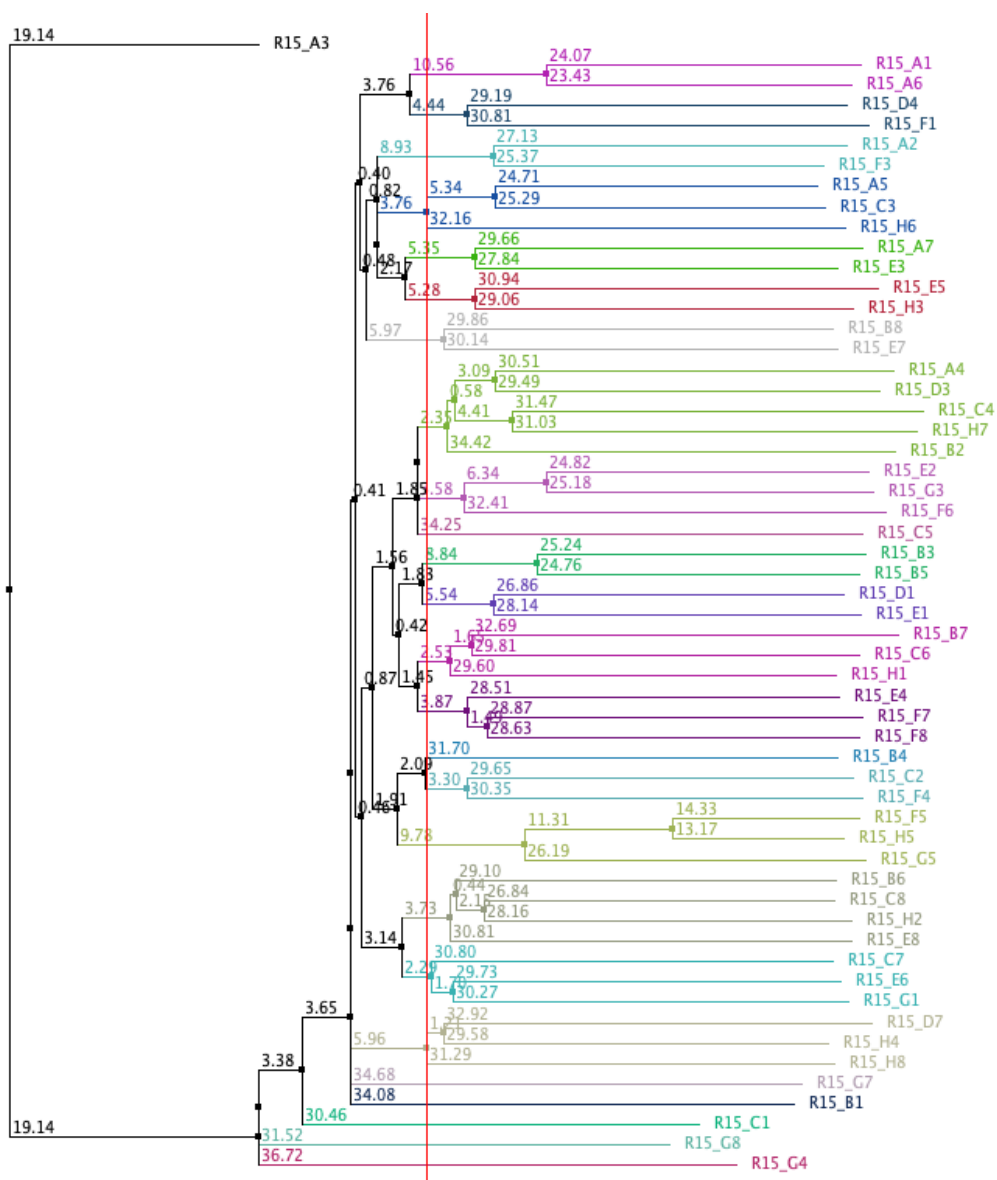


Figure A.3 **Phylogenetic tree of R15s sub-library generated by Jalview 2.11.1.3 software using a neighbour joining algorithm.** The threshold for sequence clustering is indicated by the red vertical line and each group is colour-coded.

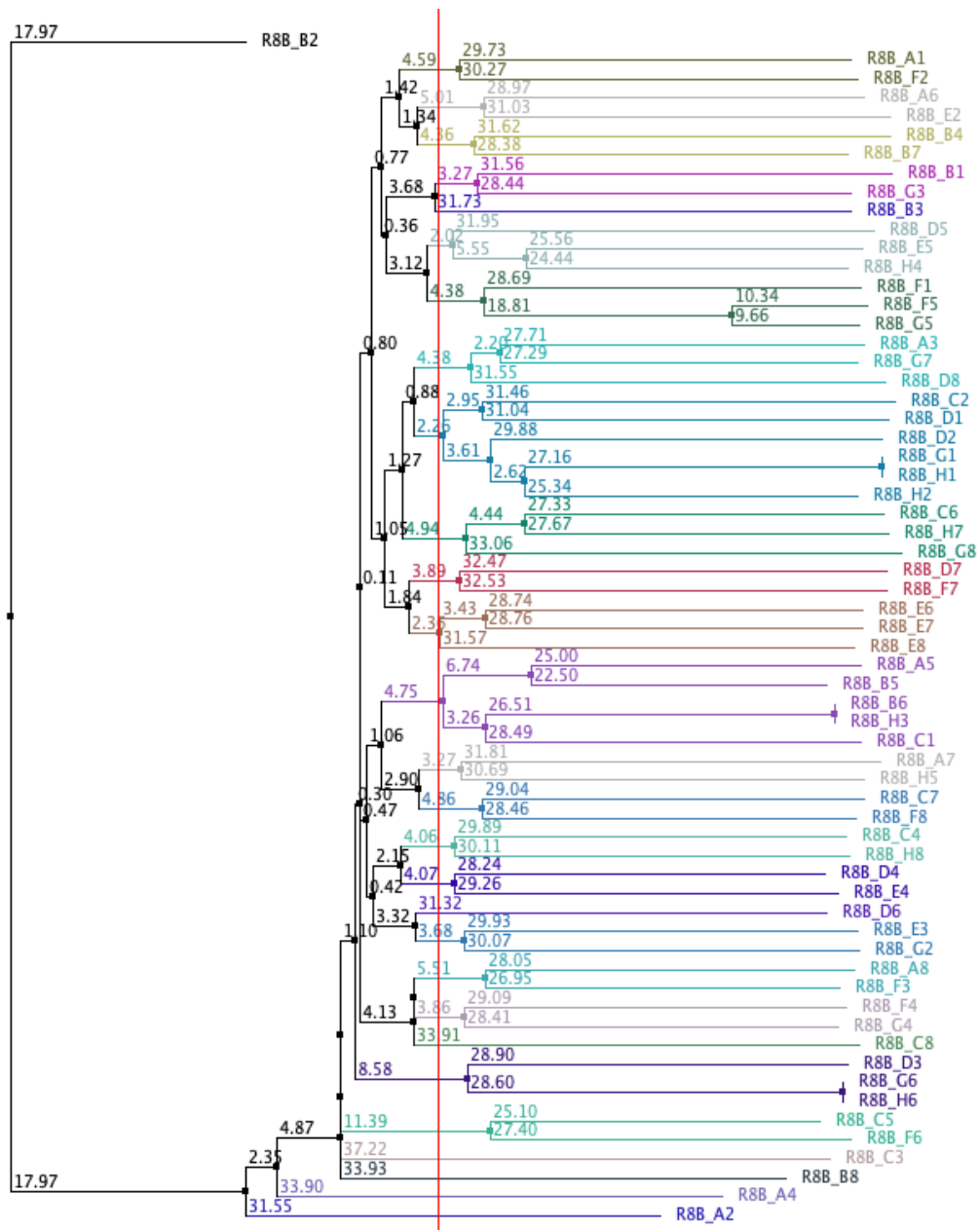


Figure A.4 **Phylogenetic tree of R8Bs sub-library generated by Jalview 2.11.1.3 software using a neighbour joining algorithm.** The threshold for sequence clustering is indicated by the red vertical line and each group is colour-coded.

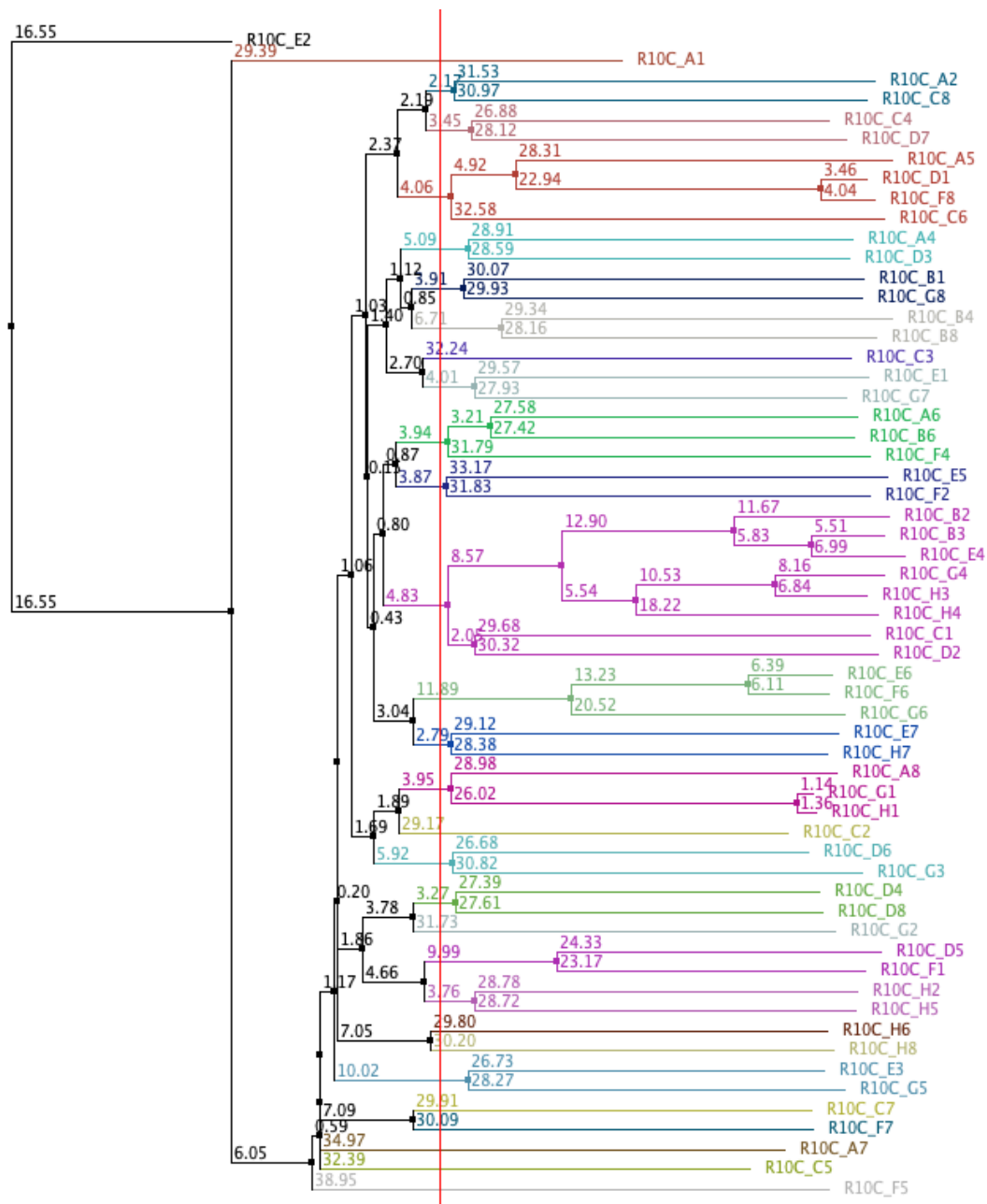


Figure A.5 Phylogenetic tree of R10Cs sub-library generated by Jalview 2.11.1.3 software using a neighbour joining algorithm. The threshold for sequence clustering is indicated by the red vertical line and each group is colour-coded.

Appendix B: Penetration level of negatively charged CPNs with different sizes followed the same trend as those of neutral CPNs.

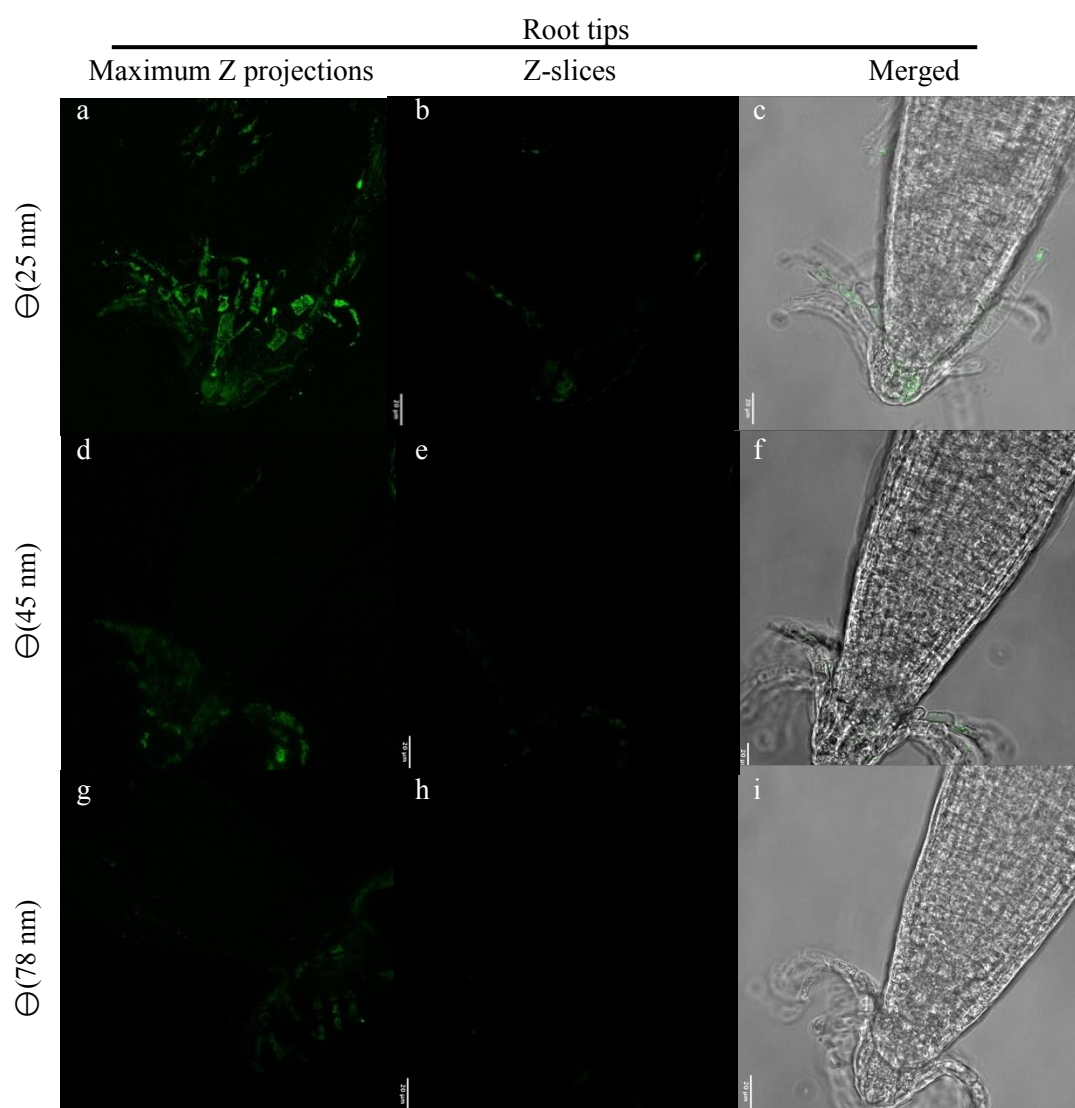


Figure B.1 **Significant influence of CPN size on penetrance in *A. thaliana* root tips.** Penetrance and accumulation of (a-c) $\Theta(25 \text{ nm})$, (d-f) $\Theta(45 \text{ nm})$, and (g-i) $\Theta(78 \text{ nm})$ were evaluated under ZEISS 880 LSM. Maximum Z projections were analysed alongside the Z-slices and merged with brightfield images using ImageJ software. Scale bar, 20 μm . The images are representatives of experimental replicates (n=3).

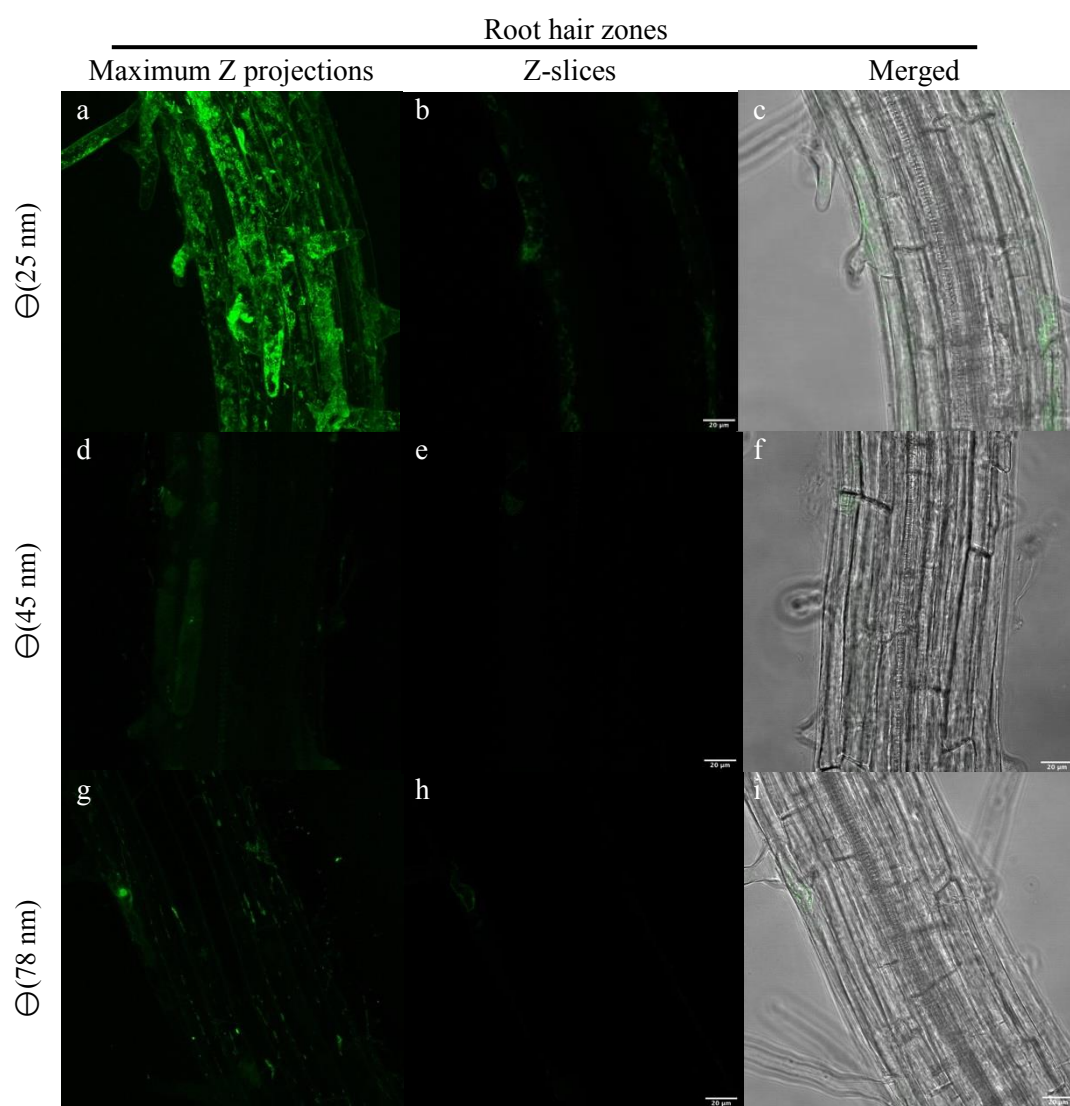


Figure B.2 **Significant influence of CPN size on penetrance in *A. thaliana* root tips.** Penetrance and accumulation of (a-c) $\Theta(25 \text{ nm})$, (d-f) $\Theta(45 \text{ nm})$, and (g-i) $\Theta(78 \text{ nm})$ were evaluated under ZEISS 880 LSM. Maximum Z projections were analysed alongside the Z-slices and merged with brightfield images using ImageJ software. Scale bar, 20 μm . The images are representatives of experimental replicates (n=3).

**Appendix C: A sheet-like accumulation of positively charged CPNs
was observed regardless of the particle sizes**

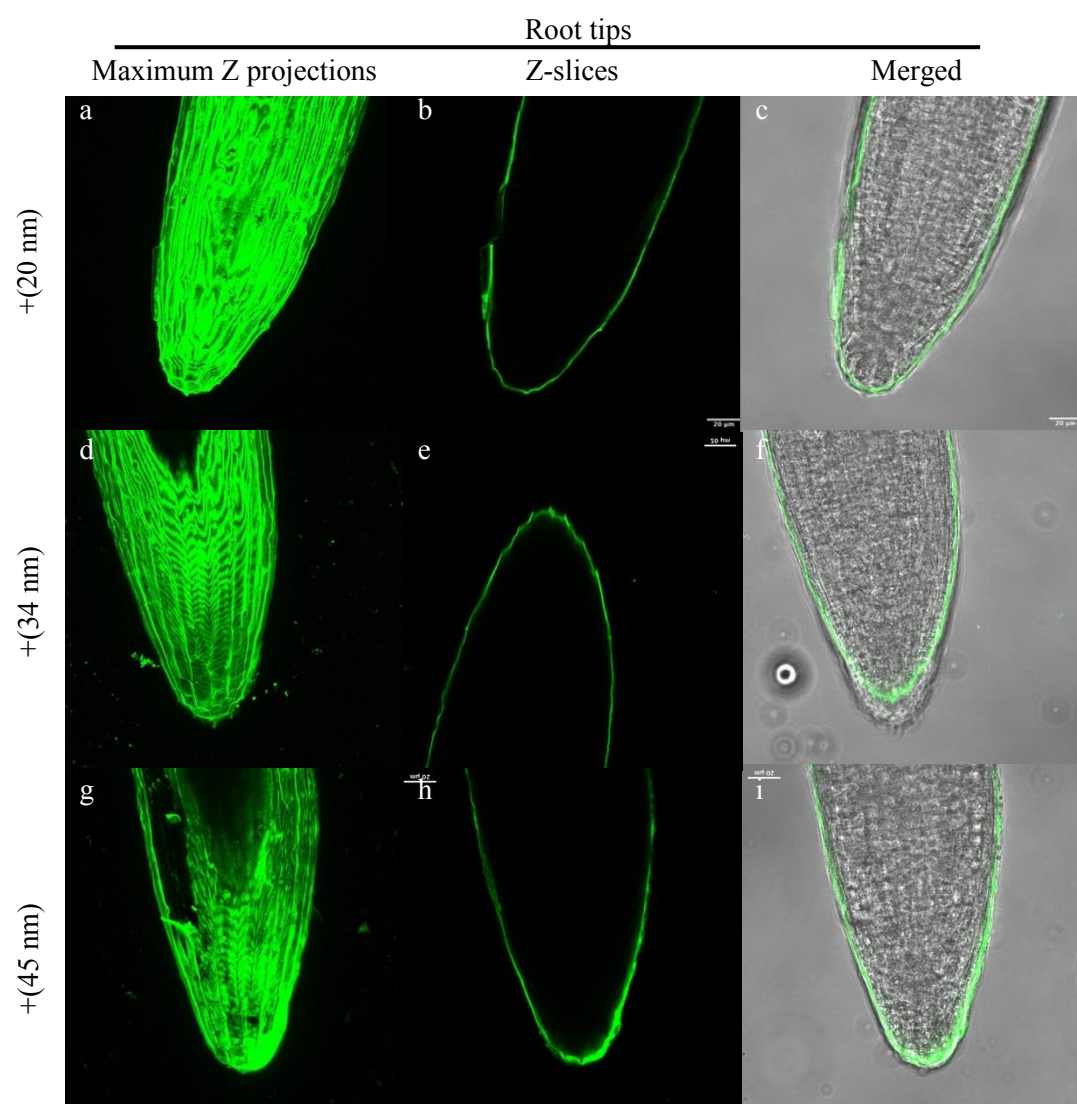


Figure C.1 **Sheet-like accumulation of positively charged CPNs regardless of the particle sizes was observed in *A. thaliana* root tips.** Penetrance and accumulation of (a-c) +(20 nm), (d-f) +(34 nm), and (g-i) +(45 nm) were evaluated under ZEISS 880 LSM. Maximum Z projections were analysed alongside the Z-slices and merged with brightfield images using ImageJ software. Scale bar, 20 μ m. The images are representatives of experimental replicates (n=3).

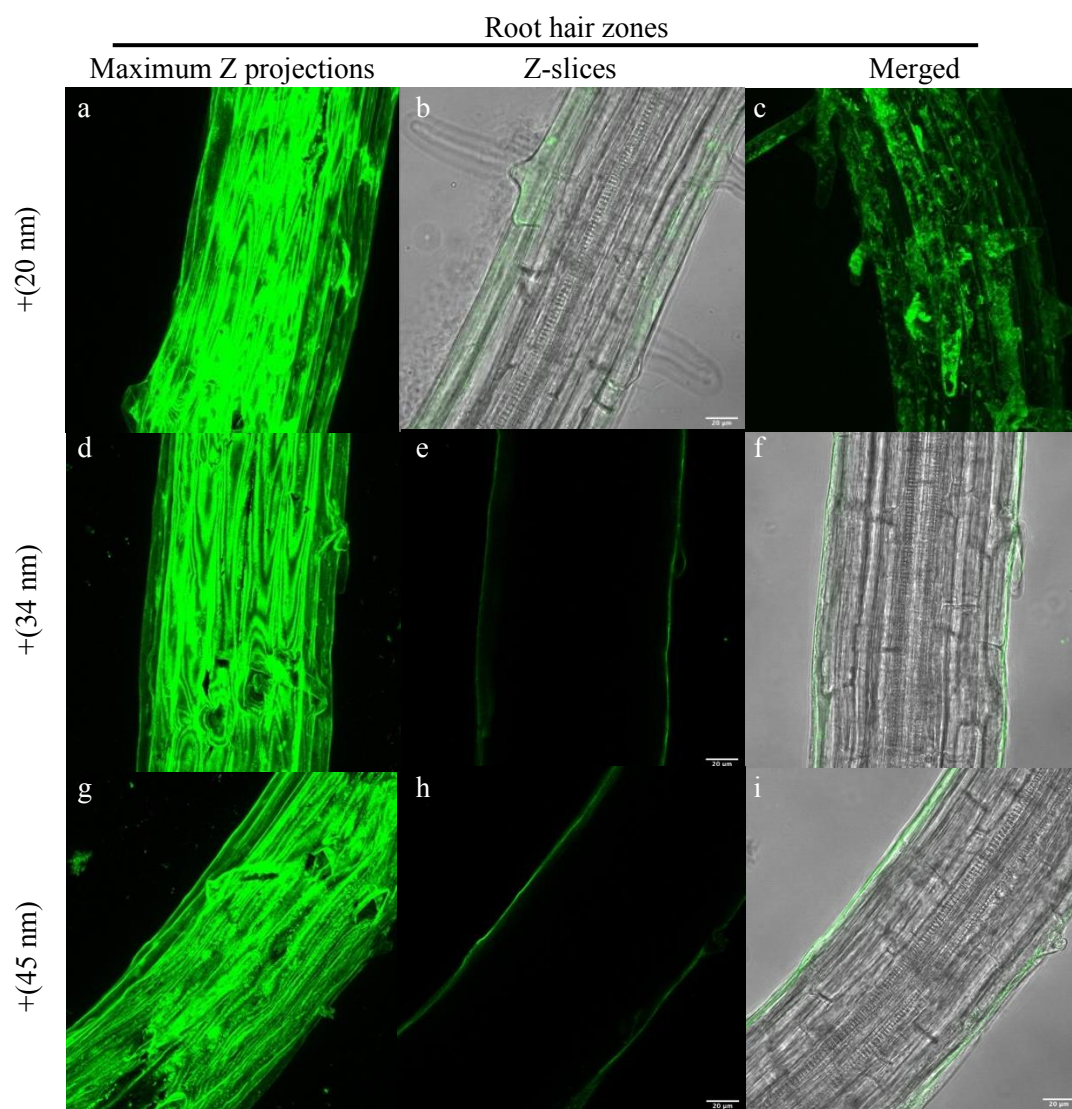


Figure C.2 **Sheet-like accumulation of positively charged CPNs regardless of the particle sizes was observed in *A. thaliana* root hair zones.** Penetrance and accumulation of (a-c) +(20 nm), (d-f) +(34 nm), and (g-i) +(45 nm) were evaluated under ZEISS 880 LSM. Maximum Z projections were analysed alongside the Z-slices and merged with brightfield images using ImageJ software. Scale bar, 20 μ m. The images are representatives of experimental replicates (n=3).

**Appendix D: Sheet-like accumulation of +(20 nm) around *A.*
thaliana intact roots over time**

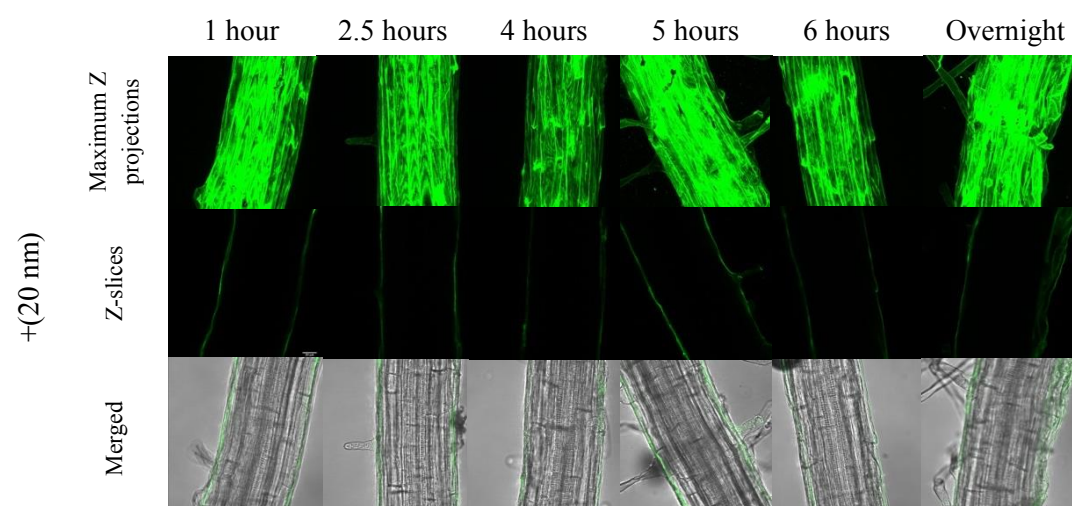


Figure D.1 **A saturated sheet-like accumulation of + (20 nm) in root hair zones over time.** Penetrance and accumulation of + (20 nm) was evaluated under ZEISS 880 LSM. Maximum Z projections were analysed alongside the Z-slice images along the xylem files and merged with brightfield images.